Universidade de Lisboa

Faculdade de Ciências
Departamento de Física

3D Image Reconstruction for a Dual Plate Positron Emission Tomograph: Application to Mammography.

Mónica Vieira Martins

Doutoramento em Biofísica

2007

Universidade de Lisboa

Faculdade de Ciências
Departamento de Física

3D Image Reconstruction for a Dual Plate Positron Emission Tomograph: Application to Mammography.

Mónica Vieira Martins

Thesis supervised by Prof. Doutor Pedro Dinis de Almeida
Instituto de Biofísica e Engenharia Biomédica
Faculdade de Ciências da Universidade de Lisboa

Doutoramento em Biofísica

2007

Contents

Resumo **xi**

Abstract **xv**

Acknowledgments **xvii**

I Introduction **1**

1 Introduction **3**

II Background **7**

2 Breast Cancer Imaging **9**

2.1 Introduction 9
2.2 X-ray Mammography 11
2.3 Breast Ecography 12
2.4 Magnetic Resonance Imaging 13
2.5 Scintimammography 15
2.6 Positron Emission Tomography 16
2.7 Conclusions 18

3 Positron Emission Mammography **19**

3.1 Introduction 19
3.2 Positron emission and detection 20
3.3 The performance of a scanner 20
3.3.1 Photon sensitivity 21
3.3.2 Spatial resolution 22
3.3.3 Energy Resolution 23
3.3.4 Time resolution 24
3.3.5 Photodetectors 24

3.4 Dedicated scanners for breast imaging . . . 25
3.4.1 The PEM-I system . . . 25
3.4.2 The Naviscan PEM Flex system . . . 27
3.4.3 The West Virginia University - Jefferson Lab PEM system . . . 29
3.4.4 The Duke University - Jefferson Lab PEM system . . . 30
3.4.5 The maxPET system . . . 31
3.4.6 The LNBL PEM system . . . 31
3.4.7 The YAP-PEM system . . . 32
3.5 Conclusions . . . 33

4 Image Reconstruction in PET **35**
4.1 Introduction . . . 35
4.2 Organizing the data . . . 36
4.3 Statistical Iterative Reconstruction Algorithms . . . 39
4.3.1 A model for the image . . . 39
4.3.2 A model for the physics of the measurement process . . . 40
4.3.3 A model for the data . . . 41
4.3.4 An objective function . . . 42
4.3.5 A numerical algorithm . . . 46
4.4 Expectation-Maximization Algorithms . . . 47
4.4.1 ML-EM . . . 47
4.4.2 OS-EM . . . 50
4.5 Bayesian iterative algorithms . . . 51
4.5.1 Defining a prior . . . 51
4.5.2 The One Step Late algorithm . . . 53
4.5.3 The Median Root Prior . . . 54
4.6 Conclusions . . . 55

III Materials and Methods **57**

5 The Clear-PEM scanner and Monte Carlo simulations **59**
5.1 Introduction . . . 59
5.2 The Clear-PEM scanner . . . 59
5.3 Monte Carlo Simulations . . . 61
5.3.1 Clear-PEM Monte Carlo simulation framework . . . 62
5.3.2 The simulated scanner geometries . . . 63
5.3.3 The Phantoms used . . . 64
5.4 Planes of the breast . . . 67
5.5 Conclusion . . . 68

6 The STIR library **69**
6.1 Introduction . . . 69
6.2 Images . . . 70
6.2.1 Image Coordinates and Conventions . . . 70
6.3 Projection Data . . . 71
6.3.1 Projection Data Coordinates and Conventions . . . 74
6.4 Projection operators . . . 74
6.4.1 Projection Matrix By Bin Hierarchy . . . 74
6.4.2 Forward Projection Hierarchy . . . 75
6.4.3 Backprojection Hierarchy . . . 77
6.5 Geometrical Symmetries . . . 82
6.6 Image Reconstruction Algorithms . . . 83
6.6.1 The OSMAPOSL algorithm . . . 84
6.6.2 The sensitivity image . . . 86
6.6.3 The MAP model and priors . . . 86
6.7 Conclusions . . . 87

IV Results **89**

7 Enhancements in the STIR framework **91**
7.1 Introduction . . . 91
7.2 The information on the projection data . . . 91
7.2.1 The class ProjDataInterfile . . . 92
7.2.2 The class ProjDataInfoPlanar . . . 92
7.2.3 Building the sinogram header . . . 96
7.2.4 Computing the sinogram indexes . . . 98
7.2.5 Dealing with the DOI information . . . 99
7.3 The projection operators for Clear-PEM . . . 100
7.4 The geometrical symmetries . . . 101
7.5 The test utilities . . . 102
7.6 Preliminary Evaluation . . . 102
7.6.1 Number of Subsets . . . 105
7.6.2 Number of rays to trace each bin . . . 111
7.6.3 Geometrical Symmetries . . . 116
7.6.4 One angular detector plates position . . . 121
7.7 Conclusions . . . 122

8 3D OS-EM image reconstruction for the Clear−PEM scanner 123
8.1 Introduction . . . 123
8.2 Simplified Scanner Geometry Studies . . . 123
8.2.1 Methods . . . 124
8.2.2 Results . . . 124
8.2.3 Discussion . . . 126
8.3 Effect of DOI information and rotation . . . 129
8.3.1 Methods . . . 130
8.3.2 Static Simulated Acquisition . . . 130
8.3.3 Dual Angle Simulated Acquisition . . . 140
8.3.4 Discussion . . . 146
8.4 Studies with the NCAT phantom . . . 150
8.4.1 The sensitivity image . . . 150
8.4.2 Methods . . . 152
8.4.3 Results . . . 153
8.4.4 Discussion . . . 162
8.5 Conclusions . . . 163

9 Bayesian Image Reconstruction for the Clear−PEM Scanner 167
9.1 Introduction . . . 167
9.2 Methods . . . 167
9.3 Results . . . 168
9.3.1 Chain Phantom . . . 168
9.3.2 NCAT Breast Phantom . . . 169
9.4 Conclusions . . . 186

V Main Conclusions and Future Work 191

10 Main Conclusions and Future Work 193

A Publications 201

Bibliography 215

To Paulo, Francisco, Júlia
and to the little one who is already on her way.

To all the women who will eventually
benefit from some of the work presented here.

Resumo

A imagiologia é um campo do conhecimento humano capaz de unir diversas áreas científicas em torno de objectivos comuns: física, engenharia, matemática, bioquímica, ciências médicas. Ao longo do último século, a imagiologia dotou a humanidade de uma plêiade de ferramentas que têm contribuído de forma decisiva para a compreensão do funcionamento do corpo humano. Entre outras aplicações, essas ferramentas são utilizadas como meios (praticamente) não invasivos de diagnóstico e estadiamento de doenças, assim como de planeamento e avaliação de terapias. A imagiologia do cancro da mama é um bom exemplo de como os vários métodos de imagem médica podem contribuir de forma decisiva para a diminuição do impacto de uma doença de elevadas incidência e mortalidade. A mamografia de raios-X é a técnica imagiológica mais utilizada no rastreio e avaliao imagiológica no caso do cancro da mama. Outros métodos, como a Ecografia mamária ou a Imagem de Ressonância Magnética da mama, são importantes técnicas adjuvantes da mamografia por raios-X. No entanto, a informação fornecida pelas técnicas acima mencionadas é essencialmente de natureza anatómica. As alterações anatómicas e morfológicas são precedidas por alterações funcionais. Assim, técnicas imagiológicas que forneçam informação complementar sobre alterações funcionais e metabólicas dos tecidos, como a Tomografia por Emissão de Positrões (TEP) ou a Cintimamografia podem também contribuir para a diminuição da morbilidade e mortalidade associada a esta doença. Estas técnicas, no entanto, são especialmente direccionadas para exames de corpo inteiro, pelo que possuem uma sensibilidade limitada para a detecção de pequenos tumores na mama. De facto, estudos clínicos indicam que a TEP possui uma baixa sensibilidade para a detectacção de lesões mamárias com menos de 1 cm. Neste contexto assistiu-se, nos últimos anos, a um esforço significativo no sentido de desenvolver sistemas de imagem comnpactos e dedicados à detecção de cancro da mama baseadas nas técnicas de Cintigrafia ou de TEP. Em especial, a técnica denominada Mamografia por Emissão de Positrões (MEP) ambiciona obter imagens da mama com instrumentos dedicados utilizando traçadores marcados com emissores de positrões.

Um dos intrumentos MEP em desenvolvimento é a câmara Clear-PEM. Este sistema,

que na altura de finalização deste trabalho se encontra em fase de montagem, foi projectado com o objectivo de ser um equipamento de elevadas resolução e sensibilidade, capaz de detectar pequenas lesões presented na glândula mamária. O sistema é constituído por duas placas de detecção com capacidade para realizar aquisições em várias posições em torno da mama da paciente e, adicionalmente, realizar um exame axilar complementar. O sistema possuirá a capacidade de medir a profundidade de interacção da radiação nos cristais detetores, uma medida conhecida por DOI (acrónimo do termo inglês *Depth of Interaction*) que é fundamental para a obtenção de uma resolução espacial elevada e isotrópica. Resultados experimentais indicam que deverá ser possível obter uma resolução em DOI para a câmara Clear-PEM da ordem de 2 mm FWHM. De entre os vários componentes que contribuem para o desempenho de um sistema de imagem MEP encontram-se os métodos utilizados para realizar a reconstrução de imagem a partir dos dados de projecção adquiridos pelo sistema. O objectivo do trabalho apresentado nesta tese era o desenvolvimento e caracterização de software de reconstrução tridimensional de imagem para a câmara Clear-PEM. Para esse efeito, foram abordadas questões tais como a enorme quantidade de dados a ser processados, a complexidade associada a métodos 3D de reconstrução de imagem, o facto da geometria de aquisição ser bastante diferente da geometria das câmaras TEP convencionais e a necessidade de incorporar no processo de reconstrução de imagem a informação DOI fornecida pelo equipamento. A biblioteca *open-source* de reconstrução de imagem STIR, originalmente desenvolvida para as câmaras TEP convencionais, de geometria cilíndrica, foi utilizada como base para os métodos 3D de reconstrução de imagem para a câmara Clear-PEM. A estrutura modular da biblioteca, escrita em linguagem de programação C++, permitiu a incorporação de novas classes e métodos adequados à geometria de aquisição particular da câmara em estudo. O método tradicional de histogramização dos dados em formato sinograma 3D foi adaptado para os dados adquiridos pela câmara Clear-PEM. O teste e a validação inicial das novas ferramentas introduzidas na biblioteca de reconstrução de imagem foram efectuados com recurso a dados simulados por métodos de Monte Carlo e por métodos analíticos, com fântomas geométricos simples. As imagens foram reconstruídas com o algoritmo iterativo estatístico OS-EM, após optimização do mesmo. Os resultados obtidos demonstraram a capacidade de reconstruir imagens em acordo visual com os objectos simulados, com elevada resolução espacial e características de ruído em concordância com o simulado e com o algoritmo iterativo estatístico utilizado. As ferramentas de reconstrução de imagem desenvolvidas e optimizadas foram utilizadas para estudar o impacto da resolução DOI e da aquisição em duas posições angulares das placas por oposição à aquisição com as placas de detecção numa única posição angular. Para esse efeito utilizaram-se dados simulados por Monte Carlo de fontes pontuais colocadas em diferentes pontos do campo de visão da câmara

(FOV, acrónima da expressão inglesa *Field of View*). Como seria de esperar, os resultados obtidos indicam que a aquisição em posição única das placas resulta em artefactos significativos nas imagens quando é considerada uma resolução em DOI baixa ou inexistente. Esses artefactos são significativamente reduzidos nas regiões próximas do centro da FOV quando se considera 2 mm FWHM DOI (o valor expectável para a câmara Clear-PEM) ou um valor ideal correspondendo a informação DOI exacta. Quando se considera a aquisição em dupla posição angular das placas de detecção e o valor de 2 mm FWHM DOI , não se verifica a existência de artefactos nas imagens. No entanto, a evolução irregular da resolução espacial medida em fontes próximas da periferia da FOV com o processo iterativo parece indicar que, nessas regiões da FOV, a qualidade da imagem teria a ganhar com aquisição de dados em posições adicionais das placas de detecção. Globalmente, os resultados obtidos indicam que, considerando a aquisição em duas posições perpendiculares das placas e o valor de resolução em DOI que se espera para a câmara Clear-PEM, a resolução espacial das imagens é $1.3\times1.3\times1.3$ mm^3 no centro do campo de visão da câmara e $1.5\times1.8\times2.0$ mm^3 a 1 cm da periferia da FOV da câmara. A capacidade de reconstruir imagens e de detectar lesões em condições mais realistas e próximas do cenário de um exame real foram avaliadas recorrendo a simulações de Monte Carlo. Nessas simulações foi utilizado um fântoma antropomórfico da mama contendo lesões modeladas como estruturas esféricas de diâmetros variáveis entre 3 mm e 10 mm. Os valores de fixação de radiofármaco considerados para os tecidos mamários (que não lesões) foram obtidos da literatura e corresponderam aos diferentes tipos de glândulas mamárias As imagens foram reconstruídas utilizando quer o algoritmo OS-EM quer o algortimo iterativo estatístico Bayeseano OS-MAP-OSL com o Median Root Prior. Os resultados obtidos demostram que o algoritmo OS-EM permite obter imagens de elevado contraste, embora com valores de razão sinal sobre ruído relativamente baixos para lesões localizadas próximo da parede toráxica. A utilização do algoritmo Bayseano permite controlar de forma mais eficaz o ruído produzido nas imagens no decorrer do processo iterativo. Consequentemente, os valores da razão sinal sobre ruído são mais elevados nestas imagens, por comparação com as obtidas com o OS-EM, embora com valores mais baixos de contraste entre as lesões e os tecidos adjacentes. Globalmente, os resultados da reconstrução indicam que deverá ser possível visualizar lesões de 3 mm em glândulas mamárias consituídas essencialmente por tecido adiposo e de 5 mm em glândulas mamárias ricas em tecido fibroglandular denso. Em conclusão, o software para reconstrução 3D de imagem apresentado nesta tese contribuiu para a avaliação do desempenho esperado da câmara Clear-PEM, dedicada à imagem da glandula mamária. Espera-se que possa também vir a contribuir para o

bom desempenho da câmara em ambiente clínico.

Palavras Chave: Cancro da mama; Tomografia por Emissão de Positrões; Geometria Planar em Medicina Nuclear; Algoritmos 3D de Reconstrução de Imagem; Algoritmos Iterativos Estatísticos.

Abstract

The Clear-PEM scanner is a compact, dedicated, dual plate positron emission tomograph that is being developed for imaging the breast. This scanner has been designed to be a high sensitivity, high resolution instrument, able to detect small breast cancerous lesions at an early stage of the disease. The scanner will acquire data using two detector plates at two perpendicular angular positions around the breast. It will be able to measure the Depth-of-Interaction (DOI) of the photons within the detector crystal with a foreseen resolution of 2mm FWHM. The work presented in this thesis deals with 3D image reconstruction for the Clear-PEM scanner.

A number of issues such as the unconventional nature of the acquisition geometry, the incorporation of the DOI information in the reconstruction process, the large amount of data to be processed and the complexity of 3D image reconstruction were addressed in this thesis. The STIR library, an open-source image reconstruction library, originally developed for conventional Positron Emission Tomography ring scanners was used as the basis for 3D image reconstruction of the Clear-PEM scanner. The modular structure of the library allowed incorporating classes and methods adequate to the particular geometry under study.

The validation and optimization of the enhanced library was performed with geometrical phantom Monte Carlo(MC) and analytical simulated data and with the 3D OS-EM algorithm available in STIR. The results obtained indicate that, with the tuned 3D image reconstruction algorithm the image spatial resolution is expected to be $1.3\times1.3\times1.3\text{mm}^3$ in the Field-of-View (FOV) center and $1.5\times1.8\times2.0\text{mm}^3$ at 1cm from the FOV edge. The ability to reconstruct data acquired in a realistic, clinical scenario was tested with MC simulated data of an anthropomorphic breast phantom. Images were reconstructed both with the OS-EM algorithm and with a Bayesian algorithm. The results obtained show that the OS-EM algorithm allows obtaining high contrast images, albeit with low signal-to-noise ratio values in lesions located near the chest wall. The use of a Bayesian algorithm allows improving the signal-to-noise ratio, albeit resulting in lower contrast images. Globally, the results indicate the possibility of visualizing 3mm diameter lesions in essentially fat tissue breasts and 5mm diameter lesion in dense fibroglandular breasts.

Keywords: Breast Cancer; Positron Emission Tomography; Dual Plate Geometry Scanners in Nuclear Medicine; 3D Image Reconstruction; Iterative Statistical Algorithms.

Acknowledgments

The work presented in this document is the result of many individual working hours but also, and probably more significantly, of the interaction with so many teachers, co-workers, colleagues and friends. I would like to express my gratitude to those who have contributed to this work:

- To Professor Pedro Almeida who has introduced me to the field of Nuclear Medicine and who has supervised my investigation work and the writing of this thesis. I want to thank him not only for the scientific advisement and guidance but also for his support, generosity and patience. His words of trust and encouragement throughout these years were very meaningful. His enthusiasm, creativity and long working hours toward new ideas and projects are an inspiration and an example to me.

- To Professor Eduardo Ducla-Soares, who, with his contagious enthusiasm and never ending good humor, introduced me to the fascinating world of biophysics, and who, since then, has never saved acts nor words of encouragement.

- To Professor João Varela, who is the soul of the Clear-PEM project and who consequently has contributed significantly for the work here presented. If he did not had the courage to initiate this project, this work would certainly not have been possible. His coordination, scientific and human skills are an example to me.

- To Professor Christian Morel, who has welcomed me at the PET Instrumentation Group at the Institute for High Energy Physics (IPHE) of the University of Lausanne in the distant beginning of my PhD, and who has guided my first steps with the STIR library.

- To the colleagues I had the luck to find at IPHE, specially Daniel Strul, Luc Simon, Giovanni Santin, Magalit Krueger and Jean-Baptiste Mosset.

- To the colleagues at LIP - Laboratório de Instrumentação e Partículas, Pedro Rodrigues and Andreia Trindade, who have developed the Monte Carlo simulation framework and produced the data that was used in this work.

- A very special thanks goes to the colleagues from IBEB that made part of the team that worked in the context of the image reconstruction and visualization software for the Clear−PEM scanner, namely Nuno Matela, Nuno Oliveira, Hugo Cordeiro and Marta Correia. Besides the richness that arouse from sharing common scientific questions, your constant good moods and good humor have greatly helped throughout these years.

- To Nuno Matela I am deeply thankful to the many elucidating discussions regarding image reconstruction issues, as well as the unmeasurable help on other scientific and practical questions. You really are a great working fellow!

- To Nuno Oliveira I must thank the visualization and image analysis tool he has developed. Many of the laborious procedures used to analyze the images for this work were made infinitely easier thanks to Quasimanager, formerly known as Quasianalyst.

- To my IBEB colleagues who also work in the field of Nuclear Medicine and Molecular Imaging, and with whom I have had the pleasure of learning so much: Luís Janeiro, Paula Alexandra Santos, Luís Freire and Susana Silva.

- To Ana Sousa and Beatriz Lampreia, for the important help in so many formal questions, and also for their friendship.

- To the teachers and many colleagues at IBEB with whom I have been privileged to share a common working place and who daily contribute for making IBEB such an enjoyable place to work: Professor Pedro Miranda, Professor Alexandre Andrade, Sandra, Sofia, Patrícia, Ricardo, Paula, Teresa, Gilberto....

- To everyone in my big family who, in so many different ways, has helped me to find the means and the strengths to finish this work.

- To Francisco and Júlia, for the delight they give to my life. They are my personal reminder of the fact that there are things by far more important in life than debugging a program or obtaining good quality reconstructed images.

- To Paulo, for being my shelter harbour. I am deeply grateful for your love, care, patience, understanding and sacrifice during these years.

This work was financed in part by Fundação para a Ciência e Tecnologia under grant SFRH/BD/3002/2000 and by AdI-Agência de Inovação.

Part I

Introduction

Chapter 1

Introduction

The medical imaging field has the power of bringing together many different areas of scientific knowledge: physics, engineering, mathematics, biochemistry, medical sciences. During the last century, the medical imaging field has provided humanity with a variety of tools that have decisively contributed to the understanding of the functioning of the human body and of its constituents, either in health or in disease. Among other applications, these tools have been invaluable as (almost) non invasive means to diagnose and to evaluate disease, as well as to plan and to evaluate treatment. Breast cancer imaging is a good example of how medical imaging modalities can diminish the number of patients suffering from this highly prevalent (at least in the western world [1]) and deadly disease. X-ray mammography is the most used technique for breast cancer imaging. This technique is used either as a complementary tool to clinical diagnosis or as an irreplaceable screening tool for the early detection of the disease. Other imaging methods such as breast Ecography and breast Magnetic Resonance Imaging play important roles as adjunct techniques to X-ray mammography. The information provided by the aforementioned techniques is, however, mainly anatomical, thus leaving space for imaging methods that are able to obtain information regarding functional or metabolic changes in tissues. Among these, molecular imaging methods such as Scintimammography and Positron Emission Mammography (PET) have been found to provide useful complementary information to the anatomical methods. However, both these techniques are tunned for whole body imaging, resulting in low sensitivity for the detection of small lesions in the breast.

In this context, last years have witnessed the birth of a tremendous effort to develop dedicated compact cameras for breast cancer imaging based in Scintimammography or in PET technologies. In particular, the approach that aims to image the breast with dedicated instruments that use tracers labeled with positron emitters has been named Positron Emission Mammography (PEM).

[1] Data for other countries is usually difficult to obtain.

One of the PEM instruments currently being developed is the Clear−PEM scanner. This scanner, which, by the time this works is being finished, is at its assembling stage, is designed to be a high resolution, high sensitivity instrument, able to detect small cancerous lesions in the breast at an early stage of the disease. The scanner is based in a dual detector plate with the capability of acquiring data around the breast of the patient and additionally perform a complementary axillary exam. The scanner also has Depth-of-Interaction capabilities, a fundamental measure to meet the requirements of a high resolution system. Among the several components that contribute to the performance of an imaging system, the methods used for the reconstruction of the images from the projection data acquired by the system play a fundamental role. The present thesis deals 3D image reconstruction software for the Clear−PEM scanner.

The aim of the work here presented was to develop and characterize the 3D image reconstruction software for the dual plate Clear-PEM scanner. A number of issues need to be addressed for that purpose, such as the large amount of data to be processed and the complexity implied in 3D image reconstruction methods, the non-standard acquisition geometry of the scanner and the incorporation in the image reconstruction process of the Depth-of-Interaction information measured by the system. The approaches followed to address these issues, the tests performed to test and tune the image reconstruction algorithms and the results obtained with Monte Carlo simulation data, which allow to foreseen some of the aspects of the performance of the Clear-PEM scanner, will be presented.

The **Part I−Introduction** is composed of the present **Chapter 1−Introduction**, where the context, motivations and general organization of the work are provided.

The **Part II−Background** comprises three chapters which include a review of the state of the art on the main knowledge fields that are related to the work developed in the present thesis. **Chapter 2−Breast Cancer Imaging** presents a review of the most important breast imaging modalities, focusing on the strengths and weaknesses of each technique. In this chapter it will became clear why technical improvements in some of these imaging methods, namely in Nuclear Medicine techniques, have the potential to push further the limits of breast imaging. In the following chapter, **Chapter 3−Positron Emission Mammography** we present an overview of some of the instrumentation issues that impact on the performance of positron emission tomography equipments. Emphasis is given on the most demanding aspects of dedicated instruments, such as the ones used to image the breast, the PEM systems, with respect to conventional whole body scanners. A literature review of the PEM scanners that are or have been developed, including the strategies used to reconstruct the data from these scanners is presented therein. The final chapter of the second part of this work, **Chapter 4−Image Reconstruction in PET** presents an overview of the fundamental characteristics of a class of image reconstruction algorithms that are commonly

used in Position Emission Tomography, the iterative statistical image reconstruction algorithms.

The **Part III−Methods** is composed of two chapters that describe the Clear-PEM scanner and the main utilities that were used in the development of this thesis. **Chapter 5−The Clear-PEM scanner and Monte Carlo simulations** is devoted to providing a general overview of the design of the Clear−PEM scanner. References are included to some of the expected performance characteristics of the scanner. The description of the Monte Carlo simulation framework that was developed for the design of the Clear−PEM scanner, and the results used to test and to tune the image reconstruction methods are presented. The simulation settings, as well as the analytical and anthropomorphic phantoms used are described in this chapter. The following chapter, **Chapter 6−The STIR library**, describes the image reconstruction software library that was used as the basis for the 3D image reconstruction software for the Clear−PEM scanner.

The **Part IV−Results** begins with **Chapter 7−Enhancements in the STIR framework** that describes the features that were introduced in the STIR library in order to use it with data proceeding from a non standard acquisition geometry such as the Clear−PEM scanner. This chapter also includes some initial tests that were performed with analytical phantom data and the tuned image reconstruction software. The following chapter, **Chapter 8−3D OS-EM image reconstruction for the Clear−PEM scanner** presents the results of the studies that were performed with 3D image reconstruction software and the Clear−PEM scanner Monte Carlo simulation data. The final chapter of Part IV is **Chapter 9−Bayesian Image Reconstruction for the Clear−PEM Scanner**, which describes the results of the image reconstruction of the Clear−PEM scanner simulation data with a Bayesian image reconstruction algorithm.

A summary of the work presented is this thesis is given in **PartV−Main Conclusions and Future Work**, together with a discussion of the main findings and the perspectives of future work. Finally, Appendix A lists the publications in which parts of the work presented in this thesis was published.

Part II

Background

Chapter 2

Breast Cancer Imaging

2.1 Introduction

Breast cancer is the second major cause of cancer-related mortality among the occidental female population [1]. Statistics indicate that one in ten women in the western world will develop breast cancer during her lifetime

Given the high incidence of breast cancer, as well as the high mortality rate associated with the disease, there have been great efforts to technically improve breast cancer imaging methods. These mainly aim at improving the capacity to detect lesions at an earlier stage, since early detection is the best means to reduce mortality, and to better differentiate malignant from benign lesions.

The breast is constituted by fibrous, glandular and adipose tissue. The fibrous and glandular tissues are structured into ducts and lobules, which are surrounded by the adipose tissue. The earliest form of breast cancer is Ductal Carcinoma *in Situ* (DCIS). In DCIS the cancer cells are confined to the breast ducts and have not invaded the surrounding fat tissue. This form of cancer is usually associated with microcalcifications that can be detected by mammography. Breast cancer can also appear confined to the lobules, in which case it is named Lobular Carcinoma *in Situ* (LCIS). Both DCIS and LCIS can degenerate into invasive carcinoma, if the carcinoma spreads to surrounding breast tissues. When a carcinoma is found in the breast, there is a need to ascertain if it has spread to other regions of the body. If so, the first sites to receive lymph from the tumor are the axillary lymph nodes. A sentinel lymph node biopsy can be performed in order to detect if and which lymph nodes are cancerous, and those will be removed. If the tumor has spread beyond the lymph nodes, whole body imaging techniques such as Computed Tomography (CT), Positron Emission Tomography (PET) or Single Emission Computed Tomography (SPECT) can be used to localize the metastasis.

X-ray mammography is the gold standard imaging technique for the detection and screening of breast cancer. Despite its success, x-ray mammography is not a perfect

technique, as we will see further in this chapter. Other imaging methods, such as breast ecography, magnetic resonance imaging (MRI), and nuclear medicine techniques (scintimammography (SM) and PET) have also an important role in the management of this disease, providing additional or complementary information to x-ray mammography. They are employed either to further characterize tissue lesions detected by mammography, or when the physical characteristics of the women's breast make mammography inconclusive, or when a women has known risk factors for breast cancer.
High risk factors for breast cancer include inherited genetic mutations in the BRCA1 and BRCA2 genes (these account for $5\% - 10\%$ of all breast cancer cases), a personal or familial history of breast cancer and high breast tissue mammographic density (that is, a high amount of glandular tissue relative to fatty tissue in the breast).
In this chapter we will briefly review the most significant modalities which are employed on breast cancer imaging, namely mammography, ecography, MRI and nuclear medicine techniques. We will overview the physical principles inherent to each of these modalities, as well as the morphological or functional characteristics of the lesions to which they are sensitive to. When possible, the sensitivity and specificity values available in the literature for the imaging modalities discussed will be presented. Sensitivity and specificity are two important parameters when evaluating the utility of a given imaging technique on detecting disease. Sensitivity refers to the ability of detecting lesions and is computed as the ratio of the true positive findings to the total number of positive exams. Specificity is the ability to distinguish malignant from benign lesions. It is computed as the ratio of the true negative findings to the total number of false exams. We will focus on the main advantages and pitfalls of each of these techniques, emphasizing how the most recent technical advances in each area are allowing to push further the boundaries of breast imaging.
Examples of images of the breast obtained with each of the techniques that will be presented in this chapter can be seen in Figure 2.1.

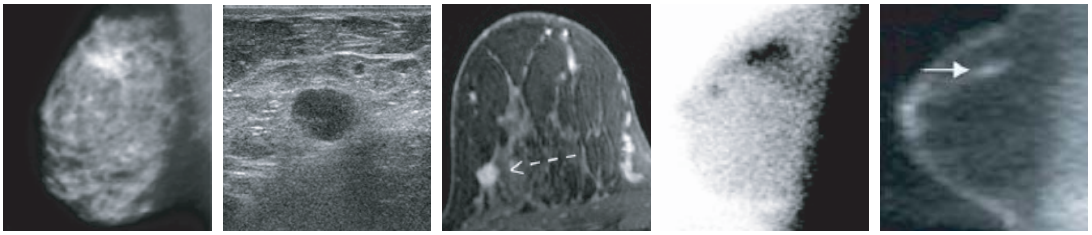

(a) (b) (c) (d) (e)

Figure 2.1: Breast cancer images obtained with (a)X-ray mammography [2], (b) Ecography [3] , (c) breast MRI [3], (d) scintimammography [2] and (d) PET [4].

.

2.2 X-ray Mammography

Conventional X-ray mammography has long been used for the detection of breast pathologies. It is used either as a screening tool or as a diagnostic tool, allowing further evaluation of suspected lesions found in clinical diagnosis (palpation). Screening mammography is the only screening test that has been proven in large clinical trials to decrease mortality from breast cancer [3]. Up to 30% decrease in breast cancer mortality in the screened population has been demontrated [5].

Mammography uses low energy X-rays that penetrate through the compressed breast and then exposes a photographic film placed on the opposite side of the breast. The image that is produced by mammography results from the variation in breast tissue densities that the X-ray beam has encountered along its path to the detector. Structures that more strongly attenuate the X-ray beam appear as whiter areas in the image. Mammographic features that are characteristic of breast cancer are masses, particularly irregular ones, architectural distortions of breast structures and clusters of microcalcifications. Microcalcifications can be detected by mammography due to its high resolution images. In fact, under optimal conditions, a resolution smaller than 150 μm can be obtained [3].

Unfortunately, areas of dense glandular tissue attenuate the X-ray beam similarly to masses and calcifications. As a consequence, cancers that present as small masses can be obscured by overlapping dense glandular tissue. Hence, the sensitivity of mammography for the detection of small breast cancers is reduced in women with dense breast tissue. Unfortunately, dense breast tissue is also a risk factor for breast cancer. Sensitivity is also diminished if there is a breast prosthesis or if the patient has scars resulting from previous surgery, biopsy or radiation procedures. With the optimal technique and patient conditions, mammography has a reported sensitivity between 69% and 90% [6]. Denser breasts are the main responsible for the lowest sensitivity values. Sensitivity is also dependent on the tumour size. In fatty breast, the size of detected tumour with mammography can be as small as 5 mm, but it is rarely less than 1-2 cm in dense breast.

The specificity of mammography relies on the ability to distinguish cancerous from noncancerous breast lesions based on their shapes and margins, that is, on morphology. Unfortunately, as malignant and benign lesions may have similar appearances, X-ray mammography has specificity between 10% and 40% [6], which means that there is a large fraction of false-positive results. As a result of its low specificity, breast lesion evaluation based solely on X-ray mammography results frequently in unnecessary biopsy procedures.

Other clinical areas in which mammography is of restricted use include the detection of lobular cancer and of ductal carcinoma *in situ*. The detection of DCIS is usually based

on the detection of the associated microcalcifications. However, it may happen that DCIS does not present microcalcifications, and, in this case, it usually is undetected by mammography.
Recently, digital mammography, which uses a digital receptor instead of the traditional screen film, resulting in a computer-generated image, was introduced for the detection of breast cancer. The use of imaging processing algorithms with the digital mammograms allows manipulating fine differences in image contrast. As a result, subtle differences, even in dense tissue, can be evaluated. Despite these promising characteristics, early experience with digital mammography has shown that the difference in cancer detection was not significant [5], although it reduces the number of unnecessary breast biopsies.
Mammographic breast cancer screening reduces breast cancer mortality, but, due to its low specificity and sensibility, breast mammography results in a considerable number of missed cancers and a large number of unnecessary breast biopsies. This is specially true if the breast is dense. Because of this limitations, other imaging modalities have been proposed as additional diagnostic tools for improving breast cancer detection.

2.3 Breast Ecography

Breast ecography is a technique that, when used as an adjunct to mammography, has been shown to improve the overall sensitivity of conventional breast imaging [7]. Furthermore, breast ecography systems are currently used to perform guided biopsies.
Medical ecography imaging involves the use of very high frequency sound waves (7-12 MHz)[8] that are produced by a transducer. These waves interact with the patient tissues, producing echoes whose amplitudes depend on the acoustic impedance of the tissues. The depth of the structures that produce the echoes are determined by the time difference between the emission and the return of the sound wave. The echoes amplitudes are encoded in a gray scale image.
The images obtained with breast ecography represent a two-dimensional cross section through the breast tissue. Therefore, unlike mammography, ecography imaging of the breast is not hindered by overlying dense tissue. Hence, some cancers that are not detected on mammography due to dense overlying tissue may be detected with breast ecography. However, although uncommon, some cancers have acoustical impedance similar to normal tissue and therefore may not be detected by breast ecography. Furthermore, current ecography image resolution is not enough to detect the small cancerous microcalcifications seen on mammography.
The major advantage of breast ecography over mammography is its capacity for differentiating solid from cystic breast lesions, which are fluid in nature and almost always

benign. Since they are fluid, cysts respond differently from solid masses when penetrated by the sound waves. Breast ecography can also be used in a limited fashion to characterize solid masses. It is not, however, recommended as a primary screening method, because of a variable false-negative rate (ranging from 0.3% to 47%) [5] and of the operator-dependent nature of efficacy.
Breast ecography can also be used as a vascular imaging tool with the use of the Doppler technique. A vascular imaging tool can be useful in the detection of malignancies due to tumor angiogenisis. Angiogenisis, which is considered a hallmark of cancer, is defined as the emergence of new vessels to sustain the growth of the tumor. Therefore, breast cancers are expected to demonstrate increased vascularity compared with benign masses. The future role of vascular imaging in breast ecography remains yet to be defined, since there are contradictory results regarding the reliability of Doppler evaluation in differentiating benign from malignant breast masses [9, 10].
To take the evaluation of lesion vascularity with ecography a step further, contrast agents can be used. The most common type of contrast agents in ecography are encapsulated bubbles and solid particles. These allow visualizations of blood flow in the area of interest by increasing the backscatter echoes. Improved visualization of lesion vascularity and characterization using contrast agents compared with Doppler alone has been found [11]. However, it remains to be seen whether there will be acceptance of these agents in routine breast ecography.

2.4 Magnetic Resonance Imaging

Magnetic Resonance Imaging has been used consistently in the detection of breast cancer since the late 90's. Since them, MRI has shown to have a very high sensitivity for detecting invasive breast carcinoma (at least 95%) [5], although with a very wide range of specificity values (37% to 97%) [5]. Several studies have clearly established that MRI can detect mammographically and clinically occult breast cancer [12], although with low specificity. MRI can be used as a tool to detect breast cancer recurrences and in the staging of the disease [13]. Since its sensitivity is not affected by the presence of underlying dense breast tissue, MRI has also been found particularly valuable in screening young women at high risk [14, 15]. Recently, it has been recommended by the American Cancer Society that MRI should be used as an adjunct tool to mammography for women at high risk for breast cancer [16].
Breast MRI is performed in a magnetic field ($0.5T - 1.5T$) [12] created by a magnet that surrounds the body of the patient and with a small breast surface coil that acts as an antenna. This dedicated surface coil is needed to ensure adequate spatial resolution at high signal to noise levels [17]. The static magnetic field acts on the hydrogen nucleus of the media, aligning them. The coil emits a radio frequency pulse that induces

a change in the alignment of the protons and is then turned off. The time taken by the protons to return to their original alignment is then converted into an MRI image. Since the main reservoir of hydrogen in the cell is in water molecules, MRI allows to observe the water contents of the tissues, thus providing high contrast levels between tissues with different water contents.

The differences in water content between normal and malignant tissues in the breast are not enough to provide breast cancer detection with MRI. Therefore, it is necessary the use of intravenous contrast agent. This agent is usually a small molecule containing gadolinium. Due to their increased angiogenesis, cancer cells present increased vascularity. The contrast agent will thus accumulate in the cancerous lesions, highlighting them in the MRI image. Unfortunately, many benign lesions will also highlight. The difference in the lesion morphology can then be used to distinguish the malignant from the benign lesions [3]. These morphological differences may, however, not be enough to provide a good discrimination between benign and malignant lesions. Improved specificity may be achieved through the analysis of lesion kinetics, that is, by evaluating the time intervals of wash in and wash out of the contrast agent in the lesion. Since the malignant lesions vasculature has higher capillary permeability than the normal vasculature, malignant lesions tend to present quicker enhancement and clearance of the contrast material [12].

A point where breast imaging with MRI falls short consists on the difficulty to detect DCIS lesions. In fact, MRI sensitivity for DCIS can be as low as 40% [18]. On the one side, MRI is uncapable of detecting the microcalcifications that typically appear with DCIS, since MRI can only identify breast masses as small as 1-2 mm [19]. On the other side, DCIS lesions do not present increased vascularity, since their nutrition is performed by difusion. Therefore, these lesions are commonly missed by MRI.

One other handicap of MRI arises when suspicious lesions found on MRI cannot be visualized with mammography or ecography. In these cases, ecography guided biopsy systems are of no use. Therefore, MRI-based guidance systems are needed for needle biopsy or placement of localization needles before surgery. MRI guided systems are not yet well established, and still present many problems. However, systems exist that are based on anatomical navigation using fiducial markers placed either on the coil or on the breast [20]. In alternative, an interactive placement of needles can be performed directly with MRI guidance if open-architecture MR coil is available [21]. Yet another alternative is MRI guided vacuum assisted biopsy [22]. In either case, MRI compatible needles must be used. There are, however, many unsolved problems associated with its use, such as artifacts in some of the MRI sequences [12].

2.5 Scintimammography

Scintimammography (SM) is a functional imaging technique that uses a radiation detector camera, named Anger Camea, and single-photon emitter radiotracers to image the breast. The radiopharmaceuticals used are administrated intravenously in the patient body, and since they are designed for such purpose, they accumulate in the cancerous cells. The emitted gamma rays can be detected externally by an Anger Camera, thus providing information of the location of the cancerous cells.

Currently, the most used radiopharmaceuticals used for SM are ^{99m}Tc-sestamibi (MIBI) and ^{99m}Tc-tetrofosmin [23]. Of these two, the highly complex uptake mechanism of ^{99m}Tc-sestamibi is better understood, although they both share common biophysical, chemical and pharmacokinetic properties [24]. The uptake of both radiopharmaceuticals rely on the higher aerobic metabolism of tumor in comparison with normal breast tissue cells, and are related to tumor cell apoptosis, blood supply and cell proliferation [24].

Scintimammography is a highly sensitivity technique for the detection of breast cancer. The reported sensitivity values range from 85% to 93% [22, 25]. Since SM is not affected by the breast density [26], it is often able to visualize lesions in dense fibroglandular tissue that can not be seen by mammography. Thus, it is of special value when the mammography findings are equivocal or when there are palpable masses that are not seen in mammography.

The specificity of scintimammography is also high, since SM images do not reflect morphological changes in the breast tissue, but rather changes in the cells metabolism. Thus, SM is better able to distinguish malignant from benign lesions than conventional techniques. The reported specificity for SM is around 87% [22, 25, 27]. When used in combination with mammography, SM can improve its overall sensitivity and specificity [28].

It is important to emphasize that the sensitivity of SM depends utterly on the size of the lesions, dropping drastically for lesions lower than 1 cm [23]. This is due to the poor intrinsic spatial resolution of the Anger Camera, and to the sub optimal detection geometry, since there is a big distance between the detector and the imaged breast. Attempts to overcome these pitfalls have resulted in the development of small dedicated gamma cameras that provide higher spatial resolution and higher detection sensitivity. The firsts clinical trials using these dedicated cameras have shown a significant improvement in sensitivity for smaller lesions [29, 30, 31, 32] indicating that this new technique might become useful in the clinical practice [33].

As any other nuclear medicine technique, the quality and type of information provided by scintimammography relies tremendously on the radiopharmaceuticals used. Different radiotracers will provide information on different cellular processes. Thus, another

approach to improve scintimammography's accuracy is the development of radiopharmaceuticals that are more specific of breast cancer. Examples of such developments are radiopharmaceuticals that are used to target tumor associated antigens or receptors that are expressed in most primary breast cancers such as somatostatin receptors [28].

2.6 Positron Emission Tomography

Just like scintimammography, Positron Emission Tomography is a form of diagnosis imaging that uses radiolabeled tracers to track functional or metabolic changes in tissues. However, unlike scintimammography, PET is a tomographic technique where the radionuclides used decay by the emission of positrons.

The most used radiotracer for imaging cancer in PET is ^{18}F-fluorodeoxyglucose, or ^{18}FDG, a glucose analogue that is labeled with the positron emitter ^{18}F. This radiotracer is used to detect glucose consumption, which is known to be increased in cancerous cells compared to normal cells. This is due to the higher metabolism of cancerous cells. Just like in scintimammography, the advantage of being able to image metabolism instead of anatomy is that, usually, the accelerated metabolic activity of cancerous cells occurs before the changes in the anatomical structures.

The tracking mechanism of ^{18}FDG inside the cancerous cells is as follows. FDG is a glucose analog and, just like glucose, is transported into the cells by glucose transporters named GLUT1. These transporters are known to be overexpressed in breast cancerous cells, thus contributing to increased FDG uptake [34]. Once inside the cell, FDG is phosphorylated into deoxyglucose-6-phosphate (FDG-6-PO4) by an enzyme named hexokinase. Hexokinase is also thought to be overexpressed in cancerous cells. Unlike glucose, FDG-6-PO4 does not enter further enzymatic reactions and, due to its negative charge, remains trapped inside the cell [28]. This metabolic trapping of FDG inside the cell constitutes the basis for imaging the in vivo distribution of the tracer [35].

The sensitivity and specificity values found for PET in the detection of primary breast cancer are moderate: 85% and 79%, respectively [3]. The fact that FDG can be taken by non malignant processes such as infection or inflammation accounts for the not so high specificity values. It has also been found a high variability in the metabolic rate of tumors, and consequently in FDG uptake [36]. The low to moderate sensitivity values are due to the fact that primary breast cancer detection by PET is lesion size dependent. In fact, due to its limited spatial resolution, PET has litle capability of detecting lesions of less than 1 cm. For instance, in a given clinical study, the sensitivity for detecting tumors less than 1 cm was only 57%, compared with 91% for tumors larger than 1 cm [37]. FDG uptake is also dependent on the breast composition, with fibroglandular breasts exhibiting a significantly higher FDG uptake than breasts that

are constituted mainly by fat. However, this does not seem to preclude PET from being able to detect lesions in dense breasts [38]. Therefore, in primary breast cancer PET may help on detecting tumors in high risk patients with dense breasts, to whom conventional tecniques are of little use [3].

Due to its moderate sensitivity in detecting small cancers, PET is not considered a first choice technique for the diagnosis of primary disease. The role of PET in breast imaging has been mainly focused on other applications. PET has been found to be invaluable in the determination of unsuspected metastatic disease resulting from breast cancer, mainly in the detection of distant metastasis, since it is a whole body imaging technique. It has also been shown to be of great value in the evaluation of the response to therapy and in the detection of recurrent breast cancer. This is because PET, unlike anatomical techniques, is able to differentiate viable tumors from scars resulting from previous therapies [28].

The detection of metastasis in the axilla is an important prognostic status, especially for early stage breast cancer patients, as it was previously said. Initial evaluations of PET as a predictor of axillary node status were very promising. However, it was soon found that the ability of PET do detect metastatic disease in the axilla was hampered by its limited spatial resolution [39]. In fact, PET seems to be unable to detect small metastasis in the axilla (less than 5 mm). Published studies have shown a wide range of sensitivity values for PET in the case of axillary staging, ranging from 79% to 100%. Specificities have ranged from 66% to 100% [40].

PET-CT in one integrated unit that allows both functional and anatomic imaging in a single study has also revealed to be a valuable technique for breast cancer imaging. Besides providing anatomical information, the low-dose CT exams also allows for attenuation correction of the emission scan. The use of PET-CT in breast cancer imaging has shown to yield a clear improvement in diagnostic accuracy [35, 41]. Figure 2.2 is an example of a FDG PET-CT exam.

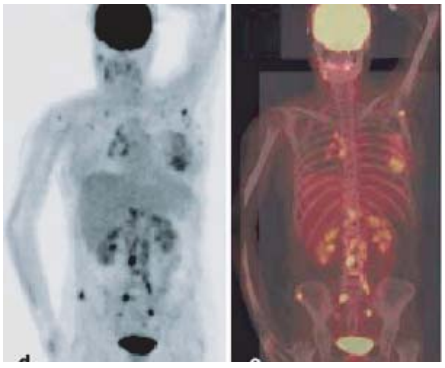

Figure 2.2: FDG PET-CT breast exam. The image on the left shows the reconstructed PET image, while the image on the right shoes the PET-CT fused image. From [41].

Such as in scintimammography, some of the aspects that prevent whole body PET from being more useful in the diagnosis of primary breast cancer are related to technological aspects and not with fundamental limits of the technique. This has lead to a tremendous surge of interest on the conception and development of small, dedicated PET cameras for breast imaging [42, 43, 44, 45], as we will see in the next chapter. The first preliminary clinical trials using this technology seem to be very promising [46, 47, 48, 49], but technical improvements of these cameras are still taking place.
Another means to improve the usefulness of PET in breast cancer imaging is through the development of new radioligands. Although FDG continues to play an important role in the evaluation of breast cancer, there is a chance that other radiopharmaceuticals will play a role in the management of breast cancer in the future [4]. Besides energy metabolism, other tumor surrogates can be used for imaging breast cancer with PET. For instance, genetic changes in breast cancerous cells comprise increased oestrogen receptors, increased protein synthesis and enhanced proliferation activity. The evaluation of such processes with newly developed radiopharmaceuticals such as ^{18}F-fluroestradiol (FES), ^{11}C-methionine and ^{18}F-fluorothymidine (FLT), respectively, may provide additional functional information to that obtained with FDG [4].

2.7 Conclusions

In this chapter an overview of the main technologies used for breast cancer imaging was given. Mammography remains the gold standard for breast cancer screening and diagnosis, together with biopsy. Adjunct techniques such breast ecography and magnetic resonance imaging provide information when the findings on mammograms are equivocal, but this information is still mainly anatomical. Functional imaging such as scintimammography and PET have been reported to offer advantages over anatomically based imaging modalities. However, both these imaging techniques suffer from lack of ability to detect small lesions, mainly due to their limited spatial resolution and whole body geometry. In this context, there has emerged a tremendous effort in the development of dedicated instruments for breast cancer imaging, either based in scintimammography or in PET technology. These efforts have been crowned with very promising initial clinical results. In the next chapter we will overview the main instrumentation issues regarding the development of breast imaging dedicated PET scanners.

Chapter 3

Positron Emission Mammography

3.1 Introduction

We have seen in the previous chapter that the use of labeled radiotracers has shown promise for the detection, diagnosis and staging of breast cancer. However, the standard technology of whole body scanners, due to its limited spatial resolution and to the disadvantageous geometry, which limits sensitivity, are in part precluding molecular imaging using radiotracers from contributing with its full potential to the imaging of the breast.

These limitations have prompted an active interest in the development of compact positron emission tomography cameras dedicated for breast imaging, or Positron Emission Mammography (PEM) cameras. In the last ten years, a variety of detector designs and geometries has been studied in order to optimize the technique. Several geometries have been exploited to fulfill the requirements of imaging the breast, the most commonly adapted being rectangular or planar detector geometries with or without rotation. Regarding the design of the detectors, most of the instrumentation issues raised by the development of PEM scanners are common to the ones of small animal positron emission tomography (PET) scanners, since they also must meet high resolution, high sensitivity requirements.

This chapter will begin with a brief description of the positron emission and detection processes, that are common to PEM and PET. Then, we will review the performance parameters and instrumentation issues more challenging in the design of dedicated PEM scanners. We will finalize the chapter with a literature review of the state of the art in Positron Emission Tomography scanners.

3.2 Positron emission and detection

As it was seen in the previous chapter, Positron Emission Tomography, as well as Positron Emission Mammography, uses radiopharmaceuticals that are labeled with a positron emitting radionuclide. Besides ^{18}F, which is used in FDG, other radionuclides, such as ^{82}Rb, ^{15}O, ^{13}N and ^{11}C, among others, can be used to label the molecular probes used in PET.

The emitted positron travels a given amount of space in matter, while dissipating its kinetic energy through interactions with electrons and surrounding nuclei. At the end of its path, the positron combines with an electron in its vicinity, in an annihilation reaction whereby the total mass of the electron and the positron is converted into high energy photons. The rest-mass energy of both positron and electron is 511 keV. If both particles were at rest at the time of annihilation, the two resulting 511 keV photons will be emitted in opposite directions.

The gamma rays thus emitted can interact with the tissues of the patient either by photoelectric effect or by Compton scatter. Both photon attenuation and scatter result in image degradation since, in the first case, emission counts are lost and, in the second, the measured spatial information is inaccurate. Whereas attenuation correction is fairly simple if a transmission scan is available, the scatter correction is not as straightforward.

If the photons are not absorbed by the matter in the patient body, they can be detected externally in coincidence by using opposed pairs of scintillator crystals. Each luminous signal produced in the crystals is transformed into an electrical signal. A coincidence event happens when such two electrical signals are registered in a coincidence electronic circuit within a time frame that is defined by a coincidence time window.

The imaginary line that unites the two activated crystals in a coincidence event is called a line of response (LOR). The number of counts that are detected along the several LORs during an exam is stored in an histogram and used for image reconstruction purposes. Alternatively, list mode format can be used. In list mode format, the relevant information regarding the event, such as the activated crystals, the deposited energy and a time stamp, is stored sequentially on disk and used directly for image reconstruction.

3.3 The performance of a scanner

Of main importance for the performance of a PET scanner are its photon sensitivity and its spatial, energy and temporal resolutions. The geometry, the detector crystals and the electronics of the system all impact on the above mentioned parameters. In this paragraph we will overview the main aspects that affect these parameters, highlighting the most common differences between traditional clinical scanners and high resolution scanners.

3.3.1 Photon sensitivity

The photon sensitivity is defined as the fraction of 511 keV photon pairs emitted from the imaging subject that are detected by the imaging system [50]. It is important that a scanner has the higher photon sensitivity possible since a higher fraction of detected photons will impact on better statistics of the acquired data and, consequently, on lower noise level of the final reconstructed images. The photon sensitivity in a clinical PET system is less than 1%. In dedicated or high resolution scanners, this value is usually improved by increasing the scanner geometric efficiency, that is, the probability that the emitted photon transverses the detected material, or by increasing the intrinsic detector efficiency.

Usually, the scanner geometric efficiency is enhanced in dedicated scanners relatively to traditional scanners mainly because the detector is brought closer to the imaging subject. The geometric efficiency can also be increased by packing the detector elements as tightly as possible and by covering the region to be imaged with as much detector as possible.

The other aspect that influences the scanner photon sensitivity is the intrinsic detector efficiency. This is defined as the likelihood that photons transversing the detector material will be stopped [50]. It depends mainly on the scintillator crystals that are used as detector elements. Scintillator crystals that have high density (ρ), with high effective atomic number (Z_{eff}) have maximum ability to stop the 511 keV photons. In fact, a high density crystal favors the photon interaction and a high effective atomic number maximizes the probability of photoelectric interactions within the crystal, with respect to Compton events. The quantity that maximizes the crystal stopping power is ρZ_{eff}^2. A scintillator that has a high stopping power will have a short attenuation length.

Table 3.1 lists the values of Z_{eff}, ρ, the attenuation length and some other properties of the most common scintillator crystals used in PET scanners. The decay time determines the time resolution of the scanner and the light output determines the detector energy resolution and has effects also in the image resolution. Both these parameters will be discussed later.

Sodium Iodine doped with Thallium (NaI(Tl)) was the detector initially used in PET scanners. It has a very high light output (38 photons/keV), resulting in good energy and spatial resolutions [51]. However, its slow decay time leads to increased detector dead time and a high random coincidence rate (see below the discussion for system time resolution). Its low density results in a low stopping power (high attenuation length) when compared to the other crystals used in PET.

Sodium Iodine was first replaced by BGO (Bismuth Germanate) that, despite its high decay time and poor light output, has an excellent stopping power.

	Effective Z	Density (g/cm^3)	Attenuation length (mm)	Relative light output (% NaI)	Decay time (ns)
Sodium Iodide	51	3.7	29.1	100	230
BGO	75	7.2	10.4	15	300
LSO	66	7.4	11.4	75	42
GSO	59	6.7	14.1	20	60
LYSO	65	7.1	1.2	107	40

Table 3.1: Properties of common scintillator crystals used in positron emission tomography. Adapted from [50].

More recently, other crystals that combine better light output with high stopping power have been introduced to PET. LSO (Lutetium Oxyorthosilicate) has a high stopping power and a good light yield but, due to intrinsic properties of the crystal, its overall resolution is not as good as NaI(Tl) [52]. GSO (Germanium Orthosilicate), despite its lower stopping power and light output, has better energy resolution than LSO. Both crystals are in use in PET scanners.

3.3.2 Spatial resolution

The spatial resolution describes the ability of the system to distinguish two closely spaced point sources. In PET, the fundamental limit of spatial resolution is imposed by the nature of positron annihilation. In fact, the emitted positron describes, before annihilating, a given path of variable length and direction. Therefore, the detected LOR contains the positron annihilation point, not the positron emission point, and these two points can be several millimeters apart. This positron range effect degrades the spatial resolution of the images. (Figure 3.1 (a)). The positron range depends upon the energy of the emitted positron and upon the electronic density of the medium. It has been estimated a value of 0.22 mm FWHM for the positron range emitted from ^{18}F in water, the major component of human cells [53].
In addition to the positron range, the acollinearity effect also leads to resolution degradation in PET systems. This effect is caused by the fact that the annihilation photons are almost never anti-parallel, since usually the positron and the electron are not exactly at rest when they annihilate. As a consequence, the detected line of response does not contain the point of positron-electron annihilation (Figure 3.1 (b)). The degradation of the spatial resolution due to the accolinearity effect worsens as the detector diameter increases.
Another significant factor that limits PET spatial resolution is the size of the detector element. Spatial resolution may be improved significantly by reducing the detector pixel size. This is specially important in small diameter or dedicated PET scanners,

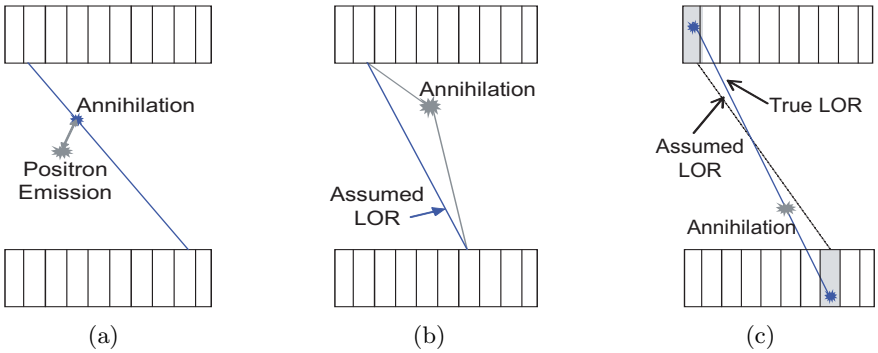

Figure 3.1: Schematic drawings of some of the effects that degrade spatial resolution in PET: a) the positron range, b) the accolinearity effect and c) the Depth of Interaction effect or parallax error.

where the pixel size dominates image resolution over the non-collinearity effect, which is minor for small detector diameters. Typical clinical systems use $4-6$ mm^2 detector pixels, whereas small animal use detector pixels of $1.5-2.0$ mm^2 and positron emission mammography scanners use pixels of $1.8-3.0$ mm^2.

A final important factor that affects PET spatial resolution is the parallax error. This error occurs when the crystal depth at which the photon interaction takes place, known as Depth of Interaction (DOI), is not known. In this case, the LOR that unites the two activated crystals does not necessarily contain the true LOR (Figure 3.1 (c)). For photons entering the scintillators at oblique angles there will be a mismatch between the true and the measured line of response. This degrading effect has greater impact in scanners where the distance between opposed detectors is smaller, like dedicated cameras. These are also the cameras to which a good spatial resolution is of crucial importance. Furthermore, the scintillator crystals that compose these cameras are usually long crystals, to improve photon sensitivity. Therefore, it does not surprise that the ability to obtain information on the DOI has became an important factor in the design of high resolution PET scanners [54, 55, 56], with different strategies being followed to perform such measure.

3.3.3 Energy Resolution

The energy resolution indicates the precision with which the system can measure the incoming photon energy. A good energy resolution is important because it allows the use of a narrow energy window without significantly compromising photon sensitivity. A narrow energy window helps to prevent contamination from photons that undergo scatter before interacting with the scintillator crystal, since the scatter process implies the loss of energy. It may also help to reduce the rate of random photon events, since a part of these photons undergo scatter. Random, or accidental, coincidences,

occur when photons proceeding from different annihilations are detected within a same timing window and, although spatially uncorrelated, its detection is considered as a valid coincidence.
Energy resolution may be improved by using crystals with hight scintillation light output. A typical value for clinical PET scanners energy resolution is 25% FWHM at 511 keV [50].

3.3.4 Time resolution

The time resolution determines how well the system can decide whether two incoming photons arrived simultaneously. Good time resolution allows the use of a narrow time window, thus reducing the random events without compromising photon sensitivity. The reducing of random events is also important as it helps to prevent the system from saturating in high count statistics studies. The parameter that most strongly determines the temporal coincidence timing window is the scintillator decay time: a fast scintillator allows the selection of a narrow time window. A typical value for clinical PET scanners time resolution is 3 ns FWHM at 511 keV [50].

3.3.5 Photodetectors

The scintillation light from the crystals is read from photodetectors that, in PET, are most commonly either photomultiplier tubes (PMT) or semiconductor based photodiodes.
Photomultiplier tubes are the oldest and most reliable technology to detect and measure low levels of scintillation light. They have a high gain in the photoelectric conversion, which leads to high signal-to-noise ratios.
Besides simple PMT's, a class of PMTs has been developed that provides not only energy information but also spatial information about the detected light. These PMTs, named Position-Sensitive PMTs (PS-PMT) have found to be useful in the design of high resolution PET scanners [57, 58].
PMTs have two major drawbacks. They have low quantum efficiency, meaning that the ratio between the incident photons and the primary produced electrons is low. In addition, PMTs are big devices, often with a small field of view, and this may constitute a drawback, specially when they are to be used in small dedicated scanners.
In recent years there has also been great progress in the development of semiconductor photodetector arrays. These can be the PIN photodiode, the avalanche photodiode (APD) and the silicon drift detector (SDD). Of these, the APDs are the most used in PET cameras. Semiconductor photodetectors have many advantages over PMTs: they are very compact, are insensitive to magnetic fields, which makes them good candidates for PET-MRI devices, they are available with large active areas and they have

a very high efficiency [59]. The main disadvantages of APDs are their sensitivity to temperature and bias voltage.

3.4 Dedicated scanners for breast imaging

In this section we will present a review from the literature of the main equipments that are or have been developed for Positron Emission Mammography, emphasizing the different approaches followed in the design of these scanners. When such information is available, we will also refer to the most significant results already obtained in clinical trials.

3.4.1 The PEM-I system

A design of a dedicated positron emission imaging system for breast cancer was first presented in 1994 by Thompson *et al* [60] from the Montreal Neurological Institute of the McGill University, Canada, as a feasibility study for a positron emission mammography unit.
The developed scanner was designed to fit a mammographic unit, so that conventional mammograms could also be performed in the same gantry, thus allowing exact registration of the emission and of the conventional mammographic images [61]. For such purposes, the system included a co-registration tool to facilitate registration between radiographic and metabolic images [62]. A schematic diagram of the scanner is presented in Figure 3.2.

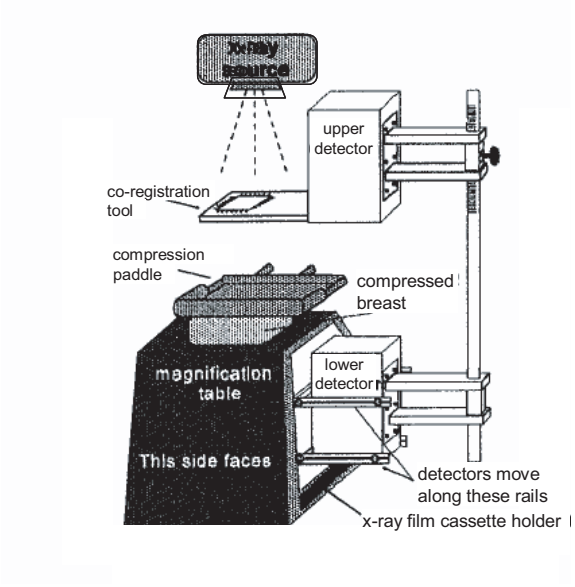

Figure 3.2: Schematic drawing of the PEM-I detector plates (white areas) mounted on a conventional mammographic unit (gray areas). From [62].

The developed scanner consists on two planar 2×2 detector arrays of blocks of bismuth germanate (BGO) crystals placed above and below the compressed breast. The detector blocks measure 36×36×20 mm^3 and are segmented into 1.9×1.9 mm^2 pixels [63]. The separation between the detector heads can be adjusted to match the thickness of the breast. The system uses position sensitive photomultiplier tubes (PS-PMT) that are optically coupled to the crystal blocks. Although the PS-PMTs cover a surface of 72×72 mm^2, their useful field-of-view (FOV) is only of 65×55 mm^2. The coordinates of the coincidence on opposing PS-PMT faces are decoded by the system electronics and corrected for spatial distortion and efficiency [64].
The images from this system are obtained by performing a limited-angle weighted-backprojection algorithm. This consists on dividing the image into several equidistant planes and backprojecting the lines or response (LOR) onto those planes. With this technique, the image plane closest to the site of the tumor has the most focused image, while all the other planes present more blurred images, as it can be seen in the schematic diagram of Figure 3.3. This is known as the focal plane effect. The reconstruction scheme is said to be 'weighted backprojection' because the values that are added to a given plane in the image matrix are weighted accordingly to the probability of detection of an annihilation in that plane, the crystals efficiencies and the photon attenuation along the path to the crystal [61].

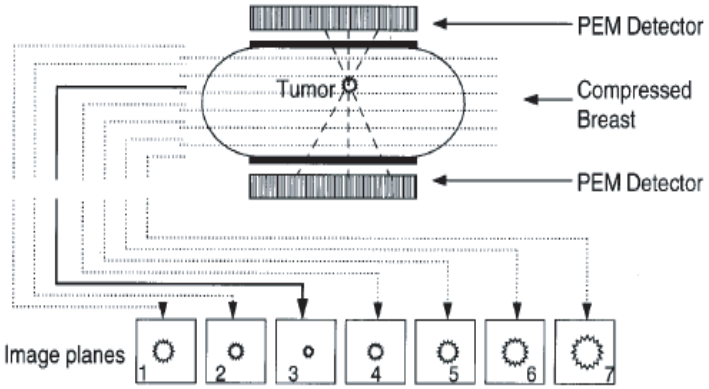

Figure 3.3: Weighted backprojection used in the PEM-I scanner. From [65].

The complete system has a spatial resolution of 2.8 mm FWHM, a time resolution of 12 ns and an efficiency of 3% at a detector separation of 55 mm [66]. It is estimated that the system is not able to detect tumors with a tumor-to-background ratio lower than 6:1 [67].
The preliminary clinical trials, performed with 16 subjects, reported a 80% sensitivity, 100% specificity and 86% accuracy [65]. For mammography exams performed on the

same subjects, those values were, respectively, 90%, 50% and 81%. The smalest cancerous lesion detected with PEM-I was $1.1 \times 1.1 \times 0.9$ cm^3. The lower value of sensitivity with PEM, with respect to mammography, was due, according to the authors, to the small FOV of the PEM device and to the impossibility of imaging tumours localized close to the chest wall (less than 2 cm). These limitations are related to the PMTs used, whose useful field of view is significantly smaller than its area, preventing imaging near their edges. Figure 3.4 shows a typical set of PEM images, each image corresponding to a plane of the sample, with a visible site of FDG uptake in a region close to the chest wall [66].

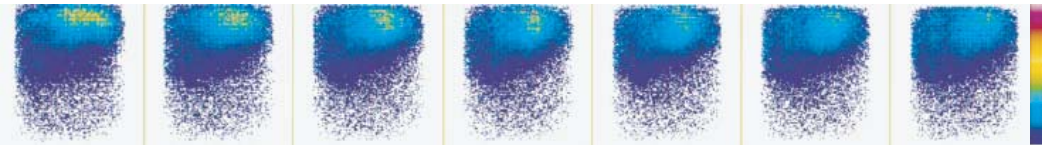

Figure 3.4: A typical set of images obtained with the PEM-I scanner. Each image corresponds to a plane, with the leftmost image corresponding to the image plane closer to the upper detector. A visible site of FDG uptake can be seen in a region close to the chest wall. From [66].

3.4.2 The Naviscan PEM Flex system

The original idea of Thompson for a PEM system was further developed by Weinberg and colleagues, for the Naviscan PET Systems (previously known as PEM Technologies Inc.). The Naviscan PEM Flex consists of two 5,6 cm $\times$ 17,3 cm^2 opposed detector heads [68] that can be fit on a steriotactic mammography unit [69]. This way, emission and transmission scans can be obtained. Data acquisition is performed by moving the detectors along a linear path, in order to image as much breast as possible. The PEM detectors translation allows to image an area equal to the entire X-ray field of view [70]. The system can also work separately from the mammography unit, allowing closer chest wall access. Figure 3.5 shows the PEM Flex system mounted in a stereotactic x-ray mammography unit.
Each detector head contains twelve 13 $\times$ 13 crystal blocks, each coupled to a compact PS-PMT. The crystals are 2 mm$\times$2 mm$\times$10 mm of a mixed-lutetium silicate [68].
For each segment of the scan, list mode data are acquired, histogrammed and reconstructed by backprojection. This allows the operator to view partial images during the scan acquisition. At the end of the entire scan, the complete list mode data are reconstructed using a maximum-likelihood expectation-maximization (ML-EM) algorithm. ML-EM is a statistical iterative reconstruction algorithm commonly used for PET whose principles will be explained in the next chapter.

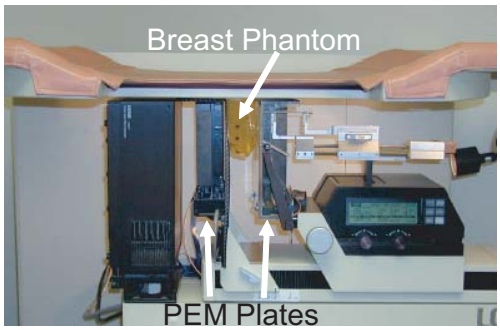

Figure 3.5: The PEM Flex system mounted in a stereotactic x-ray mammography unit. From [69].

.

The intrinsic spatial resolution of the system is 1,5 mm FHWM [70]. The image resolution is 2.5 mm FWHM in the plane perpendicular to the displacement and 6 mm between planes. Energy resolution was measured as 14% for 511 keV. The timing window used was 9 ns.

The clinical trials performed so far [46, 48, 49] were all performed on patients with known breast cancer or suspected lesions. Hence, they provide little information on the specificity of the technique. In one of these studies [48], PEM was able to visualize 39 out of 44 lesions. The non visualized lesions ranged in size from a 1 mm ductal carcinoma *in situ* (DCIS) to a 1 cm infiltrating ductal carcinoma. Some lesions could not be visualized due to limitations on how posterior the breast tissue is observable by the device. Others, as interpreted by the authors of the study, due to the variability in the metabolic activity of breast cancer cells, similarly to what happens with whole body PET.

The most encouraging finding in this trial was the fact that PEM was able to visualize DCIS not visualized by mammography, breast ecography or MRI. An example of such a case can be seen in Figure 3.6. The smallest lesion detected by PEM in this study was a 2 mm duct of DCIS. This preliminary clinical trial seem to indicate that the technology is promising and worthy of further investigation.

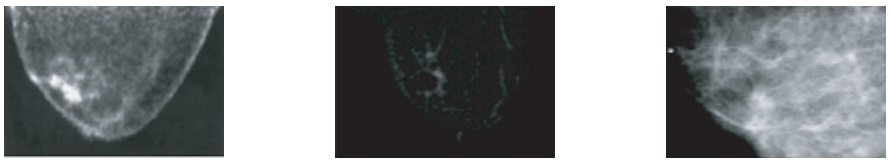

(a) (b) (c)

Figure 3.6: Image of DCIS obtained with the PEM Flex scanner a), with MRI b) and with mammography c). Neither MRI nor mammography could detect the DCIS lesion seen in the PEM image. From[48].

3.4.3 The West Virginia University - Jefferson Lab PEM system

Another PEM system was developed and tested at the West Virginia University and at the Jefferson Laboratory by Raylman and colleagues [43]. This PEM system, which is mounted on a stereotactic biopsy table, consists of two square 10 cm × 10cm detector arrays of discrete 3×3×10 mm^3 GSO crystals. The scintillation light is collected by arrays of PS-PMTs. An image of the scanner mounted on the biopsy table, together with a torso phantom can be seen in Figure 3.7.

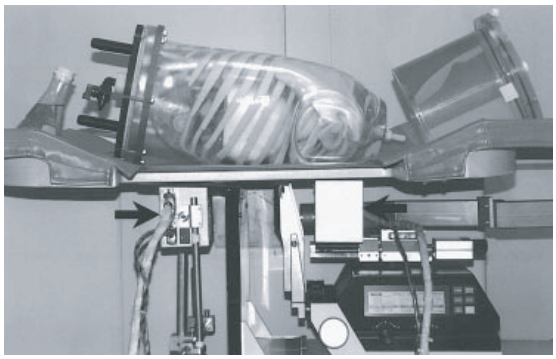

Figure 3.7: Image of the West Virginia University - Jefferson Laboratory PEM system. The PEM detector heads, mounted in a biopsy table, are highlighted by the black arrows. A torso phantom can be seen in the table. From [71].

Since one of the goals of the system is to perform PEM guided biopsies, a trigonometric algorithm was developed to determine the lesion stereotactic coordinates. This algorithm uses two PEM images that are acquired at two symmetric angles (±15°).
PEM images acquired in a single detector position were initially reconstructed using a weighted backprojection algorithm similar to the used for the PEM-I system described above [72], or by a limited angle tomography scheme [73]. Later, the use of acquired data at two detector positions (±15°) [74] to guide stereotactic biopsy motivated the use of an adapted Maximum Likelihood - Expectation Maximization (ML-EM) algorithm.
The described acquisition scenario was compared with multiple acquisitions between the same limiting angles, at small uniform increments [75]. The results were somehow mixed, with no clear evidence of significant advantage of one acquisition scenario over the other, although less artifacts were observed with the multiple angle acquisition. This lead to a study of the complete angular sampling around the breast [76] through step and shoot acquisitions. Not surprisingly, this study showed that the complete angular sampling provided better image quality with respect to a single acquisition with stationary detectors. The study also revealed some of the weaknesses of the system, such as the low rate acquisition capability and the lack of DOI information.
More recent work reports on a new design of the scanner, now named PEM-PET [77], as

it means to be a tomographic system. This system will have four planar detector heads that will rotate about the breast. The detector crystal used will now be LYSO, with $2\times2\times15$ mm^3 individual detector elements. Simulation studies indicate that the PEM-PET system is expected to have 2 mm FHWM resolution, possessing, as its anterior version, the ability to guide biopsy.

3.4.4 The Duke University - Jefferson Lab PEM system

Another system was developed at the Jefferson Laboratory and Duke University to image the compressed breast [78]. This PEM system has two opposed planar 15×20 cm^2 detectors that acquire data without rotational or translational movements. The detector arrays are composed of $3\times3\times10$ mm^3 of lutetium gadolinium oxyorthosilicate, LGSO. The scintillation light is collected by arrays of PS-PMTs. This system is used mounted on an x-ray mammography unit, although the PEM detector heads must be removed to acquire the x-ray image. The distance between the detector heads can be adjusted to match the size of the breast. Image reconstruction is performed by means of the backprojection scheme described in Paragraph 3.4.1. The image spatial resolution varied from 4.8 mm to 6 mm, depending on the acceptance angles of the lines of response. An image of the system can be seen in Figure 3.8

A pilot clinical trial was performed using this system [47]. This trial included 23 patients with suspected breast malignancies. Therefore, it does not provide meaningful information concerning the specificity of the technique. In this study, where the majority of the evaluated lesions had diameters smaller than 2.5 cm, PEM presented a sensitivity of 86%. The size of the three malignant lesions that PEM was unable to detect varied from 8 mm to 15 mm. The system was able to detect a 4 mm DCIS that was not detected by mammography.

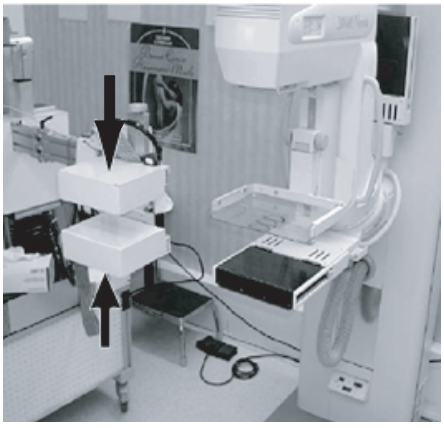

Figure 3.8: Image of the Duke University - Jefferson Laboratory PEM system positioned in a mammography unit. The PEM detectors are highlighted by black arrows. From [47].

3.4.5 The maxPET system

A dedicated PET camera for *m*ammary and *ax*illary region imaging, *max*PET, was designed and constructed at the Crump Institute for Biological Imaging [44]. This group used an alternative scheme to couple the crystal arrays to the PMT's, in order to avoid the problems associated with the inactive area near the PMT edges. The maxPET system consisted of two 15×15 cm^2 planar scintillation detector plates, each composed of several modular detectors. The detectors are composed of arrays of 3×3×20 mm^3 LSO crystals, each crystal array being coupled to an optical fiber which in turn is coupled to a PS-PMT. The use of the optical fiber allows the exact match between the crystal area and the active PMT dimensions, thus avoiding gaps between detector modules. It also provides better imaging close to the chest wall, since the plates are active out to the edge of the field-of-view. The main disadvantage of the of fiber-optic coupling is the loss of scintillation light.
The two detector plates can be mounted in a gantry allowing variable plates separation, detector plates rotation and angular motion. Based on Monte Carlo simulation, the expected intrinsic spatial resolution of the scanner was about 2.3 mm [79]. A prototype of this system was assembled but, to our knowledge, no clinical test were ever performed. Recently, it has been reported that a second prototype of this detector was build, with modified geometry and electronics. On going work is exploring the integration of this system with a dedicated CT system [80].

3.4.6 The LNBL PEM system

The PEM scanner developed at the Lawrence Berkeley National Laboratory (LBNL), has two major differences from the PEM scanners here described: it has a rectangular geometry, with four detector plates surrounding the breast (Figure 3.9), and it has Depth of Interaction measurements capabilities [81].
In the context of the development of this scanner, a simulation study was done to compare the presented rectangular detector configuration with a dual stationary detector system, such as some of the systems presented above. For such purpose it was used the Fisher information matrix, an analytical computation that allows to characterize how easily a change of one parameter in the source distribution can be identified from the measured data [83]. This study has shown that the rectangular system with Depth of Interaction capability has a higher signal-to-noise ratio for detection tasks and a lower bias at a given noise level for quantitation tasks [83]. It is worth stressing that this study did not include the case of a rotating dual head scanner.
The LBNL PEM system consists of four detector plates that cover a rectangular 8.2×6.0×5.0 cm^3 field of view. The detector modules contain arrays of 3×3×30 mm^3 LSO crystals that are coupled to a single photomultiplier tube (PMT) in one end and to

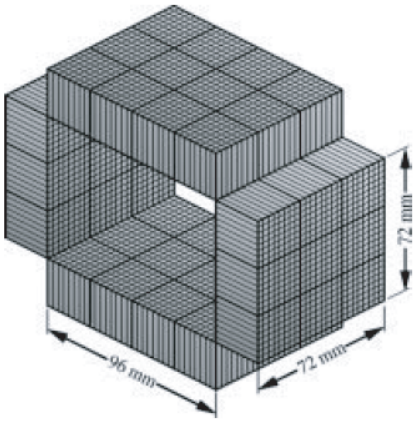

Figure 3.9: Representation of the geometry of the LBNL PEM scanner. From [82].

a photodiode array (PD) on the other end. The ratio between the signals of the PMT and the PD allow the estimation of the Depth of Interaction of the photon [84]. The achieved DOI resolution ranges from 6 mm FWHM at the PD end to 11 mm FWHM at the PMT end [85].
The system uses a 6 ns time window and has 5% sensitivity at the center of the FOV [81]. The measured spatial resolution of the scanner is almost uniform in the entire field-of-view, ranging from 1.9 mm FWHM at the FOV centre to 2.1 mm at the FOV corner [81]. Images of a mini-Derenzo phantom show that the smallest lesion resolved by the system is 2.4 mm in diameter.
The image reconstruction task for this scanner has been subject of an intense work. In an initial stage, image reconstruction was performed with a filtered backprojection based reconstruction algorithm that took into account the existence of DOI information and the irregular angular sampling of the scanner [86, 87]. Later, a list mode penalized maximum likelihood algorithm using Gaussian priors was developed [88, 82, 89]. A Monte Carlo based scatter correction algorithm was also developed [89].
To our knowledge, this scanner has never been tested with clinical data.

3.4.7 The YAP-PEM system

The YAP-PEM prototype is being developed within a collaboration of the Italian Universities of Pisa, Ferrara, Bologna and Roma [90]. The technology of this device derives from a small animal scanner, YAP-(S)PET previously developed by the group. The YAP-PEM scanner has been designed with the aim of detecting 5 mm breast lesions in diameter in an activity ratio of 10:1 between the cancer and the breast tissue. The device is composed of two stationary detector heads made of Yttrium Aluminum Perovskite scintillators doped with Cerium (YAP:Ce). This is a scintillator crystal that

produces a light output of about 20 photons/keV, has a decay constant of 30 ns and a density of 5.4g/cm^3 [91]. It has, however, a low Z number. Each detector head has a detection area of 6×6 cm^2 that comprises 30×30 detection elements with 2×2×30 mm^3 each. The system uses PS-PMTs to collect the scintillation light. The distance between the detectors can range from 5 to 10 cm, depending on the breast compression used.
For image reconstruction purposes, the ML-EM algorithm has been adapted to the planar nature of the acquired data, in order to obtain a pseudo-tomographic imaging method [92]. This method works on data that is converted into histograms that are indicated for planar data. These are known as planograms [93]. Geometrical symmetries are used to speed up the computations.
Monte Carlo simulation and image reconstruction studies performed for the YAP-PEM scanner indicate that the scanner is expected to have capability of discriminating 5 mm tumors in a target-to-background ratio of 10:1. However, due to the planar nature of the data, if two sources lie on the same axial plane, the system can not discriminate them, as it can be seen in Figure 3.10

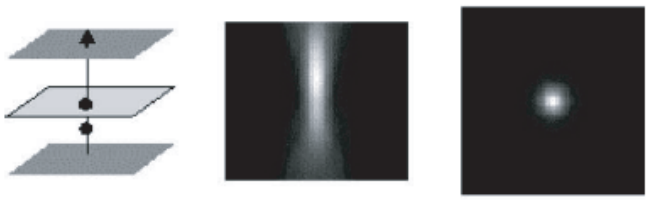

Figure 3.10: Phantom images obtained with the YAP-PEM prototype. Due to the planar nature of the scanner's data, if two sources lie on a same axial plane, the system cannot discriminate them. From [92].

3.5 Conclusions

In this chapter we have reviewed some of the instrumentation issues that impact on the performance of equipments that use positron emission tomography to image disease. We have emphasized on the most demanding aspects of dedicated instruments, with respect to conventional whole body scanners.
We have also reviewed the literature for the scanners that are or have been developed for imaging breast cancer with positron emitting radiotracers. In this review, we have briefly mentioned one of the important aspects of an imaging system, the image reconstruction strategies. We have seen that reconstruction methods used in PEM devices vary from simple backprojection algorithms to more sophisticated ones that are adapted from methods commonly used for PET image reconstruction. In the next chapter we will look with detail to a class of image reconstruction methods that are commonly used in PET, the statistical iterative image reconstruction algorithms.

Chapter 4

Image Reconstruction in PET

4.1 Introduction

For many years, the problem of reconstructing an image from the projection data acquired in Positron Emission Tomography was addressed with analytic approaches which were inherited from x-ray computed tomography. Analytic algorithms such as filtered backprojection (FBP) are based on the direct inversion of the Radon transform. They are fast, linear, predictable, and their properties are very well known [94]. The inversion of the Radon transform is derived for a continuous sampling and discretised afterward for sampled data [95]. Analytic algorithms are based on an idealized mathematical model for the data, the linear integral model, according to which the number of coincidence photon pairs detected along a LOR is approximately linearly proportional to the integral of the tracer density along a LOR. This model over-simplifies the physics inherent to the emission and detection processes in PET, limiting the accuracy of the images reconstructed with analytical algorithms.

In alternative to the analytic image reconstruction algorithms, model based algorithms, which can include accurate physical and statistical models of the systems, can be used. In opposition to analytical algorithms, these algorithms incorporate the discreteness of the data from the beginning. Their use usually results in improved image accuracy. As their formulation results frequently in large sets of nonlinear equations that must be solved by iterative methods, this class of algorithms is usually referred to as iterative image reconstruction algorithms. Further, if statistical functions are used to derive them, they are said to be statistical iterative reconstruction algorithms.

The use of iterative methods based on probability models for image reconstruction was already used in the field of astronomy in the early 1970's (Lucy, 1974, Richardson, 1972). Later, in 1976, Rockmore and Macovsky [96] introduced the Maximum Likelihood approach in the field of medical imaging. Nowadays, the most used algorithms for image reconstruction in PET belong to the class of iterative statistical algorithms.

In this chapter we will give an overview of the characteristics of the most important statistical iterative reconstruction algorithms used in PET image reconstruction. Previous to that, in Section 4.2, we will explain how the measured data can organized in order to be used with these algorithms.
In 3D PET, in order to reduce the computation time and to simplify the reconstruction algorithms, a rebinning step that manipulates 3D projection data into 2D projection data can be used prior to the image reconstruction. The most simple rebinning methods, such as the Single Slice Rebinning (SSRB) [97], lead to significant resolution degradation, whereas with Fourier based rebinning algorithms, such as FORE [98], degradation is less significant. After rebinning, 2D image reconstruction methods can be used. As we shall see, 2D reconstruction algorithms, which reconstruct stacks of 2D images separately to obtain an image volume, can be regarded as a particular case of 3D reconstruction algorithms. The algorithms that will be presented in the following sections can thus be implemented to be used with 3D projection data, as well as with data that has been rebinned.

4.2 Organizing the data

A Line of Response (LOR) in a PET scanner may be specified in a set of four coordinates (s, ϕ, z, θ), where s is the transaxial distance from the LOR to the scanner axis, ϕ is the azimuthal angle of the LOR, θ measures the axial distance between the points intersected by the scanner and z measures the axial distance relative to the scanner mid-plane. Figure 4.1 shows a graphical interpretation of the LOR coordinates.

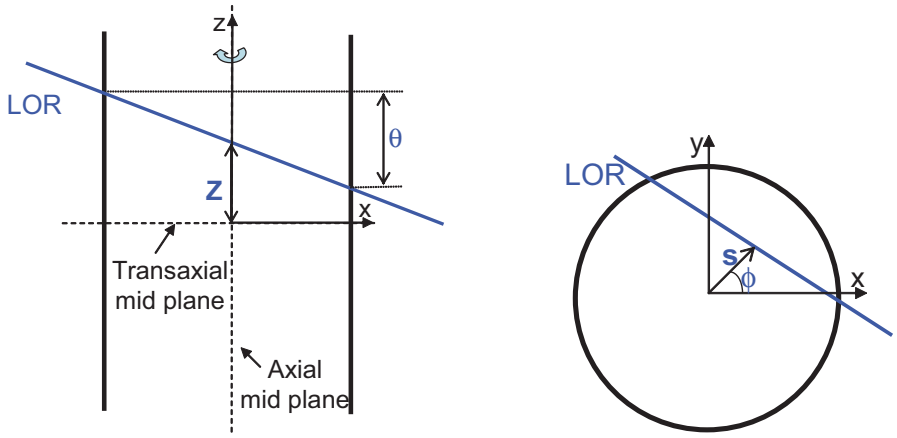

Figure 4.1: Representation of the coordinates of the Lines of Response in a 3D Sinogram. (a): view of a LOR in a plane parallel to the scanner rotation axis. (b): view of a LOR projected into the transaxial plane. Adapted from [99].

The reconstruction algorithms that will be presented in this chapter assume that the projection data space is partitioned into I bins, and that the individual counts are accumulated in this set of bins, thus defining an histogran in the data space. For the Lines of Response specified by the polar coordinates defined above, such an histogram is named *sinogram*.

Let us first consider only the transaxial component of the LORs, (s, ϕ). Sinograms group in a same row all the LORs that have the same transaxial angle, ϕ, that is, all the LORs belonging to a projection of the object along ϕ. This is represented in Figure 4.2.

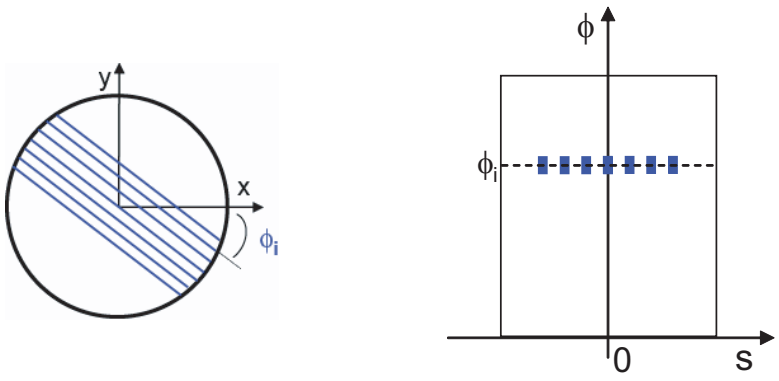

(a) (b)

Figure 4.2: A parallel projection of the object (a) corresponds to a row in the sinogram (b). Adapted from [95].

LORs that have the same radial position, s, are stored in a column of the sinogram. As represented in Figure 4.3, the LORs that cross a point source not centered in the field of view describe a sinusoidal curve on the sinogram, whereas a point source located in the center of the field of view corresponds to a straight line in the sinogram. The sinograms described above correspond either to LORs contained in a same detector ring, in which case the sinogram is called a direct sinogram, or to LORs in two different detector rings. In this later case, the sinogram is known as an oblique sinogram. For a scanner of N detector rings, there are N direct sinograms and $N\,(N-1)$ oblique sinograms, for a total of N^2 sinograms. This is exemplified in Figure 4.4 for the case of a four ring detector scanner.

Depending on the ring difference associated with a sinogram, the sinogram is said to belong to a given segment. The segment of a sinogram is indexed by the LOR coordinate θ. A segment is a set of sinograms with a given average ring difference, $ringB - ringA$. For instance, a direct sinogram belongs to segment 0, while LORs between ring 1 and ring 4 belong to segment 3 and LORs between ring 4 and ring 1 belong to segment -3. This is exemplified in Figure 4.4, where the LORs belonging to the direct sinograms

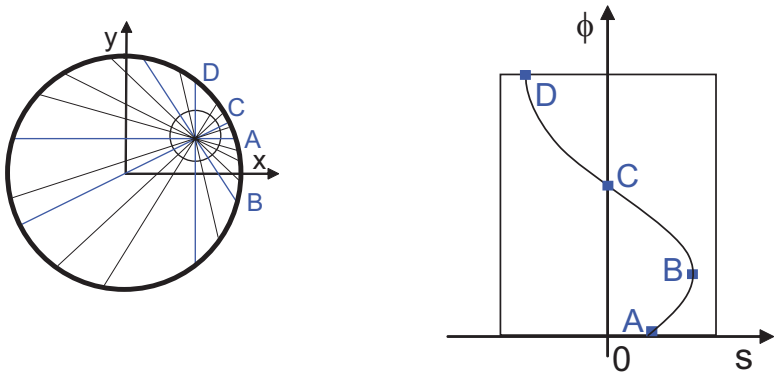

(a) (b)

Figure 4.3: A centered point source and an off-centered point source in the scanner (a) describe, respectively, a straight line and a sinusoidal line in the sinogram (b). Adapted from [95].

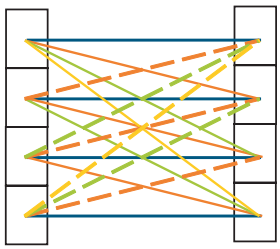

Figure 4.4: LORs belonging to direct segments (blue lines) and to oblique segments (orange, green and yellow full and dot lines) in a four ring scanner.

are represented in blue, while the LORs belonging to the different segments are represented in full and dot orange lines (segments -1 and $+1$), in full and dot green lines (segments -2 and $+2$) and in full and dot yellow lines (segments -3 and $+3$). The sign of the segment usually depends on the convention used. Usually, the view angle in a given segment runs only on half of the detector ring, that is, over 180°. The other half corresponds to the sinogram in the symmetric segment [100].

With respect to segments, we would like further to stress that a two-dimensional sinogram contains data belonging only to segment 0. Hence, a 2D reconstruction algorithm can be seen as a special case of a 3D algorithm where only data from segment 0 is used in the reconstruction process.

A complete 3D sinogram of a scanner with N detector rings contains $2N-1$ segments: one direct segment plus $N-1$ positive oblique segments plus $N-1$ negative oblique segments.

The axial position of the sinograms, indexed by z, is the last sinogram coordinate. The number of axial positions of a given segment depends on the segment, since more oblique segments, corresponding to a higher ring difference, exist only for the most

central rings. For instance, in the example depicted in Figure 4.4, the sinograms from segment 0 have four possible axial positions, while segment 3 (or segment -3) contains sinograms with a single axial position only. This is true if the segments have not been compressed, an operation that is known as *span*.
A more general data format than sinograms is named the list mode format (LMF). In the LMF, the activated detector coordinates, along with other kind of information such as the deposited energy or a time stamp, are stored sequentially as the photons are detected. The data can then be binned to the histogram mode and reconstructed with the conventional algorithms that will be presented in the following sections. Alternatively, iterative statistical algorithms that were developed for list mode data can be used [101]. The description of those algorithms is, however, beyond the scope of this work.

4.3 Statistical Iterative Reconstruction Algorithms

In general, the formulation of statistical iterative reconstruction algorithms requires the definition of the following five components [102, 103, 51]: a model for the image, a model for the data, a model for the physics of the measurement process, a cost function and an algorithm to optimize the cost function. Although the choices made for each of these components are usually made implicitly rather than explicitly, they can substantially influence the results obtained [104]. In the next paragraphs we will present the above mentioned five components, briefly discussing the main options that can be used for their choice.

4.3.1 A model for the image

For computing and display purposes, the true radiotracer distribution, which is a continuous function, is represented by a discrete domain function. This function, $\lambda(\mathbf{r})$, where $\mathbf{r}$ is a vector denoting spatial coordinates in the image domain, is represented as a finite set of basis functions, $\{b_j(\mathbf{r})\}$, according to :

$$\lambda(\mathbf{r}) \approx \sum_{j=1}^{J} \lambda_j b_j(\mathbf{r}) \tag{4.1}$$

The set of coefficients $\{\lambda_j\}$, j=1,...,J, which is intended to represent the expected number of emissions from the basis functions, has to be determined by the reconstruction algorithm from the photon pairs coincidence measurements $\{y_i\}$, i=1,...,I.
The most simple and common basis elements used in PET are non-overlapping small cubic volume elements - voxels - with unitary value inside and zero value elsewhere, arranged in a rectangular grid. Representing an image with voxels has the advantage

that they perfectly match the digital displays.
However, alternative classes of basis functions have been proposed and are under investigation, namely the *blobs* [105], the wavelets [106] and the natural pixels [107]. *Blobs*, in particular, have attracted great interest. Significant improvements in image quality have been demonstrated when using these basis functions, namely an increased accuracy and a reduction of the noise in the reconstructed images [108, 109]. *Blobs* are a generalization of window functions named Kaiser-Bessel. They are spherically symmetric bell shaped functions, with smooth transitions from one to zero. The represented image is also a smooth function, since it is composed of the superimposition of *blobs*. However, their generalized used has been hindered by the fact that, depending on their spacing and size, the associated processing time can be extremely high.
In the remainder of this work, we will consider that the basis functions in use are voxels.

4.3.2 A model for the physics of the measurement process

The system matrix $\mathbf{A}$, also known as the system model or the forward projection matrix, relates the unknown image $\boldsymbol{\lambda}$ to the expectation of each detector measurement, $E[\mathbf{y}]$ according to,

$$E[\mathbf{y}] = \mathbf{A}\boldsymbol{\lambda} \tag{4.2}$$

The element a_{ij} of the system matrix contains the probability that an annihilation in the jth basis function is detected by detector pair i. The mean of the ith detector pair, $\bar{y}_i$ is, then,

$$\bar{y}_i = \sum_{j=1}^{j} a_{ij}\lambda_j \tag{4.3}$$

for a tracer distribution defined by 4.1. The operation given by Equation 4.3 is also known as forward projection, since it is a model for the measurement.
The set of linear equations given by Equation 4.3 can be solved by direct inversion if a_{ij} and y_i are given. Although this approach has been investigated [110], such procedure is difficult due to the large dimensions of the projection matrix. Moreover, the solution of Equation 4.3 is unstable for small perturbations of the data. This is known as the ill-conditioned nature of the reconstruction problem. For those reasons, iterative methods are preferred to solve Equation 4.3.
There are several approaches to compute the system matrix $\mathbf{A}$. The simplest one is to compute the elements a_{ij} when they are needed, that is, during the reconstruction process. This approach, also known as *on-the-fly* computation, is best suited for models including, besides the geometric mapping between the source and the data, corrections for the effect of photon attenuation and for the different detection efficiency of the detector pairs .
An alternative approach consists on pre-calculating the system matrix, to store it on

disk and to load it when it is necessary. This allows to develop more complex models that include the corrections mentioned above, but also degrading effects such as those due to the positron range before annihilation or the detector blurring.
These more sophisticated models may lead to matrices with a very low degree of sparseness, and thus difficult to store and to manipulate. The system matrix can be factorised into a product of several matrices, each corresponding to a specific component of the physical model [111, 112].
The improvement of the system matrix can lead to a significant improvement in image characteristics such as spatial resolution, contrast, quantitative accuracy, lesion detectability, etc. However, it also must be considered the existence of a trade-off between system model accuracy and the associated computation time.
The geometric part of the system model can be computed either by methods based on the solid angle model, by methods based on the bilinear interpolation or by methods based on ray driven approaches [113]. Among the last, the contribution of one basis function to a projection element can be computed as a line length of intersection of the ray with the voxels [114] or, more accurately, as a volume of intersection of the tube of response with the voxel. Figure 4.5 illustrates both these approaches for a two-dimensional pixel array. A more detailed description of these algorithms will be given in Chapter 6.

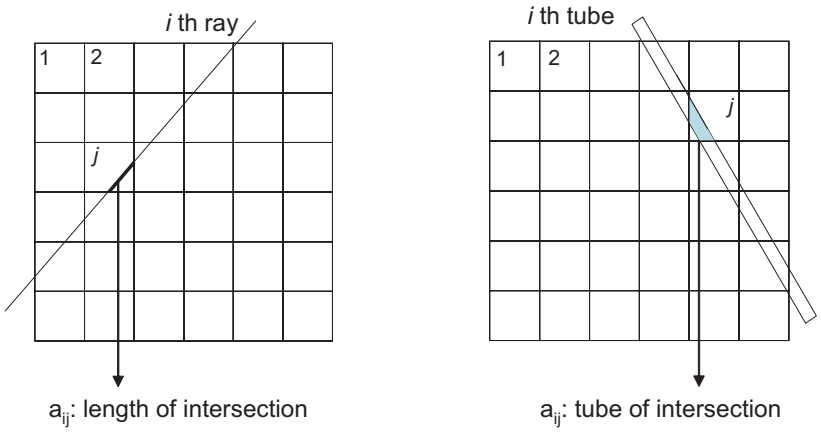

Figure 4.5: Computation of the a_{ij} element of the system matrix as the Length of Intersection of the line of response with the voxel (a) and as the Tube of Intersection between the tube of response and the voxel (b).

4.3.3 A model for the data

The output of the PET acquisition process reflects the statistical variation of a process that is essentially random, the radioactive decay. The emission of a positron is a rare

event, but, for a large number of radioactive nuclei, the emission of positrons follows a Poisson distribution [115]. Under the assumption that the detection of each photon pair by the system is independent of every other detection, then the data collected in a PET experiment is a collection of Poisson random variables. For a given unknown image $\boldsymbol{\lambda}$, the measured data vector $\mathbf{y}$ has mean $\bar{y}$ given by Equation 4.3 and distribution given by

$$p(\mathbf{y}|\boldsymbol{\lambda}) = \prod_{i=1}^{I} e^{-\bar{y}_i} \frac{\bar{y_i}^{y_i}}{y_i!} \tag{4.4}$$

In PET, the assumption that each measurement is independent of every other measurement is valid only when the system dead-time can be considered negligible. Moreover, Poisson statistics is a good data model only if no corrections for the effect of detecting random coincidences have been applied to the data. In fact, when one considers the mean given by Equation 4.3, one is ignoring the existence of random data. Some authors refer to this approach as the ordinary Poisson model [94]. A more accurate approach would consider that the expected value of the measured data vector is given by

$$E[\mathbf{y}] = \mathbf{A}\boldsymbol{\lambda} + \mathbf{R} \tag{4.5}$$

where $\mathbf{R}$ stands for the vector of random coincidences. With this model, the handling of the random data is incorporated in the reconstruction algorithm. Alternatively, if a correction is performed on the raw data by means of the subtraction of random estimated data, the outcome is no longer Poisson distributed. In such cases, a more correct approach would be to consider other models for the data [116]. For the sake of simplicity, in the present work we will consider the ordinary Poisson model given above.

4.3.4 An objective function

The objective function, also known as the cost function, is one of the key components of the iterative reconstruction methods. It is the criterion that is used to determine which image, among all the possible images, is the one to be considered as the best estimate of the true image. In the case of statistical algorithms, the cost function is a statistical function. Other important class of iterative algorithms used in PET that do not use statistical objective functions are known as algebraic reconstruction techniques [117]. These algorithms use algebraic distances as objective functions.

Among the statistical estimation criteria used in PET, one can distinguish the classical methods from the Bayesian methods. The classical methods, such as the Maximum-Likelihood (ML), the Least-Squares (LS) or the Weighted Least Squares (WLS) all try to find a solution that maximizes solely the consistency between the observed data and the reconstructed image. The term *classical* refers to the fact that these criteria are

based on the assumption that the object to be estimated, the image, is an unknown entity [103]. In contrast, Bayesian criteria such as the Maximum *a posteriori* (MAP), assume that the unknow image is itself random and can be described by a probability density function (pdf) that is known in advance of data collection [118].
In the next paragraphs we will present the aforementioned most prominent statistical objective functions used in PET.

4.3.4.1 Maximum-Likelihood

The maximum-likelihood is a standard statistical estimation cost function proposed by Fisher in 1921 [119]. The ML estimation is a way of estimating the parameter of an unknown distribution based upon observed data. It assumes that the observed data is drawn according to the underlying distribution [120].
Let $\boldsymbol{\lambda}$ be the parameter vector one wishes to estimate, and $\mathbf{y}$ the measured data vector, with pdf $p(\mathbf{y}|\boldsymbol{\lambda})$. The key idea in ML estimation is to determine the parameter vector, $\boldsymbol{\lambda}$, for which the probability of observing the measured data vector, $\mathbf{y}$, is as high as possible [120]. In the case of image reconstruction, $\boldsymbol{\lambda}$ is the image that one wishes to reconstruct and $\mathbf{y}$ is the vector of the measured projections. The objective function to be maximized, $\phi(\mathbf{y}|\boldsymbol{\lambda})_{ML}$, is the likelihood function, given by

$$\phi(\mathbf{y}|\boldsymbol{\lambda})_{ML} = p(\mathbf{y}|\boldsymbol{\lambda}) = l(\mathbf{y}|\boldsymbol{\lambda}) \tag{4.6}$$

Symbolically, the ML criterion to find an estimate on the parameter $\widehat{\lambda}$ can be written as

$$\widehat{\boldsymbol{\lambda}} = \arg\max_{\lambda} l(\mathbf{y}|\boldsymbol{\lambda}) \tag{4.7}$$

Usually, in order to simplify the maximization, the objective function used is the logarithm of the likelihood function, also known as the log-likelihood, $L(\mathbf{y}|\boldsymbol{\lambda})$:

$$\phi(\mathbf{y}|\boldsymbol{\lambda})_{ML} = L(\mathbf{y}|\boldsymbol{\lambda}) = \ln l(\mathbf{y}|\boldsymbol{\lambda}) \tag{4.8}$$

Since the logarithm is a monotonically increasing function, maximizing the log-likelihood yields similar results to maximizing the likelihood.
There are two main reasons that justify the preference of ML estimators over other estimators and those are related to the concept of bias and variance.
ML estimators are asymptotically unbiased because, as the number of observations becomes large, the estimates become unbiased, that is, $E\left[\widehat{\boldsymbol{\lambda}}\right] \rightarrow \boldsymbol{\lambda}$.
ML estimators are asymptotically efficient because, for a large number of observations, they yield minimum variance. In fact, among all the unbiased estimators, ML estimators are the least susceptible to noise [118]. Even so, image reconstruction methods based on the ML estimation criterion tend to yield noisy images. This happens because

it is in the nature of the method to produce images that are consistent with the data. Unfortunately, in the case of emission tomography, the data itself are noisy. Hence a good ML image estimate will be a noisy image.
A common approach in medical imaging is to allow a certain degree of bias in the reconstructed image in exchange for reduced variance [118]. Perhaps the most common way to accomplished this is to prematurely stop an iterative ML algorithm before it actually reaches the ML solution. The use of stopping rules for the iterative process has been investigated [121], but the definition of such rules is problematic, since different structures in the image converge at different rates. Other forms of explicitly introducing spatial smoothing in the images is by applying low-pass filtering or by using Bayesian methods, as it will be discussed later.

4.3.4.2 Least-Squares and Weighted-Least-Squares

The Least Squares principle is another statistical estimation criterion that, when used in the context of image reconstruction, also aims at maximizing the consistency between the observed data and the reconstructed image. The measurement of this consistency is an Euclidiean distance that should be minimized - the least squares. In other words, the estimated image $\widehat{\boldsymbol{\lambda}}$ is the one that, if observed through the system matrix $\mathbf{A}$, would yield projections $\mathbf{A}\boldsymbol{\lambda}$ that are the most similar to the observed projections $\mathbf{y}$ [118]. The fitting criterion is, in this case, the least squares.
Symbolically, the LS criterion can be expressed as

$$\begin{aligned} \widehat{\boldsymbol{\lambda}} &= \arg\min_{\lambda} \|\mathbf{y} - \mathbf{A}\boldsymbol{\lambda}\|^2 \\ &= \arg\min_{\lambda} \sum_{i=1}^{I} \left(y_i - \sum_{j=1}^{J} a_{ij}\lambda_j \right)^2 \end{aligned} \tag{4.9}$$

When there is available knowledge about the variance of the data, the weighted-least-squares method can be used [102]. With this approach, a different weight is given to data with different variance in the summation of Equation 4.9:

$$\begin{aligned} \widehat{\boldsymbol{\lambda}} &= \arg\min_{\lambda} (\mathbf{y} - \mathbf{A}\boldsymbol{\lambda})^T \mathbf{H} (\mathbf{y} - \mathbf{A}\boldsymbol{\lambda}) \\ &= \arg\min_{\lambda} \sum_{j=1}^{J} h_j (y_i - a_{ij}\lambda_j)^2 \end{aligned} \tag{4.10}$$

where $\mathbf{H}$ is a diagonal matrix with elements h_b on the diagonal. The weights h_b are usually chosen to be $var[y_b]^{-1}$. Under the assumption of Poisson distributed data, the variance equals the mean so $h_b = \bar{y}_b^{-1}$
The LS and the WLS methods suffer from the same problem of yielding highly noisy images as the ML method, since they both try to find a solution that is as consistent

as possible with the data. A different approach is used with Bayesian methods, as we shall see in the next paragraph.

4.3.4.3 Maximum *a posteriori*

The Bayesian approach to image reconstruction assumes that there exists some *a priori* knowledge about the nature of the image to be reconstructed. Therefore, the image is required to be consistent not only with the data, as it happened with the two objective functions previously described, but also with some additional criteria that are known independently of the data. The probability distribution of the tracer is treated as a Bayes prior distribution.
In the context of Bayesian estimation, the quantity to be determined is not a deterministic constant but a random variable. The *a piori* information about the nature of the image is given by the pdf $p(\boldsymbol{\lambda})$. The objective function to be maximized, $\phi(\boldsymbol{\lambda}|\mathbf{y})_{MAP}$ is the *a posteriori* probability density function, also known as maximum *a posteriori* (MAP). The MAP objective function can be written in the following form:

$$\begin{aligned} \phi(\boldsymbol{\lambda}|\mathbf{y})_{MAP} &= p(\boldsymbol{\lambda}|\mathbf{y}) \\ &= \frac{p(\mathbf{y}|\boldsymbol{\lambda})\, p(\boldsymbol{\lambda})}{p(\mathbf{y})} \end{aligned} \tag{4.11}$$

where the Bayes' law was used:

$$p(\boldsymbol{\lambda}|\mathbf{y}) = \frac{p(\mathbf{y}|\boldsymbol{\lambda})\, p(\boldsymbol{\lambda})}{p(\mathbf{y})} \tag{4.12}$$

According to the MAP criterion, the estimate $\widehat{\boldsymbol{\lambda}}$ of the true image is found by maximizing the objective function given by Equation 4.11. Similarly to what was done with ML estimation, it is the likelihood of the MAP function that will be maximized. Since it is the argument that is important in the estimation, and not the value of the maximum, the term that does not depend on $\boldsymbol{\lambda}$ will be omitted. With these considerations, the MAP objective function can be written as

$$\begin{aligned} \phi(\boldsymbol{\lambda}|\mathbf{y})_{MAP} &= [\ln p(\mathbf{y}|\boldsymbol{\lambda}) + \ln p(\boldsymbol{\lambda})] \\ &= L(\mathbf{y}|\boldsymbol{\lambda}) + P(\boldsymbol{\lambda}) \end{aligned} \tag{4.13}$$

where $P(\boldsymbol{\lambda})$ is known as the prior. The MAP criterion can then be written as

$$\widehat{\boldsymbol{\lambda}} = \arg\max_{\lambda} [L(\mathbf{y}|\boldsymbol{\lambda}) + P(\boldsymbol{\lambda})] \tag{4.14}$$

This shows that the MAP criterion is a composition of two terms. The data fitting term, given by the log-likelihood, $L(\boldsymbol{\lambda}|\mathbf{y})$, enforces the image to be consistent with the data. The image property term, given by the prior $P(\boldsymbol{\lambda})$, sets a penalty if the estimated image violates whatever assumptions were made about the nature of the image. The

maximization in Equation 4.14 attempts to obtain a balance between these two terms. For instance, if a prior assumption was made about the smoothness of the image, the MAP criterion would penalize a noisy image, even if this image was very consistent with the data. Further on this chapter we will discuss the prior terms that can be used in PET image reconstruction.

4.3.5 A numerical algorithm

The numerical algorithm is needed to optimize the objective function, producing the values of the coefficients of the basis functions chosen, given the measured data and the choices made for modeling the physics of the measurement process [103]. Such an algorithm is designed to produce a sequence of estimates of the coefficients of the basis functions that converge to a solution that optimizes the objective function.
A general scheme for most of the iterative algorithms used to optimize the objective functions presented in Section 4.3.4 is shown in Figure 4.6.

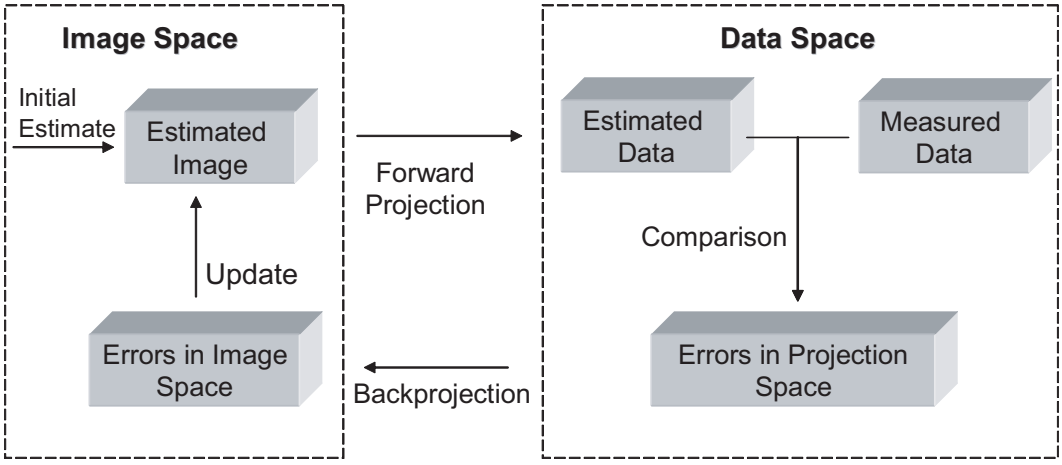

Figure 4.6: Schematic representation of a generic iterative reconstruction algorithm.

The reconstruction process begins with an initial image estimate $\widehat{\boldsymbol{\lambda}}^0$, usually uniform, of the basis function coefficients. A forward projection operation (Equation 4.3) is applied to the current image estimate, $\widehat{\boldsymbol{\lambda}}^{\boldsymbol{n}}$, yielding a set of estimated measured data, $\widehat{\mathbf{y}}^n$. These are the data that would have been observed if the true image was $\widehat{\boldsymbol{\lambda}}^n$, given the system matrix $\mathbf{A}$. The estimated data are compared with the actual measured data, $\mathbf{y}$, and a set of projection-space error values are generated. These are backprojected into the image space, originating the image-space error vectors that are used to update the image estimate. This, in turn, becomes the new estimate, $\widehat{\mathbf{y}}^{n+1}$. This process is repeated until it is stopped, either automatically or by the user.
The details of the projection, backprojection, comparison and update steps presented on the previous scheme make each algorithm unique. There are, however, some common

features that depend on the choice of objective function and on the procedure used to optimize it. In the following paragraphs we will review some of the most used algorithms in PET image reconstruction, namely those currently used to maximize the ML and the MAP objective functions.

4.4 Expectation-Maximization Algorithms

The Expectation-Maximization procedure for producing Maximum Likelihood estimates was formally presented as a prescription for developing algorithms for incomplete data problems in statistics by Dempster in 1977. It was with Shepp and Vardi [122] in 1982, who proposed using the Poisson model explicitly in PET, and Lange and Carson [123] in 1984, who extended it to the transmission case, that this approach gained high popularity in the field of medical imaging. Later, in 1994, Hudson and Larkin [124] developed a faster variation of the ML-EM algorithm, the OS-EM algorithm. In 1996, the OS-EM was first applied to 3D PET data [125]. Since its introduction in the 1990's, OS-EM has become the most popular iterative reconstruction method used in PET [126].
In the following paragraphs, we will present the Expectation Maximization solution for the Maximum Likelihood cost function. This will be followed by the presentation of the same solution using ordered subsets.

4.4.1 ML-EM

The Maximum Likelihood cost function can be easily optimized when the data are complete [127]. In emission tomography, however, the measured data are not complete, and a special algorithm − the Expectation Maximization − must be used to optimize the ML cost function. The Expectation Maximization algorithm is an iterative optimization method to estimate some unknown parameters $\boldsymbol{\lambda}$, given the measurement data, $\mathbf{y}$, when the complete data is not available. The concept of complete data is used in the sense that, if it was available, it would greatly simplify the estimation of the parameters. For example, in PET, the available information is the total number of photons recorded along each detector tube i. If additionally we new which photons detected at i were originated from voxel j, for every tube i and every voxel j, then the complete data would be available and the reconstruction problem would be fairly simple.
The EM algorithm to find a ML estimative of the parameters is composed of two main steps, an expectation step (E-step) that is followed by a maximization step (M-step). The algorithm starts with an initial estimate, usually an uniform distribution of the parameters. The expectation is then computed based on the current estimate of the parameters, with respect to the unknow underlying variables, and conditioned to the

observed data. The maximization step then provides a new estimate, by maximizing the expectation with respect to the parameters. The algorithm iterates between these two steps until convergence is achieved or it is stopped by the user.

In what follows, we will refer to the (unobserved) complete data vector as $\mathbf{x}$. Each element x_{ij} refers to the number of emissions in basis function j that are detected by detector tube i. Each variable x_{ij} is Poisson distributed with mean λ_{ij} given by [120]:

$$\lambda_{ij} = \lambda_j a_{ij} \tag{4.15}$$

The complete data vector is not observed directly, but only by means of the observed data vector, $\mathbf{y}$. The probability density function of the complete data is $p(\mathbf{x}|\boldsymbol{\lambda})$.

The basic idea behind the ML-EM algorithm is that we would like to find the parameter vector $\boldsymbol{\lambda}$ to maximize $\log p(\mathbf{x}|\boldsymbol{\lambda})$, but, as we do not have access to the complete data $\mathbf{x}$, instead we maximize the expectation of $\log p(\mathbf{x}|\boldsymbol{\lambda})$ given the data $\mathbf{y}$ and our current estimate of $\boldsymbol{\lambda}$ [120, 123]. Symbolically, the E-step can be written as :

$$\begin{aligned} Q\left(\boldsymbol{\lambda}|\widehat{\boldsymbol{\lambda}}^n\right) &= E\left[\log p(\mathbf{x}|\boldsymbol{\lambda})\,|\mathbf{y}, \widehat{\boldsymbol{\lambda}}^n\right] \\ &= E\left[L(\mathbf{x}|\boldsymbol{\lambda})\,|\mathbf{y}, \widehat{\boldsymbol{\lambda}}^n\right] \end{aligned} \tag{4.16}$$

The first argument in the expectation function given by Equation 4.16 is the conditioner of the complete data log-likelihood. The second argument is the conditioner argument to the expectation and is regarded as fixed and known at every E-step.

In the M-step of the algorithm, a maximization of the Q function is made with respect to its first argument :

$$\widehat{\boldsymbol{\lambda}}^{n+1} = \arg\max_{\boldsymbol{\lambda}} Q\left(\boldsymbol{\lambda}|\widehat{\boldsymbol{\lambda}}^n\right) \tag{4.17}$$

To write the E-step, we first note that, under the Poisson statistics, the likelihood function of the complete data is

$$l(\mathbf{x}|\boldsymbol{\lambda}) = \prod_{\substack{i=1,\ldots,I \\ j=1,\ldots,J}} e^{-\lambda_{ij}} \frac{\lambda_{ij}^{x_{ij}}}{x_{ij}!} \tag{4.18}$$

The log-likelihood function, combined with Equation 4.15, can be written as

$$\begin{aligned} L(\mathbf{x}|\boldsymbol{\lambda}) &= \sum_{\substack{i=1,\ldots,I \\ j=1,\ldots,J}} \{-\lambda_{ij} + x_{ij}\log\lambda_{ij} - \log x_{ij}!\} \\ &= \sum_{\substack{i=1,\ldots,I \\ j=1,\ldots,J}} \{-\lambda_j a_{ij} + x_{ij}\log\lambda_j\} + C \end{aligned} \tag{4.19}$$

where C contains the terms independent of λ_j. We then note that the expectation of a Poisson random variable (x_{ij}) conditioned to its sum (y_i) can be written as

$$E[x_{ij}|y_i, \lambda^n] = y_i \frac{\lambda_j^n a_{ij}}{\sum_{j'} \lambda_{j'}^n a_{ij'}} = \overline{x}_{ij} \tag{4.20}$$

Combining Equation 4.19 and Equation 4.20 the E-step can be written as

$$Q\left(\lambda|\lambda^n\right) = \sum_{\substack{i=1,\ldots,I \\ j=1,\ldots,J}} \left\{-\lambda_j a_{ij} + \overline{x}_{ij} \log \lambda_j\right\} + C \tag{4.21}$$

In the M-step, we maximize the conditional log-likelihood function 4.21 with respect to λ_j:

$$\frac{\partial Q\left(\lambda, \lambda^n\right)}{\partial \lambda_j} = 0 \Longleftrightarrow$$

$$\frac{\partial}{\partial \lambda_j}\left\{\sum_{i,j} -\lambda_j a_{ij} + \overline{x}_{ij} \log \lambda_j\right\} + C = 0 \Longleftrightarrow$$

$$-\sum_i a_{ij} + \sum_i \frac{\overline{x}_{ij}}{\log \lambda_j} = 0 \tag{4.22}$$

The ML estimate for λ_j is, then,

$$\widehat{\lambda}_j = \frac{\sum_i \overline{x}_{ij}}{\sum_i a_{ij}} \tag{4.23}$$

Combining Equation 4.20 and Equation 4.23 the general formula for the ML-EM algorithm is obtained:

$$\widehat{\lambda}_j^{n+1} = \frac{\widehat{\lambda}_j^n}{\sum_i a_{ij}} \sum_i \frac{y_i a_{ij}}{\sum_{j'} a_{ij'} \widehat{\lambda}_{j'}^n} = \widehat{\lambda}_j^n \frac{c_j^{L_k}}{\sum_i a_{ij}} \tag{4.24}$$

It is interesting to note that, as we have previously stated in paragraph 4.3.5 with respect to general iterative algorithms, the ML-EM algorithm can be viewed as an iterative forward and backprojection technique. In fact, the computation of the estimated data by $\sum_j \lambda_j a_{ij}$ corresponds to a forward projection operation, while the use of $\sum_i y_i a_{ij}$ is a backprojection operation.

The algorithm computes the value of a new voxel by iteratively multiplying the current voxel by the likelihood coefficient $c_j^{L_k}$. Since the update is multiplicative, it is ensured the non-negativity of the estimated images, provided that the initial estimate is also nonnegative [122]. Other particular characteristic is that the algorithm preserves the total number of counts for every iteration, $\sum_j \lambda_j = \sum_i y_j$ [122]. Further, it can also be proved [120] that the ML-EM algorithm increases the likelihood at each iteration, until a point where it does not increase anymore, but where it does not decrease, neither [128].

This algorithm has two main pitfalls. First, the sequence of estimated images converge at a very slow rate. Second, its has a tendency to develop noisy images. As it was discussed in paragraph 4.3.4.1, this property is in agreement with the objective function

used.

One strategy to overcome the first of these shortcomings is to partition the entire data set in several subsets, increasing the number of update steps while using only one subset in each update. Among the several methods that use this strategy, the most successful and widespread in PET is the Ordered Subsets - Expectation Maximization algorithm that will be presented in the next paragraph. To overcome the second of the above mentioned shortcomings, low pass filtering or Bayesian image reconstructions methods such as those that will presented in Section 4.5 can be used.

4.4.2 OS-EM

The OS-EM algorithm was proposed in 1994 by Hudson and Larkin [124] as an accelerated version of the ML-EM method and has since gained wide acceptance as a standard reconstruction method in PET [126].

The reasoning behind OS-EM is quite simple: the complete projection data set is divided into non-overlapping subsets and the standard ML-EM algorithm is applied sequentially to every subset. The image is updated at every sub-iteration, that is, at each pass to a single subset. An OS-EM iteration is complete when all the subsets have been processed. This is equivalent to an ML-EM iteration. However, at the end of an ML-EM iteration, the image would have been updated only once, whereas after a complete OS-EM iteration the image will have been updated m times, with m being the number of subsets. Provided that the subsets are mutually exclusive, each OS-EM iteration will have similar computation time as a single ML-EM iteration. This means that with OS-EM the convergence speed is accelerated by a factor proportional to the number of subsets used.

The general formula for the OS-EM algorithm [124] is:

$$\widehat{\lambda}_j^{n+1} = \frac{\widehat{\lambda}_j^n}{\sum_{i \in S_k} a_{ij}} \sum_{i \in S_k} a_{ij} \frac{y_i}{\sum_{j'} a_{ij'} \widehat{\lambda}_{j'}^n} \tag{4.25}$$

where $S_0, S_1, ..., S_{m-1}$ denotes a partition of the projection space into m subsets, $n = 0, 1, 2,$ is the sub-iteration number and k is the subset number, $k = n \mod m$. Obviously, when $m = 1$ the iterative formula reduces to the classical ML-EM algorithm.

The number and the constitution of the subsets must be chosen with care. In fact, the number of subsets defines the degree of acceleration, but it also influences the level of noise in the reconstructed images. If the number of subsets if chosen too high in order to obtain high acceleration, each subset will contain a small number of projections, and the resulting estimated images will be very noisy.

Regarding the choice of subsets, to avoid artifacts, the projections are usually chosen to have maximum separation in angle in each subset, as is shown in Figure 4.7

Further, it is also recommended [124] that the subsets are chosen so that an emission

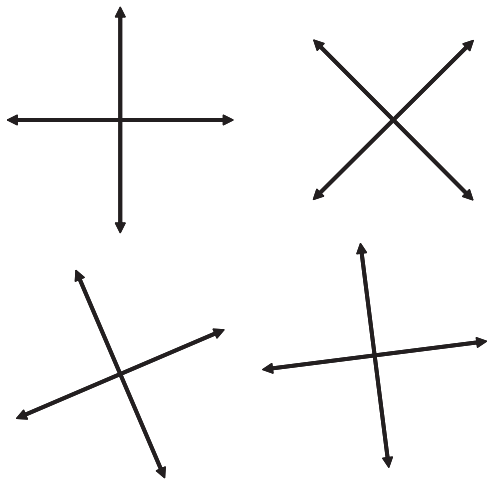

Figure 4.7: Schematic drawing of the use subsets. Adapted from [118].

from each voxel has equal probability of being detected in each of the subsets. This condition, also known as balanced subsets, may be difficult to achieve, but is usually verified in high count statistics situations.
It must be noted that the OS-EM solution is not truly a ML estimator, and, as a consequence, there is no global proof of its convergence [104]. However, even when the convergence to a ML-EM estimate is not guaranteed, the sequence of OS-EM estimates converges to an image that is often clinically useful.
As with the original EM algorithm, OS-EM produces high noise in the reconstructed images, so the same techniques used with ML-EM to control noise can be used with OS-EM.

4.5 Bayesian iterative algorithms

As we have previously seen in paragraph 4.3.4.3, image reconstruction using the Bayesian approach assumes that *a priori* information about the nature of the image can be used in the reconstruction process. A fundamental step in this approach is the definition of the prior term, which we will discuss in the next paragraph. This will be followed by the derivation of one possible algorithm that can be used to maximize the MAP objective function.

4.5.1 Defining a prior

The mathematical formulation of very specific and efficient priors can be very difficult. For that reason, in PET image reconstruction the priors used simply assume that the spatial distribution being imaged consists of different uniform regions with sharp transitions between them [103]. The designing of such term can be very challenging,

since it involves not only encouraging local smoothness within uniform regions but also avoiding blurring of their boundaries.

A smooth image can be described as one in which the intensity values of neighboring voxels are highly correlated, while distant voxels are not [118]. A simple mathematical model having this property can be described by the Gibbs probability distribution [129]. The Gibbs distribution has the general form

$$\begin{aligned} p(\boldsymbol{\lambda}) &= \frac{1}{Z}\exp\left[-\beta U(\boldsymbol{\lambda})\right] \\ &= \frac{1}{Z}\exp\left[-\beta\sum_{j}U(\boldsymbol{\lambda},j)\right] \end{aligned} \tag{4.26}$$

where Z is a normalization constant called the partition function; β is a scalar weight that controls the degree of smoothing introduced by the prior and $U(\boldsymbol{\lambda})$ is the energy function. The notation $U(\boldsymbol{\lambda}, j)$ is used to indicate that the value of the energy function is evaluated on $\boldsymbol{\lambda}$ at voxel j.

The energy function is a weighted sum of potential functions, each of which are functions of small sets of neighborhood voxels, named cliques [130]. The cliques for a particular neighborhood system must satisfy the condition that each pair of sites in each clique c_k are mutual neighbors [129].

A common choice for the $U(\boldsymbol{\lambda}, j)$ is an energy function that is computed using a potential function of the differences between pixels in clique N_j:

$$U(\boldsymbol{\lambda}, j) = \sum_{s\in N_j} w_{sj}\phi(\lambda_s - \lambda_j) \tag{4.27}$$

where w_{sj} are factors that give more weight to voxels in N_j nearer to voxel j compared to those further away [103]. The value of the potential function $\phi(\lambda_s - \lambda_j)$ increases with the increase in the difference of values in a pair of voxels. A quadratic function is an usual choice for the potential function [131], but it results in over-smoothed images, with the undesired suppression of sharp contrasts in the reconstructed images. Modified quadratic functions can be used that allow better edge preserving [132]. Many other potential functions have been studied that aim at maximizing the degree of smoothness of the reconstructed image, while maintaining abrupt transitions when true boundaries exist [104, 130]. An interesting approach is the use anatomical information obtained from anatomical modalities such as MRI or CT [133, 134]. This approach is justified by the fact that, since different anatomical structures have different physiological functions, there is a strong correlation between the anatomical image and the corresponding emission image [104]. However, the risk exists that the resulting emission image excessively reflects the anatomical information given by the prior, with the loss of important functional information in the data.

In this work we are specially interested in the use of an alternative prior named the

Median Root Prior (MRP) [135]. Before introducing such a prior, we will first present an algorithm that can be used to maximize the MAP objective function, given a Gibbs distribution function.

4.5.2 The One Step Late algorithm

Substituting the log of the Gibbs prior given in Equation 4.26 into the MAP objective function given in Equation 4.13, the objective function becomes

$$\begin{aligned} \phi(\boldsymbol{\lambda}|\mathbf{y}) &= L(\mathbf{y}|\boldsymbol{\lambda}) - P(\boldsymbol{\lambda}) \\ \phi(\boldsymbol{\lambda}|\mathbf{y}) &= L(\mathbf{y}|\boldsymbol{\lambda}) - \beta U(\boldsymbol{\lambda}) \end{aligned} \tag{4.28}$$

This equation shows very clearly that the weighting parameter β, also known as hyperparameter, determines how much smoothing is present in the MAP solution. If β is zero, the MAP solution is equivalent to the ML solution. As β increases, the prior term becomes more important in the maximization.
The MAP-EM algorithm can be derived in a similar fashion as the ML-EM algorithm was derived. Considering the objective function given above, the E-step becomes

$$L_p(\lambda|\lambda^n) = E\left[\log p(\mathbf{x}|\boldsymbol{\lambda})\,|\mathbf{y}, \widehat{\boldsymbol{\lambda}}^n\right] + \log p(\boldsymbol{\lambda}) = Q\left(\boldsymbol{\lambda}|\widehat{\boldsymbol{\lambda}}^n\right) - \beta U(\boldsymbol{\lambda}) \tag{4.29}$$

In maximizing Equation 4.29, we use Equation 4.21. The MAP M-step is then written as:

$$\frac{\partial L_p(\lambda, \lambda^n)}{\partial \lambda_j} = 0 \Longleftrightarrow$$

$$\frac{\partial Q(\lambda, \lambda^n)}{\partial \lambda_j} - \beta \frac{\partial}{\partial \lambda_j} U(\lambda_j) = 0 \Longleftrightarrow$$

$$-\sum_i a_{ij} + \sum_i \frac{\overline{x}_{ij}}{\lambda_j} - \beta \frac{\partial}{\partial \lambda_j} U(\lambda_j) = 0 \tag{4.30}$$

The MAP-EM estimate for λ is, then,

$$\widehat{\lambda}_j = \frac{\sum_i \overline{x}_{ij}}{\sum_i a_{ij} + \beta \frac{\partial}{\partial \lambda_j} U(\lambda_j)} \tag{4.31}$$

The partial derivate of $U(\lambda)$ in Equation 4.31 should be evaluated from the next estimate, which is not yet available. The MAP-EM algorithms differ essentially in the strategies used to determine that term [118]. Although there are several proposed algorithms to address that problem, the most common are the generalized EM (GEM) [136] and the One Step Late algorithm (OSL) [137].
The One Step Late approximation proposed by Green [137] and modified by Lange [138]

evaluates the partial derivate of $U(\lambda)$ at the current parameters estimation, λ^n. Taking this approximation into account and substituting x_{ij} in Equation 4.31 by the definition given in Equation 4.20, the iterative formula for the Maximum *a posteriori*−One Step Late (MAP-OSL) algorithm becomes

$$\widehat{\lambda}_j^{n+1} = \frac{\widehat{\lambda}_j^n}{\sum_i a_{ij} + \beta \frac{\partial}{\partial \lambda_j} U(\boldsymbol{\lambda}, j) \mid_{\lambda_j = \lambda_j^n}} \sum_i a_{ij} \frac{y_i}{\sum_{j'} a_{ij'} \widehat{\lambda}_{j'}^n} \tag{4.32}$$

4.5.3 The Median Root Prior

The median root prior (MRP) [135, 139] was developed based on the general assumption that an ideal PET image consists of constant neighborhoods with monotonous transitions between them. This is also the structure of the root signal of a median filter. By definition, a root signal is a signal that remains unaltered when the filter is applied. Since the median filter presents good results both in terms of noise reduction and edge preservation, one should expect to obtain high quality images through the application of a prior based on the median filter.
For the MRP, the prior distribution is Gaussian [139],

$$p(\lambda_j) = \frac{1}{\sqrt{2\pi M\beta}} \exp -\frac{1}{2} \frac{(\lambda_j - M)^2}{M/\beta} \tag{4.33}$$

where $M = Med(\lambda^n, j)$ stands for the median of voxels in a neighborhood centered at voxel j.
The OSL algorithm with the MRP, that we will refer to as the MRP algorithm, becomes defined as

$$\widehat{\lambda}_j^{n+1} = \frac{\widehat{\lambda}_j^n}{\sum_i a_{ij} + \beta \frac{\lambda_j - M}{M} \mid_{\lambda_j = \lambda_j^n}} \sum_i a_{ij} \frac{y_i}{\sum_{j'} a_{ij'} \widehat{\lambda}_{j'}^n} \tag{4.34}$$

One should stress that using the median filter is quite different from using an average, since repetitive averaging of the image would result in a blurred image, whereas the repetite application of the median filter produces an unaltered root image. Thus, with MRP, both smooth and abrupt spatial changes between areas of different activity are accepted [139].
The MRP algorithm was originally used with ML-OSL algorithm for 2D reconstruction [140], but was later used with the ordered subsets scheme for 3D image reconstruction [141]. One of the advantages of using the Median Root Prior is that, in contrast to other priors, the only parameter that needs to be adjusted is the β parameter, with no need to define or to optimize any extra parameter [135, 109].

4.6 Conclusions

In the present chapter we have focused on the general properties of the main statistical algorithms used actually in Positron Emission Tomography. Traditionally, these algorithms are used with data that proceeds from cylindrical scanners. Reconstructing the data that proceeds from scanners with alternative geometries, such as those presented in Chapter 3, poses additional demands on the image reconstruction algorithms. In the remainder of this work we will present the strategies that were followed to perform 3D image reconstruction from data proceeding from a dual plate PET scanner, the Clear-PEM scanner. A general overview of the Clear−PEM scanner is provided in the next chapter.

Part III

Materials and Methods

Chapter 5

The Clear-PEM scanner and Monte Carlo simulations

5.1 Introduction

In recent years there has been a significant progress in the development of small and compact dedicated scanners for Positron Emission Mammography, as we have seen on Chapter 3. The Clear-PEM scanner is one of such scanners. It is being developed by the Portuguese consortium PET-Mammography within the framework of the Crystal Clear Collaboration, at CERN [142]. In the present chapter we will overview the main technical characteristics and the design of the Clear-PEM scanner. This will be followed by a short description of the Monte Carlo simulation framework dedicated to Clear-PEM. Then, we will give an overview of the system geometry, phantoms and acquisition conditions that were simulated for the purpose of image reconstruction and software testing and refinement.

5.2 The Clear-PEM scanner

The Clear-PEM system is composed of a dual-plate detector head that is housed in a robotic mechanical gantry, as represented in Figure 5.1. The system has been designed to allow the examination of the breast and the axilla regions. For the breast examination, the patient will lay in the prone position with the breast hanging through an aperture in an imaging table. The two detector heads will be positioned in each side of the breast, as represented in Figure 5.1, and will have the ability to acquire data at several angular positions. The detector heads can also be positioned at different separation distances, which allows for the accommodation of different breast sizes.
Each detector plate, whose surface is, approximately, 16.2 cm$\times$ 14.1 cm, is constituted of a total of 3072 LYSO:Ce crystals, each crystal having $2\times2\times20$ mm^3. A scheme of

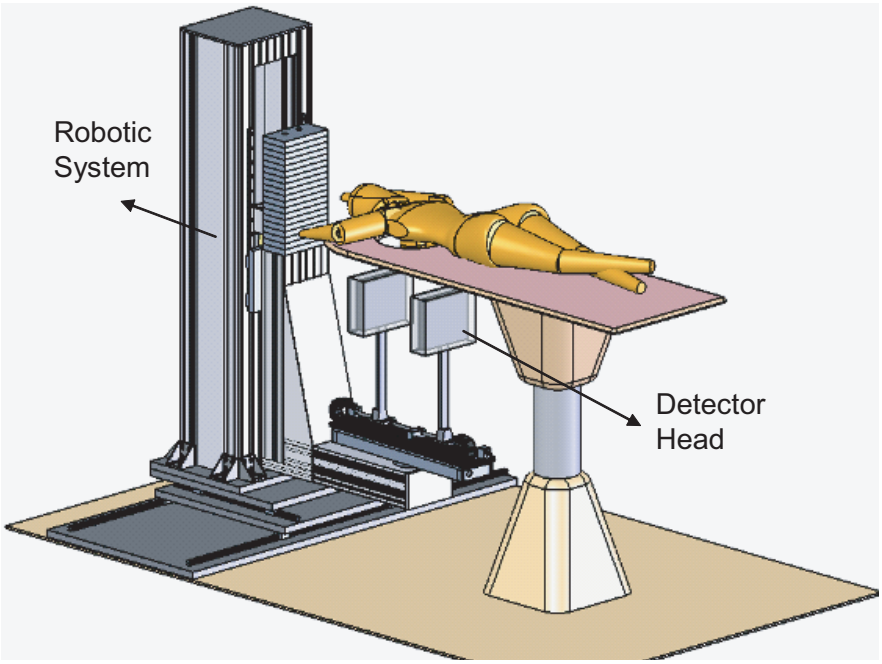

Figure 5.1: Representation of the Clear-PEM system. From [143].

a detector head is shown in Figure 5.2. The distribution of the crystals within the detector plates is as follows. Each detector plate is constituted of a set of four structures named *supermodules*, each one with 14×4 cm^2, placed side by side. Each supermodule is composed of 12×2 modules that, in turn, are composed of an array of 4×8 LYSO:Ce crystals. Therefore, each detector plate is constituted of 48×64 LYSO:Ce crystals.

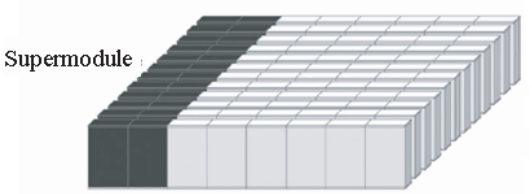

Figure 5.2: Representation of a Clear-PEM detector head, with an highlighted detector supermodule. From [144].

The readout of each module is performed by two 32-pixel avalanche photodiodes that are optically coupled to each side of the module, as shown in Figure 5.3. This double readout scheme allows for the measurement of the point of interaction of the incoming photon along the crystal length, a measure that is known as Depth Of Interaction (DOI). The DOI coordinate within the crystal is estimated from the asymmetry of the collected light at the top and bottom APD pixels. Experimental results have shown that, with this scheme, it is possible to obtain a 2 mm FWHM DOI resolution [145].

This measurement is important since, as we have seen in Chapter 3, it increases the uniformity of measure all over the field-of-view of the scanner. This feature is not common in the universe of the positron emission mammography dedicated scanners and therefore is perhaps one of the most important characteristics of the scanner (Chapter 3).

Figure 5.3: Representations of a Clear-PEM detector module with the double readout scheme. From [144].

The processing of the detector analogical signals, including the readout, the low noise amplification, the sampling and the storage are implemented in dedicated ASICs (Application Specific Integrated Circuits) that are integrated in the detection plates. The output analogue sampled pulses are digitized by Analogue Digital Converters (ADC) and transmitted to the data acquisitions system (DAQ). This system, based on FPGA (Field Programmable Gate Arrays), is responsible for the data reduction and storage. Data is send from here to a trigger system that selects two-photon events in coincidence within a programmable timing window and, at each trigger, the relevant data frames are send to the acquisition PC where energy and time information are analyzed [143]. For events with more than one active crystal in a detector head, due to Compton scattering, an event reconstruction position algorithms is used to assign the coordinates of the interaction. Those events that are within the selected energy window are validated, their final coordinates being used to define the LORs that are stored in a list-mode file [145].
The design and the development of the Clear-PEM system has been made with the help of the Monte Carlo simulation toolkit that will be described in the next section.

5.3 Monte Carlo Simulations

Monte Carlo (MC) simulation methods can be described as statistical methods that use random numbers to perform a simulation of a specified situation [146]. They can be used in almost all disciplines where particle interactions in matter play a role. In

particular, the evaluation and development of an imaging system can be greatly aided by the use of Monte Carlo simulations. Some of the MC simulation toolkits that are of public domain were developed for high energy physics experiments and hence contain detailed descriptions of processes involved in particle and radiation detection. One example of such a toolkit is GEANT4 [147], developed in the framework of an international collaboration at CERN.

GEANT4 has been the basis for the dedicated simulation framework that was developed to be used in the design and development of the Clear-PEM scanner. In particular, it allowed obtaining data for testing, evaluating and refining the image reconstruction software. This simulation framework was developed at LIP, one of the partners of the PET-Mammography consortium, by A. Trindade and P. Rodrigues [148, 149]. It contains several aspects of the simulation process, such as the definition of phantoms and phantom data, a detailed description of the geometry of the system and the digitization of the signals. In the following paragraphs we will provide a brief overview of the simulation toolkit that was developed for the Clear-PEM scanner. This will be followed by the description of the scanner geometry, phantoms and acquisition conditions that were considered in the Monte Carlo simulations.

5.3.1 Clear-PEM Monte Carlo simulation framework

The Geant4-based framework developed for Clear-PEM simulation studies is organized in three modules, as shown in Figure 5.4[148]. The *PhantomFactory* module is responsible for the simulation of the radioactive decay and photon tracking in user-defined phantoms. The *PEMsim* module performs the simulation of the detector response. In this module the several parameters that define the detector are defined. This includes, for instance, the number and the dimensions of the crystals, the dead spaces between them, the distance between the two detector plates and the possibility of rotations. The *DIGITsim* module simulates the front-end electronics and the data acquisition and trigger system. The output data of each simulation module can be stored in dif-

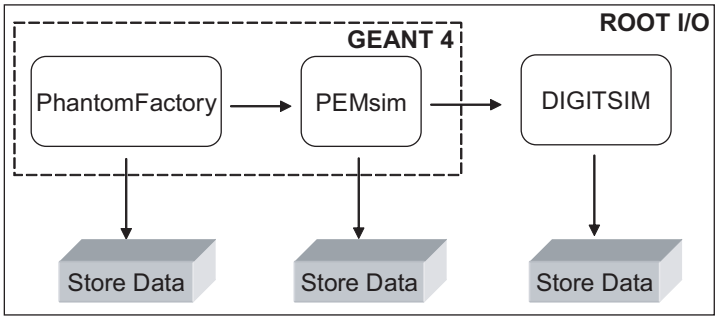

Figure 5.4: Schematic representation of the Monte Carlo framework developed for Clear-PEM simulation studies. Adapter from [148].

ferent output data formats (ROOT trees [150]). In particular, the output data from the *PETSim* module was used as an input to the image reconstruction algorithms. For purposes of 3D image reconstruction, the output files are read and the selected information on photon coincidences is binned into 3D sinograms, as it will be explained in Chapter 8.

As it was said before, this dedicated simulation framework was used to generate data that allowed testing the image reconstruction software. In the next paragraphs we will describe the simulated scanner geometries, the implemented phantoms and the simulated acquisition parameters used for such purpose.

5.3.2 The simulated scanner geometries

The testing of the image reconstruction methods developed for the ClearPEM scanner relied on the simulated data of a standard geometry of acquisition. Such a standard acquisition consisted on the detector heads placed 10.0 cm apart, acquiring data in two perpendicular positions around the breast (0° and 90°). A representation of the positions of the detector heads, as well as of the coordinate system of the detector is shown in Figure 5.5.

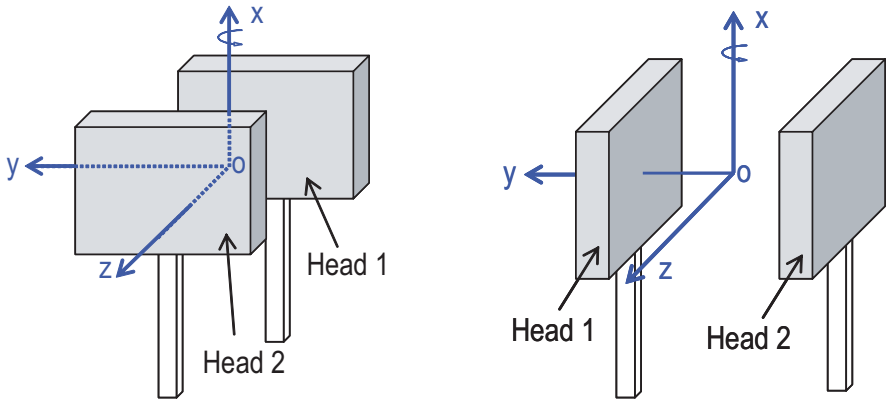

(a) Detector Plates at 0°. (b) Detector Plates at 90°.

Figure 5.5: Scheme of a ClearPEM standard acquisition.

The first approach for testing the image reconstruction software for the Clear-PEM scanner used a simplified description of the scanner geometry that was implemented in the *PEMsim* module. The simulated data of simple geometrical phantoms in the simplified scanner geometry allowed to isolate pure image reconstruction issues from other detector related artifacts. A second approach aimed at testing and refining the reconstruction algorithms in acquisition scenarios resembling a real examination. For that purpose, a more realistic scanner geometry was used, and the image reconstruction algorithms were tested both with simple geometrical phantom data and with more

complex, anthropomorphic phantom data.
The simplified scanner geometry consisted on two 9.6 cm × 12.8 cm detector plates placed 10.0 cm apart, acquiring data in two orthogonal projections. Each detector plate was pixelized into a set of 48×64 individual detector elements, each one with 2×2×20 cm^3. Therefore, no inter-crystals dead spaces were considered. The exact distance between the faces of the crystals in the two opposing detector heads was exactly 10.0 cm, since neither the front-end electronics nor the housing box of the detector heads were simulated.
The realistic scanner geometry described the Clear-PEM detector plates in a more realistic way. The detector heads were described as a set of several supermodules, each one composed of several modules that in turn are composed of several crystals, as it was explained in Section 5.2 above. This means that the inter crystal dead spaces are now considered, with different distances separating crystals inside a module, crystals in the edge of two contiguous modules or between crystals in the edge of two contiguous supermodules. The detector plates dimensions were 14.2 cm × 16.1 cm and they were placed 10.0 cm apart. However, due to the housing box and the front end electronics, whose physical presence was also simulated, the distance between the faces of the crystals in the two opposing detector heads was 13.4 cm. Simulated acquisitions were performed in two orthogonal projections.

5.3.3 The Phantoms used

Two kinds of phantoms were used for the Monte Carlo simulations performed: geometrical phantoms and anthropomorphic phantoms. The geometrical phantoms allowed for the evaluation of image intrinsic characteristics such as spatial resolution or image uniformity. The simulated data from the anthropomorphic phantom allowed to test the reconstruction algorithms in acquisition scenarios close to a real examination. In the following paragraphs we will provide a description of these phantoms.

5.3.3.1 The Geometrical Phantoms

Two geometrical phantoms were used in the simulations with the simplified scanner geometry, allowing the measurement of both the reconstructed images spatial resolution and of the image uniformity. How these figures of merit are computed will be in subsequent chapters:

The Cross Phantom consisted on seven point sources located in different regions of the field of view: a centered point source surrounded by the other six, each one 25 mm away from the center in three orthogonal directions. A representation of this phantom can be seen in Figure 5.6(a).

The Sphere Phantom consisted on a 16 mm diameter sphere with homogeneous activity located at the center of the FOV. A representation of this phantom is shown in Figure 5.6(b).

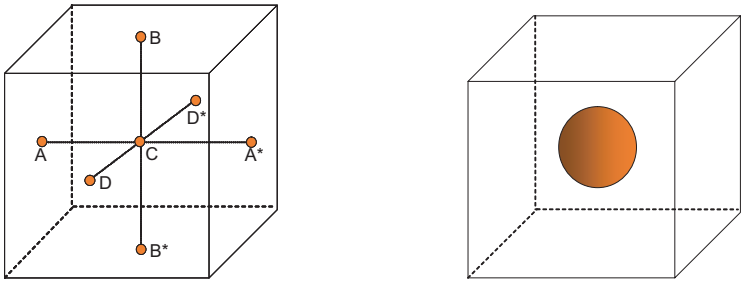

Figure 5.6: Geometrical phantoms used in the simplified geometry studies: The Cross Phantom (a) and the Sphere Phantom (b).

Simulation of these phantom data included exact depth of interaction information, detector Compton scattering, no positron range and no background activity. The energy window considered ranged from 350 keV to 700 keV, and an energy resolution of 16% for 511 keV was considered. The simulations performed with these phantoms were stopped when a total of 10^6 coincidence events were detected.
To access the spatial resolution in the reconstructed images in the realistic scanner geometry studies, a different geometrical phantom was used:

The Chain Phantom consisted on a sequence of nine point sources placed along the three main detector axes, at 10 mm intervals, as represented in Figure 5.7.

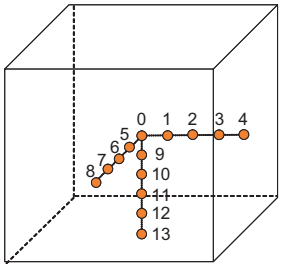

Figure 5.7: The Chain Phantom that was used in the realistic scanner geometry studies.

With respect to the Cross Phantom described above, this phantom allowed the evaluation of the spatial resolution over a wider region in the field of view. The simulations using this phantom included exact DOI information, detector Compton scattering, no positron range and no background activity. A total of 10^6 events for each point source was simulated, in the $350 - 700$ keV energy window.

5.3.3.2 The Anthropomorphic Phantom

The studies involving the realistic scanner geometry described above aimed at evaluating the image quality foreseen to be obtained with the Clear-PEM system and the considered reconstruction algorithms, in acquisition conditions that were as realistic as possible. Besides the realistic scanner geometry, an anthropomorphic breast phantom and realistic acquisition conditions needed to be considered. The anthropomorphic phantom used was the NURBS Cardiac Torso (NCAT) phantom of the breast [151] that was used decoupled from the torso. Therefore, the effect of scattered or random events from annihilations proceeding from organs inside the torso were not included in the simulations. The volume chosen for the breast phantom (747cc) corresponds to a medium sized breast. For simulating attenuation a density of 0.85 g/cc, corresponding to adipose tissue, was attributed to the breast tissue.
The NCAT breast phantom was used together with pairs of spherical simulated lesions, with diameters 3 mm, 5 mm, 7 mm and 10 mm, located in a central and in a periphery plane within the breast. An overview of the breast phantom with the centered and the off-centered lesions and the detector heads is presented in Figure 5.8.

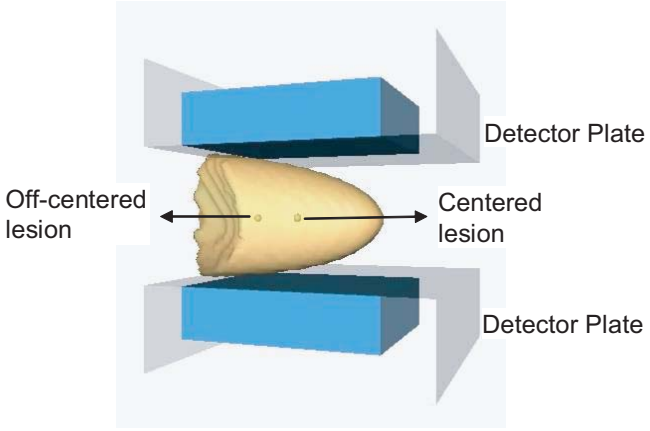

Figure 5.8: The NCAT Brest Phantom with two simulated lesions. Adapted from [152].

As we have seen in Chapter 2, the FDG uptake in the breast normal tissue is related to the radiographic density of the breast [38]. Therefore, in this study, four different types of breast tissue were considered: predominantly fat, fat with some fibroglandular tissue, heterogeneously dense and extremely dense. These correspond to the four different groups of breast densities, as defined by the Breast Imaging Reporting Data system (BI-RADS) of the American College of Radiology [153]. The FDG concentration values in the normal tissue for each of the breast tissue type were computed from data available in the literature [154]. The computed values were: 1.59 kBq/ml for predominantly fat breast tissue; 2.04 kBq/ml for fat breast tissue with some fibroglandular breast tissue; 3.81 kBq/ml for dense breast tissue and 4.81 kBq/ml for extremely dense

breast tissue. The simulated FDG concentration in the lesions was 20.35 kBq/ml, a value that corresponds to the average uptake in malignant breast lesions [155]. The use of these concentrations lead to the lesion-to-background ratios that are summarized in Table 5.1.

FDG Uptake (kBq/ml)		Lesion to Background ratio
Background	Lesion	
1.59	20.35	13:1
2.04	20.35	10:1
3.81	20.35	5:1
4.81	20.35	4:1

Table 5.1: FDG concentration in normal breast tissue and in simulated lesions used with the NCAT breast phantom and the corresponding lesion-to-background ratios.

The simulated NCAT breast phantom data included exact DOI information, detector scattering and the positron range before annihilation.

5.4 Planes of the breast

In this section we will define the terminology that will be used for the breast image planes throughout the rest of this work. In whole body imaging the sections of the body are referred to in terms of axial, coronal and sagittal planes as shown in Figure 5.9(a). The axial plane divides the body into upper and lower parts. In Nuclear Medicine techniques, the axial plane corresponds to the plane that is perpendicular to the axis of rotation of the scanner. By analogy, in the present work we will refer to the plane that is perpendicular to the axis of rotation of the Clear-PEM scanner as the axial plane, as depicted in Figure 5.9(b). This plane divides the breast into the parts closer and farther from the torso.

In whole body techniques, the sagittal plane refers to the plane that divides the body or its parts into right and left sides. In the images of the Clear-PEM scanner, the sagittal plane is the plane of the breast that is parallel to the whole body sagittal plane. This plane divides the breast into its medial and lateral sides, in the mammographic nomenclature.

In whole body techniques the coronal plane is the plane that is perpendicular both to the sagittal and the axial planes. In the breast planes nomenclature the sagittal plane is also normal both to the sagittal and the axial planes. This plane divides the breast into its upper and lower parts.

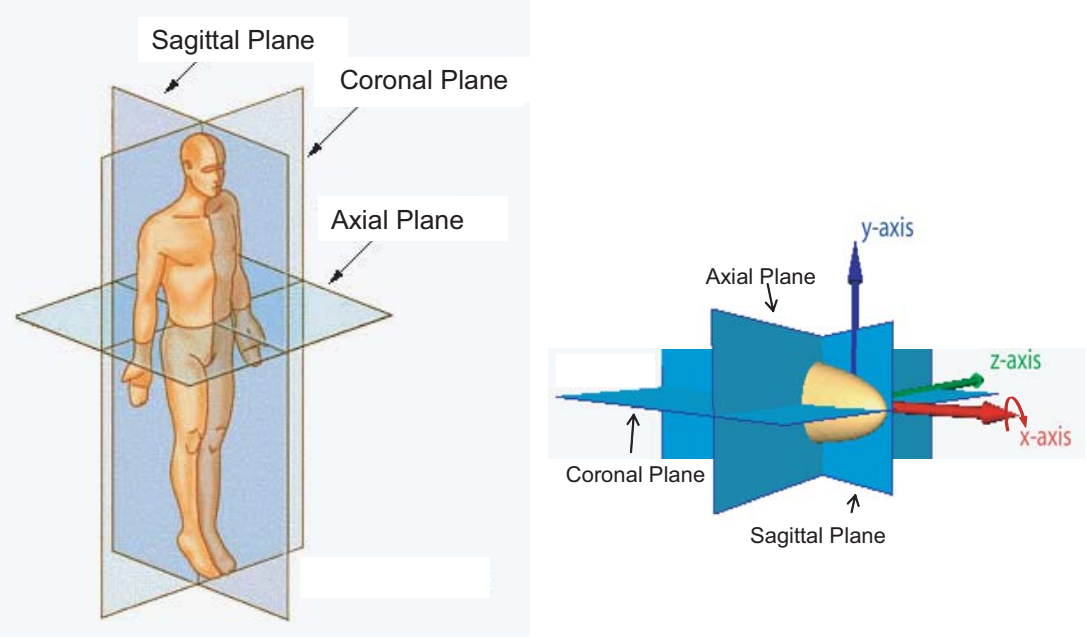

(a) (b)

Figure 5.9: Terminology for (a) the body planes (adapted from [156]) and for (b) the breast planes (adapted from [152]).

5.5 Conclusion

In this chapter we have described the main technical features of the Clear-PEM scanner and the simulation software that was used in its development. The simulated acquisition data that was obtained with the phantoms and scanner geometries described will be used to test the 3D image reconstruction software that was implemented for the Clear-PEM scanner. Such implementation will be presented in Chapter 7. The performed tests and results will be presented in Chapter 8 and in Chapter 9. Prior to this, we will describe, in the next chapter, the image reconstruction library that has been used as the basis of the Clear-PEM 3D image reconstruction.

Chapter 6

The STIR library

6.1 Introduction

STIR, the acronym of 'Software for Tomographic Image Reconstruction', is an open source, object oriented library for 3D PET image reconstruction that has been the basis for 3D image reconstruction in the Clear−PEM scanner. STIR, which was originally developed for the PARAPET project [157], was designed to be used with data proceeding from cylindrical PET scanners. and, eventually, dual-head rotating gamma cameras. It is an image reconstruction platform that combines several high-speed features, such as fast projection and backprojection operators and the use of geometrical symmetries, allowing for the implementation of 3D reconstruction algorithms that perform at reasonable speeds.

STIR is composed of several building blocks that correspond to the components necessary to define an image reconstruction algorithm. Since this library is written using the C++ programming language, these building blocks are implemented as classes, or hierarchy of classes. STIR is structured in four main hierarchies of classes: classes for describing images, classes for the projection data, classes for the projection operators and classes for the reconstruction algorithms.

In this chapter, the general structure of the library will be explained, with focus on the description of its main building blocks and on the special features of the implemented projection operators and reconstruction algorithms.

The work presented in this thesis was developed from the Version 1.2 of STIR, released in June 2004. Therefore, in this chapter we shall limit our description to the features implemented at that time, despite the fact that later releases (actual STIR version is Version 1.4) have presented more features.

The documentation in which this chapter is based is the STIR's documentation [158, 159], source code comments and the code itself.

6.2 Images

As it was discussed in Chapter 4 (in paragraph 4.3.1), for computer display and for image reconstruction purposes, the images are described as a set of basis functions. In STIR, the corresponding discretisation of the images is implemented in the class *DiscritisedDensity*. The image hierarchy implemented in STIR is represented in Figure 6.1.

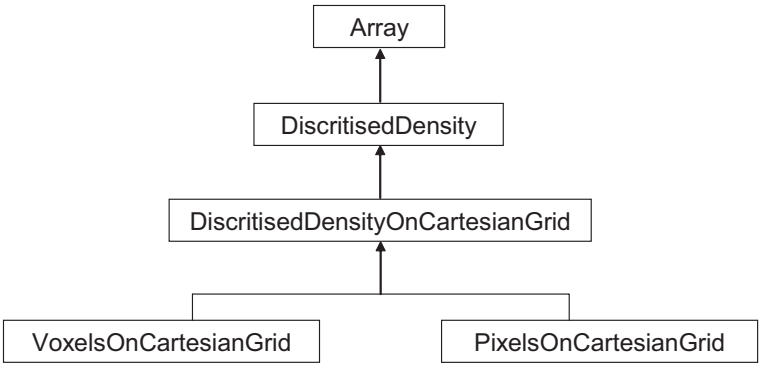

Figure 6.1: Hierarchy of classes for describing images. Adapted from [159].

As it is shown in this figure, the class *DiscritisedDensity* inherits the properties of the class *Array*. This base class provides the methods for memory allocation of multi-dimensional numeric arrays. The class *DiscretisedDensityOnCartesianGrid*, which follows *DiscritisedDensity* in the hierarchy, implements the case where the image grid is formed by an orthogonal class of vectors (in opposition, for instance, to a cylindrical grid). The last level in the hierarchy is the specification of the basis function themselves. In STIR's Version 1.2 only voxels and pixels are implemented, in classes *VoxelsOnCartesianGrid* and *PixelsOnCartesianGrid*, respectively. Other basis function, such as *blobs* can be implemented as well.

6.2.1 Image Coordinates and Conventions

The coordinate system for Cartesian Grids are chosen as represented in Figure 6.2.
The scanner axis, z, is pointing from the gantry toward the bed and its origin is in the middle of the first ring of detectors in the scanner. The horizontal and vertical axis, x and y, respectively, have their origin on the central slice of the scanner. The horizontal axis is pointing right when looking from the bed into the gantry and the vertical axis is pointing downwards. In STIR, the X and Y dimensions of the images must be odd, so that the center of the scanner coincides with the center of a pixel.
The voxel space is a partitioning of the field of view into voxels whose transaxial edge lengths, d_s, equal the size of a projection bin and whose axial length equal half the distance between two adjacent detector rings. The reason for choosing the axial sampling distance of the image as half the distance between detector ring is shown in

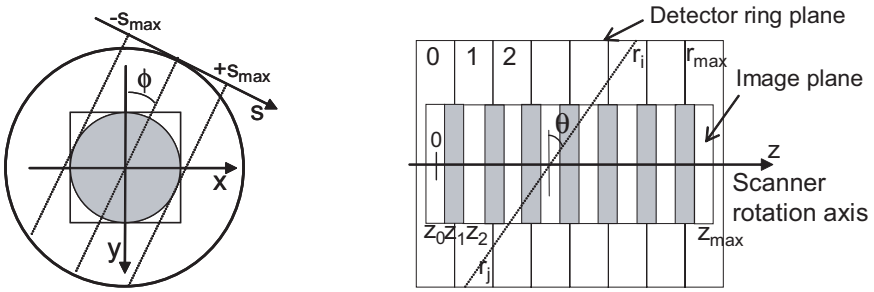

(a) (b)

Figure 6.2: Coordinate system for the projection data and for the images used in STIR. Transaxial coordinate system in 6.2(a) and axial coordinate system in 6.2(b). Adapted from [100].

Figure 6.3. In fact, if forward projection is performed with an axial sampling distance equal to the detector width, small details, such as the shaded voxels in Figure 6.3(a), remain unseen. On the contrary, for the sampling chosen, a better axial image resolution is achieved [113, 160].

(a) (b)

Figure 6.3: Axial section through the image volume and the detector rings. If the axial sampling distance chosen for the image is equal to the detector width, small details remain unseen (b). When forward projecting, the sampling distance of the projection must match that of the image (b). From [113].

6.3 Projection Data

The relevant classes for dealing and describing the projection data are included in the *ProjData* hierarchy and in the the *ProjDataInfo* hierarchy.

The class *ProjData*, whose inheritance diagram is shown in Figure 6.4, is the general class to access the projection data. It has two derived classes: the class *ProjDataGEAdvance*, used to read projection data from a specific General Electric (GE) scanner and the class *ProjDataFromStream*. The latter is a more general class that allows to read/write projection data from/to a binary stream. This stream can be

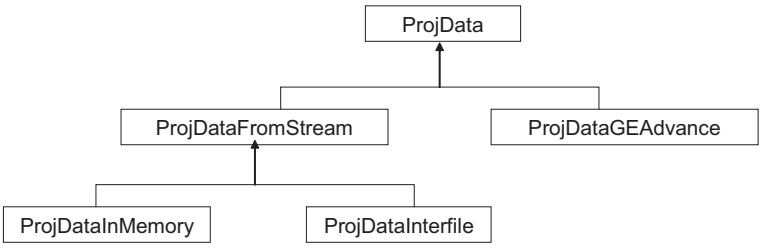

Figure 6.4: File Formats for Projection Data [159].

stored either temporarily in memory (*ProjDataInMemory*) or in a file in Interfile format (*ProjDataInterfile*).
An interesting feature of class *ProjData* is that it allows to deal with subsets of the projection data. This is specially useful since 3D projection data can be huge. Thus, being able to handle only a small part of the data leads to a simplification of many procedures. As was explained in Chapter 4, the projection data from a 3D PET study are stored as a four dimensional structure with coordinates (s, ϕ, z, θ). STIR provides several means for storing data on disk. Projection data organized on segments can be stored either as a *SegmentByView* object or as a *SegmentBySinogram* object. The hierarchy of classes for storing segments is shown in Figure 6.5.

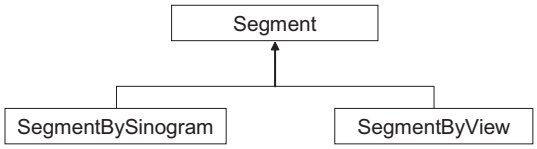

Figure 6.5: Hierarchy of classes for storing segments.

In *SegmentByView* objects the segment number is fixed and the data is ordered by view angle, axial position and tangential position. This is also known as the View Mode. In *SegmentBySinogram* objects the segment number is also fixed but the data are ordered by axial position, then view angle, and finally the tangential position. This is also known as the Volume Mode. A representation of these objects can be seen on Figure 6.6.
One can also work with 2D subsets of segments, organized either as 2D sinograms or as viewgrams:

- In 2D sinograms the segment number and the axial position indices are fixed, and the resulting histogram is organized as tangential position against view angle, as we have seen in Chapter 4. A representation of a 2D sinogram is shown as the shaded area in Figure 6.6(a).

- In viewgram the segment number and the view number indices are fixed, and the resulting histogram is organized as the tangential position against the axial

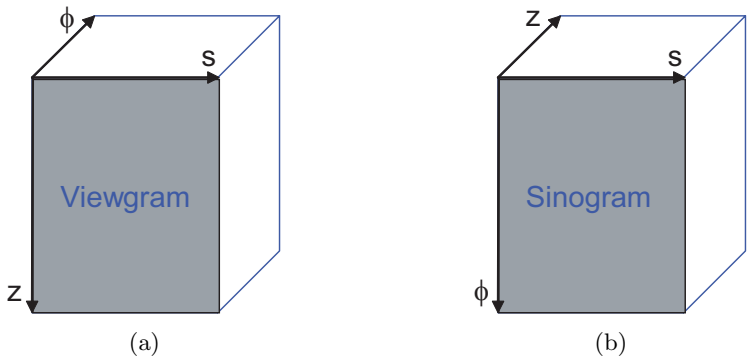

Figure 6.6: View Mode (a) and Volume Mode (b) storage for 3D PET data sets. Adapted from [100].

position. A representation of a viewgram is shown as shaded area in Figure 6.6(b).

The projectors implemented in STIR, which will be described in the next paragraph, use input data that is organized in View Mode, which means that the tangential position s and the axial position z coordinates are processed in the inner loops of the computations. This organization was found to be the fastest one for backprojection operations [161]. Besides, the projector operators can also work with viewgrams that are related by geometrical symmetries, since this further speeds the computations. Related viewgrams are implemented in class *RelatedViewgrams*. The geometrical symmetries used will be discussed later.
Another important feature of class *ProjData* is a member function that allows access to *ProjDataInfo* objects. These are objects that completely describe the data, including its dimensions, the scanner type, its geometry, etc. The hierarchy for class *ProjDataInfo* is represented in Figure 6.7.

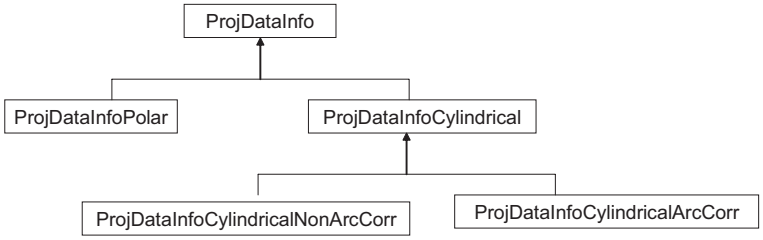

Figure 6.7: Hierarchy of classes for geometric information of the projection data.

The derived class *ProjDataInfoCylindrical* implements the information on projection data proceeding from a cylindrical scanner. This data can be either arc corrected (*ProjDataInfoCylindricalArcCorr*) or not (*ProjDataInfoCylindricalNoArcCorr*). The arc correction is usually applied on the data prior to reconstruction. It corrects for the fact that, due to the curved nature of the cylindrical scanners, the LORs passing near

the center of the ring are spaced farther apart than the LORs on the periphery of the scanner. The reconstruction algorithm will need to have the information on whether this correction was applied (in which case the LORs will all be equally spaced) or not.

6.3.1 Projection Data Coordinates and Conventions

In STIR, the 3D projection data is organized in 3D sinograms. The coordinate system used is shown in Figure 6.2. The number of measured projection elements along the s axis is odd, so that $s = 0$ is positioned at the center of the central projection element. The value of the smaller ring index of the sinogram fixes the axial position.

6.4 Projection operators

As we have seen on Chapter 4, paragraphs 4.3.5 and 4.4.1, most iterative algorithms can be written in terms of forward projection and backprojection steps. In STIR, the forward projection operations are based on Siddon's algorithm [114], while the backprojection operations use bilinear interpolation between the projection elements and the four nearest voxels. Both these algorithms will be explained in the following paragraphs, as well as the use of geometrical symmetries to enhance the algorithm's performance.
The need to use different algorithms for forward projection and backprojection arises from the fact thatif Siddon's algorithm is used for backprojection, it causes artifacts at certain angles between the direction of projection and the cubic image grid. The same happens if the bilinear interpolation algorithm is used in forward projection [113].
In STIR, corresponding to the forward projection and to the backrojection operation there exists the hierarchy *ForwardProjectionByBin* and the hierarchy *BackProjectionByBin*, respectively. In the following paragraphs we will look with more detail into both these hierarchies, describing the projection algorithms that they implement. The basic objects handled by these projector classes are *RelatedViewgrams* and *DiscretisedDensity*. Besides these two hierarchies, STIR also provides an hierarchy to use the projectors in a single projection matrix. This hierarchy is named *ProjMatrixByBin*.

6.4.1 Projection Matrix By Bin Hierarchy

The *ProjMatrixByBin* is a base class for creating projection matrices objects to be used instead of separate projection/backprojection pairs. It provides methods to access to the rows of the projection matrix. Its simple hierarchy is shown in Figure 6.8.
The derived class *ProjMatrixByBinUsingRayTracing* implements a function that calculates the projection matrix elements using the algorithm explained in paragraph 6.4.2.1. As it is shown in Figure 6.8, it would be possible to add to this hierarchy another derived

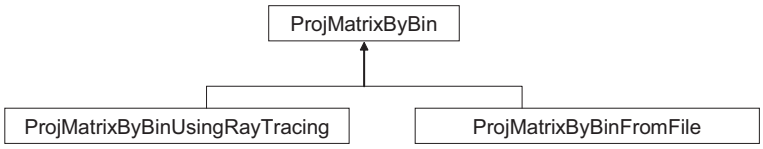

Figure 6.8: Hierarchy of classes for Projection Matrix. [159].

class, *ProjMatrixByBinFromFile* to be used to deal with a pre-calculated projection matrix.

6.4.2 Forward Projection Hierarchy

The *ForwardProjectionByBin* class is a base class for all the forward projector operators. Its hierarchy diagram is shown in Figure 6.9.

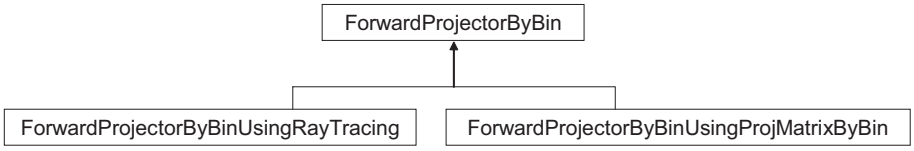

Figure 6.9: Hierarchy of classes for Forward Projection operators. [159].

The base class has members to store all the needed geometrical information, to inform on what symmetries the projector handles and to project the volume either into the entire projection data or into a subset (a viewgram, more specifically). The functions belonging to this class are virtual functions, which, in object oriented programming, means that their functionality is determined by its derived classes. Therefore, it is up to the derived classes to implement the functions that actually perform the computations. The derived class *ForwardProjectionByBinUsingProjMatrixByBin* implements an interface of *ForwardProjectorByBin* given any *ProjMatrix* object. This is done by storing the *ProjMatrix* object, and, when necessary, extracting the relevant information of the projection matrix.
The other forward projector operator available in STIR is implemented in class *ForwardProjectorByBinUsingRayTracing*. It implements the forward projection using Siddon's algorithm for ray tracing. In STIR, Siddon's algorithm is enhanced by the use of geometrical symmetries and by the possibility of using an approximation to a Tube of Response. How this is done will be explained in the next paragraph. Two special characteristics of this class is that the image to be forward projected must be of type *VoxelsOnCartesianGrid* and that the projection data must be of type *ProjDataInfoCylindrical*.

6.4.2.1 Siddon's algorithm in STIR

Ray tracing approaches for computing the forward projection use the length of intersection between a given LOR and a voxel to determine the weight that voxel contributes to the projection element corresponding to the LOR. Siddon's algorithm [114] reduces the complexity of the computations by considering that, rather than being independent elements, the voxels consist on the intersection of orthogonal sets of equally spaced parallel planes. Consequently, one must find the line of intersection of the LOR with a set of parallel planes, a more efficient task than to compute the intersection of the LORs with the individual voxels. Figure 6.10 illustrates the central idea beyond Siddon's algorithm in the two-dimensional case. The points of intersection of the LOR with the grid (black circles on the left scheme of Figure 6.10) consist in two sets of points: the points of intersection of the LOR with the vertical lines (white circles on the right scheme of Figure 6.10) and with the horizontal lines (black circles on the right scheme of Figure 6.10). In the three dimensional case, there is also a third set of points of intersection of the LOR with the set of parallel lines corresponding to the third dimension.

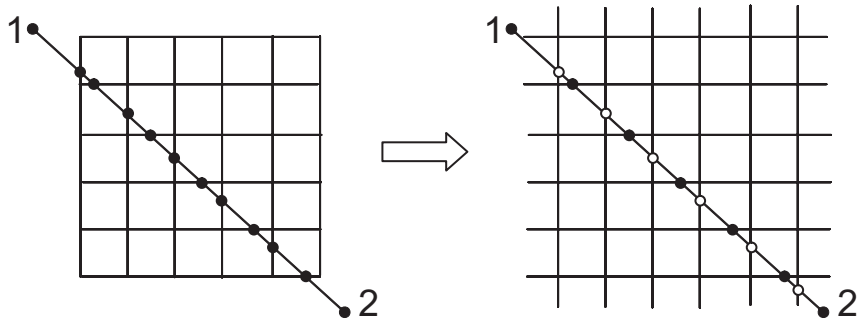

Figure 6.10: Central idea beyond Siddon's algorithm: the length of intersection of a LOR with the pixels of an image can be computed independently for every pixel (left) or, more efficiently, as the intersection of the LORs with two orthogonal sets of equally spaced, parallel lines. Adapted from [114].

As the lines in each plane are equally spaced, it is only necessary to find the first intersection and then generate all the others by recursion. The algorithm first computes the three independent sets $\{\alpha_x\}, \{\alpha_y\}, \{\alpha_z\}$ of parametric intersections of the LOR with each orthogonal set of parallel planes. Then, the sets are merged in order to obtain one sorted set of parametric intersections of the LOR with the three-dimensional grid. The length of the LOR contained by a particular voxel is simply the difference between two adjacent parametric values in the merged set. The corresponding voxels indices are also calculated. Starting from the first voxel transversed by the LOR and moving toward the last, the voxel values are weighted by the corresponding intersection length and summed to yield the contribution to the projection of the image along that LOR.

6.4.2.2 The use of geometrical symmetries

There are LORs in a sinogram that are linked by simple geometrical symmetries. These symmetries are exploited to substantially reduce the amount of computation of the forward projection operations, since the length of intersection that is computed for one LOR can be reused for other LORs [113]. The symmetries acting on each of the the coordinates of a LOR are summarized in [113] as follows:

Translational symmetry along the z axis: since the axial imaging sampling is the double of the axial data sampling, parallel LORs shifted by one detector ring will traverse the image in geometrically equivalent positions than those shifted by double the voxel size along the z-axis;

s **symmetry** , or symmetry about the center of the image volume: voxel $A_0(X, Y, Z)$ on LOR (s, ϕ, θ, z) has its counterpart on voxel $A_s(-X, -Y, Q)$, with $Q = 4r_0 + 2 + 2\delta - Z$ on LOR $(-s, \phi, \theta, z)$. Here, r_0 is the lowest ring in the LOR and δ is the ring difference between the two rings that define the LOR.

ϕ **symmetry** , which is a four fold symmetry. A voxel $A_0(X, Y, Z)$ lying on a LOR (s, ϕ, θ, z) between detector rings $(r_0; r_0 + 1)$ shares its geometrical properties with voxel $A_1(Y, X, Q)$, (Q defined as previously) on LOR $(s, \pi/2 - \phi, \theta, z)$; with voxel $A_2(-Y, X, Z)$ on LOR $(s, \pi/2 + \phi, \theta, z)$; and with voxel $A_3(-X, Y, Q)$ on LOR $(s, \pi - \phi, \theta, z)$.

θ **symmetry** : a voxel $A_0(X, Y, Z)$ on LOR (s, ϕ, θ, z) possesses equivalent positions of voxel $A_\theta(X, Y, Q)$ on LOR $(s, \phi, -\theta, z)$

6.4.3 Backprojection Hierarchy

The abstract base class for all backprojectors is the class *BackProjectorByBin*. Similarly to base class for forward projection, it has members to store all the geometrical information and to inform on which symmetries the projector handles. It also has members to project the whole projection data into the volume and to project only a part of the projection data (viewgrams or a specified range of viewgrams) into the volume. The hierarchy diagram for this class is shown in Figure 6.11.

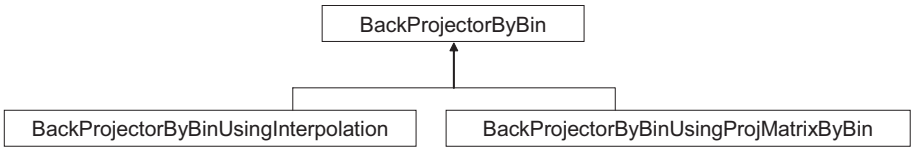

Figure 6.11: Hierarchy of classes for Backprojection operators [159].

The *BackProjectorByBinUsingProjMatrixByBin* class implements a BackProjectorByBin given any ProjMatrix object. The derived class *BackProjectorByBinUsingInterpolation* implements the backprojection by interpolating the LOR through the center of the voxel. The algorithm that this class implements, and that will be described in the next paragraph, is a 3D incremental backprojection method which combines with the use of the symmetries of the image volume to speed up the computations [160]. In the axial direction, this algorithm has been modified to include a piecewise linear interpolation scheme, which approximates a Tube of Intersection for data that has not been compressed in the axial direction [162].

6.4.3.1 Incremental Bilinear Interpolation

The principles underlying the backprojection algorithm by bilinear interpolation is illustrated in Figure 6.12.

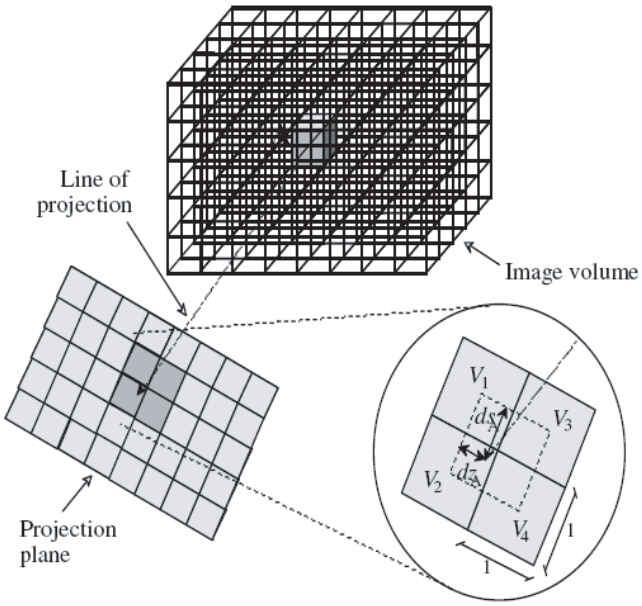

Figure 6.12: Basic principle of backprojecting by bilinear interpolation. The center of voxel A is projected onto the projection plane, and a bilinear interpolation between the four nearest projection elements allows the determination of the contribution of the defined projection elements to the intensity of voxel A. From [113].

The center of every voxel (in Figure 6.12, only voxel A is projected) is projected onto the projection plane, and a bilinear interpolation between the four nearest projection elements, (V_1, V_2, V_3, V_4) allows the determination of the contribution of the defined projection elements to the intensity of voxel A.
The algorithm uses the concept of beam, where a beam is defined by the center of four adjacent projections elements, as shown in Figure 6.13.

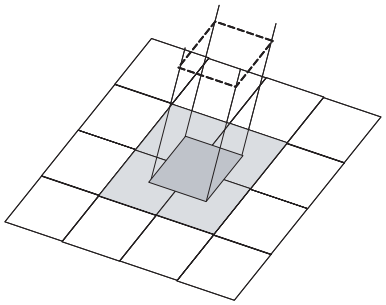

Figure 6.13: A beam, defined by four adjacent projection elements. Adapted from [113].

For a voxel A contained in the beam, the bilinear interpolation between the four projection elements that define the beam is given by

$$V_A = (1 - ds_a)(1 - dz_a) V_1 + ds_a (1 - dz_a) V_2 + (1 - ds_a) dz_a V_3 + ds_a dz_a V_4 \quad (6.1)$$

where ds and dz are as defined in Figure 6.12. The voxel value is obtained by summing the update values V_A over the projections at all available angles. To increase the computation speed, the backprojection of a particular beam can be performed by an incremental method , as described next. Fist, Equation 6.1 is re-written as

$$\begin{aligned} V_A &= V_1 + ds_A K_1 + dz_A K_2 + ds_A dz_A K_3 \\ &= V_{A,incr} + ds_A dz_A K_3 \end{aligned} \quad (6.2)$$

where

$$\begin{aligned} K_1 &= V_1 - V_1 \\ K_2 &= V_3 - V_1 \\ K_3 &= V_4 - V_2 - V_3 + V_1 \end{aligned} \quad (6.3)$$

and

$$V_{A,incr} = V_1 + ds_A K_1 + dz_A K_2 \quad (6.4)$$

A similar relations holds for a voxel B contained in the beam and that is adjacent to A:

$$V_B = V_{B,incr} + ds_B dz_B K_3 \quad (6.5)$$

with

$$V_{B,incr} = V_1 + ds_B K_1 + dz_B K_2 \quad (6.6)$$

Combining Equation 6.6 and Equation 6.4, one obtains

$$V_{B,incr} = V_{A,incr} + (ds_B - ds_A) K_1 + (dz_B - dz_A) K_2 \quad (6.7)$$

The quantities K_1, K_2, K_3 are beam invariants and can be calculated only once for all voxels inside a given beam. The quantities $ds_B - ds_A$ and $dz_B - dz_A$, which are also beam invariants, are functions of ϕ and θ. Due to symmetry considerations, only $0 < \phi < \frac{\pi}{4}$ and $\theta > 0$ need to be considered. Therefore, the values of $ds_B - ds_A$ and $dz_B - dz_A$ for a particular beam can only take four values each, depending on the position of voxel B with respect to voxel A. Those values are as follows:

- $\delta s_x = ds_B - ds_A$ and $dz_x = dz_B - dz_A$ if B is reached from A by a displacement of -1 along the x-axis;

- $\delta s_y = ds_B - ds_A$ and $dz_y = dz_B - dz_A$ if B is reached after a displacement of $+1$ along the y-axis;

- $\delta s_d = ds_B - ds_A$ and $dz_d = dz_B - dz_A$ if B is reached diagonally in the transaxial plane by a 1 displacement along x and a $+1$ displacement along y;

- $\delta s_z = ds_B - ds_A$ and $dz_z = dz_B - dz_A$ if B is reached by a displacement of $+1$ along the z axis.

The backprojection of a particular beam can then performed according to the following scheme:

1. Finding the first voxel in the beam, A, and calculating its update values by Equation 6.1;

2. Determining the beam invariants K_1, K_2, K_3;

3. Determining the beam invariants $\delta s_{x,y,d,z}$ and $\delta z_{x,y,d,z}$ for ϕ and θ;

4. Determining the next voxel in the beam, B, by a searching flow algorithm;

5. Determining $ds_B = \delta s + ds_A$ and $dz_B = \delta z + dz_A$

6. Determining the update value of voxel B by Equations 6.5 and 6.7;

7. Repeating steps 4 to 6 until the update values of the last voxel in the beam is calculated.

This algorithm is known as partial incremental backprojection, since a significant part of the calculations consist on sums. Since the beam invariants $\delta s_{x,y,d,z}$ and $\delta z_{x,y,d,z}$ depend on ϕ and θ for each beam, the computations are performed for a fixed ϕ and θ. This is why the backptojection operators implemented in the library take as input the data organized as viewgrams.

6.4.3.2 Piecewise linear interpolation

As was explained in paragraph 6.2.1, for efficiency reasons, in STIR the z voxel space is equal to half the spacing between the rings. In this case, the update value for the voxel cannot be calculated from Equation 6.1, but instead, by

$$\begin{aligned} V_A^{'} &= (1-ds_a)(3/2-dz_a)V_1 + ds_a(3/2-dz_a)V_2 + (1-ds_a)(dz_a-1/2)V_3 \\ &\quad +ds_a(dz_a-1/2)V_4 \;\; if\;\; 1/2 < dz_a < 3/2 \end{aligned} \tag{6.8}$$

$$V_A^{'} = (1-ds_a)V_1 + ds_a V_2 \;\; if\;\; z_a \leq 1/2 \tag{6.9}$$

$$V_A^{'} = (1-ds_a)V_3 + ds_a V_4 \;\; if\;\; dz_a \geq 3/2 \tag{6.10}$$

Equation 6.8 can be further written in terms of the beam constant defined in 6.3:

$$V_A^{'} = V_1 - K_2/2 + ds_a(K_1 - K_3/2) + dz_a K_2 + ds_a dz_a K_3 \tag{6.11}$$

For a voxel B adjacent to A and whose center lies inside the same beam, V_B is given by :

$$V_B = V_{B,incr} + dz_B ds_B K3, \tag{6.12}$$

with

$$V_{B,incr} = V_{A,incr} + (ds_B - ds_A)(K_1 - K_3/2) + (dz_B - dz_A)K_2 \tag{6.13}$$

This is known as the piece-wise linear interpolation model, and it can be seen as an approximation of the volume of intersection of the tube of response with the voxel [162].

6.4.3.3 Searching flow algorithm

The searching flow algorithm is used to find the next voxel in the beam. Since a displacement along the axial direction does not affect the transaxial components of the voxel, the searching flow algorithm can be separated into a search in the (x, y) plane and a search along the z axis.
Given the system coordinates defined above, the s coordinate of a voxel $A(X, Y, Z)$ is given by

$$s = X_A cos\phi + Y_A sin\phi \tag{6.14}$$

Under the condition *pixel_size=bin_size* the direction of the displacement toward the next voxel in the (x, y) plane are determined by the value of ds, according to

if $ds \geq \cos\phi$ the direction of displacement is -1 along the x-axis

if $ds \inf 1 - \sin\phi$ the direction of displacement is -1 along the x-axis

if $1 - \sin\phi \leq ds \sup \cos\phi$ the direction of displacement is -1 along x and +1 along y

A necessary condition for the voxel to belong to the beam is that dz must be comprised between 0 and 1/2. For $\theta \geq 0$, the direction of displacement along the z-axis is given by

if $dz < 0$, the displacement is of one voxel along z

else, there is no displacement along z

The values of ds and dz are updated at every new position, and searching is continued until the last voxel in the beam is reached.

6.4.3.4 The use of geometrical symmetries

The computations presented in the above paragraph are only valid for $s > 0$, $0 < \phi < \pi/4$ and $\theta > 0$. Similarly to what was described in paragraph 6.4.2.2, symmetry considerations allow the determination of the quantities ds and dz for the voxels of other beams without the need to explicitly calculating them. The list of voxels directly related to one explicit calculation of ds and dz by symmetries in s, ϕ, θ and z can be found in [160]. It has been found that the more efficient results are obtained using the s, ϕ and θ symmetries only.

6.5 Geometrical Symmetries

As we have seen, the projector operators use geometrical symmetries to reduce the number of elements that need to be computed. Therefore, STIR has an hierarchy of classes for encoding and finding the symmetries between the projection data and the image grid. The base class used for such purposes is *DataSymmetriesForViewSegmentNumbers*. Its inheritance diagram is represented in Figure 6.14.

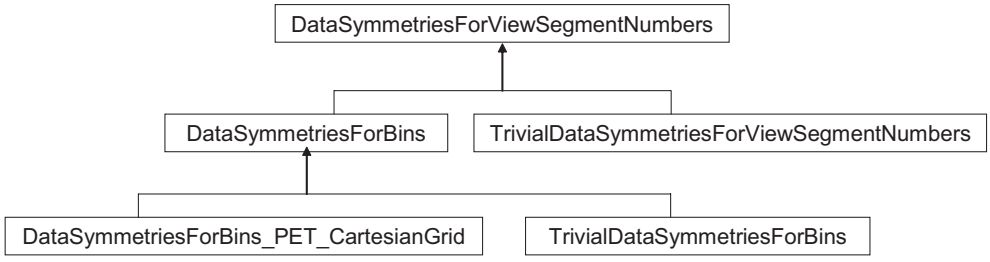

Figure 6.14: Hierarchy of classes for Data Symmetries.

The derived class *TrivialDataSymmetriesForViewSegmentNumbers* is used to encode and to find symmetries when this is needed but there is no need to use a projector operator. This class only works with pairs of view and segment numbers. For this purpose, objects from the *ViewSegmentNumbers* class, a very simple class that

is used to store view and segment numbers, are used. The class *TrivialDataSymmetriesForViewSegmentNumbers* has members to find if a given ViewSegmentNumber is 'basic', in the sense that all the related ViewSegmentNumbers objects can be obtained by using symmetry operations on the 'basic' ones. It has also members that, given a particular ViewSegmentNumber, find the corresponding 'basic' ViewSegmentNumber. The derived class *DataSymmetriesForBins* encodes and finds the symmetries that are common to the geometry of the projection data and the discretised density. This class is mainly useful for classes derived from *ProjMatrixByBin*. It is used together with class *SymmetryOperation*. Is has member functions to find if a given bin is a 'basic' bin, to find the corresponding 'basic' bin of a given bin and the respective symmetry operation. The derived class *DataSymmetriesForBins_PET_CartesianGrid* encodes the appropriate symmetries for a cylindrical PET scanner and a cartesian grid. The class *TrivialDataSymmetriesForBins* implements the trivial case where there are no symmetries at all.
The hierarchy diagram for the class *SymmetryOperation* is shown in Figure 6.15. The SymmetryOperation implements the symmetry operations between the projection data and the Cartesian grid. The class *TrivialSymmetryOperation* encodes the trivial case when there are no symmetries.

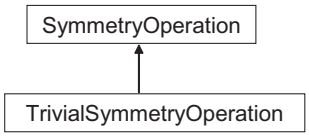

Figure 6.15: Hierarchy of classes for Symmetry Operations.

6.6 Image Reconstruction Algorithms

The hierarchy of classes for image reconstruction in STIR's version 1.2 is as represented in Figure 6.16

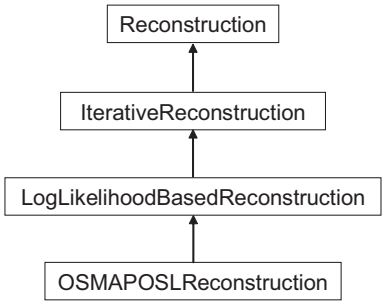

Figure 6.16: Hierarchy of classes for Image Reconstruction.

The base class *Reconstruction* is a very general class that provides the means for creating a target object (an image), calls a virtual function that performs the reconstruction and writes the result to the image. The derived class *IterativeReconstruction* defines the common methods to an iterative reconstruction scheme, namely the handling of an update image, the definition of the subsets number, the number of subsets, the end of an iteration, etc. The function that actually performs the reconstruction remains a virtual function in this class.
The next class in the hierarchy is the *LogLikelihoodBasedReconstruction* class, that provides the means for implementing algorithms that are based upon the Maximum Likelihood estimation criteria. For instance, it has functions to compute the likelihood of a given image. The last class in the hierarchy, *OSMAPOSLReconstruction* implements the OSMAPOSL algorithm, that is the ordered subsets version of the Maximum a Posteriori - One Step Late algorithm that was presented in Chapter 4, paragraph 4.5.2. In the next paragraph we will look with more detail into the implementation of this algorithm.

6.6.1 The OSMAPOSL algorithm

As it was mentioned in Chapter 4, it is possible to perform the decomposition of the system matrix into its several components. STIR uses this approach, with the following system components considered:

- n_i, the efficiency of detector pair corresponding to bin i;
- ρ_j, the 3D attenuation coefficient for bin; i
- a^g_{ij}, the probability that an emission from voxel j is detected in bin i due to geometrical considerations only.

The system matrix a_{ij} can then be written as

$$a_{ij} = n_i \rho_i a^g_{ij} \tag{6.15}$$

The quantity $\sum_j a_{ij}$ is referred to as the sensitivity image, a_j and is given by [99]:

$$\sum_i a_{ij} = \sum_{i \in S} n_i \rho_i a^g_{ij} = a_j \tag{6.16}$$

If these two equations are substituted into the OS-EM expression [163] given in Equation 4.25, the update equation of OS-EM can be written as

$$\begin{aligned} \widehat{\lambda}^{n+1}_j &= \frac{\widehat{\lambda}^n_j}{a_j} \sum_{i \in S_k} \frac{y_i n_i \rho_i a^g_{ij}}{\sum_{j'} n_i \rho_i a^g_{ij'} \widehat{\lambda}^n_{j'}} \\ &= \frac{\widehat{\lambda}^n_j}{a_j} \sum_{i \in S_k} \frac{y_i a^g_{ij}}{\sum_{j'} a^g_{ij'} \widehat{\lambda}^n_{j'}} \end{aligned} \tag{6.17}$$

As a result of the cancellations of the terms n_i and ρ_i in the previous equation, the non-geometrical' physics of the detection process (here, only attenuation and detector efficiency) are completely accounted for in the sensitivity image. Thus, once this image is obtained, the subsequent steps of the algorithm are only related to scanner geometry [99].

In a similar fashion, the update equation of the ordered subsets version of the Maximum *a posteriori* algorithm can be written as

$$\widehat{\lambda}_j^{n+1} = \frac{\widehat{\lambda}_j^n}{a_j + \beta \frac{\partial}{\partial \lambda_j} U(\boldsymbol{\lambda}, j) \mid_{\lambda_j = \lambda_j^n}} \sum_{i \in S_k} \frac{y_i a_{ij}^g}{\sum_{j'} a_{ij'}^g \widehat{\lambda}_{j'}^n} \tag{6.18}$$

This equation represents the OSMAPOSL algorithm that is implemented in STIR. The **OSMAPOSL** program works as follows:

1. Pre-compute the sensitivity image, a_j, as explained below;
2. Initialize $n = 0$, $\lambda_n = \lambda_0$, with λ_0 being an uniform image full of 1 or an image stored in a file;
3. Set the subset number as $k = n \mod m$;
4. Use the selected forward projector operator to obtain the estimated bin counts,

$$\overline{y}_i = FWDPROJ_{S_k} = (\lambda_n, i) \sum_{j'} a_{ij'}^g \lambda_j^n, \quad \forall i \in S_k$$

5. Use the selected backprojector operator to obtain the estimated image errors,

$$BACKPROJ_{S_k}(y/\overline{y}, j) = \sum_{i \in S_k} \frac{y_i}{\overline{y}_i} a_{ij}^g \quad \forall j \in J$$

6. Evaluate the derivate of the energy function in the previous image,

$$D(\lambda^n, j) = \frac{\partial}{\partial \lambda_j} U(\boldsymbol{\lambda}, j) \mid_{\lambda_j = \lambda_j^n}$$

7. Set

$$\lambda_j^{n+1} = \frac{\lambda_j^n}{a_j + D(\lambda^n, j)} BACKPROJ_{S_k}(y/\overline{y}, j) \quad \forall j \in J$$

8. Set $n \leftarrow n + 1$ and return to step (3).

Obviously, the OSMAPOSL algorithm can be reduced to the plain OS-EM algorithm, if no prior term is considered, and also to the ML-EM algorithm (or to the ML version of MAP-OSL), if the number of subsets is set to one.

6.6.2 The sensitivity image

The implementation of the OSMAPOSL algorithm described above requires the precomputation of an image representing the sensitivity of the scanner, which incorporates the attenuation and the normalization corrections. Therefore, in order to compute the sensitivity image, the detector efficiencies, n_i and the attenuation factors of the object being imaged must be obtained. How the detection efficiencies can be obtained will be discussed in Chapter 8 of this thesis. The attenuation factors are usually obtained from the ration between a transmission scan without the patient in place (a blank scan) and a transmission scan of the patient. STIR also accepts the attenuation map of the subject, from which it computes the attenuation factors, as will be seen next.
In STIR, the program that computes the sensitivity image is named **sensitivity**. It operates as follows [99]:

- Given the attenuation map of the subject, the Siddon's algorithm is used to determine the 3D attenuation coefficients ρ_i for all the bins i. The attenuation coefficients are stored in a sinogram of proper dimensions. When no attenuation map is available, the program assumes zero attenuation. If the attenuation factors are available, the sinogram containing them can be multiplied by the sinogram containing the normalization coefficients, and, since they are both multiplicative corrections, the resulting sinogram can be used as normalization factors, as described below.

- Given the normalization coefficients, also stored in a proper sinogram, a normalized sinogram, q, is obtained by multiplication of the sinograms containing the attenuation and the normalization coefficients:

$$q_i = n_i \rho_i \tag{6.19}$$

  When no normalization coefficients are available, the normalized sinogram q contains the attenuation coefficients only.

- The backprojector operator chosen among the ones available at STIR is used to backproject the sinogram q into a volume in order to obtain the sensitivity image.

6.6.3 The MAP model and priors

The hierarchy of classes for describing image priors is shown in Figure 6.17. The hierarchy consists of a base class to describe generalised priors, and a derived class. The derived class *FilterRootPrior* implements the Median Root Prior that was described in Chapter 4.
Regarding the application of the prior, the MAP model can be either additive or multiplicative [164]. The additive choice, that is the default in STIR, applies the prior on

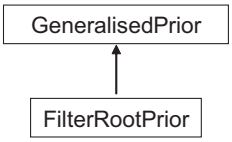

Figure 6.17: Hierarchy of classes for describing image priors

the image, accordingly to Equation 6.18.
The multiplicative model considers the following rescaled system :

$$\begin{aligned} a_{ij}^r &= \frac{a_{ij}}{a_j} \\ \lambda_{ij}^r &= \frac{\lambda_j}{a_j} \end{aligned} \tag{6.20}$$

where $\sum_i a_{ij}^r = 1$. The multiplicative form of the OSMAPOSL algorithm applies the prior multiplied by the sensitivity image, as given in Equation 6.21

$$\widehat{\lambda}_j^{n+1} = \frac{\widehat{\lambda}_j^n m}{a_j \left(1 + \beta \frac{\partial}{\partial \lambda_j} U\left(\boldsymbol{\lambda}, j\right)|_{\lambda_j = \lambda_j^n}\right)} \sum_{i \in S_k} \frac{y_i a_{ij}^g}{\sum_{j'} a_{ij'}^g \widehat{\lambda}_{j'}^n} \tag{6.21}$$

The additive choice implements a stronger penalization on regions of lower sensitivity. Of course, the choice of β must be different in each case. For the multiplicative model, β is independent of the sensitivity whereas for the additive model, that parameter must be based in the values of the sensitivity. In fact, in order to avoid instability of the algorithm caused by very high values of the prior weight, in the former case β must be chosen to be smaller than the maximum value in the sensitivity image [164].
The additive or multiplicative forms of applying the prior are embodied in functions belonging to the OSMAPOSL implementation.

6.7 Conclusions

In this chapter we have described the structure and main functionalities of the STIR library. As it was stated at the beginning of the chapter, it is a library that was designed to be used mainly with cylindrical PET scanners. In the following chapters we will describe the new features that were introduced to allow its use with the Clear−PEM scanner data.

Part IV

Results

Chapter 7

Enhancements in the STIR framework

7.1 Introduction

In this chapter we will present the reasoning behind the adaptation of the STIR framework for the geometry of the Clear -PEM scanner. The several classes and the routines that were developed to accommodate and reconstruct the Clear-PEM data within the STIR framework will be described, as well as the used organization of the data. Then, we will present a series of tests that were performed to assure the good functioning of the software and to define some of the optimum choice for the projector operators or for the image reconstruction algorithm. The implemented classes and routines were optimized for the standard Clear-PEM acquisition that was described in Chapter 5. However, some preliminary tests were also performed to access the software capability to deal to different specifications of the acquisition geometry, such as different number of angular plates positions.

7.2 The information on the projection data

An important step in the process of image reconstruction from either Monte Carlo simulated or from real acquisition projection data is the organization of such data. In STIR, as we have seen on Chapter 6, the projection data are organized as 3D sinograms, and this scheme was maintained for the 3D image reconstruction of Clear-PEM data. In fact there are other data formats that can be used to histogram the data issued from planar detector based scanners, namely linograms [165]. The use of this format was also explored for image reconstruction of Clear-PEM data by N. Matela [166]. However, that format imposes the constraint that data should be acquired only at two perpendicular positions of the detector plates. Although such a possibility is not

explored in this work, the Clear-PEM scanner has the capability of acquiring data in several angular positions around the breast, as it was described in Chapter 5. Therefore, using sinogram-based image reconstruction software does not disregard the possibility of using it in scenarios where the data are acquired in more than two perpendicular angular plates positions.
One of the input data formats accepted by STIR is the Interfile format. The class *ProjDataInterfile* is the class responsible for the definition of the Interfile format for the projection data. In this section we will explain the changes that had to be implemented in this class in order to accommodate the specificities of the Clear-PEM data. Next, we will present a new class that was added to the buildblocks of the library, *ProjDataInfoPlanar*, that is responsible for the description of the geometry of the scanner and of the geometry the acquisition of the Clear-PEM data. We will then explain the main steps in the building of the 3D sinograms, namely the filling of the sinogram header, the computation of the indexes corresponding to the variables in the sinogram and, finally, how the Depth of Interaction (DOI) information is accounted for in the sinograms.

7.2.1 The class ProjDataInterfile

The class *ProjDataInterfile*, responsible for the access of Interfile data, has been changed in order to accommodate specific information about the planar scanner acquisitions, such as the number of detector heads or the number of angular positions of the plates.

7.2.2 The class ProjDataInfoPlanar

A new class, *ProjDataInfoPlanar*, that is responsible for the complete description and organization of the Clear-PEM projection data, has been added to the *ProjDatInfo* hierarchy, according to the inheritance diagram shown in Figure 7.1.

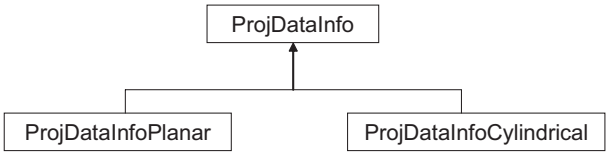

Figure 7.1: The ProjDataInfoPlanar class in the ProjDataInfo hierarchy.

The reasoning behind the formulation of this class is as follows. The sinogram format is an original format for cylindrical scanners acquired data. When using two planar detectors, there will be empty bins in the sinogram due exclusively to the geometry of the scanner and of the acquisition. The projection operators will need to rely on the information about the expected empty positions of the sinogram, given the geometry of the scanner and of the acquisition. Such information is implemented in the class *ProjDataInfoPlanar*.

A scheme of the expected empty positions of the sinograms, according to the relation between the length of the detector plates, L, and the distance between them, D, assuming two perpendicular angular acquisition positions of the plates, is shown in Figure 7.2.

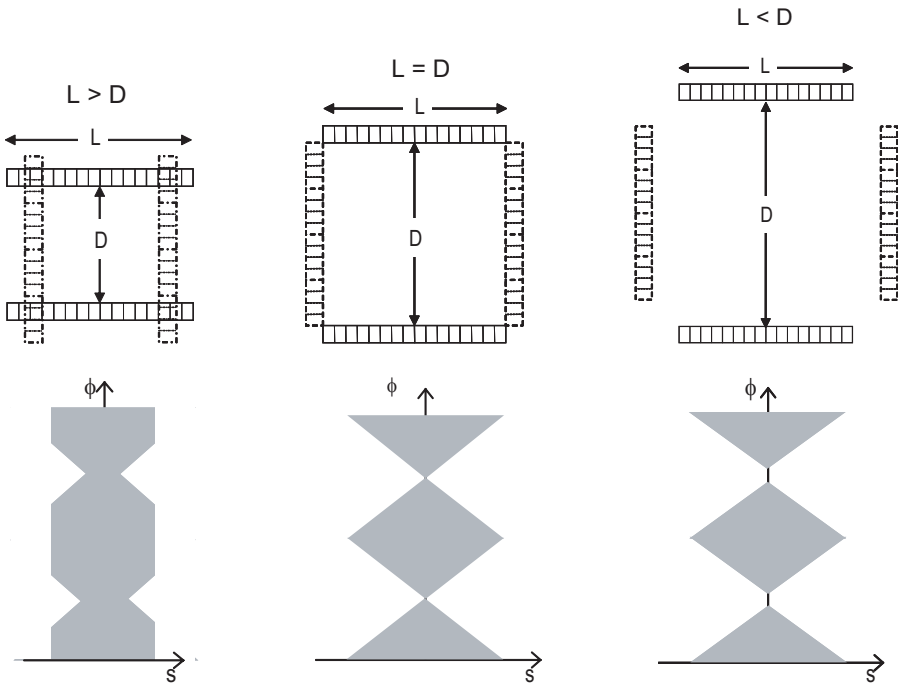

Figure 7.2: Different relations between the opposing detector heads distance and the length of the detector heads leads to different fillings of the sinogram. When $L \geq D$ (right and center) all the azimuthal angles, ϕ are sampled, but some transaxial distances, s, are not. When $L < D$ there are both azimuthal angles and transaxial distances that are not sampled.

When the distance between the two detector plates is higher than the length of the detector plates there are two sets of azimuthal angles for which there are no bins filled in the sinograms. These gaps, that are delimited by the limit angles ϕ_{lim1}, ϕ_{lim2} and ϕ_{lim3}, ϕ_{lim4}, as indicated in Figure 7.3 correspond to the angles that are not sampled at all due to the nature of the acquisition geometry. They also correspond to the limiting sampled angles with each angular position of the detectors: ϕ_1 and ϕ_2 correspond to the limit angles when the plates are at 90°; ϕ_3 and ϕ_4 correspond to the limit angles when the plates are at 0°.

In a similar fashion, to each azimuthal angle corresponds a set of tangential positions that are sampled, whereas others are not.

The constructor of class *ProjDataInfoPlanar* must have access to the following information regarding the geometry of the scanner and the acquisition geometry:

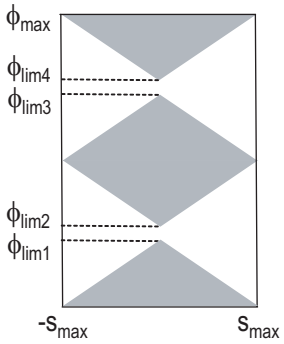

Figure 7.3: Some bins in the sinogram are expected to be empty, due to the nature of the acquisition geometry

- The number and the angular positions at which the plates acquire data. This can either be one angular position of the plates, at 0° (scheme presented in Figure 5.5(a)) or two angular position of the plates, both at 0° and 90° (the scheme of the acquisition at 90° is presented in Figure 5.5(b)).

- The number of detector rows in a detector plate, N. This is the number of detector elements along the direction parallel to the axis of rotation of the detector plates, which is also the longer axis of the detector plates.

- The number of detector elements in a detector row, n.

- The width of each detector element, d_s.

- The row spacing, d_z. This is the distance between two contiguous detector rows in a detector plate.

- The number of transaxial bins and the size of each transaxial bin. This is used as the transaxial sampling in the sinogram and in the images.

- The distance between the faces of the crystals in the two opposing detector plates, D.

Based on this information, the following quantities are computed:

- The detector plates length, L. This is computed as the product of the number of detectors per plate row multiplied by the size of each detector element.

- The azimuthal angle sampling. In order to define the azimuthal angle sampling, the azimuthal aperture of the scanner, Ψ, is first determined. When $L \geq D$ the azimuthal aperture, Ψ is given by

$$\Psi = 2 \arctan \frac{L/2}{D/2} \tag{7.1}$$

The azimuthal angle sampling, $d\phi$, is then computed as the azimuthal aperture divided by the number of detector elements per plate row,

$$d\phi = \frac{\Psi}{n} \tag{7.2}$$

- The azimuthal shift. The azimuthal shift, γ consists on the angular shift between the last azimuthal angle that is sampled with one angular position of the plates and the first azimuthal angle that is sampled with the perpendicular position of the plates, due to the gap that exist between two angular positions of the detectors when $L < D$ (Figure 7.4).

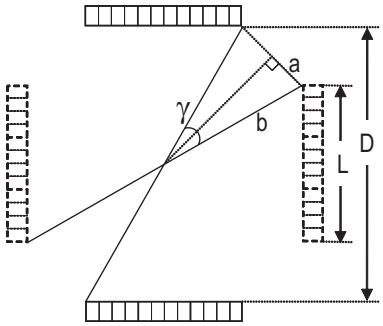

Figure 7.4: Definition of the azimuthal shift

The azimuthal shift is given by

$$\gamma = 2 \sin \frac{a}{b} \tag{7.3}$$

where a and b, which are defined in Figure 7.4, are given by

$$\begin{aligned} a &= \frac{L-D}{2\sqrt{2}} \\ b &= \sqrt{(L/2)^2 + (D/2)^2} \end{aligned} \tag{7.4}$$

The azimuthal shift is used to determine the azimuthal angle corresponding to a given azimuthal angle index in the sinogram, as explained next.

- The limit view numbers. The limit views that are represented in Figure 7.3 are determined by

$$\begin{aligned} \phi_{lim1} &= \arctan \frac{L}{D} \\ \phi_{lim2} &= \pi - \phi_{lim1} \\ \phi_{lim3} &= \arctan \frac{D}{L} \\ \phi_{lim4} &= \pi - \phi_{lim2} \end{aligned} \tag{7.5}$$

- The azimuthal angle ϕ. When the azimuthal angle index, ϕ_{index}, is given, the azimuthal angle is determined as

$$\begin{aligned} \phi = &\quad \phi_{index} d\phi &\quad if\ \phi_{index} \leq \phi_{lim1} \\ \phi = &\quad \phi_{index} d\phi + \gamma &\quad if\ \phi_{index} > \phi_{lim1} \\ \phi = &\quad \phi_{index} d\phi + 2\gamma &\quad if\ \phi_{index} \geq \phi_{lim2} \end{aligned} \tag{7.6}$$

- The tangential limits. These define, for each azimuthal angle, the set of tangential positions which are expected to contain information, as it was explained above. The previous steps to computing the tangential limits for each azimuthal angle consists on determining the azimuthal shift (Equation 7.3) and the limit views (Equation 7.5). The module of the tangential limit for each view, s_{lim}, is then computed as

$$\begin{aligned} s_{lim} = &\quad \tfrac{L}{2}\cos\phi - \tfrac{D}{2}\sin\phi &\quad if\ \phi \leq \phi_{lim1} \\ s_{lim} = &\quad \tfrac{L}{2}\sin\phi - \tfrac{D}{2}\cos\phi &\quad if\ \phi_{lim3} \leq \phi \leq \phi_{max}/2 \\ s_{lim} = &\quad \tfrac{L}{2}\sin\phi + \tfrac{D}{2}\cos\phi &\quad if\ \phi_{max}/2 < \phi \leq \phi_{lim4} \\ s_{lim} = &\quad -\tfrac{L}{2}\cos\phi - \tfrac{D}{2}\sin\phi &\quad if\ \phi_{lim2} \leq \phi \leq \phi_{max} \end{aligned} \tag{7.7}$$

- The tangent of the co-polar angle, $\tan\theta$, given the corresponding sinogram index, θ_{index}. This is determined as

$$\tan\theta = \theta_{index}.d_z/T \tag{7.8}$$

  where T is the projection of the LOR in the transaxial plane,

$$\begin{aligned} T = &\quad D/\cos\phi &\quad if\ \phi_{lim1} \leq \phi \leq \phi_{lim2} \\ T = &\quad D/\sin\phi &\quad if\ \phi_{lim3} \leq \phi \leq \phi_{lim4} \end{aligned} \tag{7.9}$$

Other important operations implemented in this class are the computation of angles and transaxial positions of a bin in the sinogram, given the bin indexes. These operations often rely on the location of the bin with respect to the angular limits defined above. Of particular importance are the computation of the azimuthal angle ϕ, given a bin, and the computation of the tangent of the co-polar angle, $\tan\theta$, given a bin.

7.2.3 Building the sinogram header

The program for organizing the acquisition data into 3D sinograms, named *PlanarPEM-Rebinner* takes as input the necessary information about the geometry of the scanner, the geometry of the acquisition and other information needed to define an object of class *ProjDataInfoPlanar* and to build a sinogram Interfile header.
The values for the needed parameters are as follows:.

- The number of detector rows in a detector plate (N). Each Clear-PEM detector plate contains 64 detector elements in that direction, as it was described in Section 5.2 of Chapter 5. The maximum number of segments in the complete 3D sinograms is $2N-1$, as it was explained in Chapter 4, Section 4.2. Therefore, the complete 3D sinograms of the Clear-PEM scanner have 127 segments, ranging from -63 to $+63$.

- The number of detectors in a row of detectors. The Clear-PEM detector plates have 48 detector elements in each detector row (Chapter 5, Section 5.2).

- The row spacing. In the Clear-PEM scanner, this distance is not constant, varying with the position of the detector elements along the short axis of the supermodule. This is because there are gaps of different dimensions between the several elements that compose the detector supermodules, mainly due to the associated electronics. For that reason, when using the realistic scanner geometry, the considered row spacing is a mean value that is computed as the quotient between the total length of a detector row and the number of detector rows.

- The width of each detector element. Each individual crystal has a square face with 2 mm side. However, when using the realistic scanner geometry, the distance between the center of two contiguous crystals in a row is higher then that value and is not constant, depending on the position of the crystals along the longer axis of the supermodule. Hence, similarly to what was done in the previous point, the width of each detector element was assigned with a value that is the shorter length of the detector plates divided by the number of detectors in a row.

The parameters about the geometry of the acquisition are the distance between the faces of the crystals in two opposing detector plates (D), and the number of angular positions of the plates to acquire data. By the time this work was written, the implemented options for the number of angular plates positions were 1 or 2, as it was previously explained.
The remainder information needed to build the sinograms are the maximum number of tangential bins that the sinogram will have, as well as their size. This is used to define the number and the size of the transaxial bins in the image. This means that these parameters define the transaxial Field of View of the image to be reconstructed. With the above settings and the dimensions of the Clear-PEM scanner, the 3D sinograms defined for the scanner have 99 radial bins, 96 polar angle bins, 127 segments with axial positions ranging from 1 to 64.
The information described above is used to create a *ProjDataFromStream* object that, in turn, is used to fill a header of an Interfile-like sinogram.

7.2.4 Computing the sinogram indexes

The data that *PlanarPEMRebinner* takes as input is a list of the impact coordinates of the annihilation photons with the detector plates, $\{(X_1, Y_1, Z_1), (X_2, Y_2, Z_2)\}$, that have previously been processed to accommodate the DOI information, as it will be explained in paragraph 7.2.5. When working with simulated data, another previous step must be performed. Such step consists on reading the ROOT files where simulated data is stored (Chapter 5), selecting the events of interest, computing the coordinates of the impact of the photons with the crystals and writing them into a list in a binary file. To compute the sinogram indexes, the first step consists on performing a change in the coordinates, since the coordinate system of the Clear-PEM scanner (Chapter 5) is different from the coordinate system in STIR (Chapter 6). In particular, the origins of the coordinates systems are different. In fact, the Clear-PEM coordinate system has its origin at the geometrical center of the crystals of the two detector heads, while the coordinate system of STIR has its origin at the middle of the first detector ring. The relationship between the two coordinate systems is given by

$$\begin{aligned} X_{STIR} &= Z_{ClearPEM} \\ Y_{STIR} &= -Y_{ClearPEM} \\ Z_{STIR} &= X_{ClearPEM} + \Delta X \end{aligned} \tag{7.10}$$

where $\Delta X = (N-1)/2$ with N being the number of detector rows, as explained above. The transaxial and the axial indexes of each line of response are then computed. The transaxial coordinates, s and ϕ are given by

$$\begin{aligned} \phi &= \arctan \frac{Y_2 - Y_1}{X_2 - X_1} \\ s &= X_1 \cos\phi + Y_1 \sin\phi \end{aligned} \tag{7.11}$$

where $\phi \in [0, \pi[$. To find the corresponding indexes, the computed value of s is divided by the tangential sampling, given by the bin size, and the computed value of ϕ is divided by the azimuthal angle sampling, respectively. How the azimuthal angle sampling is defined will be explained later.

The axial coordinates of the LOR, θ and z, are both function of the rows of detectors that comprise the LOR. The first step consists on calculating the rows corresponding to the Z values of the impact coordinates:

$$\begin{aligned} row_1 &= Z_{min}/d_z \\ row_2 &= Z_{max}/d_z \end{aligned} \tag{7.12}$$

where d_z is the row spacing, $Z_{min} = \min\{Z_1, Z2\}$ and $Z_{max} = \max\{Z_1, Z2\}$ The index of the axial position , z_{index} is given by

$$z_{index} = (row1 + row2 - \delta z\,[\theta_{index}])/2; \tag{7.13}$$

where $\delta z\,[\theta_{index}]$ is an axial offset that depends on the segment to which the LOR belongs, θ_{index}. With this definition, the first axial position in any segment is always zero.

The index of the co-polar angle, θ_{index}, which also defines the segment number, is computed as

$$\theta_{index} = (Z_{min} - Z_{max})\,/d_z; \tag{7.14}$$

After having determined the four LOR indexes, the corresponding bin in the sinogram is incremented by one value. The procedure is repeated for the next event in the input file, until all the events have been processed and stored.

7.2.5 Dealing with the DOI information

As it was explained in Chapter 5, the Clear-PEM scanner has the ability of determining the depth impact coordinate within the crystal with a foreseen resolution of 2.0 FWHM. In scanners that do not have DOI capabilities, the impact coordinate of the incoming photons with the detector crystal is assigned with a fixed value such as the coordinate of the front face of the crystal. In scanners that have the capability of measuring the DOI the amount of possible LORs increases drastically. If all the possible LORs would be stored in a separate bin in the sinogram, this entity would become excessively large. This would result in high computational burden with impact on the computation time of the image reconstruction process. To avoid this problem, we have chosen a different approach to deal with the DOI information. Such approach, whose schematic explanation that can be seen in Figure 7.5, has allowed to maintain the resolution given by the DOI information without excessively increasing the processing time.

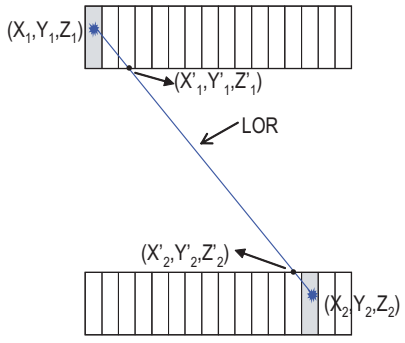

Figure 7.5: Schematic drawing of how the DOI information is taken into account in the image reconstruction process.

The coordinates of impact of the incoming photon within the detector crystals, (X_1, Y_1, Z_1) and (X_2, Y_2, Z_2), are used to determine coordinates that define the segment of the LOR that is limited by the opposing crystal faces. According to Figure 7.5 this is the segment of the line defined by the two points with coordinates $\left(X_1', Y_1', Z_1'\right)$ and $\left(X_2', Y_2', Z_2'\right)$.

Accordingly, one of the coordinates, X or Y, depending on the angular position of the detector plates, ζ, will equal half the distance between the detector plates, $D/2$. Therefore, the coordinates that will feed the program *PlanarPEMRebinner* are

$$\begin{aligned}\left(X_1', Y_1', Z_1'\right) = &\quad (X_1[D/2], L/2, Z_1[L/2]), (X_2[L/2], -L/2, Z_2[L/2]) \quad if\ \zeta = 0^\circ \\ \left(X_2', Y_2', Z_2'\right) = &\quad (L/2, Y_1[L/2], Z_1[L/2]), (-L/2, Y_2[L/2], Z_2[L/2]) \quad if\ \zeta = 90^\circ\end{aligned}$$

assuming that the data has been ordered so that (X_1, Y_1, Z_1) are the impact coordinates in plate 1 and (X_2, Y_2, Z_2) are the impact coordinates in plate 2.

7.3 The projection operators for Clear-PEM

A new class, *ProjMatrixByBinForPEM*, that is responsible for the computation of the system matrix elements for the Clear-PEM scanner was added to the *ProjMatrixByBin* hierarchy, according to the inheritance diagram shown in Figure 7.6.

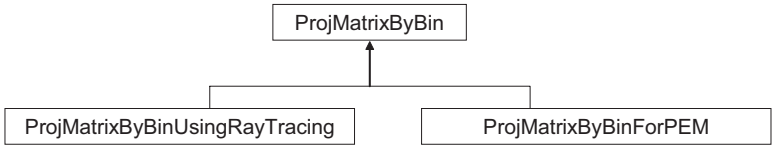

Figure 7.6: The *ProjMatrixByBinForPEM* class that has been added to the *ProjMatrixByBin* hierarchy.

This class computes the projection matrix elements for the PEM scanner, by using the Siddon's algorithm described in Chapter 6. Although the Length of Intersection (LOI) model is used, several rays (up to three rays) to trace each sinogram bin in the tangential direction are used, thus approximating a Tube of Response (TOR) model. This follows the general implementation of the TOR model used in STIR. In the axial direction, when the voxel size is exactly twice the sampling in axial direction, multiple LORs are use to avoid missing voxels, as it was explained in Chapter 6. In the transaxial direction, a number of rays to trace each bin up to 3 can be used in the computations.

This class has methods for setting up pointers both to the image, to the *ProjDataInfo* object and to the geometrical symmetries. The image has to be of type *VoxelsOnCartesianGrid* and the *ProjDataInfo* has to be of type *ProjDataInfoPlanar*. The geometrical symmetries will be discussed in Section 7.4. The default constructor of the class sets up the defaults typical of a *ProjMatrixByBin* object and also the defaults regarding the geometrical symmetries that are to be considered and the number of transaxial LORs that are to be used in the tracing of each bin.

The actual computation of the system matrix elements is made within a method that

is named *calculate_proj_matrix_elems_for_one_bin*. This method works with objects of class *ProjMatrixElemsForOneBin*. This is a class that implements a LOR, storing the non-zero projection matrix elements for every voxel that contributes to a given bin. In other words, it is a class that stores and allows access to a given row in the system matrix. The computations themselves are implemented in the method named *ray_trace_one_lor_for_pem*. Figure 7.7 shows the flux diagram for the method *calculate_proj_matrix_elems_for_one_bin*.

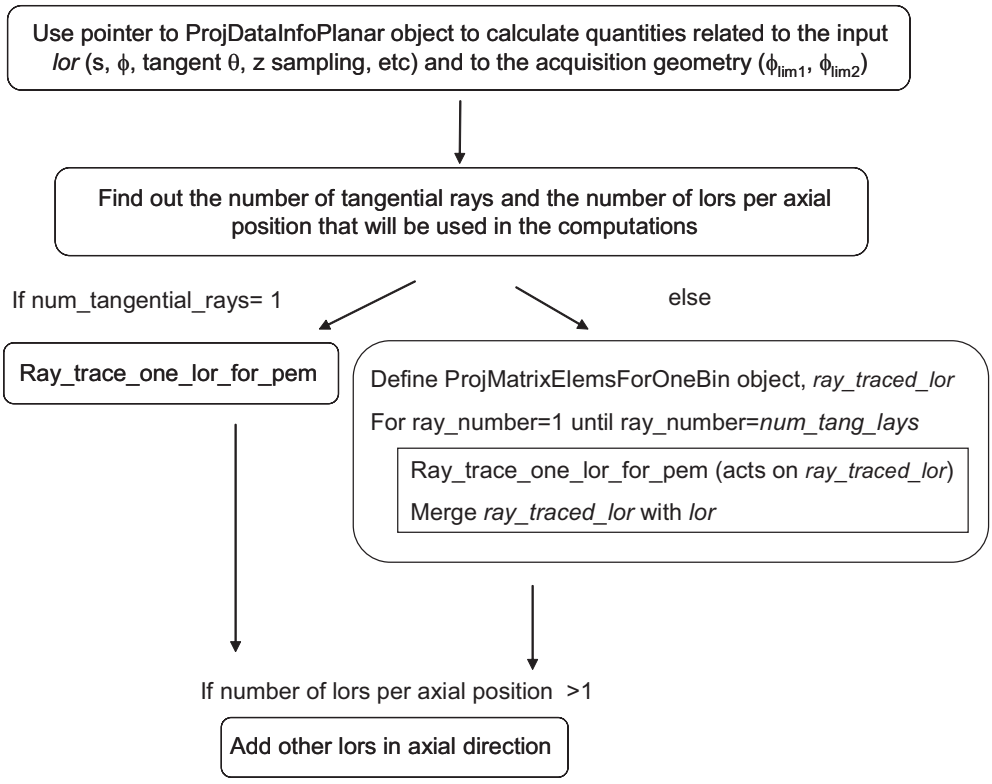

Figure 7.7: Flux diagram for the method *calculate_proj_matrix_elems_for_one_bin* in the *ProjMatrixByBinForPEM* class.

7.4 The geometrical symmetries

The use of geometrical symmetries between the projection data and the image grid can be used to speed up the computations, for some of the quantities (ds,dz,$d\phi$, see Chapter 6) used in the computations of the image matrix for a given voxel can be re-used for other voxels. The geometrical symmetries computed for the Clear-PEM scanner follow the reasoning and methods presented in [160], which are also implemented in the general STIR library. Those geometrical symmetries are as follows:

- z-symmetry: translational symmetry around the axis of rotation of the scanner.

Since the ring spacing is a the double of the voxel size, the ds and dz quantities can be reused for voxels with different Z coordinate.

- s-symmetry: symmetry about the center of the image voxel. Different voxels share the quantity ds, although with different dz;

- θ-symmetry: the quantities ds and dz computed for backprojecting a given beam with positive θ can be reused for a beam with negative θ;

A more detailed explanation of the geometrical symmetries in s, z and θ can be found in [160].

7.5 The test utilities

The test utilities were created to test the forward projection and backprojection operations.
The *PlanarFwdTest* utility performs a simple backprojection of an input sinogram. The *ProjDataInfoPlanar* and the *ProjMatrixByBin* objects are build from this input sinogram. The user may specify some parameters such as the number of segments to be backprojected.
The *PlanarBackTest* utility allows to create a set of projection data given an image. The *ProjDataInfoPlanar* object needed for the *ProjMatrixByBin* object is build from a template Interfile sinogram. The sinograms resulting from the usage of this program will have an header similar to the template. Some examples of sinograms resulting from the use of this utility will be shown in Section 7.6.

7.6 Preliminary Evaluation

A preliminary evaluation of the Clear-PEM scanner dedicated classes and utilities introduced in STIR was made with the help of analytical phantoms. An image of a Sphere Phantom and an image of a Cross Phantom similar to those described in Chapter 6 were created. The Sphere Phantom created had 10 counts/pixel and each point source in the Cross Phantom was defined in half a pixel with 65 counts. The 3D sinograms of such images were created with the use of the planar forward projector test utility described above. The geometry used consisted on the Simplified Scanner Geometry that was described in Chapter 6, which includes an acquisition in two perpendicular angular plates position. The central slice of each of these analytical phantoms, as well as the central slices of their respective sinograms (segment 0) are shown in Figure 7.8
Since the forward projector operator does not account for the random nature of the acquisition process, Poisson noise had to be added to the sinograms of the phantom data. For this purpose, an utility to add Poisson noise to images or sinograms was

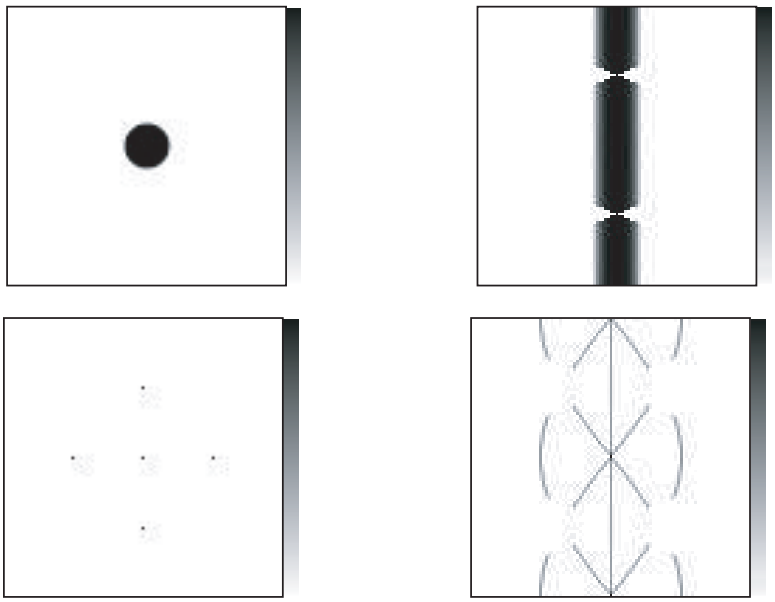

Figure 7.8: Images of the central slices of the Analytical Sphere Phantom and of the Analytical Cross Phantom (on the left) and central slices of the corresponding segment 0 sinograms (on the right).

written in IDL (Interactive Data Language). The created utility uses an IDL function that returns a random deviate for every pixel of the input image drawn from a Poisson distribution with the same mean of the input value.
To verify the appropriate functioning of the Poisson noise program, it was applied on images with an uniform central circular region with 10, 100, 1000 and 10000 counts per pixel. The resulting noisy images are shown in Figure 7.9.

(a) (b) (c) (d)

Figure 7.9: Central slice of the the images with an uniform circular area after adding Poisson noise. The images shown correspond to original with a) 10 counts per pixel, b) 100 counts per pixel c) 1000 counts per pixel and d) 10000 counts per pixel. In a) the Region of Interest that was used to analyze the images is shown.

The mean number of counts and the variance obtained in a large Region of Interest (ROI) drawn over the images after adding the Poisson noise were recorded and are presented in Table 7.1. The ROI used is shown in Figure 7.6.
The presented values confirm that the developed program produces results that are in agreement with the fundamental characteristic of the Poisson distribution, that is, the

Number of Counts in Uniform Image	Mean Number of Counts After Noise	Variance After Noise
10	10.0975	10.4994
100	99.9203	104.069
1000	999.028	978.762
10000	10002.4	10007.1

Table 7.1: Values of mean a variance in large ROIs drawn in uniform images after the addition of Poisson noise

equality between the mean and the variance.
Once confirmed its good functioning, the utility was used to apply Poisson noise to the sinograms of the analytical phantoms. Images of such sinograms are shown in Figure 7.10. These images were then reconstructed with OS-EM and 4 subsets, using all the geometrical symmetries available and the TOR model.

Figure 7.10: Images of the central slice of segment 0 sinograms of the Analytical Sphere Phantom (on the left) and of the Analytical Cross Phantom (on the right) after the addition of Poisson noise.

Figure 7.11 shows the central slice of the reconstructed images of the Sphere and of the Cross Phantom, as well as the profiles taken along a central line of the original and of the reconstructed images. This results shown that there is a good visual agreement between the created and the reconstructed images.
To further study the behavior of the image reconstruction software, in order to optimize it, several tests were performed. These tests aimed at obtaining an initial evaluation of the performance of the image reconstruction software under different options for the parameters of the projector operators. The effect of varying some parameter of the reconstruction algorithm was also studied. The parameters that were varied were the number of subsets to be used in the OS-EM algorithm, the number of rays that are used in the projectors to trace each bin in the transaxial direction and the several geometrical symmetries to be used. The ability to reconstruct data obtained in an acquisition geometry other than the standard one (as defined in Chapter 5) was also briefly evaluated by analytically simulating an acquisition with only one angular position of the

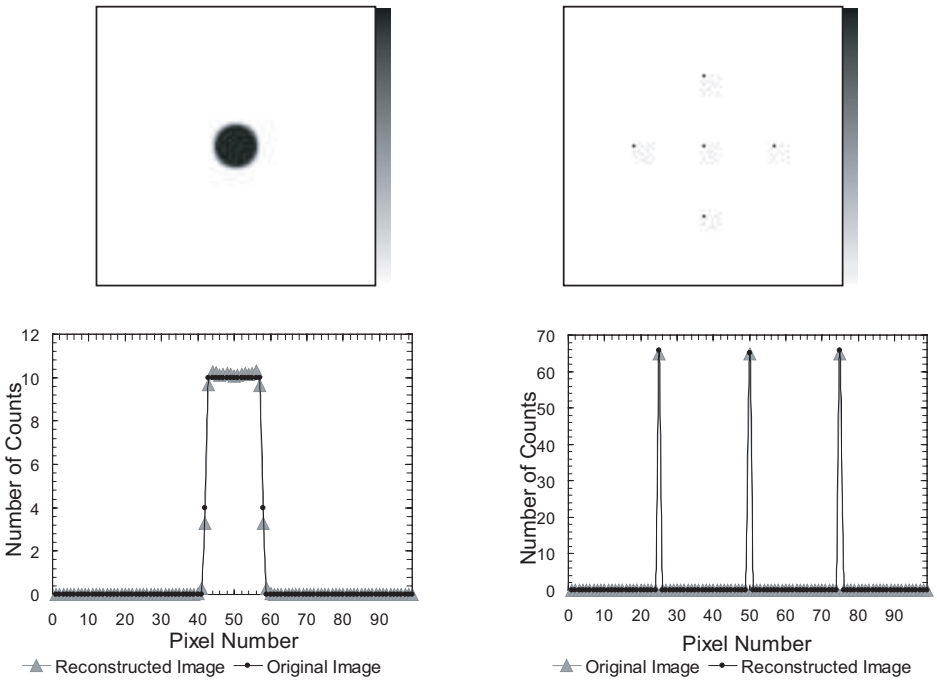

Figure 7.11: Central slice of the reconstructed images of the Analytical Sphere Phantom (on the left, above) and of the Analytical Cross Phantom (on the right, above) and the corresponding profiles taken along a central line on the central slice of the original and of the reconstructed images.

plates.

For the above mentioned purposes, the data of the Analytical Sphere Phantom and of the Analytical Cross Phantom, after the addition of Poisson noise, was reconstructed under the different conditions. The results were evaluated in terms of Figures of Merit (FOM) such as image spatial resolution and image uniformity and also the computation time associated with each image reconstruction procedure.

7.6.1 Number of Subsets

The OS-EM algorithm is the most used statistical iterative algorithm used for PET image reconstruction. Therefore, the 3D version of the OS-EM reconstruction algorithm available in STIR was naturally chosen to test the image reconstruction software for the Clear-PEM scanner. One of the image reconstruction parameters to be evaluated and optimized is the number of subsets to use in the OS-EM algorithm. In this paragraph we will present the tests performed for that purpose and the results obtained. It was already mentioned that when using one subset, the OS-EM algorithm is equivalent to the ML-EM algorithm, that has proved convergence to a ML solution. Higher

subset numbers accelerate the image reconstruction task, but, if the number of subsets is sufficiently high, the subsets become unbalanced and image artifacts may arise. Additionally, it can only be considered a number of subsets that are divisible by the number of views in the sinograms, which, in the case of the Clear-PEM scanner, is 96. Too guarantee the symmetric balancing among subsets, the number of subsets must be divisible evenly by the $number of subsets/4$. Therefore, initial test were performed by reconstructing the images of the Analytical Sphere Phantom and of the Analytical Cross Phantom data with ML-EM and with OS-EM with 2, 4, 12 and 24 subsets.

7.6.1.1 Analytical Cross Phantom

The Analytical Cross Phantom reconstructed images allowed to evaluate the image spatial resolution. This Figure of Merit was parameterized by the full-width at half-maximum (FWHM) of Gaussian fits of the profiles taken over the reconstructed point sources in all three directions, radial, transverse and axial.

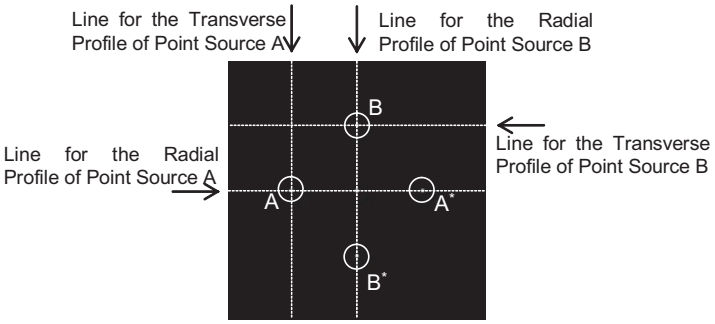

Figure 7.12: Examples of the nomenclature of the profiles of the point sources in the Cross Phantom used to analyze the spatial resolution of the images in the transaxial plane.

For the sake of clarity, we will first clarify the nomenclature used for the radial, transverse and axial directions. The axial profile refers to the profile taken along the axis parallel to the axis of rotation of the scanner. The transverse and radial profiles are both contained in the axial plane of the scanner that was defined in Figure 5.9(b). For each point source of the Cross Phantom, the radial profile corresponds to the profile taken along the line that intersects the central point source. This may be a vertical or an horizontal line, depending on the position of the studied point source in the Field of View. For instance, the radial profile of Point Source A corresponds to the profile taken along an horizontal line, as shown in Figure 7.12, whereas for Point Source B the radial profile corresponds to the profile taken along a vertical line. With respect to the special cases of the the point sources placed along the rotational axis of the scanner, we will nominate radial the profile that is taken along a vertical line and transverse the profile that is taken along an horizontal line.

Due to the geometry of the phantom and of the simulated acquisition, the profiles of Point Sources A and A^* are expected to be similar, as well as the profiles of Point Sources B and B^*. The radial profiles of Point Sources A and A^* are expected to be similar to the transaxial profiles of Point Sources B and B^*. In fact, in the idealized case studied in this paragraph, the radial and transaxial profiles of each source are similar, the profiles of point sources A, A^*, B and B^* are similar, and the profiles of the Central Point Sources are similar to the profiles located in the non central plane (see scheme of the Phantom in Figure 5.6(a), Chapter 5).

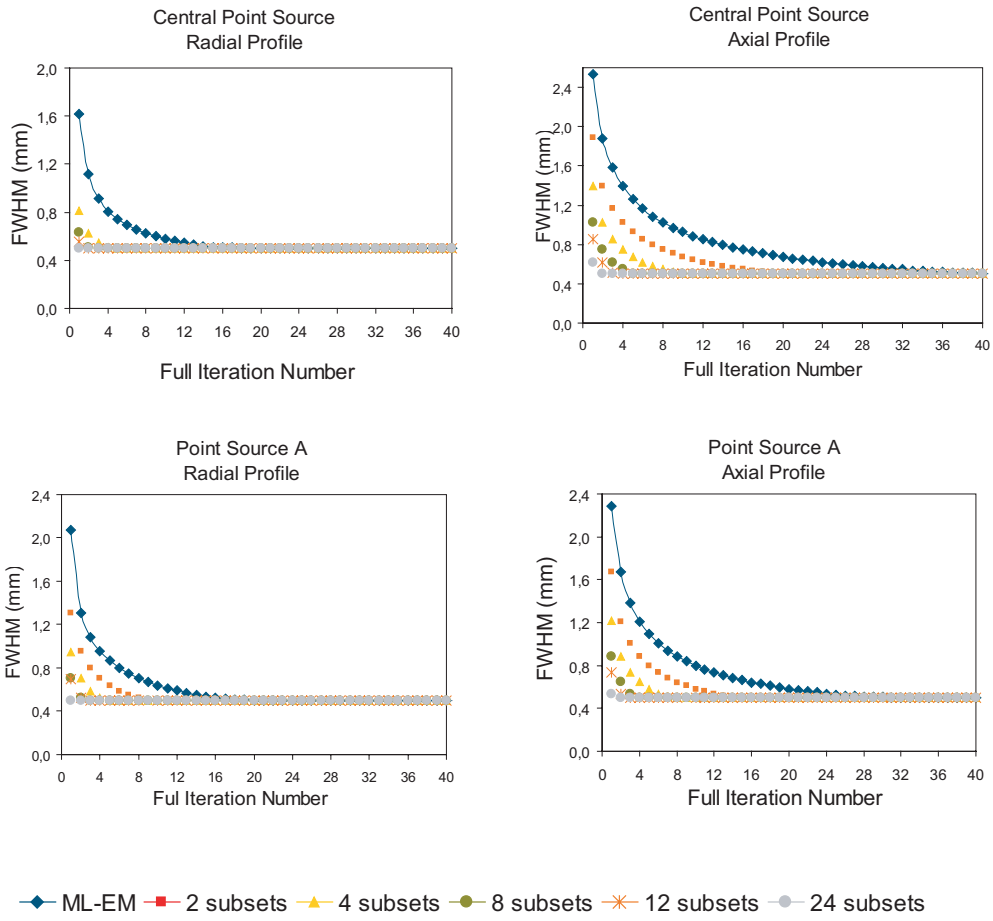

Figure 7.13: Values of FWHM against full iteration number measured along the radial and along the axial profiles of the reconstructed images of the Analytical Cross Phantom with each of the number of subsets studied.

Figure 7.13 presents the plots of the FWHM values taken along the radial and the axial profiles against the full iteration number. By full iteration we refer to a complete pass over all the subsets used. The plots shown correspond to the Central Point Source and to the Point Source A. The plots corresponding to the FWHM values measured in the

transverse profile, not shown, are equal to the corresponding plots for the radial profiles. The plots corresponding to Point Sources A^*, B and B^*, not shown, are similar to the presented plots for Point Source A, the same happening for the plots of Point Sources D and D^* with respect to the plots of the central point source.
The presented plots clearly show that, with respect to the number of subsets used in the iterative image reconstruction algorithm, all of the FWHM curves converge to a common value. However, and as expected, the higher the number of subsets used, the lower is the iteration of convergence. As a criterion of convergence, a variation of the FWHM less than 1% in the subsequent iterations in the FWHM component of the point source that took longer to converge was considered. In this case, the axial component of the Central Point Source was slower to converge.
Table 7.2 presents the number of full iterations needed to achieve convergence and the corresponding computation time for the several number of subsets considered. In a x86 64-bits processor with 4 Gb RAM a full iteration takes approximately 12 minutes for every number of subsets used. The time for convergence is thus determined as the product of 12 by the number of full iterations needed to achieve convergence.

Number of Subsets	Number of Full Iterations	Computation Time (minutes)
1	35	420
2	20	240
4	10	120
8	6	72
12	4	48
24	2	24

Table 7.2: Values of the number of full iterations of the Analytical Cross Phantom reconstructed images needed to achieve convergence and the corresponding computation times.

7.6.1.2 Analytical Sphere Phantom

The Analytical Sphere Phantom reconstructed images allowed to evaluate the image uniformity. To compute this Figure of Merit, an analysis was performed by drawing a large ROI over an area of the uniform sphere in the reconstructed images. The mean number of counts and the variance of pixel values measured in that ROI were recorded for the several iterates of the several number of subsets used in the image reconstruction algorithm. Image uniformity was computed as the fraction between the mean number of counts inside the ROI and the standard deviation inside the ROI. The value of the mean number of counts inside the ROI was also used to determine the convergence of the iterative process. As a criterion of convergence, a variation of less than 1% in

the subsequent iteration in the mean counts inside the ROI was considered. The plot of the mean counts inside the ROI against the full iteration number for the several number of subsets used in the reconstruction process is shown in Figure 7.14(a), and the corresponding standard deviation values against the iteration number are shown in Figure 7.14(b).

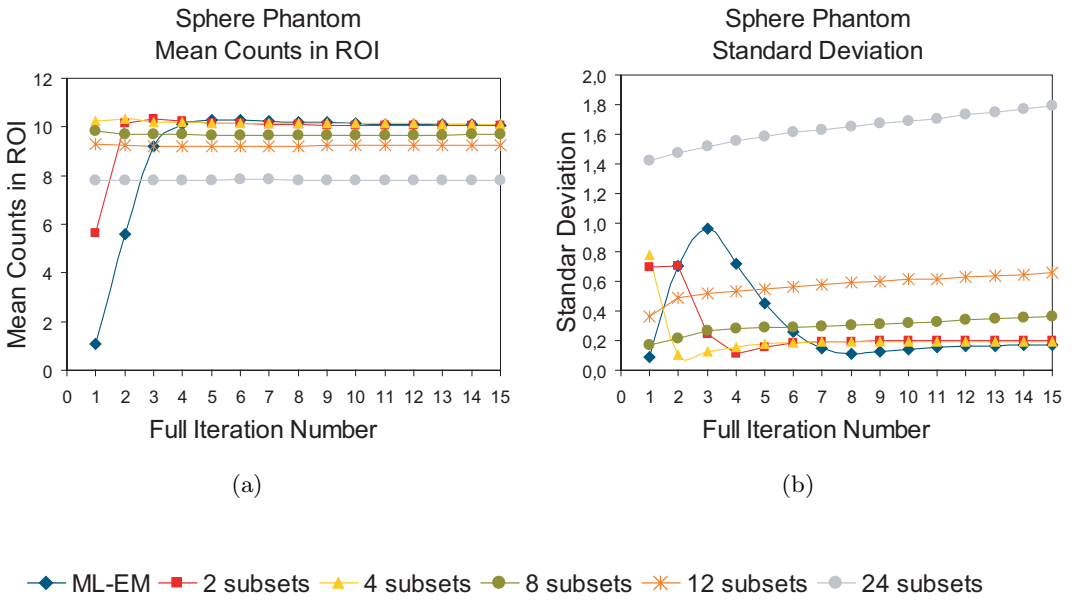

Figure 7.14: Plots of the mean number of counts and of the standard deviation measured in a large Region of Interest placed over the reconstructed images of the Analytical Sphere Phantom against the full iteration number for each of the number of subsets used in the reconstructions.

The plot of Figure 7.14(a) shows that the mean number of counts inside the ROI obtained for the images with ML-EM and OS-EM with 2, 4 and 8 subsets are similar to the number of counts in the original image, which was 10 before adding the Poisson noise. On the contrary, images reconstructed with OS-EM with 12 and 24 subsets converge to values of mean counts inside the ROI that are lower than the original image. In table 7.3 the values of the Mean Counts in ROI after convergence are presented, as well as the corresponding number of full iterations and the corresponding computation time.

The plot in Figure 7.14(b) shows that the values of the standard deviation inside the ROI in the case of 2 and 4 subsets converge to a value that is close to the value reached with the ML-EM. On the contrary, the standard deviation values obtained with 8, 12 and 24 subsets significantly deviate from the value to which the ML-EM algorithm converge. The 24 subsets reconstructed images present as the worse case, that is, the case where the measured standard deviation is the highest. This raise in the noise of

Number of Subsets	Mean Counts in ROI	Number of Full Iterations	Computation Time (minutes)
1	10.3	6	72
2	10.2	4	48
4	10.3	2	24
8	9.6	3	36
12	9.2	2	24
24	7.8	2	24

Table 7.3: Values of the mean number of counts in a ROI drawn over the reconstructed images of the Analytical Sphere Phantom after convergence is achieved, with the corresponding number of full iterations, for all the number of subsets studied.

the images with the raise in the number of subsets used is in agreement with the known behavior of the OS-EM algorithm.

As a consequence, the plot of the image uniformity index against iteration number, presented in Figure 7.15, shows differentiated behavior depending on the number of subsets used. The curves corresponding to OS-EM with 2 and 4 subsets converge to values close to the values of ML-EM. However, the maximum on those curves is reached at an earlier iteration when 4 subsets are used. The image reconstruction using higher number of subsets results in images with much lower values for the uniformity index.

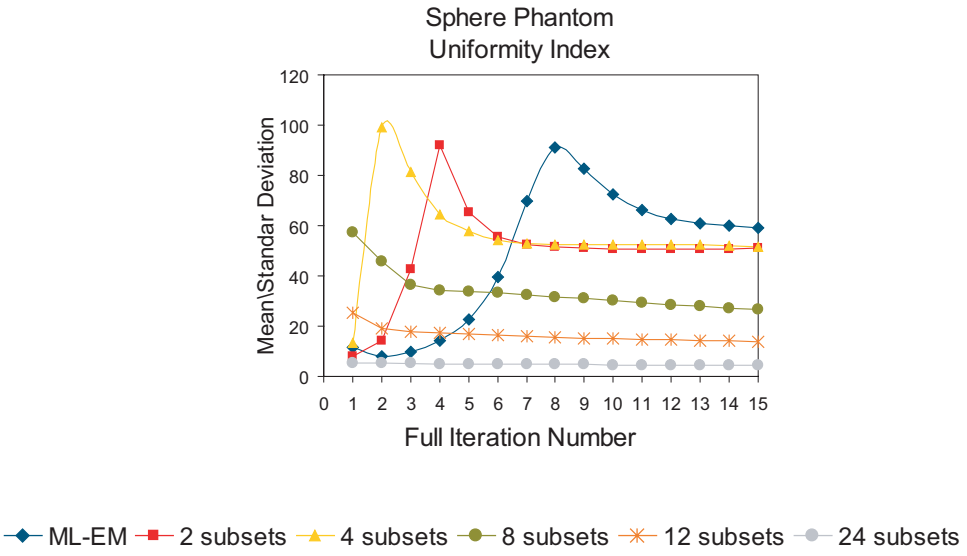

Figure 7.15: Plot of the Mean over Standard Deviation against the number of full iterations, for the images of the Analytical Sphere Phantom reconstructed with the several number of subsets of the OS-EM algorithm.

Figure 7.16 shows the central slice of the reconstructed images of the Analytical Sphere

Phantom at the iteration of convergence. These images clearly confirm what was devised in the previous plots: image reconstruction with ML-EM or with OS-EM and 2 and 4 subsets give similar results; a faint artifact begins to appear in the 8 subsets image, becoming clearly noticeable at the 12 subsets image and completely visible at the 24 subsets image. This artifact is probably related to the small number of views that are contained in each of the subsets (12, 8 and 4 views respectively for the 8 subsets, 12 subsets and 24 subsets case).
The poor quality of these images can be further confirmed in Figure 7.17. It shows the plot of the profiles taken along a central line in the central section of the reconstructed images of the Analytical Sphere Phantom with the several subsets studied. It can be observed that the profiles taken from the images corresponding to 8, 12 and 24 subsets do not match the profiles of the ML-EM case.
Given the results presented in this paragraph, the OS-EM reconstruction algorithm using 4 subsets was considered as the case where the trade-off between image quality and computation time was best. Therefore, in the remainder of this work the number of subsets used in the iterative reconstructions process will be 4.

7.6.2 Number of rays to trace each bin

As it was explained in Section 7.3, the modeling of the forward projection and of the backprojection operations can use more than one ray to trace each bin in transaxial direction. In theory, for an high number of rays, the result is approximate to a strip integral in the tangential direction. In the present STIR implementation, a number from 1 to 3 rays used to trace each bin in the transaxial direction can be used. In this paragraph the Analytical Cross Phantom and Analytical Sphere Phantom data are used to analyze the behavior of the image reconstruction algorithm using different values of this projector parameter. The data were reconstructed with OS-EM with 4 subsets and a number of rays to trace each bin in the tangential direction that ranged from 1 to 3. Images were analyzed as in the previous paragraph.

7.6.2.1 Analytical Cross Phantom

Figure 7.18 shows the plots of the FWHM values of the central Point Source and of the Point Source A measured in the axial, radial and transverse profiles for the different number of rays used in the tangential direction. Once again, the plots for these point sources are representative of the remainder.
These plots confirm what was expected: the spatial resolution measured in the axial plane (that is, along the transverse and radial profiles) significantly improves with the number of rays that are used to trace for each bin in the transaxial direction. Only when using three rays to trace each bin, the transverse and radial image resolution

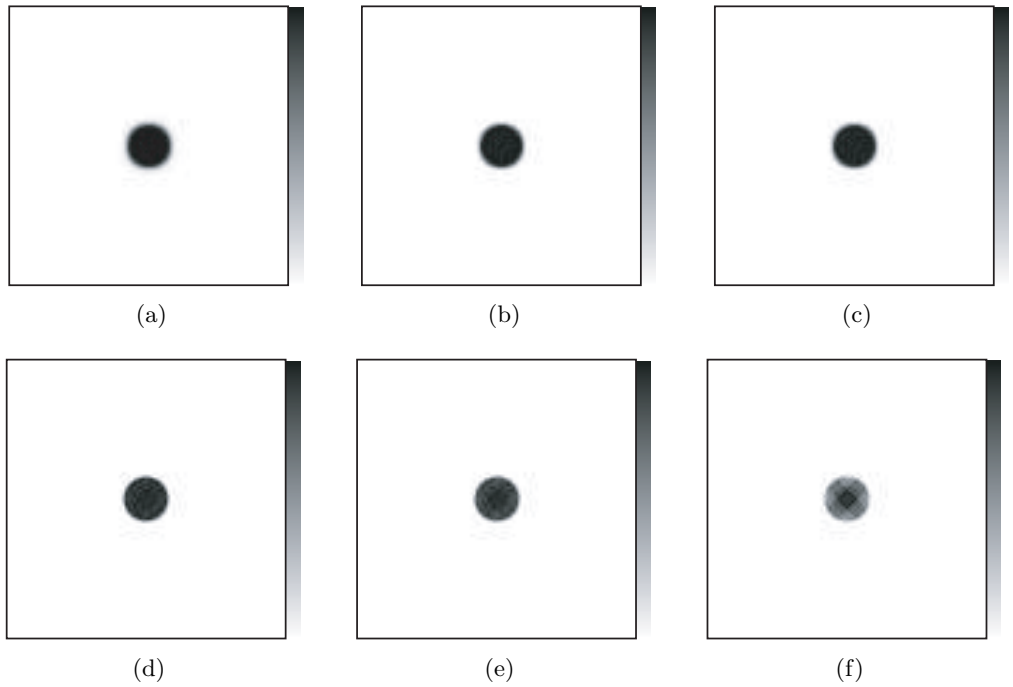

Figure 7.16: Central slice images of the Analytical Sphere Phantom reconstructed images with (a) ML-EM and OS-EM with (b) 2 subsets, (c) 4 subsets, (d) 8 subsets, (e) 12 subsets and (f) 24 subsets at the corresponding iteration of convergence.

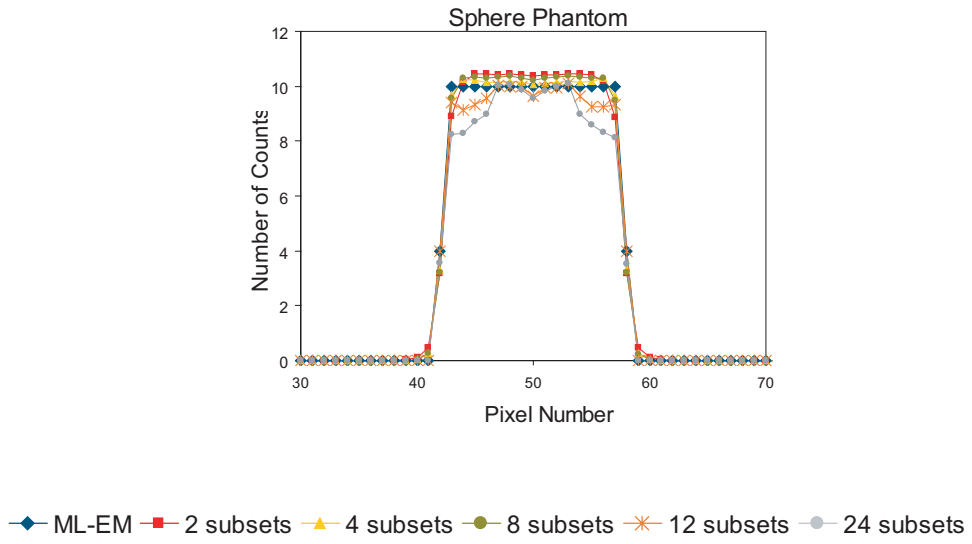

Figure 7.17: Profiles of the Analytical Sphere Phantom reconstructed images with the different number of subsets studied. The profiles were taken along a central horizontal line in the central section of the reconstructed images.

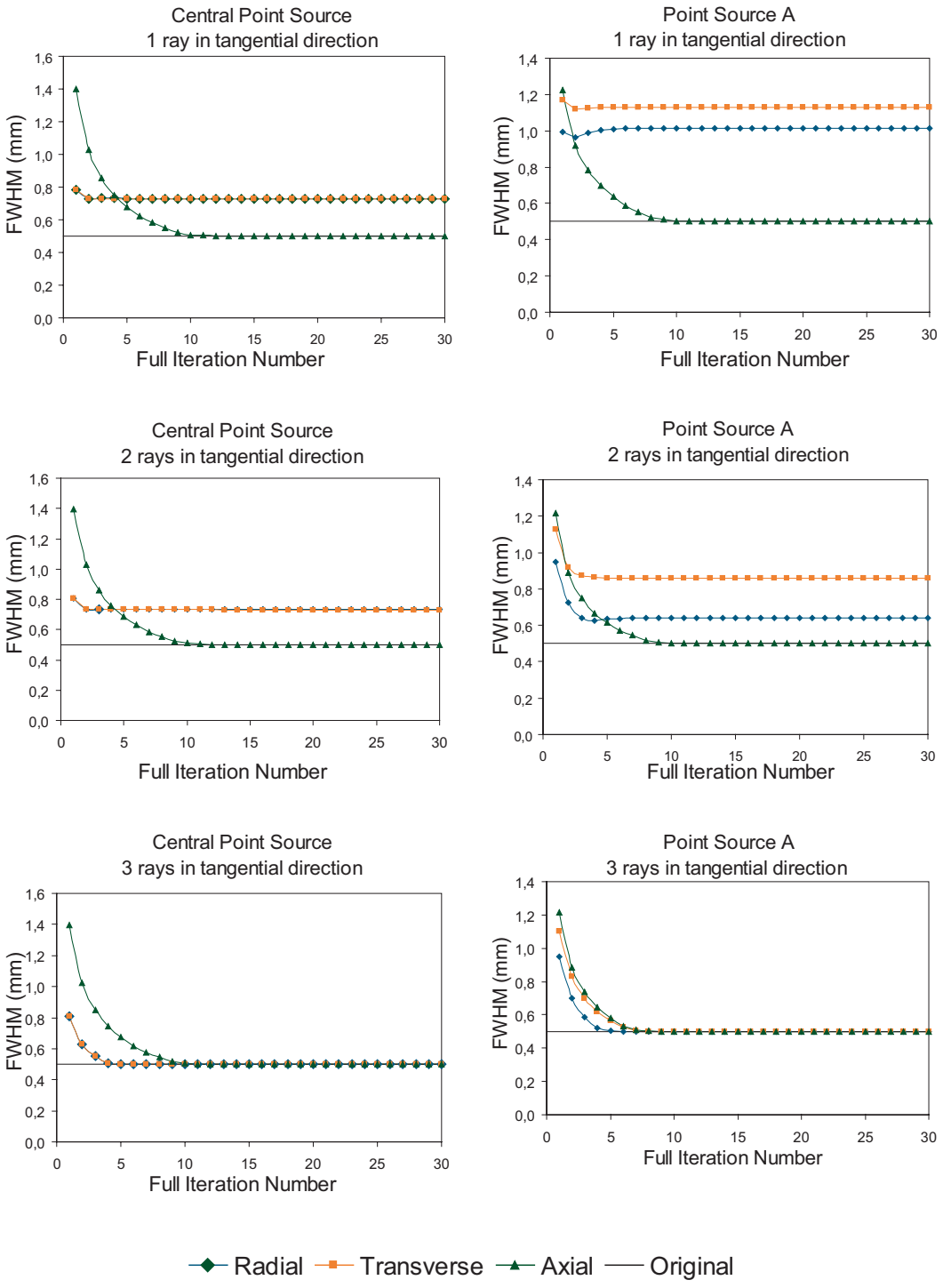

Figure 7.18: Values of FWHM against iteration number along the radial, transverse and axial profiles of the Central Point Source and of the Point Source A of the reconstructed images of the Cross Phantom with 1,2 or 3 rays to trace for each bin in tangential direction. The spatial image resolution of the original image is drawn in a black line.

values converge to the resolution values of the original image. The axial component of the image resolution is unaffected by the variation in this parameter, since it only affects the modeling of the projection operations in the transaxial component.
Figure 7.19 shows the central slice of the subtraction of original Cross Phantom image with the reconstructed images with 1 and 2 rays. The subtraction image for 3 rays is not shown because its an empty image.

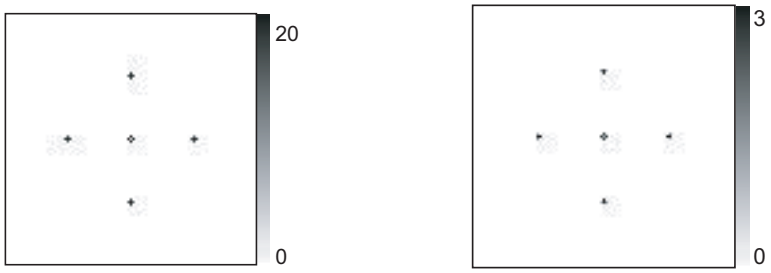

(a) (b)

Figure 7.19: Central slice images of the subtraction of original Cross Phantom image and the images reconstructed with a) 1 ray and b) 2 rays to trace each bin in the transaxial direction.

7.6.2.2 Analytical Sphere Phantom

The evolution of the mean number of counts and the standard deviation inside the ROI placed over the reconstructed images of the Analytical Sphere Phantom with the iteration number is presented in Figure 7.20 for the three used number of rays in the transaxial direction. While the plot of the mean number of counts against iteration number presents no difference for the three cases studied, the same does not happen for the standard deviation values inside the ROI. In fact, the plot presented in Figure 7.20(b) shows that the use of 3 rays to trace each bin in the transaxial direction leads to images with much lower values of standard deviation than the other two cases. Consequently, the uniformity index is also more favorable when 3 rays are used, as it can be seen in Figure 7.21.
Figure 7.22 shows the central slice images of the Analytical Sphere Phantom reconstructed with 1, 2 and 3 rays to trace each bin in the transaxial direction. The visual inspection of these images confirms the higher quality of the image reconstructed with 3 rays to trace each bin in the transaxial direction.

7.6.2.3 Computation Times

Table 7.4 presents the computation time per iteration of the image reconstruction of the Analytical Cross Phantom and of the Analytical Sphere Phantom with 1, 2 and

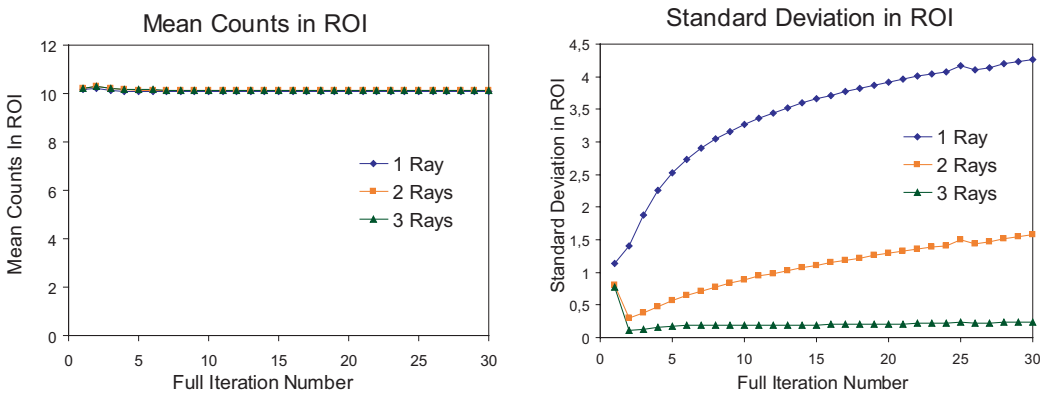

(a) (b)

Figure 7.20: Plots of the mean and standard deviation inside the ROI in the Analytical Sphere images against iteration number for the 1, 2 and 3 rays to trace each bin in the transaxial direction.

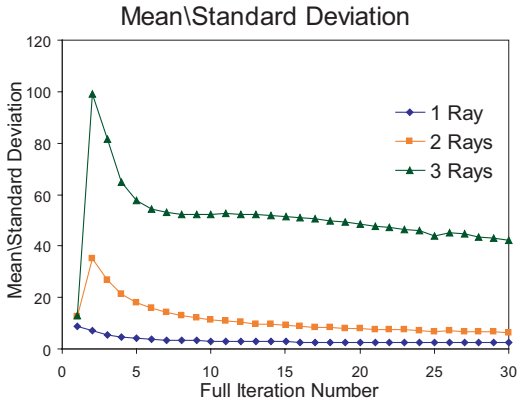

Figure 7.21: Plot of the image uniformity index against iteration number for the Analytical Sphere reconstructed images with 1, 2 or 3 rays to trace each bin in the transaxial direction.

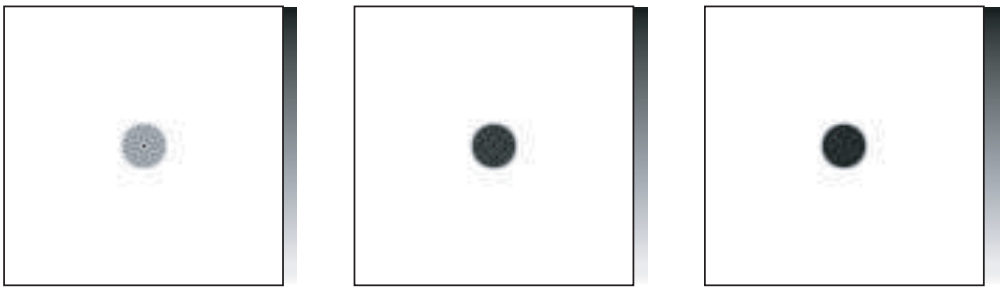

(a) (b) (c)

Figure 7.22: Central slice images of the Analytical Sphere Phantom reconstructed with a) 1 ray b) 2 rays and c) 3 rays used to trace each bin in the transaxial direction.

3 rays used to trace each bin in the transaxial direction. There is a slight increase in the computation time per iteration with the increase in the number of rays used. This increase is, however, largely compensated by the increase in the quality of the reconstructed images that was observed in the previous paragraphs. Hence, in the remainder of this work the projector operators will use 3 rays to trace each bin in the transaxial direction.

Number of Rays	Cross Phantom	Sphere Phantom
1	10 minutes	7 minutes
2	11 minutes	10 minutes
3	12 minutes	11 minutes

Table 7.4: Computation time per iteration for the image reconstruction of the Analytical Cross Phantom and of the Analytical Sphere Phantom images with 1, 2 and 3 rays used to trace each bin in the transaxial direction.

7.6.3 Geometrical Symmetries

The use of the geometrical symmetries described in Section 7.4 in the image reconstruction process was tested with the Analytical Cross Phantom and the Analytical Sphere Phantom data. Both phantom data were reconstructed with OS-EM with 4 subsets and 3 rays to trace each bin in the transaxial direction. Four different combinations of the geometrical symmetries in the reconstruction were used: no use of symmetries, use of the s-symmetry only, use of the θ-symmetry only, use of the z-symmetry only and use of all the geometrical symmetries simultaneously. Images were analyzed as described in the previous paragraphs. The set of reconstructed images with the different symmetries allowed to investigate whether the use of geometrical symmetries introduces any error in the image reconstruction process, with respect to the images reconstructed without using the geometrical symmetries. It also allowed to investigate the gain in reconstruction time achieved with the use of the geometrical symmetries.

7.6.3.1 Analytical Cross Phantom

Figure 7.23 shows the plots of the values of the image spatial resolution against the iteration number for the Central Point Source and for Point Source A of the Analytical Cross Phantom, for the used combinations of geometrical symmetries. The spatial resolution values shown were measured along the radial and the axial profiles and are representative of the remainder. These plots show that the use of geometrical symmetries, either in separate or simultaneously, lead to an evolution of the spatial resolution with the iteration number that is similar to the observed for the images reconstructed without symmetries.

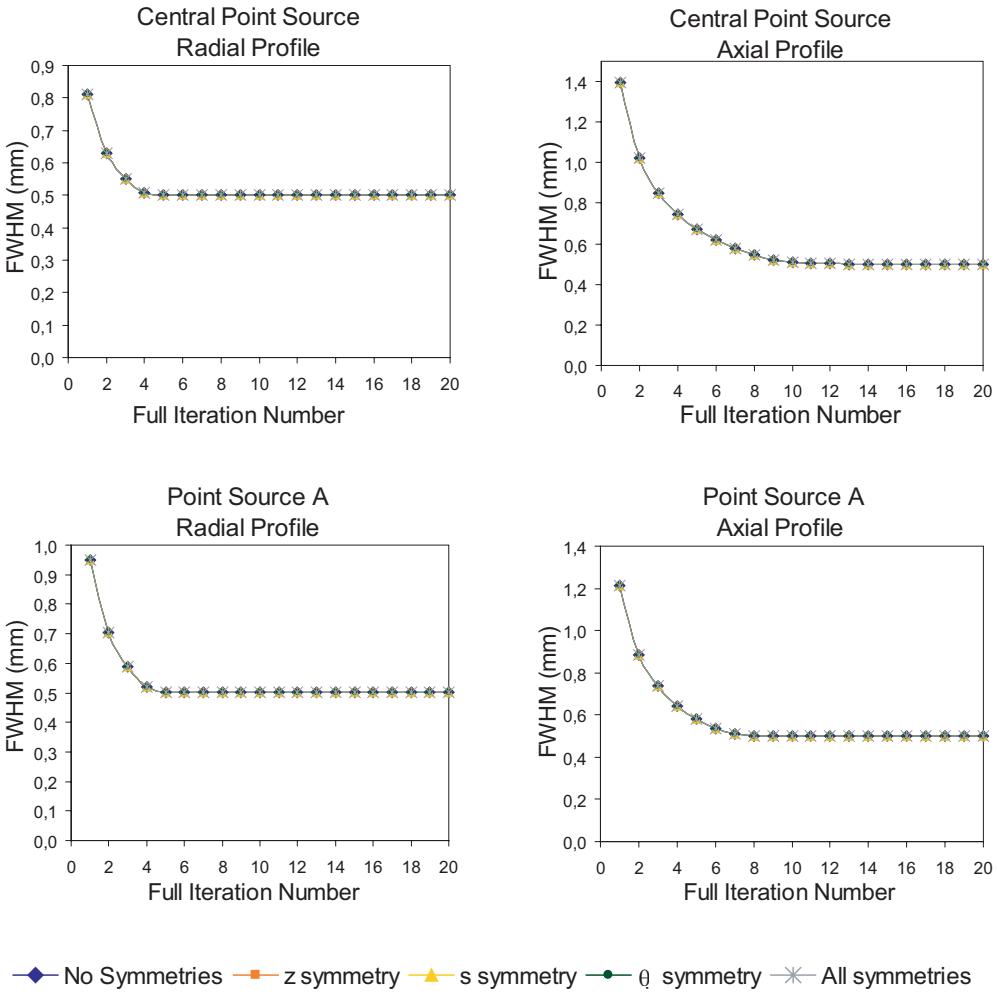

Figure 7.23: Plots of the image spatial resolution against the iteration number for the central point source and for point source A of the Analytical Cross Phantom, with different geometrical symmetries in the image reconstruction process: use of no symmetries, use of s-symmetry only, use of θ-symmetry only, use of z-symmetry only and use of all these symmetries simultaneously.

Figure 7.24 shows the central slice of the images of the Cross Phantom reconstructed without symmetries subtracted by the images reconstructed with each of the geometrical symmetries considered individually and all the symmetries together. Note that the maximum in the data range of these subtraction images (indicated in the images color scales) are at least 10^5 lower than the values of the original images (64 counts before the addition of the Poisson noise). This shows that, when using the geometrical symmetries in the image reconstruction process, the obtained images are consistent with the images that are obtained when no geometrical symmetries are considered. Thus, no significant error seems to be introduced by the use of the geometrical symmetries.

7.6.3.2 Analytical Sphere Phantom

Figure 7.25(a) shows the plot of the mean number of counts inside the ROI against the iteration number for the symmetries used in the reconstruction of the Sphere Phantom. Figure 7.25(b) shows the plot of the corresponding standard deviation values against iteration number. These plots show that the both the mean number of counts and the standard deviation inside the ROI are equal. Consequently, the evolution of the uniformity index with the iteration number is exactly the same for the different uses of the geometrical symmetries, as can be confirmed in Figure 7.26.
The images shown in Figure 7.27 are the central slices of the images that result from the subtraction of the Sphere Phantom reconstructed image without the geometrical symmetries and the images reconstructed with the geometrical symmetries considered individually and simultaneously. These images confirm that the inclusion of the geometrical symmetries in the reconstruction process does not result in image errors. Note that the data range of these subtraction images (indicated in the images color scales) are at least 10^3 lower than the values of the original images (10 counts before the addition of the Poisson noise).

7.6.3.3 Computation Times

The main goal of introducing the geometrical symmetries in the reconstruction process is the possibility of significantly reducing the computation times. Table 7.5 presents the computation times per iteration of the reconstruction of the Analytical Cross and Sphere Phantoms according to the symmetries used.
The s- and θ- symmetry allow each one a reduction of the computation time to half the time needed for an iteration when no symmetries are used. The z-symmetry allows a corresponding reduction of the computation time per iteration of approximately 6 times. When used in simultaneous, the three symmetries account for a reduction of 12 times on the computation time per iteration.
As it was shown in the previous paragraphs, the use of the geometrical symmetries in

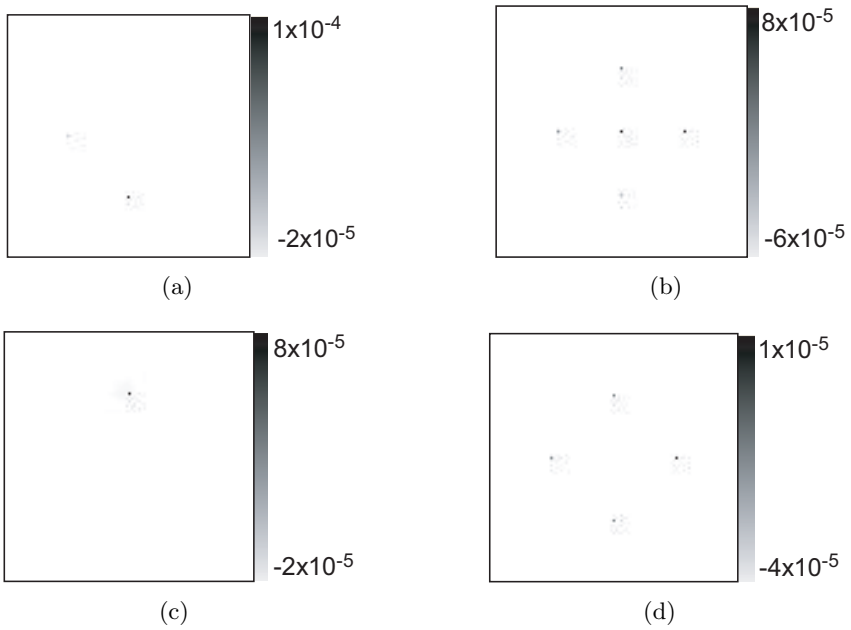

Figure 7.24: Central slice of the images resulting from the subtraction of the Cross Phantom image reconstructed without symmetries and the images reconstructed with: (a) s-symmetry only, (b) θ-symmetry only, (c) z-symmetry only and (d) all these symmetries simultaneously. The values in the color scales indicate the minimum and maximum intensity values in each image.

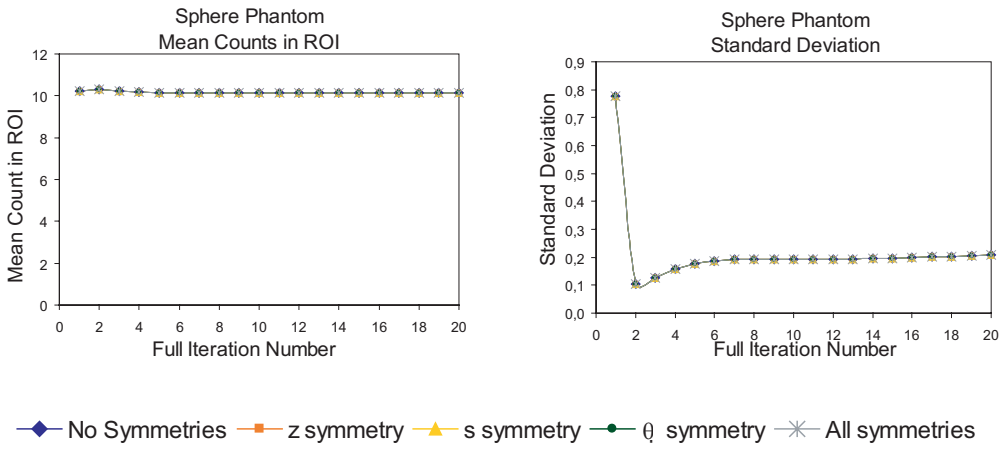

Figure 7.25: Plots of the mean counts and standard deviation inside the ROI against the iteration number for the images reconstructed with the studied uses of the geometrical symmetries.

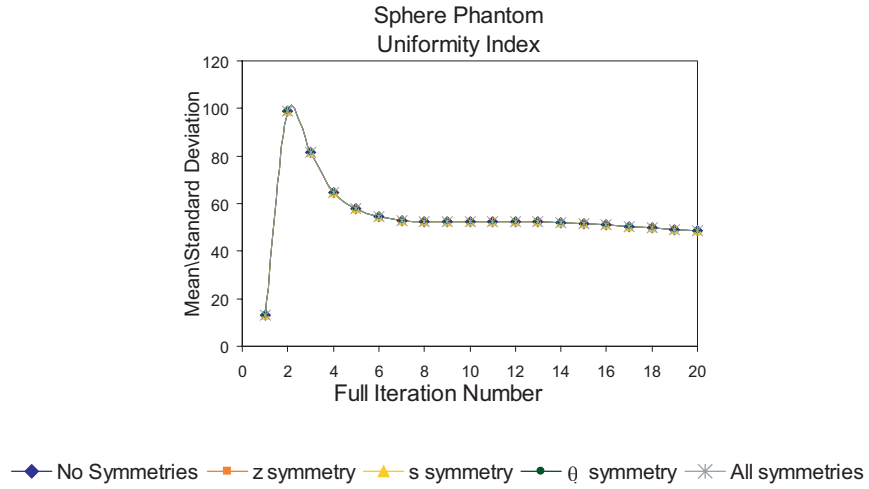

Figure 7.26: Plots of the uniformity index against the iteration number for the images reconstructed with the studied uses of the geometrical symmetries.

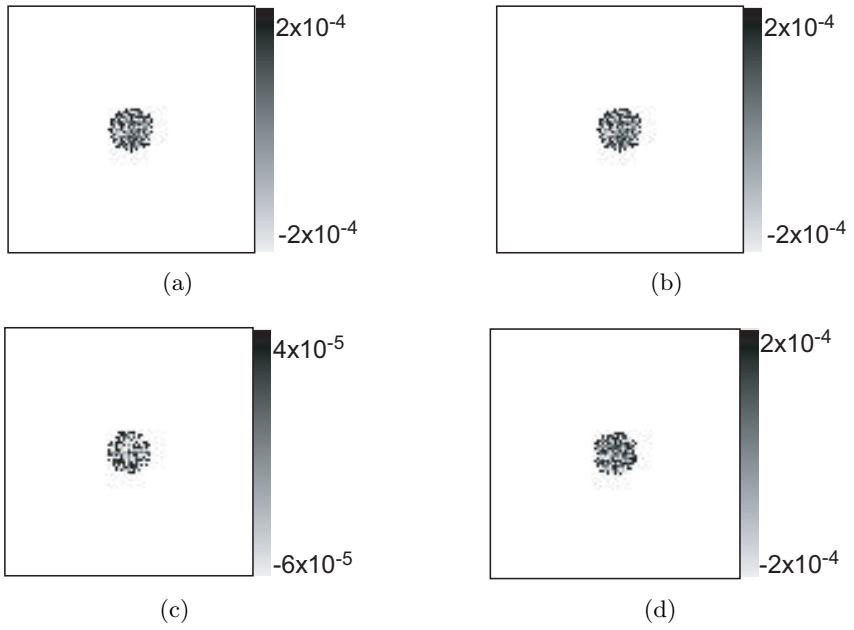

Figure 7.27: Central slice of the images resulting from the subtraction of the Sphere Phantom image reconstructed without geometrical symmetries and the images reconstructed with (a) s-symmetry only, (b) θ-symmetry only, (c) z-symmetry only and (d) all these symmetries simultaneously. The values in the color scales indicate the minimum and maximum intensity values in each image.

Symmetry	Cross Phantom	Sphere Phantom
None	2h22m	2h26m
s symmetry	1h21m	1h23m
θ symmetry	1h18m	1h21m
z symmetry	0h28m	0h24m
All	0h12m	0h12m

Table 7.5: Approximate computation time per iteration of the image reconstruction of the Analytical Cross Phantom and of the Analytical Sphere Phantom images for the studied combinations of the geometrical symmetries.

the reconstruction process does not introduce errors in the reconstructed images. As the combined use of the s-symmetry, the ϕ-symmetry and the θ-symmetry lead to a significant reduction in the image reconstruction computation times, in the remainder of this work the image reconstruction will be performed with the use of the three symmetries in simultaneous.

7.6.4 One angular detector plates position

As it was previously said, the enhancements performed in the STIR framework were optimized for the acquisition conditions that were described in Chapter 5. However, other acquisition conditions were also considered, namely the use of a different number of angular detector plates position.

An effort was made to prepare the STIR library to deal with data acquired with the detector plates at only one angular position. This aimed mainly at comparing the advantages and pitfalls of both acquisition scenarios.

In this section we present examples of the data and images that are expected to be obtained for data acquired only in one detector plates positions. The original images of the Analytical Cross Phantom and of the Analytical Sphere Phantom were forward projected into sinograms, assuming an acquisition with the detector plates at 0°. Such sinograms were then used to feed the OS-EM reconstruction software. The projector operators used in the reconstruction were also in agreement with the considered acquisition scenario.

Images of the obtained sinograms are presented in Figure 7.28(a) (Cross Phantom) and in Figure 7.28(b) (Sphere Phantom), showing that only the bins corresponding to views ranging from ϕ_{lim2} and ϕ_{lim3}, as defined in Paragraph 7.2.2, are filled. The central slices of the corresponding reconstructed images are presented in Figure 7.28(c) (Cross Phantom) and in Figure 7.28(d) (Sphere Phantom). Both these images present a blurring artifact in the direction normal to the direction of the acquisition. It is thus consistent with the lack of data acquired in that direction.

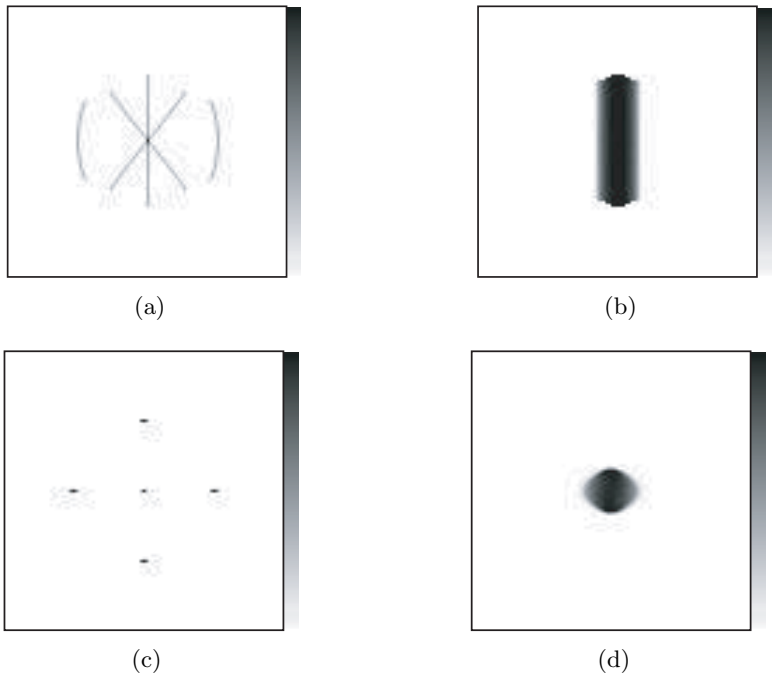

(a) (b)

(c) (d)

Figure 7.28: Central slices of the segment 0 sinogram corresponding to a simulated acquisition with only one angular position of the detector plates for the Analytical Cross Phantom (a) and for the Analytical Sphere Phantom (b). Central slice of the corresponding reconstructed images: c) Cross Phantom, d) Sphere Phantom.

Further analysis of the consequences of acquiring and reconstructing data proceeding from only one angular position of the detector plates will be carried on in the next Chapter with the use of Monte Carlo simulated data.

7.7 Conclusions

In this Chapter we have described the main classes and routines that were developed within the STIR library with the purpose to make it able to deal with data from the Clear-PEM scanner. Tests were performed with analytical phantoms and the developed projector operators, aiming at an initial evaluation of the behavior of the enhanced library. The results of such tests indicate a good agreement between the simulated and the reconstructed images. A more extended evaluation of the capabilities of the enhanced STIR library, with Monte Carlo simulated data, will be presented in the next chapter.

Chapter 8

3D OS-EM image reconstruction for the Clear−PEM scanner

8.1 Introduction

In the final section of Chapter 7 we presented a preliminary evaluation of the performance of the 3D image reconstruction software for the Clear-PEM scanner using the enhanced STIR framework. This preliminary evaluation used simple analytical simulated geometrical phantom data. In the present chapter we will present the studies that were conducted with the 3D image reconstruction software using the Monte Carlo simulated data of the Clear−PEM scanner.

As it was presented in Chapter 5, Monte Carlo simulation was performed both for a simplified version of the Clear−PEM scanner and for a more realistic, fully simulated version of the scanner. In the first section of this chapter, the studies that were performed with the simplified scanner geometry described in Chapter 5 will be presented. In the following sections, Monte Carlo simulation data obtained for the realistic scanner geometry will be used to study several aspects of the combined performance of the Clear−PEM scanner and the 3D image reconstruction algorithms used. This will include an evaluation of the effects of detector head rotation and Depth of Interaction (DOI) information on the quality of the reconstructed images, that will be presented in the second section of this chapter. In the final chapter section the NCAT breast phantom simulated data that was described in Chapter 5 will be used to study the ability of the scanner to detect simulated lesions at given clinical scenarios.

8.2 Simplified Scanner Geometry Studies

In this section we will present the 3D image reconstruction results obtained for the Sphere Phantom and for the Cross Phantom simulated data that were obtained with

the simplified geometry of the Clear−PEM scanner that was described in Chapter 5. The simplification in the Monte Carlo simulation included the geometrical aspects of the scanner and ignored degrading effects such as the parallax effect (exact DOI capabilities were considered), the positron range and the scatter. This simplification allowed isolating pure reconstruction issues from other physical or detector related artifacts.

8.2.1 Methods

The phantom data was reconstructed with the OS-EM algorithm available in STIR. According to the results obtained in the preliminary evaluation presented in the previous chapter, the OS-EM algorithm was used with four subsets and the projector and backprojector operators where used with the geometrical symmetries available and with three rays to trace each bin in the transaxial direction. The dimensions of the reconstructed images were 99×99×127 voxels, each with 1 mm^3 voxel resolution .
The quality of the reconstructed images was analyzed using the same figures of merit that were used in the preliminary evaluation presented in the previous chapter. The image spatial resolution was parameterized by the full-width at half-maximum (FWHM) of Gaussian fits of the profiles taken over the point sources in the reconstructed image of the Cross Phantom. Image uniformity was computed as the fraction between the mean number of counts inside a region of interest (ROI) drawn over the reconstructed image of the Sphere Phantom and the standard deviation measured for the same ROI.

8.2.2 Results

8.2.2.1 Cross Phantom

Figure 8.1(a) and Figure 8.1(b) show the central slice of the 0 segment of the sinogram of Monte Carlo simulation data of the Cross Phantom and the central slice of the reconstructed image, respectively. Figure 8.1(c) shows the profile taken over a central horizontal line in the central slice of the reconstructed image of the Cross Phantom. This line crosses the central point source (C) and the point sources A and A' of the phantom, as defined in the scheme of Figure 5.6(a) in Chapter 5.
Figure 8.2 shows the plots of the FWHM values against the iteration number for some of the point sources in the Cross Phantom. The plots shown refer to the FWHM values measured along the radial, transverse and axial profiles of the central point source and point sources A and B and D.
These plots show that, after a short number of iterations, the FWHM values in all the three directions converge to a given value and do not change afterward. The axial component of the FWHM of the point sources placed along the axis of rotation of the scanner (central point source and point source D, Figure 8.2 (a) and (b)) is the one

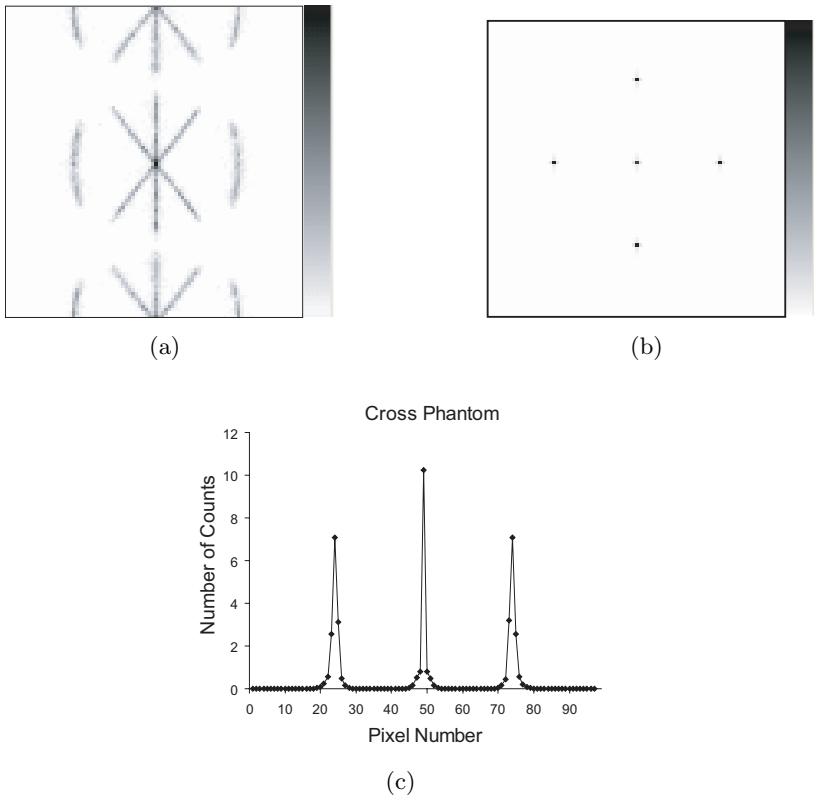

Figure 8.1: (a) Central slice of the segment 0 sinogram of Monte Carlo simulation data of the Cross Phantom in the simplified geometry of the Clear−PEM scanner. (b) Central axial slice of the respective reconstructed image and (c) profile taken across the central line of the central slice of the reconstructed image.

that takes longer to converge, but it converges to the same value of the FWMH in the transaxial profiles for those point sources. This does not happen for the point sources placed away from the axis of rotation of the scanner. In fact, for those point sources (A, A', B and B') the FWHM values measured along the axial profile always converge to a higher value than the FWHM values measured along the transaxial profiles. For all the point sources, the FWHM values measured along the transaxial profiles (radial and transverse) converge to a common value. The FWHM values measured for point source D have a similar behavior to those presented for the central point source. The same happens for point source D' (plot not shown). As expected due to geometrical symmetry reasons, the behavior of point source A and B are very similar. They are also similar to the behavior for point sources A' and B' (plots not shown).

Table 8.1 presents the FWHM values measured for the transverse, radial and axial profiles of all the point sources of the Cross Phantom at the iteration of convergence. We used here the same convergence criterion that was defined in the preliminary evaluation studies: the iteration for which there is a percentage variation of less than 1% in the

FWHM values in the subsequent iterations.

Point Source	FWHM (mm^3)
Central	0.95×0.95×0.98
D	0.94×0.94×0.98
D'	0.94×0.94×0.99
A	0.99×0.98×1.20
A'	0.99×0.98×1.21
B	0.98×0.99×1.19
B'	0.98×0.99×1.20

Table 8.1: Spatial resolution values parameterized as the FWHM of Gaussian fits to the profiles taken along the transverse, radial and axial profiles of all the point sources of the Cross Phantom at the iteration of convergence, in the simplified version of the simulated Clear−PEM scanner.

8.2.2.2 Sphere Phantom

Figure 8.3(a) and Figure 8.3(b) show the central slice of the segment 0 sinogram of the Sphere Phantom data and the central transaxial slice of the corresponding reconstructed image, respectively. Figure 8.3(c) shows the profile taken across a central line of the central transaxial slice of the reconstructed image of the Sphere Phantom.
Figure 8.4(a) shows the plot of the mean number of counts measured inside the ROI that was drawn over the reconstructed image of the sphere against the iteration number. The mean number of counts inside the ROI tends to converge to a stable value after the second iteration. Figure 8.4(b) presents the values of the standard deviation measured inside the considered ROI against the iteration number. As expected due to the nature of the image reconstruction algorithm used, this measure of noise tends to increase after a minimum value at the second iteration.
Figure 8.5 represents the evolution of the uniformity index as a function of the iteration number. This plot shows that the uniformity index reaches a maximum value at the second iteration and then continually drops. This is in agreement with the almost constant value of the mean number of counts against iteration number and the minimum value reached by the standard deviation at the second iteration, as presented in the plots of Figure 8.4

8.2.3 Discussion

In this section, the STIR library enhanced with the utilities to deal with planar scanner data was used to reconstruct Monte Carlo simulated data from the Clear−PEM scanner. The model for the scanner was a simplified one, and the phantoms used were simple

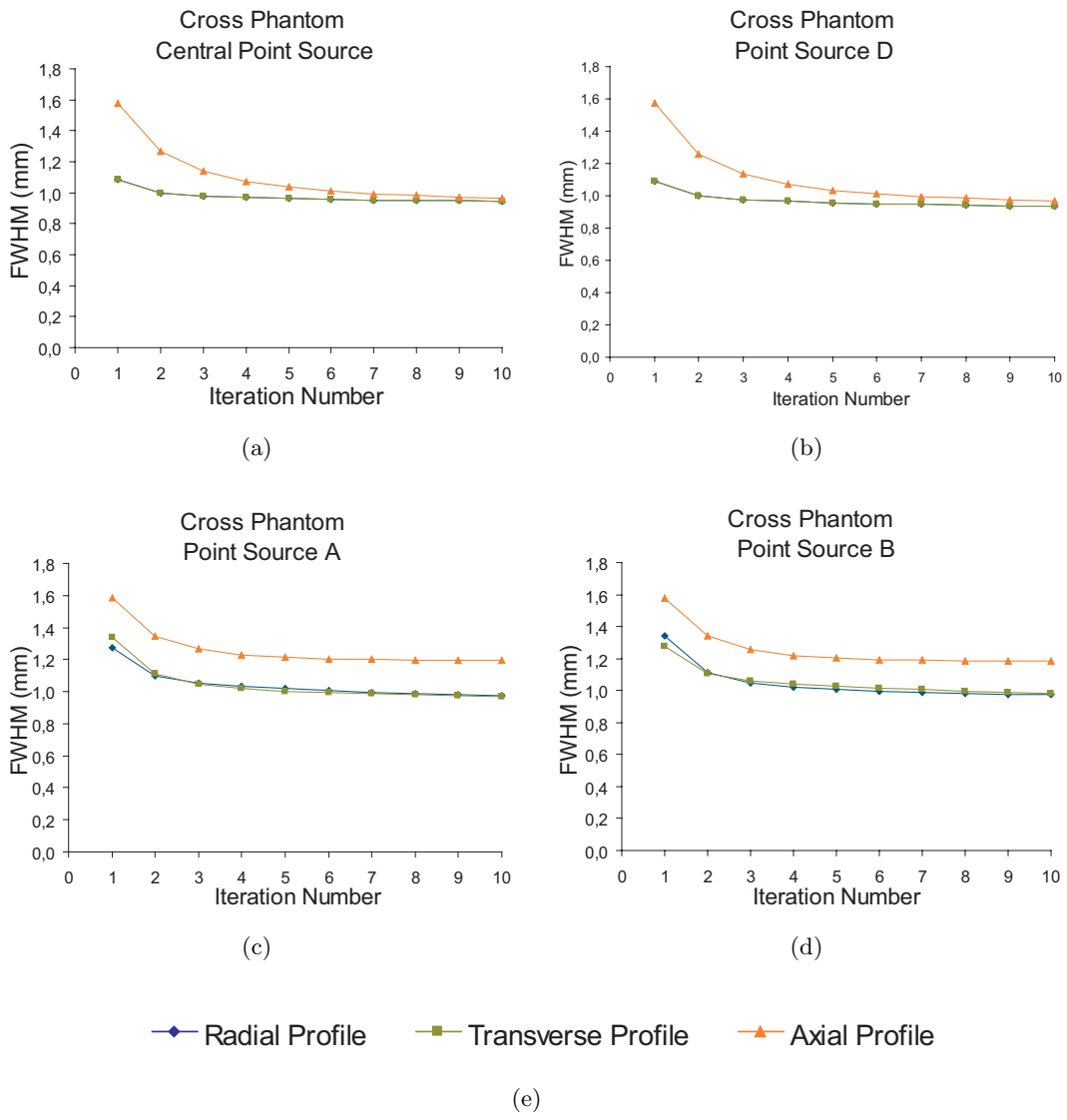

Figure 8.2: FWHM values against iteration number for the Cross Phantom reconstructed images in the simplified Clear−PEM scanner geometry. FWHM values measured along the radial, transverse and axial profiles of the (a) central point source, (b) point source D, (c) point source A and (d) point source B.

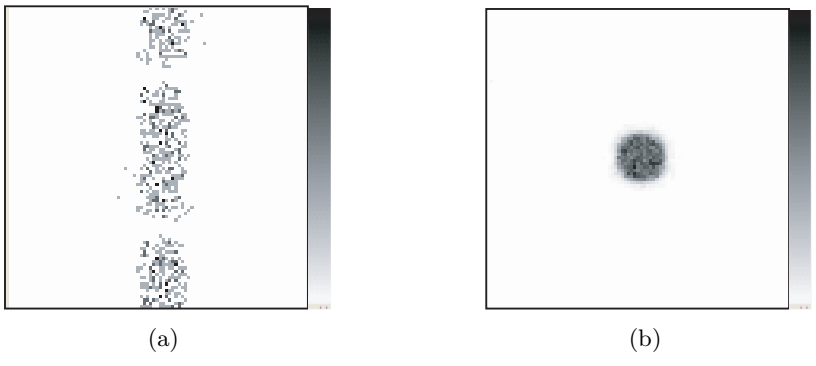

(a) (b)

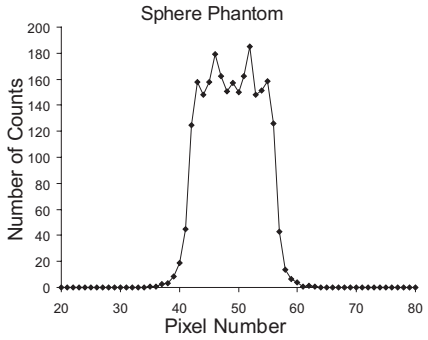

(c)

Figure 8.3: a) Central slice of the segment 0 sinogram of Monte Carlo simulation data of the Sphere Phantom in the simplified geometry of the Clear−PEM scanner. b) Central transaxial slice of the respective reconstructed image and c) profile taken across the central line of the shown image slice.

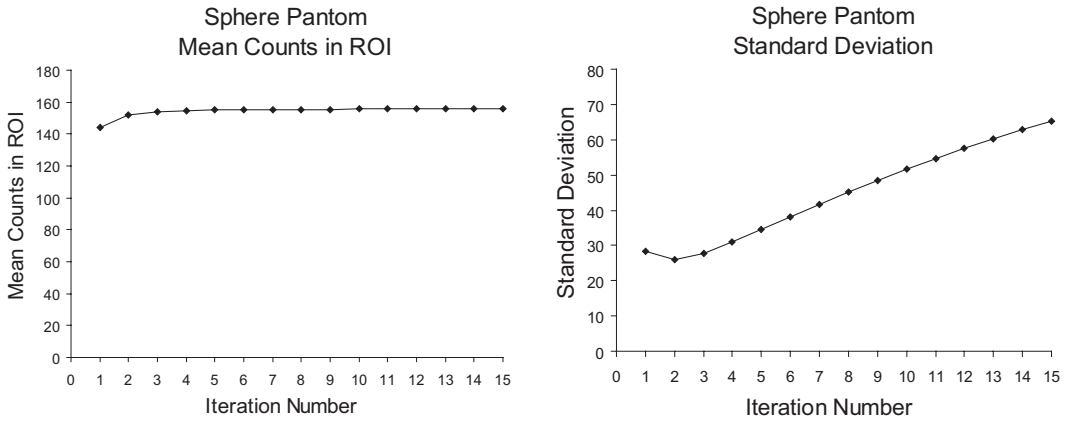

(a) (b)

Figure 8.4: (a) Mean number of counts inside the ROI against iteration number and (b) standard deviation in ROI against iteration number for the reconstructed images of the Sphere Phantom in the simplified geometry of the Clear−PEM scanner.

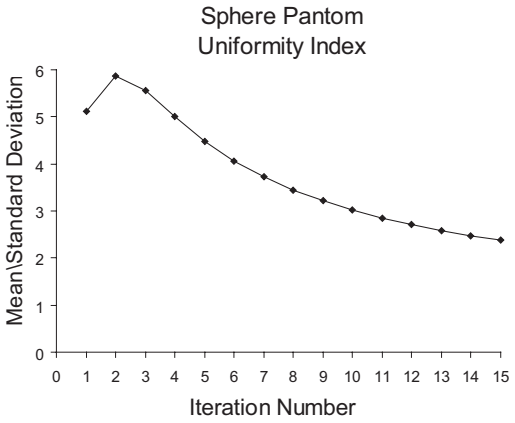

Figure 8.5: Uniformity index of the reconstructed images of the Sphere Phantom in the simplified version of the Clear−PEM scanner as a function of iteration number. The Uniformity Index is computed as the fraction of the mean number of counts inside a ROI over the standard deviation measured in the same ROI.

geometrical phantoms. The results presented show the ability to obtain images that are in visual agreement with the simulated ones. The computed Figures of Merit show an evolution with the iteration number that is as expected and in accordance with the preliminary evaluation performed in the previous chapter.
In the remainder of the chapter we will use these two tools, Monte Carlo simulation and 3D image reconstruction, to further study other aspects of the performance of the Clear−PEM scanner.

8.3 Effect of DOI information and rotation

As it was seen in Chapter 3, the Clear−PEM scanner has two unique characteristics with respect to most of the remainder PEM scanners that were described in that chapter. These characteristics are its ability of measuring the Depth of Interaction (DOI) coordinate of the photons within the detector crystals and the possibility of performing the rotation of the detector heads. In the work that is described hereafter, it is studied how different acquisition conditions regarding these two parameters, rotation and DOI information, impact on the quality of the reconstructed images. Due to constraints in the time needed to perform the Monte Carlo simulations, the sole image quality criteria that is used in this study is the image spatial resolution in several regions of the Field of View (FOV).

8.3.1 Methods

Simulated acquisitions of the 3D Chain Phantom that was described in Chapter 5 together with the realistic model for the Clear−PEM scanner were used in this work. Simulations were performed both considering the standard acquisition geometry that was previously described (two sequential acquisitions with the detector heads at two perpendicular angular positions) and a static acquisition, with the detector heads at 0°. In this section, we will refer to the standard acquisition geometry as the dual angle acquisition mode and to the static acquisition as the static mode. Both acquisitions were simulated for a same time interval, to ensure that both datasets had equivalent statistics.

For both acquisition scenarios, different resolution values for the DOI information were considered: exact DOI information, corresponding to an ideal DOI resolution, 2 mm FWHM uncertainty in DOI, corresponding to the Clear−PEM scanner foreseen DOI resolution, 5 mm FWHM DOI uncertainty, corresponding to a worse DOI resolution scenario and finally, the worst case scenario, no available DOI information.

Images were reconstructed with the 3D OS-EM available in STIR, with four subsets, with the dedicated planar projectors defined either for static or for dual angle acquisition, as was previously described. No correction for attenuation, random events or scatter were used. The dimensions of the reconstructed images were 99×99×127 voxels, each with voxel with resolution 1.0×1.0×1.3 mm^3.The planes used for the analysis of the spatial resolution were the central axial plane and the central coronal plane. The image spatial resolution was parameterized, as usual, by the FWHM of Gaussian fits to the profiles that were taken over the three orthogonal axis of the reconstructed point sources. Due to the blurring presented in some of the images, some of the Gaussian fits were more reliable than others. For such reason, an error was attributed to the computed FWHM values, based on the accuracy of the fitting. This error will be presented as an error bar in the plots.

8.3.2 Static Simulated Acquisition

Figure 8.6 shows the reconstructed images of the Chain Phantom corresponding to the static simulated acquisition with the several DOI information values considered. The visual inspection of theses images clearly shows that the most of the point sources are easily resolved in the reconstructed images. Exception goes to the point sources that are placed along an horizontal line in the central axial slice when no DOI information is available (Figure 8.6, first row, second and third column). These are the point sources that are placed in a plane normal to the detector heads surfaces, in a row parallel to the direction where there are no detectors acquiring data. However, such an effect is highly DOI dependent. In fact, it can be observed that those point sources can also be

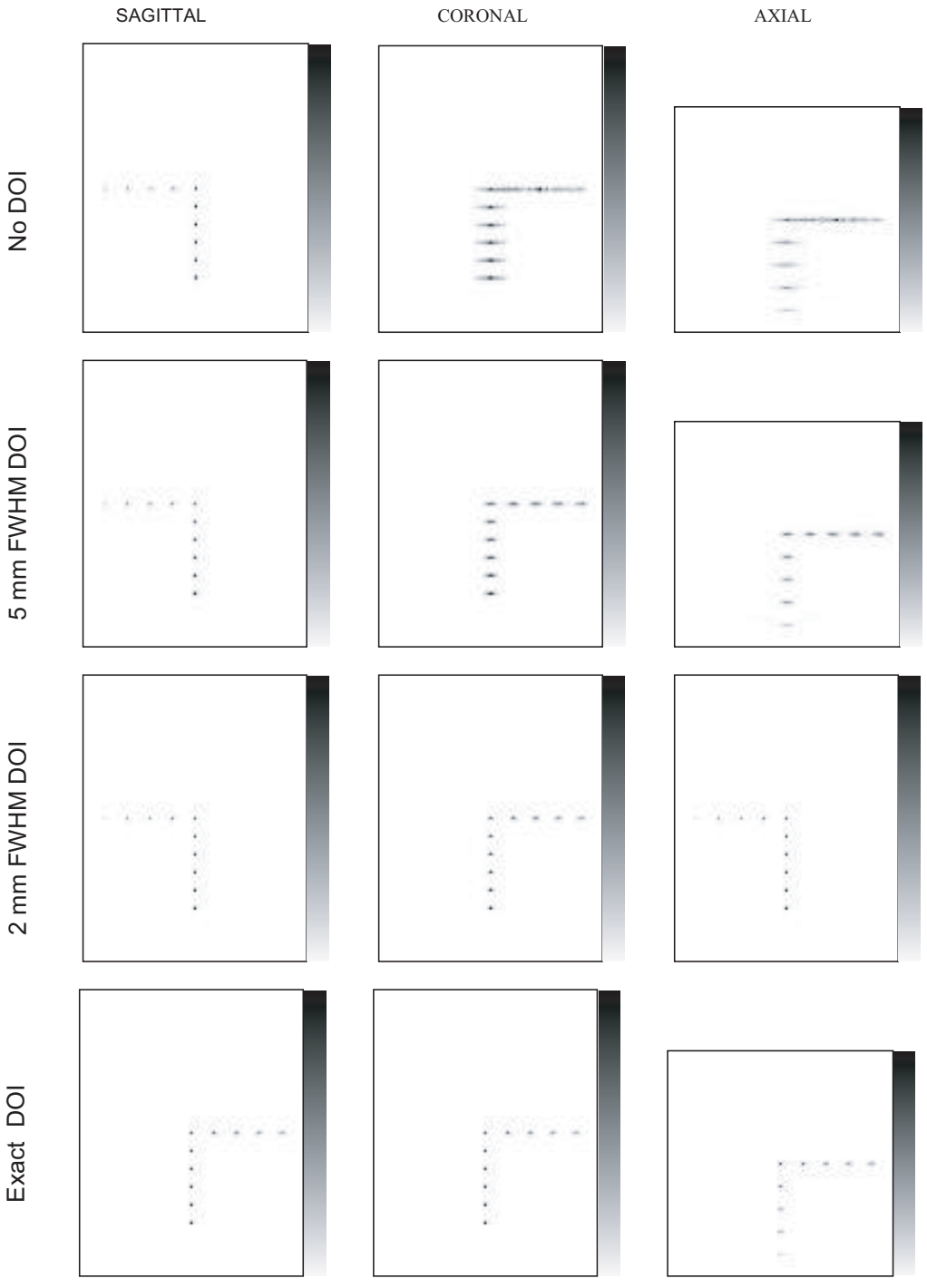

Figure 8.6: Static acquisition reconstructed images of the Chain Phantom.

resolved when better DOI resolution is available. Moreover, the improvement in the DOI resolution has a great impact in the component of the spatial resolution that, in a given plane, is normal to the direction along which there are no detectors acquiring data. For instance, this effect is clear for the point sources placed along the axis of rotation of the scanner (point sources in the vertical line of the images in the middle row of Figure 8.6).

Figure 8.7 shows profiles of some of the point sources in the reconstructed images corresponding to the cases of no DOI, 5 mm FWHM DOI, 2 mm FWHM DOI and exact DOI resolutions. Figure 8.7(a) shows the radial profiles of the point sources located in an horizontal line in the central axial slice of the reconstructed images (point sources 0 to 4, according to the scheme of Figure 5.7, Chapter 5). These profiles show strong blurring, in agreement with the images presented in Figure 8.6. Figure 8.7(b) shows the radial profiles of the point sources located in a vertical line in the central axial slice of the reconstructed images (point source 0 and point sources 5 to 8, according to the scheme of Figure 5.7, Chapter 5). These profiles show much less blurring than the previous ones.

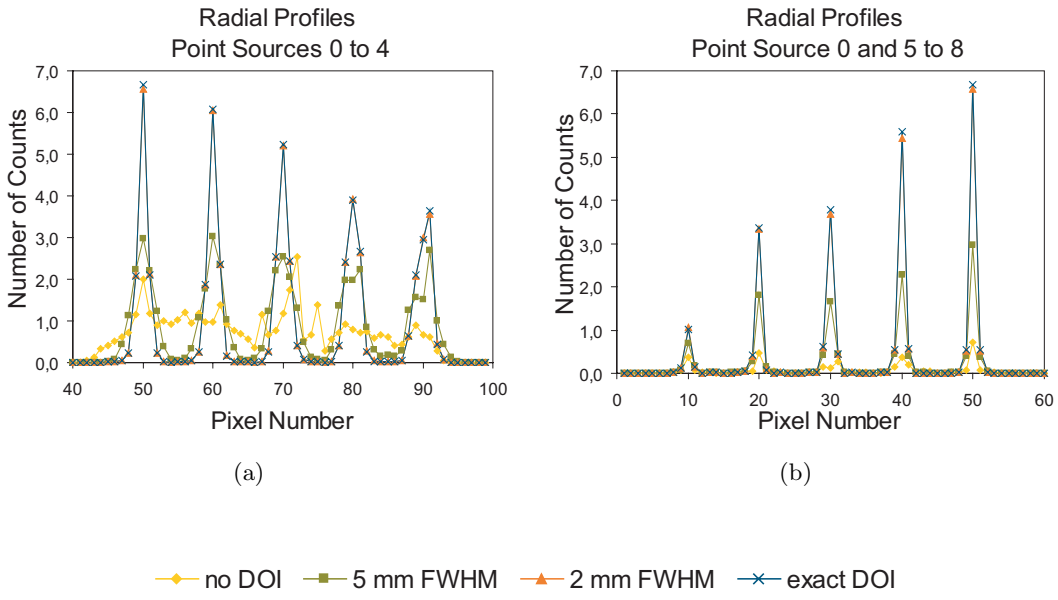

Figure 8.7: Profiles of some of the point sources of the Chain Phantom reconstructed images, corresponding to simulated acquisitions in static mode. (a) Radial profiles of point sources placed along an horizontal line in the central axial slice of the reconstructed image (point sources from 0 to 4). (b) Radial profiles of point sources placed along a vertical line in the central axial slice (point source 0 and point sources 5 to 8).

In both set of profiles, the profile corresponding to the exact DOI case is closely followed

by the profile corresponding to the 2 mm FWHM DOI resolution. The opposite happens with the profile corresponding to the case where no DOI information is available. Specially in the case of the profiles of the point sources located in an horizontal line in the central axial slice (point sources 0 to 4), the blurring is so strong that the Gaussian fit to the data becomes very difficult. When the fitting is possible, the associated errors are so significant that the fitting has little meaning. Therefore, analysis of the resolution values that will be performed next will not include the case of no available DOI information.

Figure 8.8 shows the plots of the radial, transverse and axial components of the FWHM values as a function of the iteration number, for point sources placed 3 cm away from the FOV center in the central axial slice, either along an horizontal line (point source 3) and along a vertical line (point source 7). Plots are shown for the case of 5 mm FWHM DOI resolution, 2 mm FWHM DOI resolution and exact DOI resolution. In accordance with the previous presented reconstructed images and profiles, the higher FWHM values are measured along the directions normal to the direction where there are no detectors acquiring data. This corresponds to the FWHM along the radial profile for point source 3 and transverse profile of point source 7. The scheme presented in Figure 8.9 tries to give some insight on the reason why these are the profiles that show more blurring. The scheme shows, as shaded areas, the areas defined by the possible LORs that correspond to annihilations in point source 3 (Figure 8.9(a)) and in point source 7 (Figure 8.9(b)) and that are accepted by the system. The positron range is not being considered in this scheme. During the backprojection operation of the image reconstruction process, the number of counts will be distributed along lines that have a strong horizontal component. Thus, the profiles along the horizontal lines (radial profile for point source 3 and transverse profile for point source 7) will show much more blurring than the vertical profiles. Since the number of counts are not distributed along vertical (or close to vertical) lines, the vertical profiles will be much more confined. Furthermore, point source 3 presents much more blurring along the radial profile than point source 7 due to the additive effect of the radial blurring of the remainder point sources that are placed along the horizontal line.

The values of FWHM along the horizontal profiles significantly improve with the improvement of the DOI information, whereas the same does not happen for the FWHM values along the remainder profiles (transverse and axial for point source 3, radial and axial for point source 7), which improve much more weakly with the improvement in the DOI information.

A more systematic study of the evolution of the FWHM values with the iteration number for all the point sources in the phantom was performed with the help of the volumetric FWHM. This parameter is computed as the product of the three components of the reconstructed image resolution, axial, radial and transverse, for each reconstructed

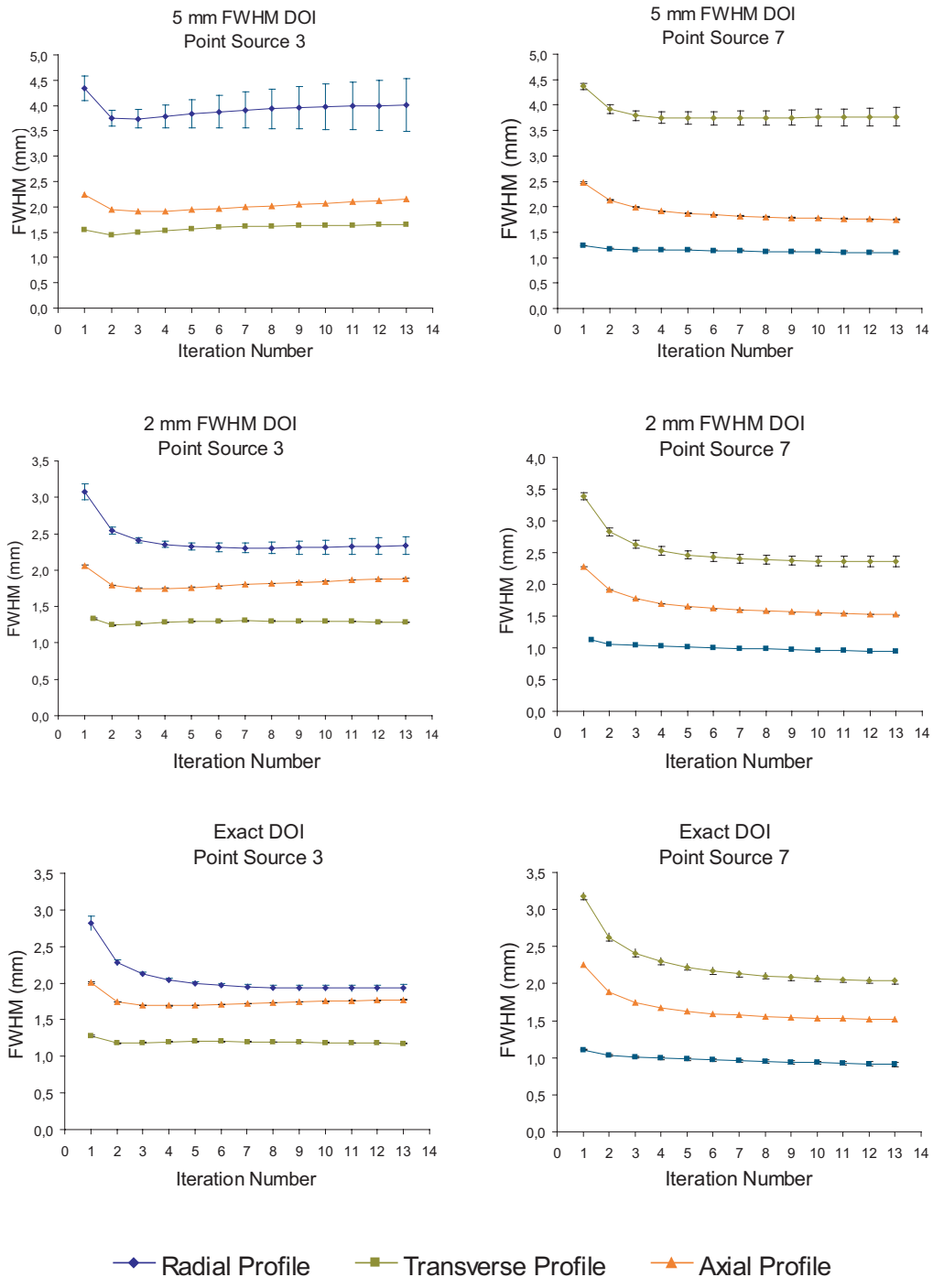

Figure 8.8: Plots of the radial, transverse and axial FWHM values against iteration number for the simulated static acquisitions, for a point source placed 3 cm away from the FOV center along an horizontal line in the central axial slice (point source 3) and for a point source placed 3 cm away from the FOV center along a vertical line in the central axial slice (point source 7). From top to bottom, the plots correspond to 5 mm FWHM DOI, 2 mm FWHM DOI and exact DOI.

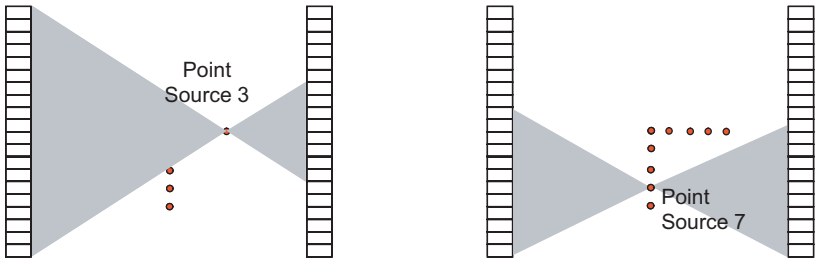

Figure 8.9: Acceptance angle for point source 3 (a) and for point source 7 (b) of the Chain Phantom in the simulated static mode acquisition. The fact that the number of detected counts are not reprojected in the vertical direction results in the profiles along that direction being much more confined than in the horizontal direction.

point source. Although the volumetric FWHM does not give any insight into differences between the radial and the transverse components of the spatial image resolution, it provides an easier means of analyzing the evolution of image spatial resolution across the FOV. Figure 8.10 shows the plots of the values of the volumetric FWHM against iteration number for point sources in the Chain Phantom, for the values of DOI resolution considered in this study. The plots presented refer to the point sources placed along an horizontal line in the central axial slice (point sources 0 to 4, right row of Figure 8.10) and to the point sources placed along the axis of rotation of the scanner (point sources 0 and 9 to 13, left row of Figure 8.10).

Let us first focus on the plots corresponding to the point sources 0 to 4. These plots show that the volumetric FWHM values of the point sources closer to the center of the FOV (point sources 0, 1 and 2) tend to improve in the first few iterations and then remain about constant. This behavior is observed independently of the value of the DOI resolution. On the contrary, the evolution of the volumetric FWHM values as a function of the iteration number for the two point sources further from the FOV center (point sources 3 and 4) are highly dependent on the DOI resolution. In fact, for the 5 mm FWHM DOI resolution, the volumetric FWHM values do not converge to a stable value. On the contrary, they tend to increase after a minimum value at the second iteration. When the DOI resolution is improved, the volumetric FWHM values for point source 3 tend to improve with iteration number and to remain stable after some iterations, but the same does not happen for the point source 4. The volumetric FWHM values measured for this point source tend to increase with the iteration number, even when an ideal case (exact DOI resolution) is considered, although less in that case. Therefore, the resolution of point sources near the edges of the FOV is critical when a static acquisition is performed, independently of the DOI resolution available.

Let us return to Figure 8.10 and focus on to the evolution of the volumetric FWHM values with iteration number and DOI for the point sources placed along the axis of

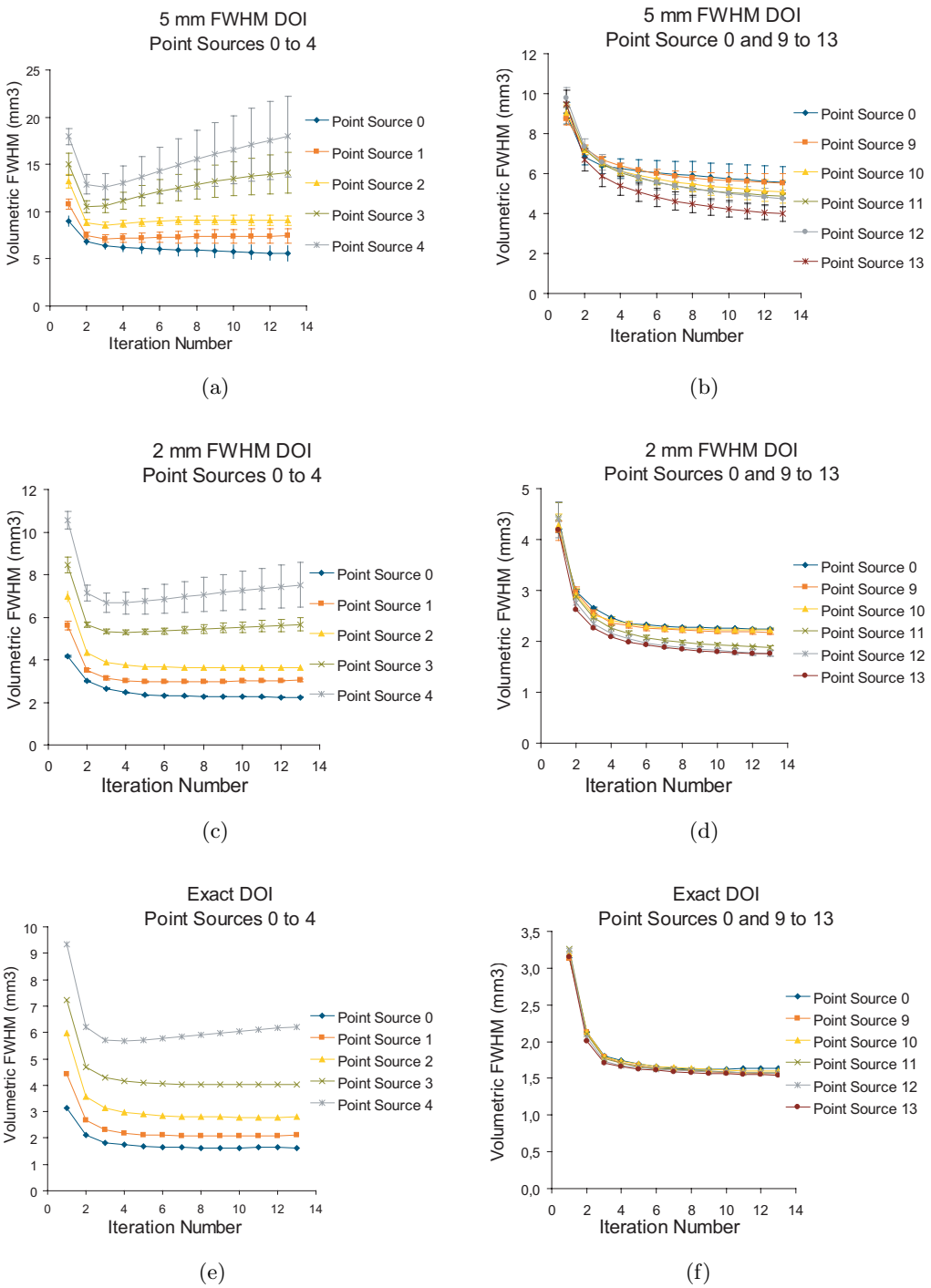

Figure 8.10: Plots of the volumetric FWHM against iteration number for the simulated static acquisitions. Plots on the left correspond to the ones placed along an horizontal line in the central axial slice (point sources 0 to 4).Plots on the right correspond the ones placed along a central line in the central coronal slice (point source 0 and point sources from 9 to 13). From top to bottom, plots correspond to simulated acquisitions with no DOI, 5 mm FWHM DOI, 2 mm FWHM DOI and exact DOI.

rotation of the scanner (point sources 0 and 9 to 13). Independently of the image plane where the sources are located and of the DOI resolution considered, the volumetric FWHM values for these point sources, all placed in the center of their respective planes, improve with the iteration number and tend to remain constant after a few iterations. The number of iteration for convergence is higher for the 5 mm FWHM DOI resolution case. As the DOI resolution improves, the lines describing the evolution of the volumetric FWHM with iteration number for the several point sources tend to come closer. For the ideal case DOI resolution, the volumetric FWHM values for all these point sources converge approximately to a common value. This means that, no DOI effects taken into consideration, the image spatial resolution does not depend on the position of the sources along the axis of rotation of the scanner.

Figure 8.11 shows the plots of the volumetric FWHM after convergence as a function of the distance to the center of the field of view. As a criterion of convergence, a maximum percent variation in the volumetric FWHM values of all the point sources of less than 3% in the subsequent iterations was used. For those cases where convergence was not achieved for a given point source, the value of the volumetric FWHM presented corresponds to the value at the considered iteration of convergence for the remainder point sources.

These plots highlight that there is a significant improvement in the image spatial resolution when the DOI resolution improves from 5 mm FWHM to 2 mm FWHM. This is true either in the center and near the edge of the FOV. The difference in the volumetric FWHM corresponding to the ideal case DOI resolution (exact resolution) and the 2 mm FWHM DOI resolution is not as pronounced.

It is also clear from the analysis of these plots, for the point sources located in the central axial slice, at different distances from the center (Figure 8.3.2 and Figure 8.3.2), that the volumetric FWHM is higher for the point sources that are placed further from the FOV center. This is in agreement with what is expected due to the nature of the acquisition geometry. As a matter of fact, the number of possible accepted LORs that result from emissions near the center of the FOV is much higher than the number of possible LORs originated by emissions near the edges of the FOV.

However, the degradation in the spatial resolution is not observed for the point sources that are placed in the center of different image planes. In fact, for a given DOI resolution, these point sources present an almost homogeneous volumetric FWHM (Figure 8.3.2), as it was already pointed out.

Tables 8.2, 8.3 and 8.4 list the spatial resolution values measured at convergence for all the point sources of the Chain Phantom, for the simulated static acquisition and for the several DOI information scenarios considered. These values range from 1.0 mm (FOV center, exact DOI resolution) to 4.2 mm (FOV edge, 5 mm FWHM DOI resolution).

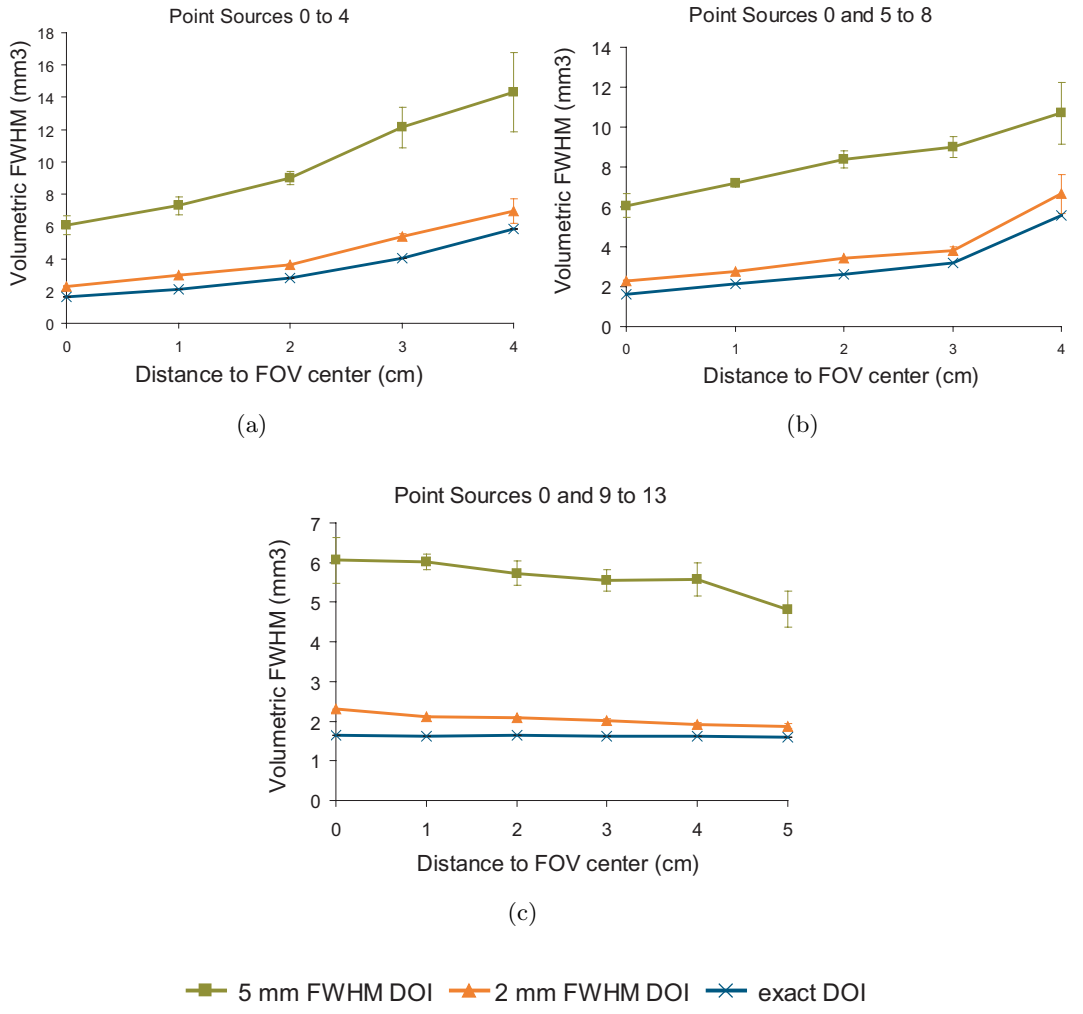

Figure 8.11: Plots of volumetric FWHM against distance to FOV center, for the simulated static acquisitions.

Distance to FOV center	Point Source	5 mm FWHM DOI	2 mm FWHM DOI	exact DOI
0 cm	0	3.4×1.1×1.5	1.6×1.0×1.4	1.2×1.0×1.5
1 cm	1	3.3×1.3×1.8	1.6×1.1×1.7	1.3×1.0×1.6
2 cm	2	3.9×1.3×1.8	2.0×1.1×1.7	1.6×1.1×1.6
3 cm	3	3.9×1.6×2.0	2.3×1.3×1.8	2.0×1.2×1.7
4 cm	4	4.1×1.9×1.8	2.6×1.6×1.6	2.4×1.6×1.6

Table 8.2: Spatial resolution values (FWHM) listed for the point sources of the Chain Phantom placed along an horizontal line in the central axial slice (point sources 0 to 4), for the simulated static acquisitions and the several DOI resolution scenarios considered. The FWHM values listed are in mm.

Distance to FOV center	Point Source	5 mm FWHM DOI	2 mm FWHM DOI	exact DOI
0 cm	0	3.4×1.1×1.5	1.6×1.0×1.4	1.2×1.0×1.5
1 cm	5	3.4×1.3×1.6	1.6×1.1×1.6	1.3×1.1×1.7
2 cm	6	3.6×1.4×1.6	1.9×1.2×1.5	1.6×1.0×1.5
3 cm	7	3.7×1.1×1.8	2.4×1.0×1.6	2.1×1.0×1.6
4 cm	8	4.2×1.2×2.1	3.1×1.1×1.8	2.9×1.0×1.7

Table 8.3: Spatial resolution values (FWHM) listed for the point sources of the Chain Phantom placed along a vertical line in the central axial slice (point sources 0 and 5 to 8), for the simulated static acquisitions and the several DOI resolution scenarios considered. The FWHM values listed are in mm.

Distance to FOV center	Point Source	5 mm FWHM DOI	2 mm FWHM DOI	exact DOI
0 cm	0	3.4×1.1×1.5	1.6×1.0×1.4	1.2×1.0×1.5
1 cm	9	3.2×1.2×1.5	1.5×1.1×1.4	1.2×1.0×1.5
2 cm	10	3.2×1.2×1.5	1.5×1.1×1.4	1.2×1.0×1.4
3 cm	11	3.1×1.2×1.4	1.4×1.1×1.3	1.2×1.0×1.4
4 cm	12	3.1×1.3×1.5	1.4×1.1×1.3	1.2×1.0×1.5
5 cm	13	2.8×1.3×1.4	1.4×1.1×1.3	1.1×1.0×1.4

Table 8.4: Spatial resolution values (FWHM) listed for the point sources of the Chain Phantom placed along the axis of rotation of the scanner (point sources 0 and 9 to 13), for the simulated static acquisitions and the several DOI resolution scenarios considered. The FWHM values listed are in mm.

8.3.3 Dual Angle Simulated Acquisition

Figure 8.12 shows the reconstructed images corresponding to the simulated dual angle acquisition with the several DOI information values considered. These images show that all the point sources in the Chain Phantom can be easily resolved with the dual angle acquisition, even in the worst considered scenario for the DOI resolution.
Figure 8.14 shows profiles of some of the point sources in the reconstructed images corresponding to the DOI resolution scenarios of no DOI, 5 mm FWHM DOI, 2 mm FWHM DOI and exact DOI. Figure 8.14(a) shows the radial profiles of the point sources located in an horizontal line in the central axial slice of the reconstructed images (point sources 0 to 4). Figure 8.14(b) shows the radial profiles of the point sources located in a vertical line in the central axial slice of the reconstructed images (point source 0 and point sources 5 to 8). In contrast to what happened with the simulated static acquisition, all the profiles are clearly defined and the radial profiles of point sources 0 to 4 are quite similar to the radial profiles of point sources 0 and 5 to 8. This is in agreement with the geometry of the dual angle acquisition. In fact, the area defined by the number of accepted LORs originating from annihilations in point source 3 is symmetric to the area defined by the LORs originating from annihilations in point source 7 that are accepted by the scanner, as depicted in Figure 8.13. This also explains why there is no strong blurring neither along the horizontal nor the vertical directions, as verified in the static mode results.
The peak-to-valley ratios of the profiles decrease either with the distance from the FOV center and with the decrease in DOI resolution. As we will see, this is in agreement with the measured spatial resolution.
In the previous analysis of the FWHM values for the static acquisition, the worst scenario for the DOI resolution (no DOI information) was not considered. This was due to the difficulty on performing Gaussian fits to some of the profiles of the Chain Phantom point sources. Although such a problem does not happen in the dual angle acquisition case, the quantitative analysis for the no DOI resolution scenario will also not be performed in the dual angle acquisition case.
Figure 8.15 shows the plots of the radial, transverse and axial components of the FWHM values as a function of the iteration number, for point sources placed 3 cm away from the FOV center in the central axial slice, either along an horizontal line (point source 3) and along a vertical line (point source 7). Plots are shown for the case of 5 mm FWHM DOI resolution, 2 mm FWHM DOI resolution and exact DOI resolution. As expected due to the nature of the acquisition geometry for the dual angle acquisition, the evolution of the FWHM components with the iteration number for the two point sources are very similar. The plots also show that the impact of the DOI information is weaker in the axial component of the FWHM than in the radial and transverse

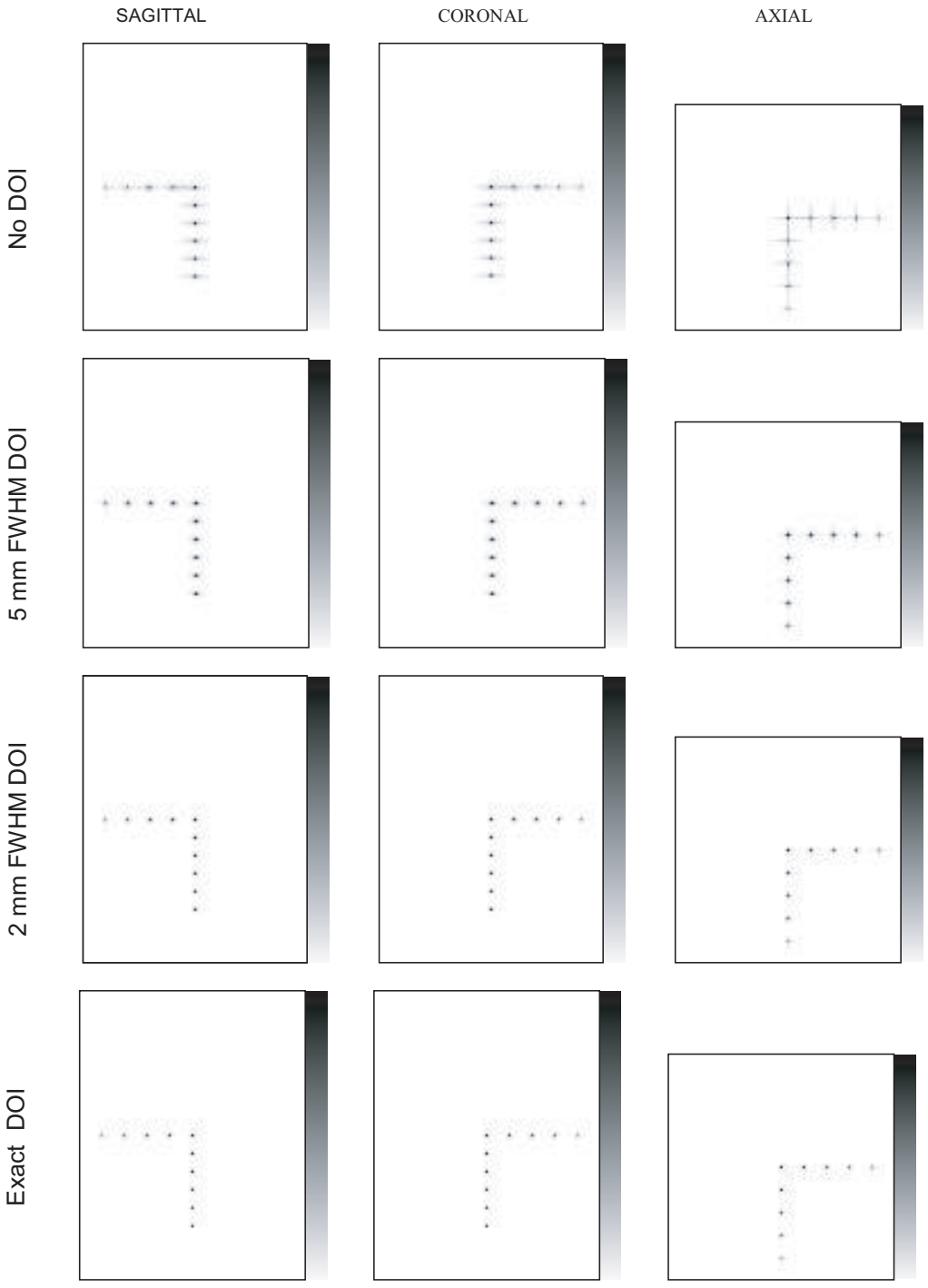

Figure 8.12: Reconstructed images of the Chain Phantom simulated data with dual angle acquisition.

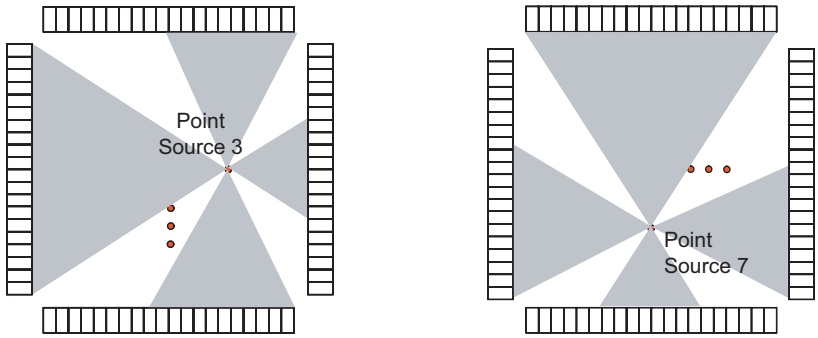

Figure 8.13: Acceptance angle for point source 3 (a) and for point source 7 (b) of the Chain Phantom in the simulated dual angle acquisition.

components. These plots show, however, that the FWHM values measured along the radial profile converge to slightly higher values than the FWHM values measured along the transverse profile. This is true when the point sources are not in the FOV center. This can be explained by considering the image presented in Figure 8.16. For a point source placed near the edge of the FOV and midway between the two detector heads, (Figure 8.16(a)), the area defined by the accepted LORs that originate from emissions from the point source is quite narrow. Therefore, since there is an enormous amount of LORs that are missing, this data will contribute to a poor resolution, in this case in its transverse component. On the contrary, when the detectors rotate, the area defined by the accepted LORs is broader (Figure 8.16(b)), hence the contribution to the resolution, in this case the radial component, will be better. As a consequence, for point sources placed far from the FOV center, the radial component of the spatial resolution is better than its transverse component.

Figure 8.17 shows the plots of the values of the volumetric FWHM against iteration number for the point sources in the Chain Phantom, for the values of DOI resolution considered in this study. In line with the plots that were presented for the static acquisition analysis, the plots here presented refer to the point sources placed along an horizontal line in the central axial slice (point sources 0 to 4, right row of Figure 8.10) and to the point sources placed along the axis of rotation of the scanner (point sources 0 and 9 to 13, left row of Figure 8.10). The plots show that there is a clear improvement in the image spatial resolution with the improvement in the DOI resolution. The point source 4, which is placed 4 cm away from the FOV center in the central axial slice, shows a behavior similar to that presented in the static acquisition mode. The FWHM values measured for that location do not converge to a stable value, independently of the DOI resolution considered. On the contrary, they tend to increase after reaching a minimum value at the first few iterations. This means that this problem is not solved

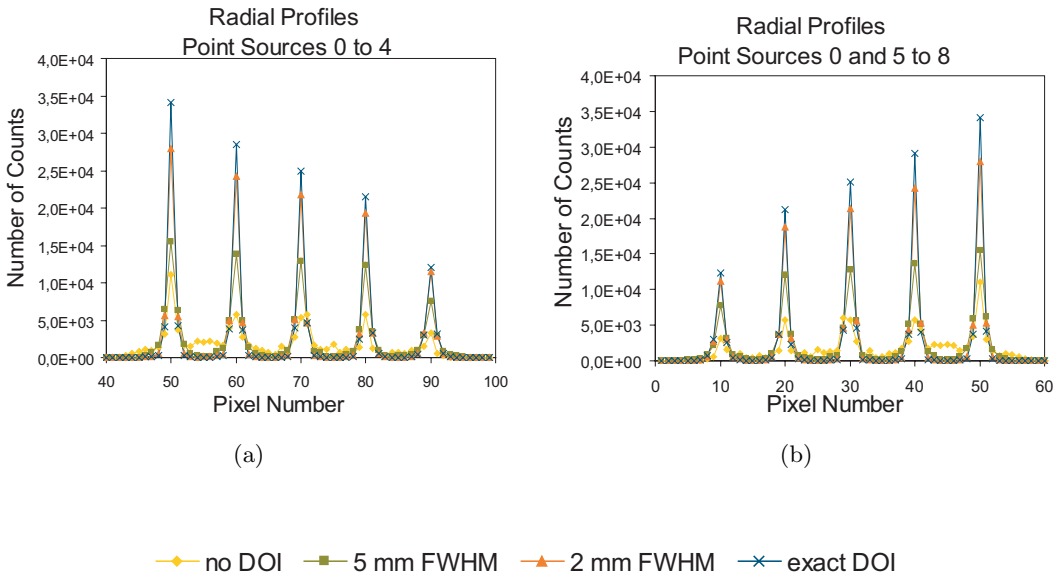

Figure 8.14: Profiles of some of the point sources of the Chain Phantom reconstructed images, corresponding to dual angle simulated acquisitions. (a) Radial profiles of point sources from 0 to 4. (b) Radial profiles of point source 0 and point sources 5 to 8.

neither by the use of DOI information nor by the presented dual angle acquisition.

Figure 8.18 shows the plots of the volumetric FWHM after convergence as a function of the distance to the center of the field of view. The convergence criterion used was the same that was used for the simulated static acquisition. The plots show, once again, that the improvement in the image spatial resolution is very significant when the DOI resolution improves from 5 mm to 2 mm FWHM and, as expected, it also improves when an ideal case exact DOI resolution is considered. For the point sources in the central axial slice (point sources 0 to 8), the volumetric FWHM values remain approximately constant until 3 cm from the FOV center, with slightly lower values at 4 cm from the FOV center. The values presented for the point sources placed along an horizontal line in the central axial slice are similar to the values found to the point sources placed along a vertical line in that same slice. This is as expected, due to the symmetries resulting from the dual angle acquisition mode. With regard to the point sources along the axis of rotation of the scanner, except for the point source 13 in the 5 mm FWHM DOI case, the presented FWHM values remain about constant throughout the planes studied.

Table 8.5 lists the spatial resolution values measured for all the point sources of the Chain Phantom, for the simulated dual angle acquisition and for the several DOI information scenarios considered. The presented values show that the FWHM values for the dual angle acquisition range from 2.3 mm (point source 8, axial FWHM component,

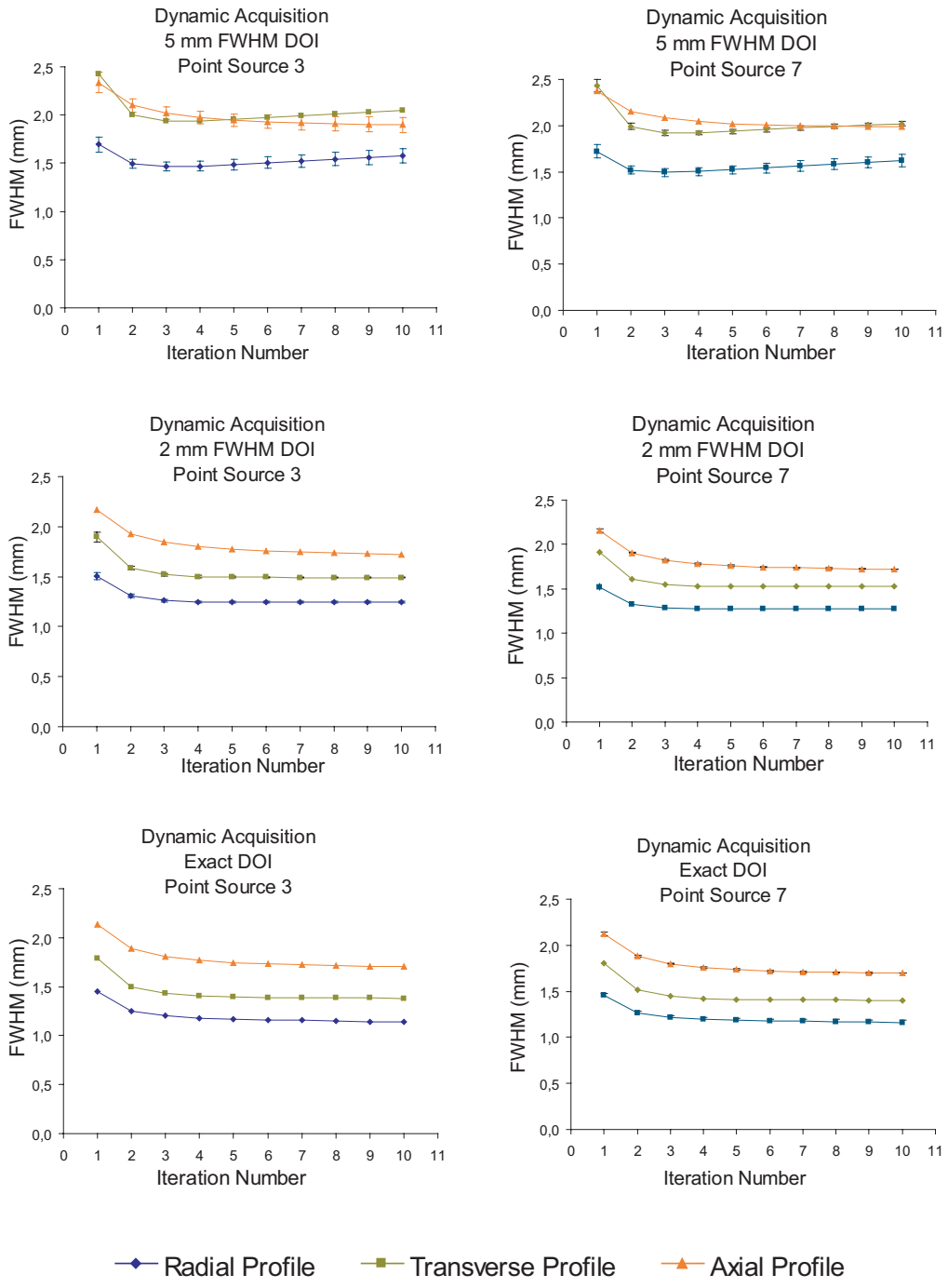

Figure 8.15: Plots of the radial, transverse and axial FWHM values against iteration number for the simulated dual angle acquisitions, for a point source placed 3 cm away from the FOV center along an horizontal line in the central axial slice (point source 3) and for a point source placed 3 cm away from the FOV center along a vertical line in the central axial slice (point source 6). From top to bottom, the plots correspond to 5 mm FWHM DOI, 2 mm FWHM DOI and exact DOI.

Distance to FOV center	Point Source	5 mm FWHM DOI	2 mm FWHM DOI	exact DOI
0 cm	0	1.8×1.8×1.6	1.3×1.3×1.4	1.2×1.1×1.3
1 cm	1	1.7×1.7×1.8	1.3×1.3×1.6	1.2×1.2×1.5
2 cm	2	1.7×1.7×1.8	1.4×1.3×1.6	1.2×1.2×1.6
3 cm	3	1.5×2.0×2.0	1.2×1.5×1.8	1.2×1.4×1.7
4 cm	4	1.7×2.2×2.3	1.5×1.8×2.0	1.5×1.7×2.0

Table 8.5: Spatial resolution values (FWHM) listed for the point sources of the Chain Phantom placed along an horizontal line in the central axial slice (point sources 0 to 4), for the simulated dual angle acquisitions and the several DOI resolution scenarios considered. The FWHM values listed are in mm.

Distance to FOV center	Point Source	5 mm FWHM DOI	2 mm FWHM DOI	exact DOI
0 cm	0	1.8×1.8×1.7	1.3×1.3×1.4	1.2×1.1×1.4
1 cm	5	1.7×1.7×1.8	1.3×1.3×1.6	1.1×1.2×1.5
2 cm	6	1.6×1.7×1.8	1.3×1.4×1.6	1.1×1.3×1.6
3 cm	7	1.9×1.5×2.0	1.5×1.3×1.7	1.4×1.2×1.7
4 cm	8	2.1×1.6×2.3	1.7×1.4×2.1	1.6×1.4×2.0

Table 8.6: Spatial resolution values (FWHM) listed for the point sources of the Chain Phantom placed along a vertical line in the central axial slice (point sources 0 and 5 to 8), for the simulated dual angle acquisitions and the several DOI resolution scenarios considered. The FWHM values listed are in mm.

Distance to FOV center	Point Source	5 mm FWHM DOI	2 mm FWHM DOI	exact DOI
0 cm	0	1.8×1.8×1.7	1.3×1.3×1.4	1.2×1.1×1.4
1 cm	9	1.8×1.9×1.6	1.3×1.3×1.4	1.1×1.1×1.3
2 cm	10	1.8×1.8×1.7	1.3×1.3×1.4	1.2×1.2×1.3
3 cm	11	1.8×1.8×1.6	1.3×1.3×1.4	1.1×1.1×1.3
4 cm	12	1.8×1.8×1.6	1.3×1.3×1.4	1.1×1.1×1.2
5 cm	13	1.6×1.7×1.4	1.3×1.3×1.4	1.1×1.1×1.2

Table 8.7: Spatial resolution values (FWHM) listed for the point sources of the Chain Phantom placed along the axis of rotation of the scanner (point sources 0 and 9 to 13), for the simulated dual angle acquisitions and the several DOI resolution scenarios considered. The FWHM values listed are in mm.

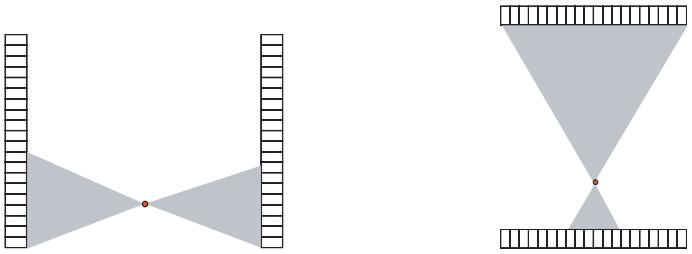

Figure 8.16: A point source near the edge of the FOV contributes differently to the radial and to the transverse components of the spatial resolution. In (a), the point source is midway between the two detector heads and contributes to a poor transverse resolution. In (b), the point source is closer to one of the detector heads and contributes to a better radial resolution.

5 mm FWHM DOI resolution) to 1.1 mm (several sources, exact DOI resolution). They also show that with detector head rotation and a DOI resolution of 2 mm FWHM is possible to achieve image spatial resolution values lower or equal to 2 mm across the entire FOV. The presented study indicates that this would not be possible neither without rotation nor with the worse DOI resolution studied (5 mm FWHM DOI).

8.3.4 Discussion

Figure 8.19 presents the plots of the volumetric FWHM values as a function of the distance to the FOV center, for all the point sources studied, for the DOI resolution scenarios studied, and both for dual angle and static acquisitions.
Regarding the point sources that are placed at several distances from the FOV center at the central axial plane, the most significant improvement in the spatial resolution values is obtained when a bad DOI resolution (in the case studied, 5 mm FWHM DOI) is improved to 2 mm FWHM DOI resolution. This improvement in the spatial resolution is more drastic than the improvement that is obtained when a static acquisition with a bad DOI resolution is substituted by a dual angle acquisition with the same DOI resolution. In order words, the presented results seem to indicate that, from the spatial resolution point of view, it is more important to have a better DOI resolution than to perform a dual angle acquisition (such as the one studied in this work) with a bad DOI resolution. This is also true when analyzing the values obtained for the point sources placed along the axis of rotation of the scanner. Of course, if a good DOI resolution is available, is always better to perform the rotation, since that provides better spatial resolution, especially near the FOV edge. For instance, it is interesting to note that, for the point sources placed further from the FOV center, the volumetric FWHM values for the 2 mm FWHM DOI resolution with rotation are equal or lower than the values obtained for the exact DOI resolution but without rotation.

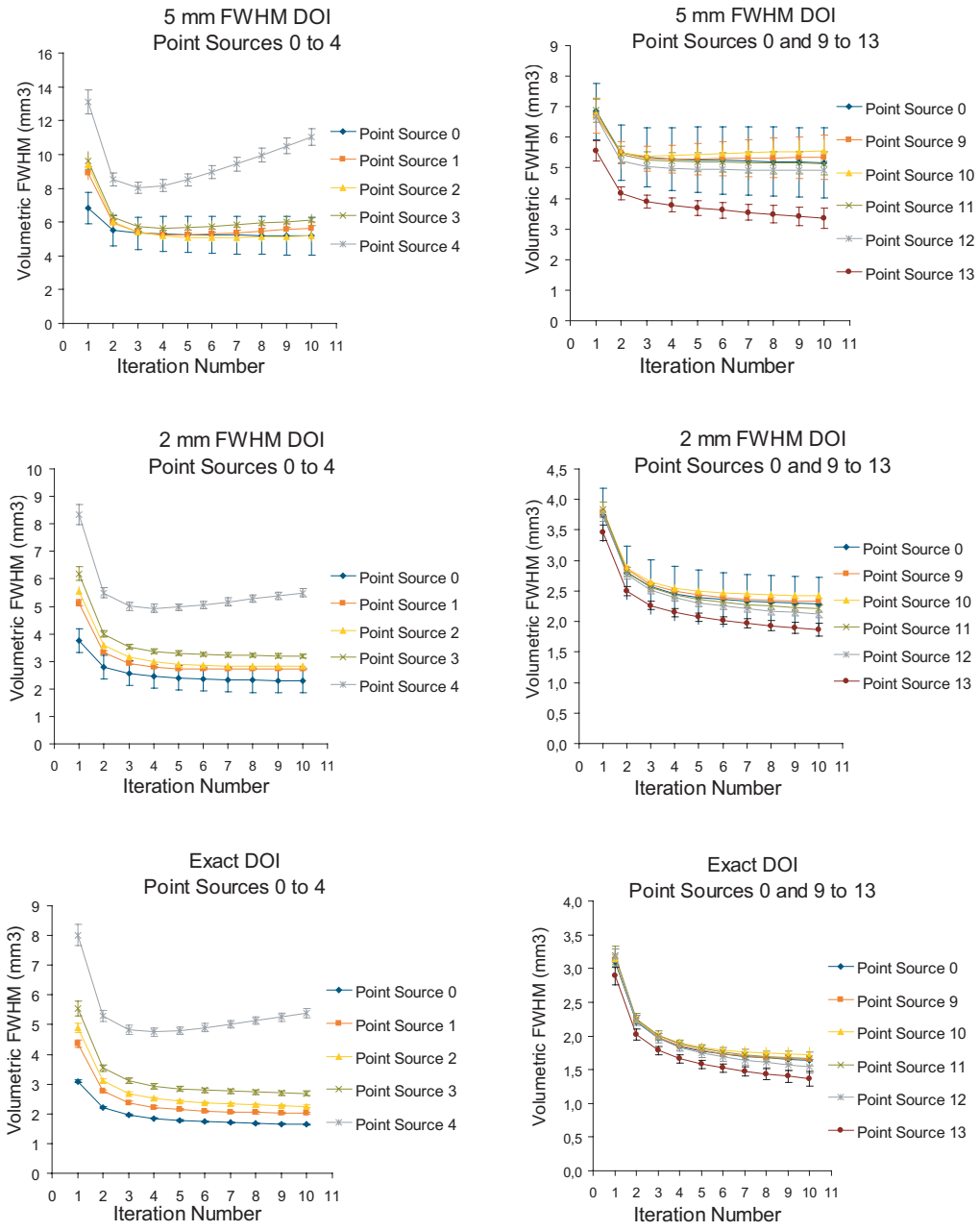

Figure 8.17: Plots of the volumetric FWHM against iteration number for simulated dual angle acquisitions. Plots on the left correspond to the point sources placed along an horizontal line in the central axial slice (point sources 0 to 4); plots on the right side correspond to the point sources that are placed along a central in the central coronal slice (point source 0 and point sources from 9 to 13). From top to bottom, plots correspond to simulated acquisitions with no DOI information, 5 mm FWHM DOI resolution, 2 mm FWHM DOI resolution and exact DOI resolution.

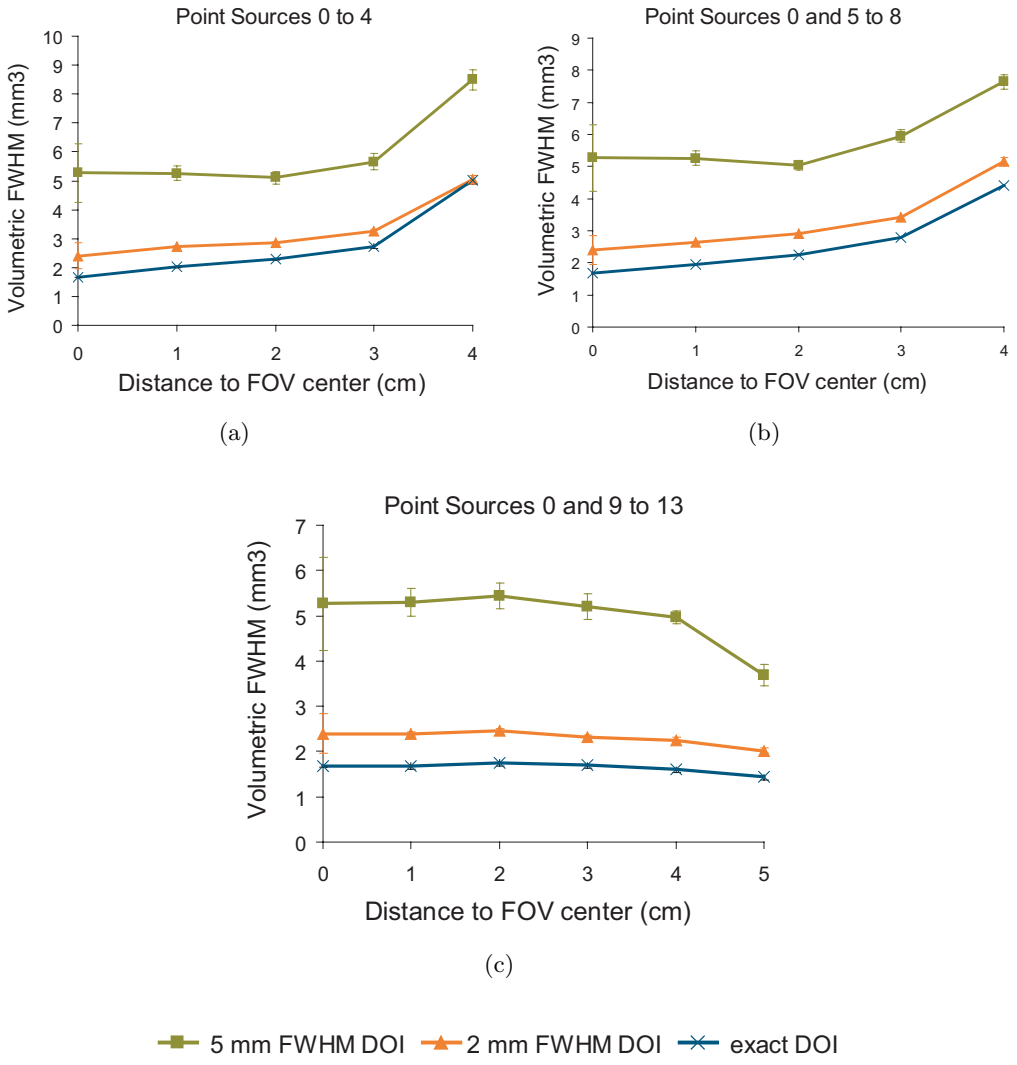

Figure 8.18: Plots of volumetric FWHM against distance to FOV center, for the simulated dual angle acquisitions.

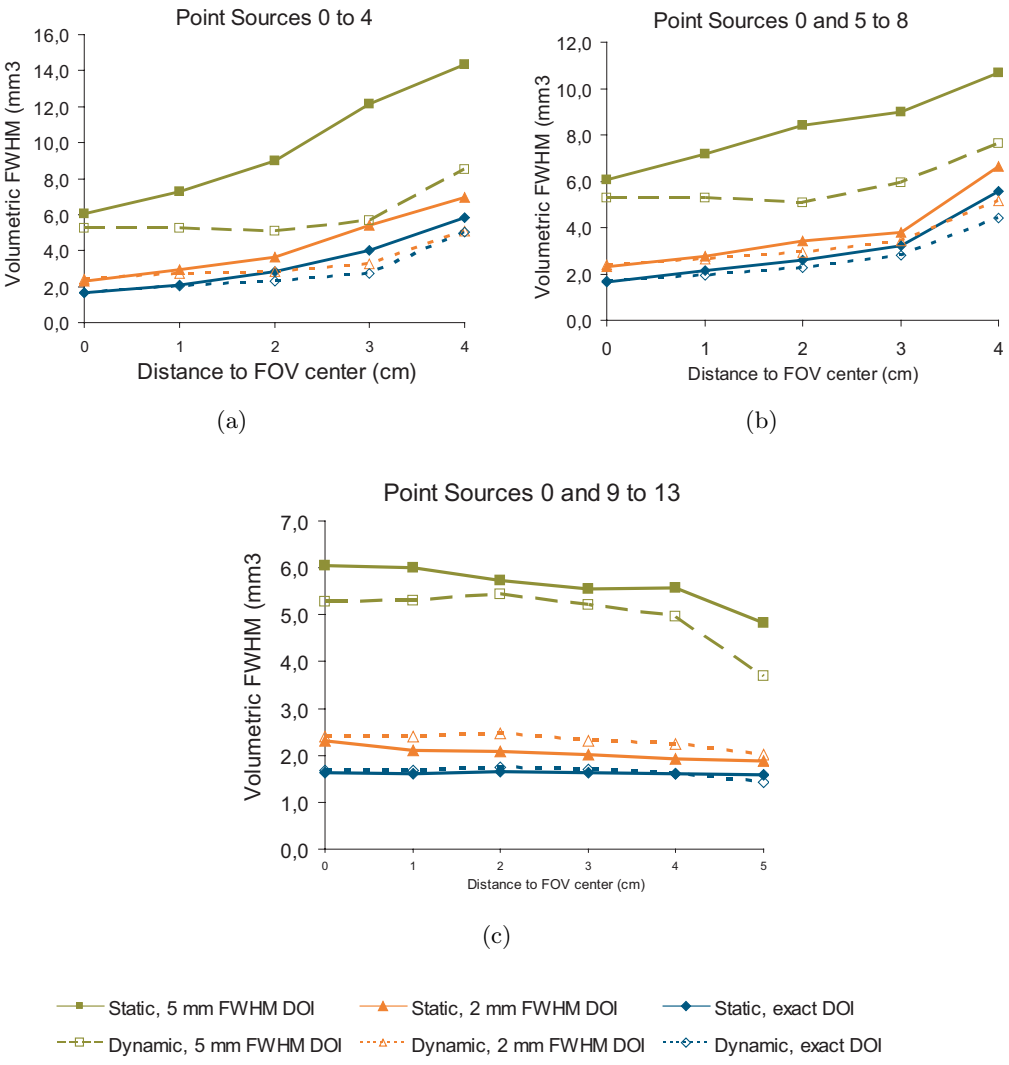

Figure 8.19: Comparison of the values of volumetric FWHM as a function of the distance to the center of the FOV, with static and dual angle simulated acquisitions and with different values for the DOI resolution (5 mm FWHM DOI resolution, 2 mm FWHM DOI resolution and exact DOI resolution).

In fact, regardless of the DOI resolution considered, the effect of the rotation in the spatial resolution is always more important for the point sources placed further away from the axis of rotation of the scanner. For this reason, the effect of rotation is weaker for the point sources that are placed along the axis of rotation of the scanner (point sources 0 and 9 to 13). The results for these point sources placed at off-center image planes indicate that, for a fixed DOI resolution, it does not seem to be advantageous to have a dual angle acquisition. However, this analysis is hindered by the fact that only point sources in the center of each plane are studied. Those conclusion would certainly be different if, for the studied planes, points placed in the edge of each plane were also considered.

8.4 Studies with the NCAT phantom

In this section the results of the studies that were performed with the anthropomorphic breast phantom simulated data will be presented. The goal of this work is to study the ability of the scanner to detect simulated lesions at different clinical scenarios. As described in Chapter 5, these studies were performed with the realistic geometry of the Clear−PEM scanner and used different clinical settings. Namely, these studies were performed with four different lesion diameters (3 mm, 5 mm , 7 mm and 10 mm) and with four different lesion-to-background ratios (13:1, 10:1, 5:1 and 4:1), for a five minute acquisition. The different lesion-to-background ratios considered correspond to different compositions of the breast, as explained in Chapter 5.

8.4.1 The sensitivity image

As it was explained in Chapter 6, the OS-EM algorithm used in STIR uses an image that represents the sensitivity of the scanner, the sensitivity image. This image is computed taking into account correcting factors for the degrading effects of tissue attenuation and of the differences in the detection efficiency of the several detection components of the scanner. When such information does not exist, the sensitivity image is build from an unitary sinogram.

The detector model used in the simplified scanner geometry assumed pixelized uniform detector heads. Therefore, normalization issues could be left aside. However, when the full simulation of the scanner was used, with the realistic scanner geometry, the non-uniformity in the detection efficiency of the scanner must be taken into account in the image reconstruction process. In fact, as it was explained in Chapter 5, the separation of the several detector elements of the Clear−PEM scanner, due to the space required by the electronics of the system, results in several gaps between contiguous detection elements. These gaps result in areas of low detection efficiency. If no correction is applied for this effect, the reconstructed images will reflect the existence of

such low detection efficiency areas. That effect is very clear when dealing with images with large areas of activity, such as the images of the NCAT Breast phantom, as can be seen in the uncorrected image of the NCAT breast phantom presented in Figure 8.20. The Monte Carlo simulation assumes that the uptake of FDG in the breast tissue is uniform. Therefore, the background tissue in the reconstructed image should appear as an uniform distribution of the number of counts. Instead, artifacts in the form of long stripes appear in the regions of the image that correspond to regions of lower sensitivity of the scanner, as can be observed in the uncorrected image. This degrading effect (as,

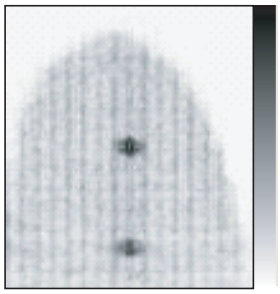

Figure 8.20: Uncorrected reconstructed image of the NCAT Breast phantom. The background region, that originally has constant activity, appears modulated due to the existence of regions of lower detection sensitivity in the scanner.

in fact, other effects that contribute to the non-uniformity in the detection efficiency) can be accounted for in the image reconstruction process in the form of normalization factors used to compute the sensitivity image.

The normalization correction methods are usually based on the definition of multiplicative factors that are applied to the number of counts in each separate detector crystal in the system [167, 168]. These factors, named normalization coefficients, can be factorized into separate components relative to different aspects that affect the scanner sensitivity. This approach to normalization correction is named component-based normalization. The computation of such components is performed with measures from an activity source that uniformly illuminates the entire FOV of the scanner.

A component-based normalization correction for the Clear−PEM scanner is being developed by one of the investigation teams in the consortium (IBILI - Coimbra) [169]. The normalization components will be computed from data acquired with a planar source placed at mid distance between the detector plates, in order to illuminate uniformly every detector element in the detector plates. A scheme of such a planar source positioned between the detector heads of the Clear-EM system can be seen in Figure 8.21.

However, such a measurement is not possible while the scanner is not assembled. Therefore, another means of correcting degrading effects due to the existing gaps between the detection elements must be used meanwhile. For the studies that were performed

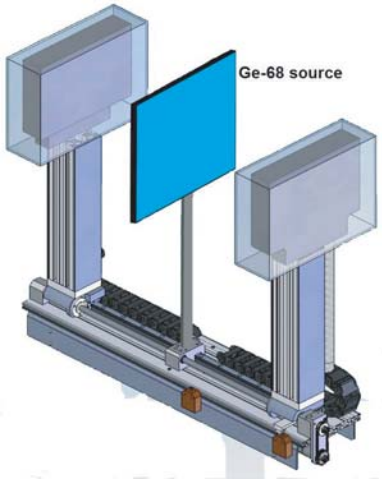

Figure 8.21: Planar source for the experimental determination of the normalization components. Adapted from [170].

with the NCAT Breast phantom simulation data the correction for the effect of the detector gaps in the reconstructed images was performed using a sensitivity image that was computed by Monte Carlo simulation. The surface plots of such an image can be seen in Figure 8.22. The effect of the gaps between the detector elements is patent in the irregular nature of these surface plots.

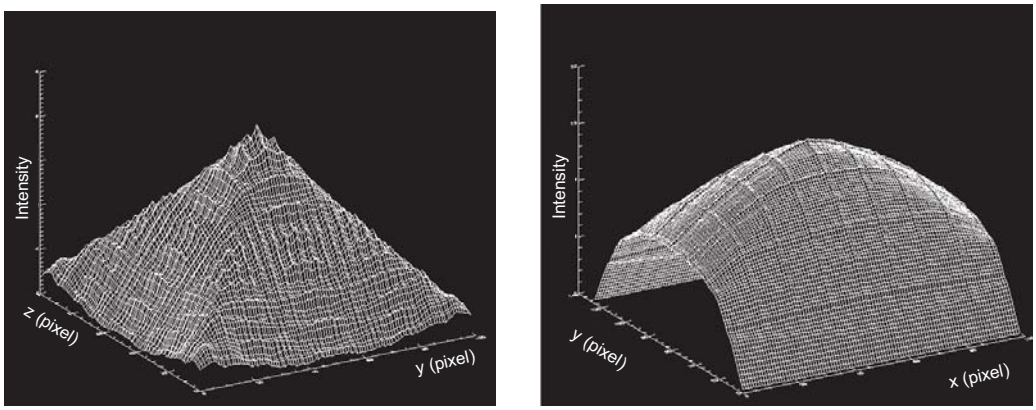

Figure 8.22: Surface maps of the sensitivity image calculated with Monte Carlo simulation techniques. The image on the right corresponds to the sum of all the axial planes. The image on the left corresponds to the sum of all the coronal planes

8.4.2 Methods

The images of the NCAT Breast phantom with the simulated lesions of four different diameters and with the four lesion-to-background ratios considered were reconstructed. The OS-EM algorithm available in STIR was used, with four subsets and no smoothing.

The dimensions of the reconstructed images were 99×99×127 voxels, each voxel with resolution 1.0×1.0×1.3 mm^3.
After a brief visual inspection of the images, several regions of interest (ROIs) were drawn either above the reconstructed lesions and over large background regions close to the lesions. The total and the mean number of counts inside the ROIs, as well as the standard deviation inside the background ROI were recorded for every iteration of every set of reconstructed images. An example of the ROIs that were used to perform the analysis is shown in Figure 8.23. The set of four ROIs that were drawn over the background regions were treated as a single ROI.

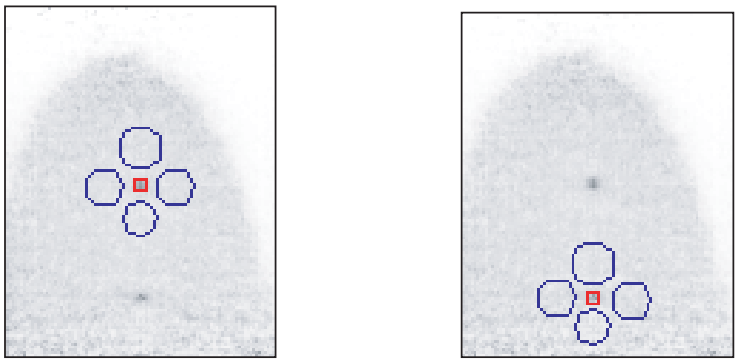

(a) (b)

Figure 8.23: Regions of interest used to perform the analysis of the NCAT breast phantom reconstructed images. The image on the left shows the ROIs that were used to study the centered lesion. The image on the right shows the ROIs that were used to study the off-centered lesion. The blue ROIs correspond to ROIs used to study the background. The red ROIs were used to study the lesion, in the presented case the 5 mm lesion.

The data recorded from the ROIs were used to compute three different figures of merit. The contrast (C) between the simulated lesions and the surrounding tissues in the reconstructed images was computed using the expression $C = (T - B)/B$, where T was the mean activity in the simulated spherical lesion ROI and B was the mean activity in the background region ROIs. The signal-to-noise (SNR) ratio was computed using the expression $SNR = (T - B)/\sigma_B$, where σ_B was the standard deviation of voxel values in the background ROI. The noise was computed as a coefficient of variation (CV) that was defined as $CV = \sigma_B/B$.

8.4.3 Results

The images presented in Figure 8.24 show the central coronal slice of the reconstructed images of the NCAT Breast phantom with the four considered lesion-to-background scenarios that correspond to different breast tissue types (L1=13:1, corresponding to a

predominantly fat breast tissue; L2=10:1, corresponding to fat breast tissue with some fibroglandular tissue; L3=5:1, corresponding to heterogeneous dense breast tissue; and L4=4:1, corresponding to extremely dense breast tissue, as explained in Chapter 5) and the 3 mm diameter lesion.

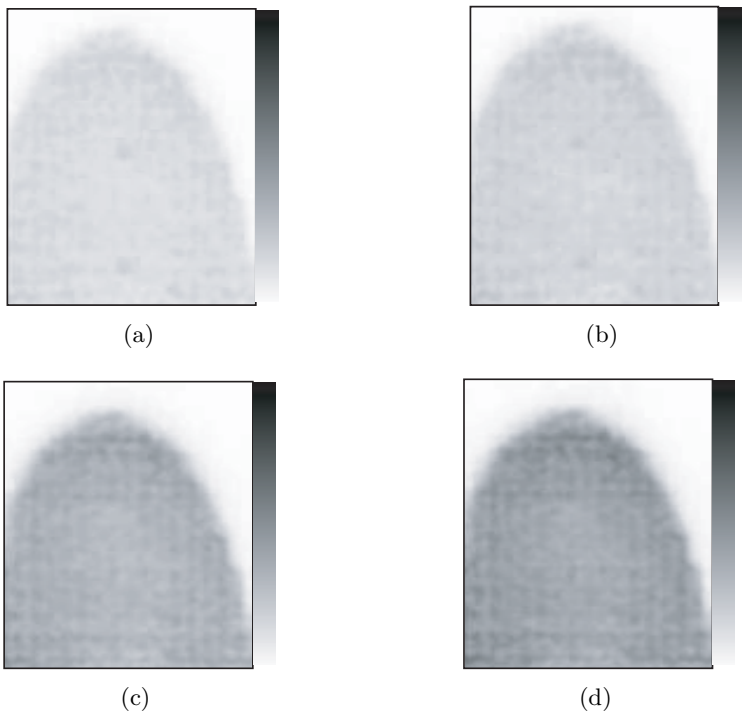

Figure 8.24: Central coronal slice of the reconstructed images of the NCAT Breast phantom with the 3 mm diameter lesions for the lesion-to-background (L:B) ratios (a) L1=13:1, (b) L2=10:1, (c) L3=5:1 and (d) L4=4:1.

Both centered and off-centered lesions can be faintly seen in the images that correspond to L1 and L2 (Figures 8.24 (a) and (b)). However, they can not be distinguished from the background regions in the case of L3 and L4. These images seem to indicate that the 3 mm lesions are not clearly recovered in all the simulated clinical settings. It remains to be seen, however, if an acquisition longer than 5 minutes improves the detectability of such small lesions. Due to the constraints imposed by the Monte Carlo simulation time, such an hypothesis was not tested. No further analysis was performed with the 3 mm diameter lesions.

The images presented in the following pages show the central coronal slice of the reconstructed images of the NCAT breast phantom with the 5 mm, 7 mm and 10 mm simulated lesions for the four considered breast uptake scenarios: L1=13:1 in Figure 8.25, L2=10:1 in Figure 8.26, L3=5:1 in Figure 8.27 and L4=4:1 in Figure 8.28. The plots of the profiles taken over a line that crosses the center of the lesions in the central slice of the image are shown below each reconstructed image slice.

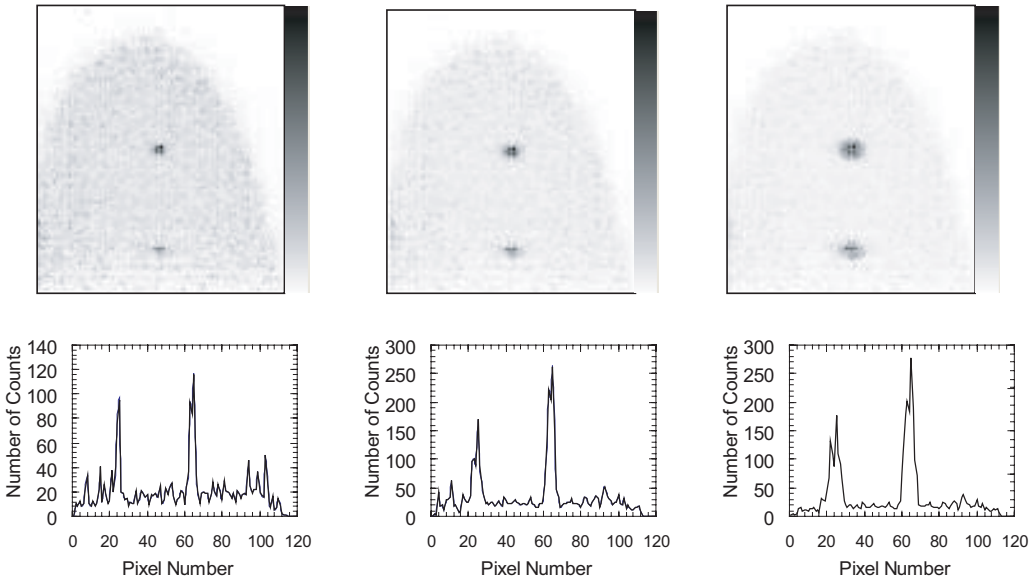

Figure 8.25: Central coronal slice of the reconstructed images of the NCAT Breast phantom with lesions for the lesion-to-background ratio L1=13:1 with the 5 mm (left), 7 mm (middle), and 10 mm (right) diameter lesion. Below each image are the profiles taken over a line that crosses the center of the lesions in the presented image slice.

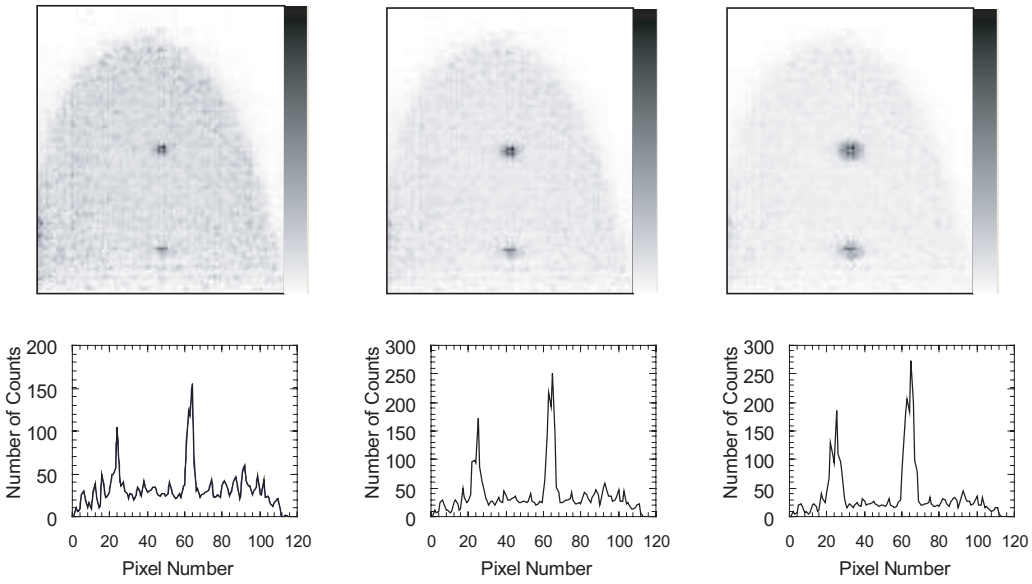

Figure 8.26: Central coronal slice of the reconstructed images of the NCAT Breast phantom with lesions for the lesion-to-background ratio L2=10:1 with the 5 mm (left), 7 mm (middle), and 10 mm (right) diameter lesion. Below each image are the profiles taken over a line that crosses the center of the lesions in the presented image slice.

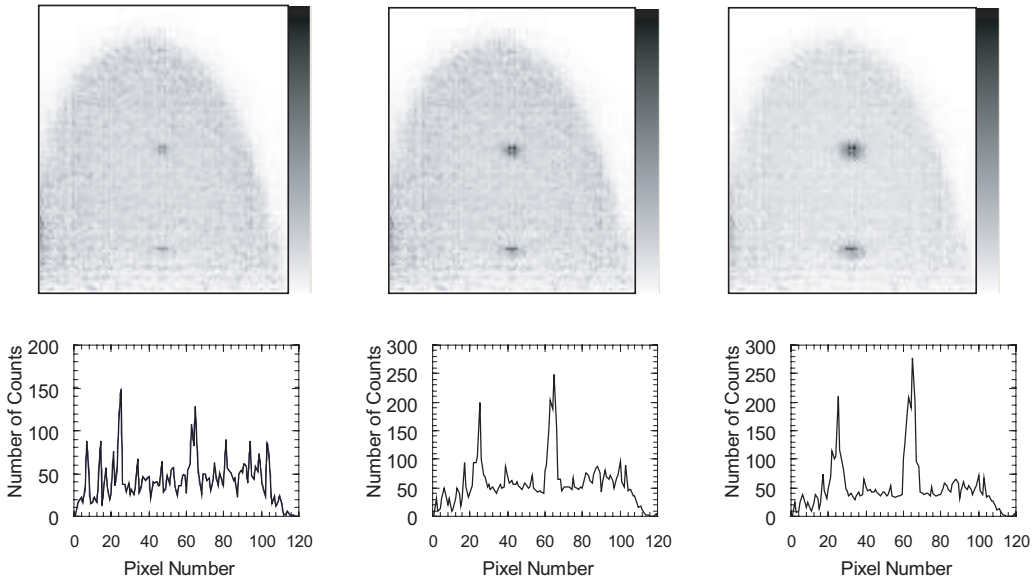

Figure 8.27: Central coronal slice of the reconstructed images of the NCAT Breast phantom with lesions for the lesion-to-background ratio L3=5:1 with the 5 mm (left), 7 mm (middle), and 10 mm diameter lesion (right). Below each image are the profiles taken over a line that crosses the center of the lesions in the presented image slice.

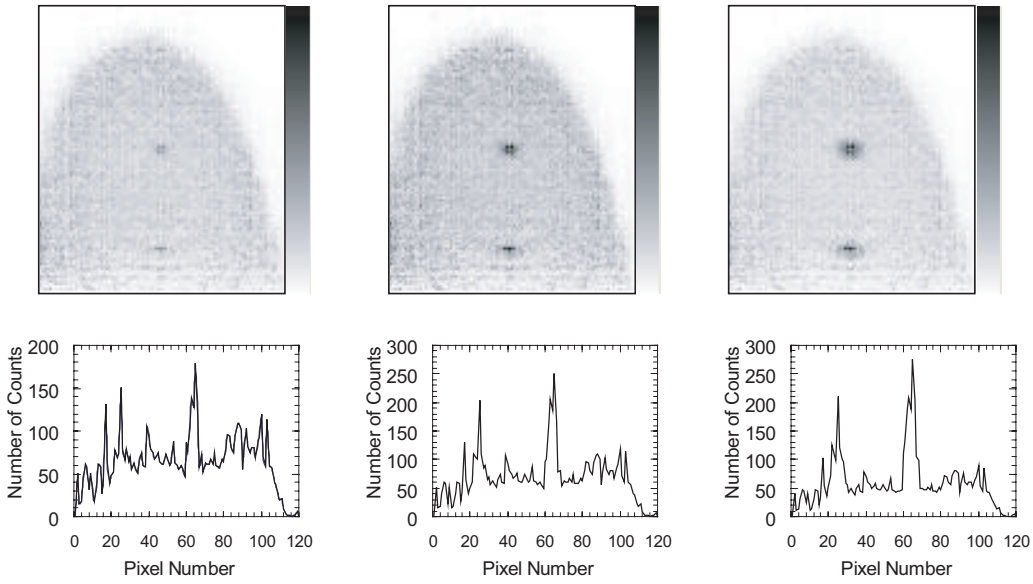

Figure 8.28: Central coronal slice of the reconstructed images of the NCAT Breast phantom with lesions for the lesion-to-background ratio L4=1:1 with the 5 mm (left), 7 mm (middle), and 10 mm diameter lesion (right). Below each image the profiles taken over a line that crosses the center of the lesions in the presented image slice are shown.

The visual inspection of these images shows that most of the lesions can be clearly distinguished from the background uniform region. The lesions with smaller diameter in the lower target-to-background ratio (5 mm lesion, L4, Figure 8.25) is the one that is less clearly distinguished.

The plots presented from Figure 8.29 to Figure 8.32 show the plots of the contrast between the simulated lesions and the normal tissue against the coefficient of variation measured both for the centered and the off-centered lesions in all the lesion-to-background ratios considered. Each point in these plots corresponds to an iteration in the image reconstruction process. The line representing the simulated contrast in each situation is also drawn.

The plots show that, for all the situations presented, the contrast tends to achieve a given value, usually not far from the simulated one, and does not change afterward. As a convergence criteria, a variation of less that 1% in the values of the contrast in the remainder iterations was considered. The contrast values achieved for each target-to-bakground ratio tend to increase with increasing lesion diameter. This means that the contrast achieved between the lesions and the surrounding tissues is closer to the simulated value for the 10 mm lesion than for the 5 mm lesion. This is true either for the centered and for the off-centered lesions. However, for a same lesion diameter and for a same L:B, the contrast values achieved by the off-centered lesions are consistently lower than the contrast values achieved by centered lesions. Also, for a same iteration, the noise measured for the centered lesion is always lower than the noise measured for the off-centered lesion. We can verify this by noting that the horizontal scale in the plots presented (coefficient of variation) is always equal or less than 1.0 for the centered lesion whereas is between 1.6 and 2.0 for the off-centered lesions. This is consistent with the fact that the region closer to the chest wall presents as more granulated in the reconstructed images, as can be observed in Figures from 8.25 to 8.28. This is most problably due to the low statistics presented by the sensitivity image in that region, as can be observed in the Figure 8.22. In fact, such a granulated region does not appear in the uncorrected images, such as the one shown in Figure 8.20.

Figure 8.33 to Figure 8.36 shows the plots of the signal-to-noise ratio against contrast for every lesion diameter studied and for every lesion-to-background ratio considered. The line of the simulated contrast is also shown in the plots as a vertical blue line. The line of SNR=5, which is also drawn in the plots, is the conventional line of detectability used in analog radiology, and that as also been used in Positron Emission Mammography images [92, 76]. Lesions for which $T - B > 5\sigma_B$ can be considered 100% visible.

The shape of the presented plots indicates that, usually, the initial iteration produces a low contrast, low SNR image. Afterward, contrast tends to increase as the signal-to-noise ratio increases, until the curves reach an inflexion point. After this point, the signal-to-noise ratio begins to decrease, as the noise in the images keep increasing,

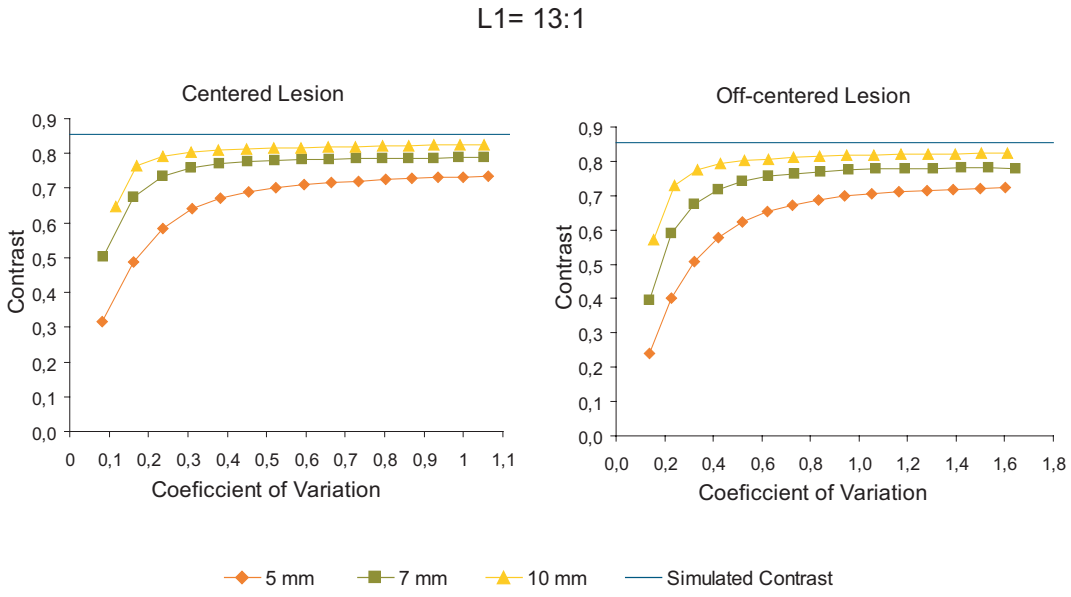

Figure 8.29: Plots of the contrast against noise measured as a Coefficient of Variation for the reconstructed images of the NCAT Breast Phantom with the 5 mm, 7 mm and 10 mm centered and off-centered simulated lesions for the lesion-to-background ratio L1=13:1. The blue line represents the simulated contrast.

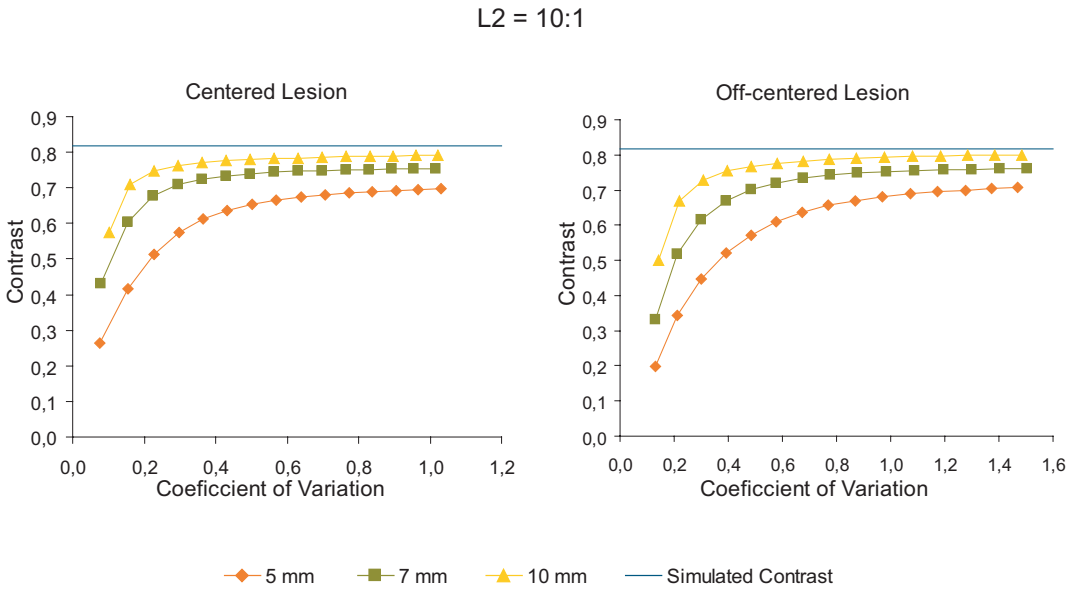

Figure 8.30: Plots of the Contrast against noise measured as a Coefficient of Variation for the reconstructed images of the NCAT Breast Phantom with the 5 mm, 7 mm and 10 mm centered and off-centered simulated lesions for the lesion-to-background ratio L2=10:1. The blue line represents the simulated contrast.

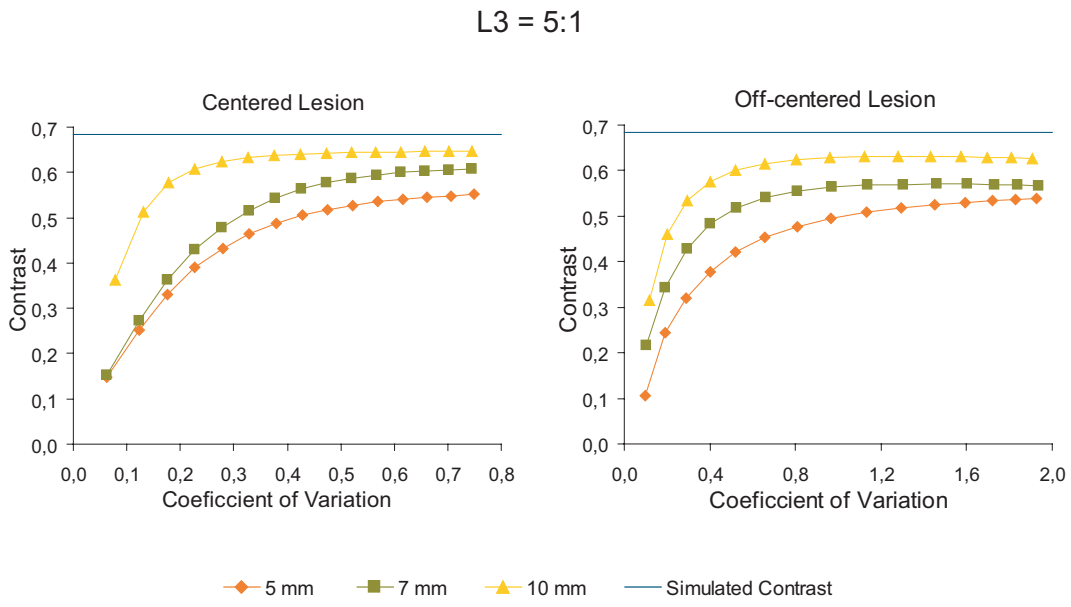

Figure 8.31: Plots of the Contrast against noise measured as a Coefficient of Variation for the reconstructed images of the NCAT Breast Phantom with the 5 mm, 7 mm and 10 mm centered and off-centered simulated lesions for the lesion-to-background ratio L3=5:1. The blue line represents the simulated contrast.

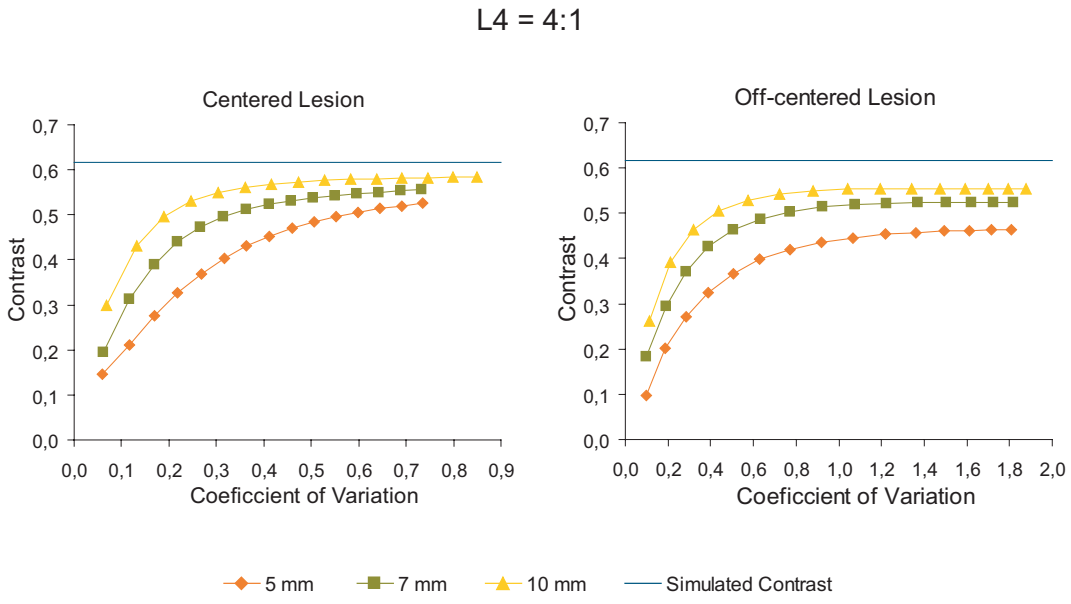

Figure 8.32: Plots of the Contrast against noise measured as a Coefficient of Variation for the reconstructed images of the NCAT Breast Phantom with the 5 mm, 7 mm and 10 mm centered and off-centered simulated lesions for the lesion-to-background ratio L4=4:1. The blue line represents the simulated contrast.

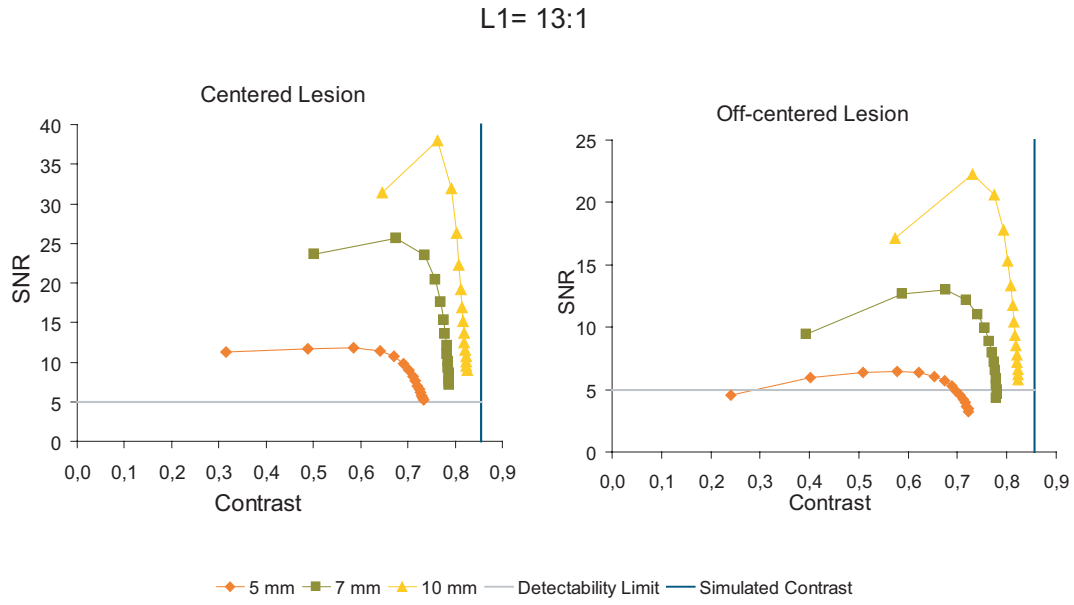

Figure 8.33: Plots of the values of the signal-to-noise ratio against Contrast for the reconstructed images of the NCAT Breast Phantom with the 5 mm, 7 mm and 10 mm centered and off-centered simulated lesions for the lesion-to-background ratio L1=13:1. The detectability limit appears in the plots as an horizontal gray line and the simulated contrast appears as a vertical blue line.

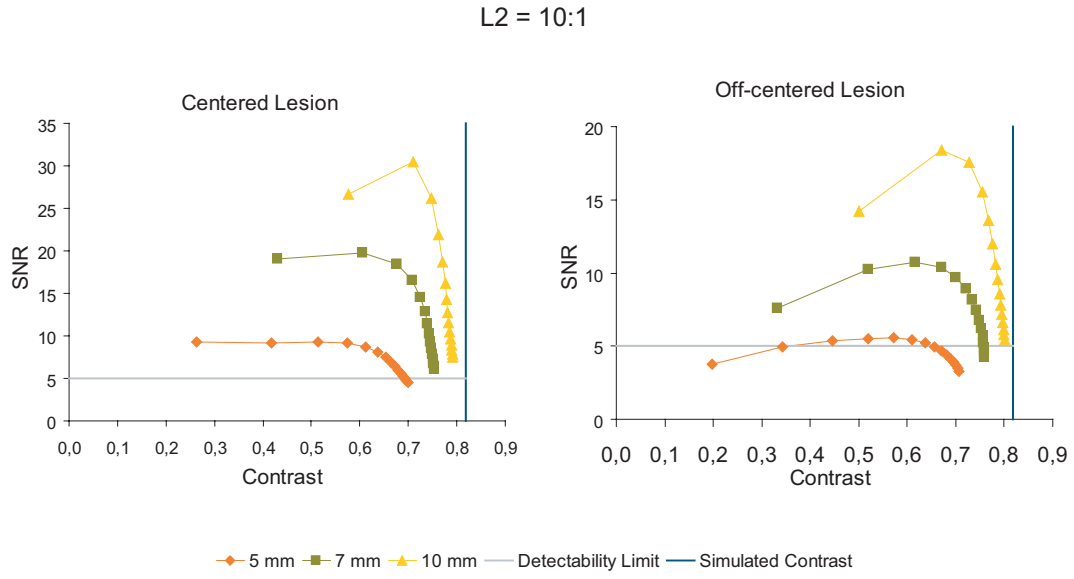

Figure 8.34: Plots of the values of the signal-to-noise ratio against Contrast for the reconstructed images of the NCAT Breast Phantom with the 5 mm, 7 mm and 10 mm centered and off-centered simulated lesions for the lesion-to-background ratio L2=10:1. The detectability limit appears in the plots as an horizontal gray line and the simulated contrast appears as a vertical blue line.

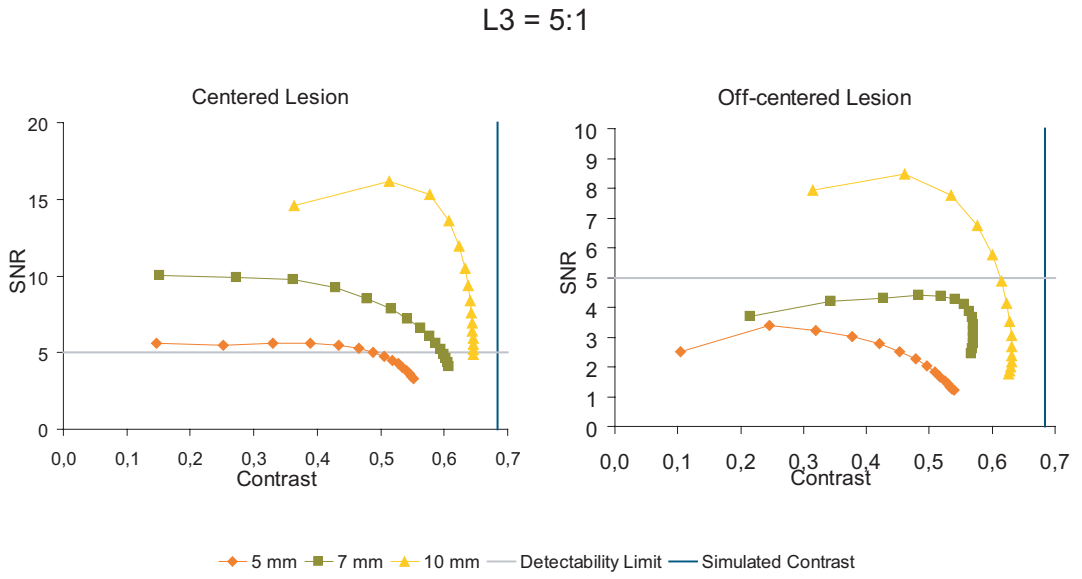

Figure 8.35: Plots of the values of the signal-to-noise ratio against Contrast for the reconstructed images of the NCAT Breast Phantom with the 5 mm, 7 mm and 10 mm centered and off-centered simulated lesions for the lesion-to-background ratio L3=5:1. The detectability limit appears in the plots as an horizontal gray line and the simulated contrast appears as a vertical blue line.

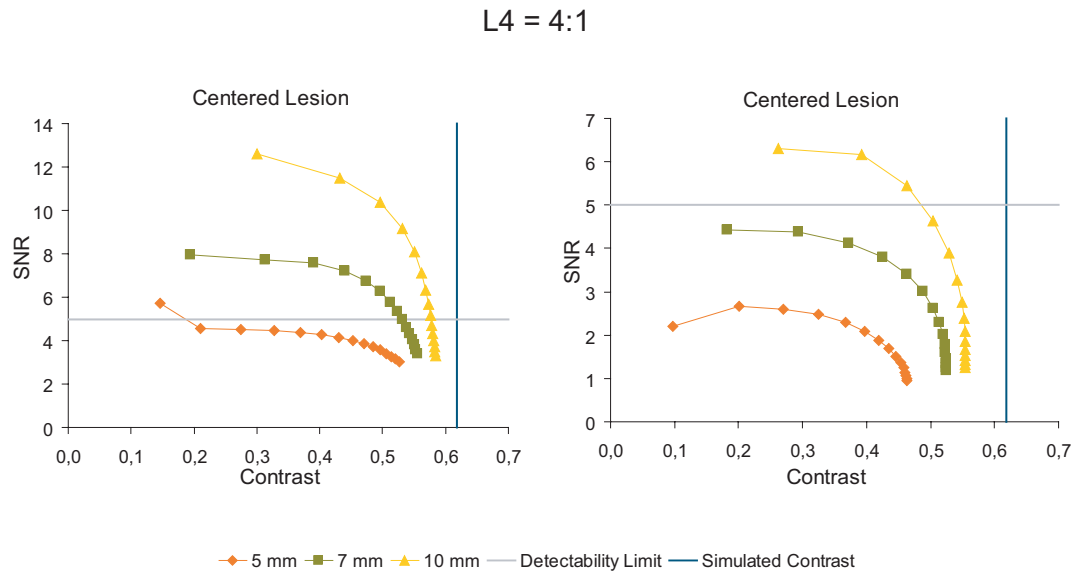

Figure 8.36: Plots of the values of the signal-to-noise ratio against Contrast for the reconstructed images of the NCAT Breast Phantom with the 5 mm, 7 mm and 10 mm centered and off-centered simulated lesions for the lesion-to-background ratio L4=4:1. The detectability limit appears in the plots as an horizontal gray line and the simulated contrast appears as a vertical blue line.

according to the characteristics of the image reconstruction algorithm used. In fact, as it was already stressed, and as it was verified in the plots of the contrast vs coefficient of variation previously presented, the increase in image noise as the iterative process proceeds is a well known characteristic of the ML based iterative image reconstruction algorithms. Meanwhile, as the SNR values drop, the contrast values tend to reach a constant value, which results in a line close to the vertical in the SNR vs Contrast plots. These points in the plots correspond to the iterations for which convergence, as defined before, was already reached. Visually, the iteration of convergence in the one corresponding to the point in the plot where this vertical trend of the curve starts. Comparing in a same plot the several curves that correspond to the different lesion diameters, it can be seen that the convergence is usually reached first for the images with the biggest simulated lesion, and last by the images with the smallest simulated lesion. Also, the point of convergence tends to be reached later as the target-to-background ratio considered decreases.

The plots presented show that, for two highest values of L:B (L1, L2), for both centered and off-centered lesions, most of the lesions converge to values of contrast that, when reached, correspond to values of SNR which are above the line of 100% visibility. This is not verified, however, for the case of the 5 mm off-centered lesion, which, for both cases, converges to contrast values that correspond to SNR values below that limit.

In the case of the lower values of L:B (L3, L4), only the 7 mm and 10 mm centered lesion tend to converge to values of contrast that correspond to SNR values above the 100% detectability line. The 5 mm off-centered lesion converges to values that are slightly below that value. As for the off-centered lesions, for these L:B, they tend to converge to contrast values that correspond to SNR values significantly below the 100% detectability line. However, according to the images that are presented at the beginning of this section, the lesions with the considered diameters in the lesion-to-background rations studied are all observable by visual inspection. This seems to indicate that the SNR=5 criterion, originating from conventional radiology, might not be a good detectability criterion for emission tomography images. Keeping this reservation in mind, we still will use this criterion as a reference for the quality of the images with respect to its signal-to-noise ratio.

8.4.4 Discussion

The plots presented in Figure 8.37 and in Figure 8.38 summarize the results obtained with the NCAT Breast phantom studies.

The plots in Figure 8.37 represent the trends of the contrasts recovery against lesion diameter, both for the centered and for the off-centered lesions, and for all the lesion-to-background ratios considered. The contrast recovery was computed as the percentage of simulated contrast reached at convergence, with the convergence criterion defined

above. As it can be seen in these plots, the contrast recovery values obtained in these studies are always high, even for the smallest diameter off-centered lesion. These plots highlight the fact that the contrast recovery depends more strongly on the lesion diameter and on its position than it depends on the L:B considered. In fact, for a given diameter and position, the contrast recovery is approximately the same for all the L:B. The plots also highlight that the contrast recovery increases with increasing lesion diameter and that, for a same lesion diameter, contrast recovery is higher for the centered lesion.

The plots in Figure 8.38 represent the trends of the signal-to-noise ratio after convergence against lesion diameter, for both the centered and the off-centered lesion, and for all the lesion-to-background ratios considered. These plots summarize what was previously devised: SNR values for the centered lesion are almost always higher than the 100% detectability limit. The exception is the smaller lesion diameter, whose SNR after convergence is slightly below that line. For the off-centered lesion, the SNR depends strongly on both the lesion diameter and on the L:B, that is, on the type of breast tissue. Lesions of 7 mm and 10 mm diameter have SRN values that indicate good visibility for high L:B. For lower L:B (L3=5:1, L4=4:1, which corresponds to dense or very dense fibroglandular tissues) the presented results indicate that the visibility of the 7 mm and the 10 mm diameter lesion, here modeled as the SNR, might be compromised, since its values are low or very low (3.0 and 1.8 for the 7 mm lesion, respectively, and 3.5 and 2.4 for the 10 mm lesion, respectively). Regarding the off-centered 5 mm lesion, independently of the L:B considered, the presented results indicate that its visibility might always be low or very low (between 1.1 and 4.2).

8.5 Conclusions

In this chapter we have presented the studies that were performed for the Clear−PEM scanner with the 3D OS-EM image reconstruction algorithm and with simulated data both using geometrical and anthropomorphic phantoms.

The results presented show that, with the foreseen DOI resolution of 2 mm FWHM, with the standard acquisition geometry described previously and with the 3D OS-EM image reconstruction algorithm, the Clear−PEM scanner is expected to provide images which have an approximately uniform resolution of about 2 mm along the entire FOV.

The studies performed with the NCAT breast phantom and the simulated lesions allowed to estimate the expected capability of the Clear−PEM scanner to detect lesions with different diameters and at two different locations, in different clinical scenarios. We have seen that, under the simulated acquisition conditions, lesions with diameters as low as 5 mm can be clearly detected in breasts that are mostly or entirely fat, with very high contrast between the lesion and the background tissue. For breasts that are

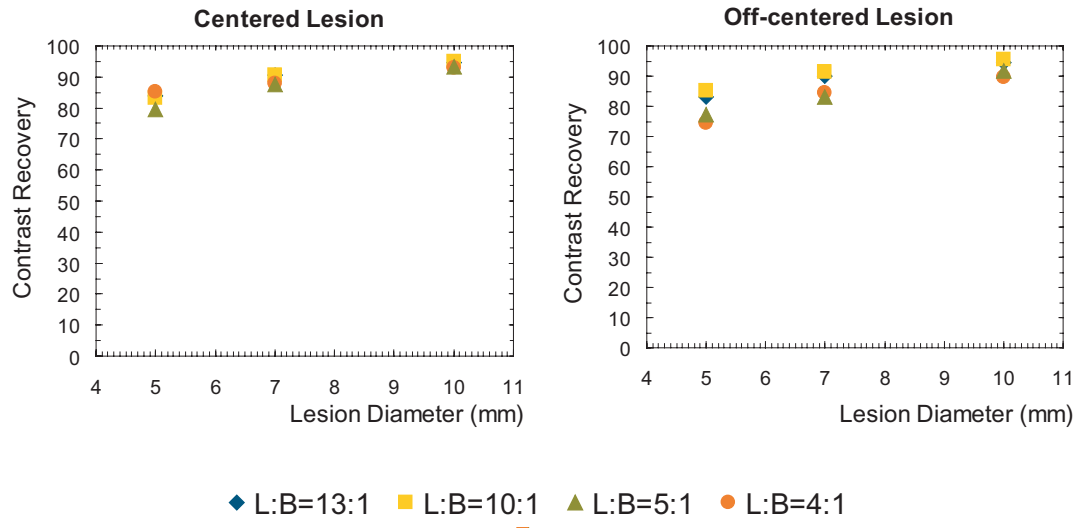

Figure 8.37: Trends of the contrast recovery against lesion diameter measured for the centered and for the off-centered simulated lesions in the NCAT breast phantom, for the four lesion-to-background ratios considered.

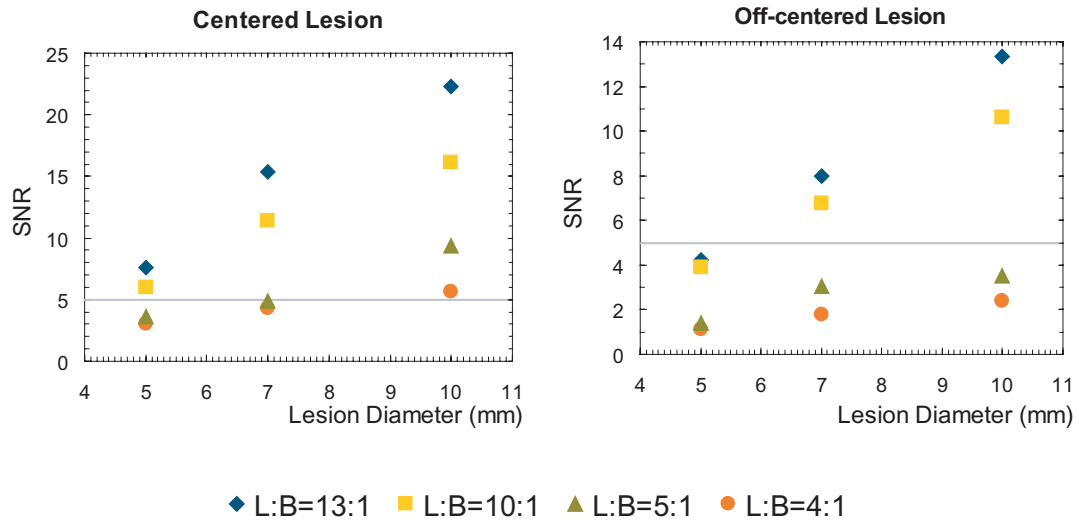

Figure 8.38: Trends of the signal-to-noise ratio against lesion diameter measured for the centered and for the off-centered simulated lesions in the NCAT breast phantom, for the four lesion-to-background ratios considered. The conventional detectability line is drawn in gray in the plots.

more rich in dense fibroglandular tissues, the capacity of detecting the lesions which are not centered becomes somewhat compromised. These results are, however, hindered by the low statistics of the sensitivity image in the region close to the chest wall, as it was already stressed. Moreover, it remains to be studied the impact of longer, yet clinically feasible, acquisition times on the Figures of Merit studied.

Another means of trying to improve some of the Figures of Merit studied consists on using alternative image reconstruction algorithms, such as the Bayesian algorithms that were described in Chapter 4. In the next chapter we will present the studies that were performed with a Bayesian image reconstruction algorithm on the Clear−PEM scanner simulation data.

Chapter 9

Bayesian Image Reconstruction for the Clear−PEM Scanner

9.1 Introduction

In the last section of the previous chapter we have presented the studies that were performed with the 3D OS-EM image reconstruction algorithm and the NCAT Breast phantom simulated data. Those studies showed, among other things, that the image noise developed in the regions closer to the chest wall prevented a good visibility of the simulated lesions in that region.
As it was stressed in Chapter 4, the production of noisy images is a characteristic of the image reconstruction algorithms based on the Maximum Likelihood estimation, such as the OS-EM algorithm. We have also seen that the use of Bayesian image reconstruction algorithms allows to effectively control the noise in the reconstructed images. The Median Root Prior (MRP) is one prior that allows obtaining high quality images both in what concerns noise and edge preserving.
In this chapter we will present the studies and the results that were obtained using the Maximum *a Posteriori*-One Step Late algorithm (MAP-OSL) with the Median Root Prior to reconstruct Monte Carlo simulated data for the Clear−PEM scanner.

9.2 Methods

The simulated data that was used to test the image reconstruction with the Bayesian algorithm was obtained for the Chain Phantom and for the NCAT Breast Phantom, under the same acquisition scenario that was described in the previous chapters. As previously, the NCAT Breast phantom was used together with the simulated spherical lesions of 5 mm, 7 mm and 10 mm in diameter, placed at the two different axial

locations, and for different simulated contrast levels between the lesions and the background tissues.
The analysis of reconstructed images from the Chain Phantom data allowed evaluating image spatial resolution for the different prior weights considered. As before, spatial resolution was computed as the FWHM of Gaussian fits to profiles taken over the reconstructed point sources in the phantoms.
Analysis of the NCAT Breast Phantom reconstructed images allowed to evaluate the trade-off between contrast, noise and signal-to-noise ratio (SNR) in images reconstructed with different prior weights. Contrast, SNR and noise were all computed using Regions of Interest (ROI) analysis. The definitions of contrast, SNR and noise, which was modeled as a coefficient of variation, were the same as the ones used in the previous chapter.
All simulated data were organized in 3D sinograms. Data were reconstructed with the Ordered-Subsets Maximum a Posterior - One Step Late algorithm available in STIR (OS-MAP-OSL) using the Median Root Prior. The prior weights (β) used were 0 (corresponding to OS-EM reconstruction), 0.1, 0.2 and 0.3. The spatial size of the median mask used was 3x3x3 pixels, the smallest possible. All the reconstructions were performed using 4 subsets. The sensitivity correction was performed using a Monte Carlo based sensitivity image that accounted for the presence of gaps between the detection elements, as explained in Chapter 8.

9.3 Results

9.3.1 Chain Phantom

Figure 9.1 shows the central coronal and the central axial slices of the Chain Phantom reconstructed images with OS-EM and with the Bayesian algorithm with the prior weights used, $\beta = 0.1$, $\beta = 0.2$ and $\beta = 0.3$.
The values of FWHM along the three main axis obtained after convergence for the β parameters used are presented in Table 9.1. Values are presented for the point sources of the Chain Phantom numbered as 0, 3, 7 and 11, as indicated in Chapter 5. Point source 0 is at the center of the Field of View (FOV). Point sources 3, 7 and 11 are placed at 3 cm from the center of the FOV in the central axial plane (point sources 3 and 7) and in the central coronal plane (point source 11).
The values presented show that, as expected, the higher the value used for the β parameter, the higher is the degradation of the spatial resolution in the reconstructed images. This degradation is specially pronounced in the axial component of the spatial resolution. For the transaxial component of the resolution, if the prior weight is not too high, resolution values are still below 2.5 mm close to the FOV periphery.

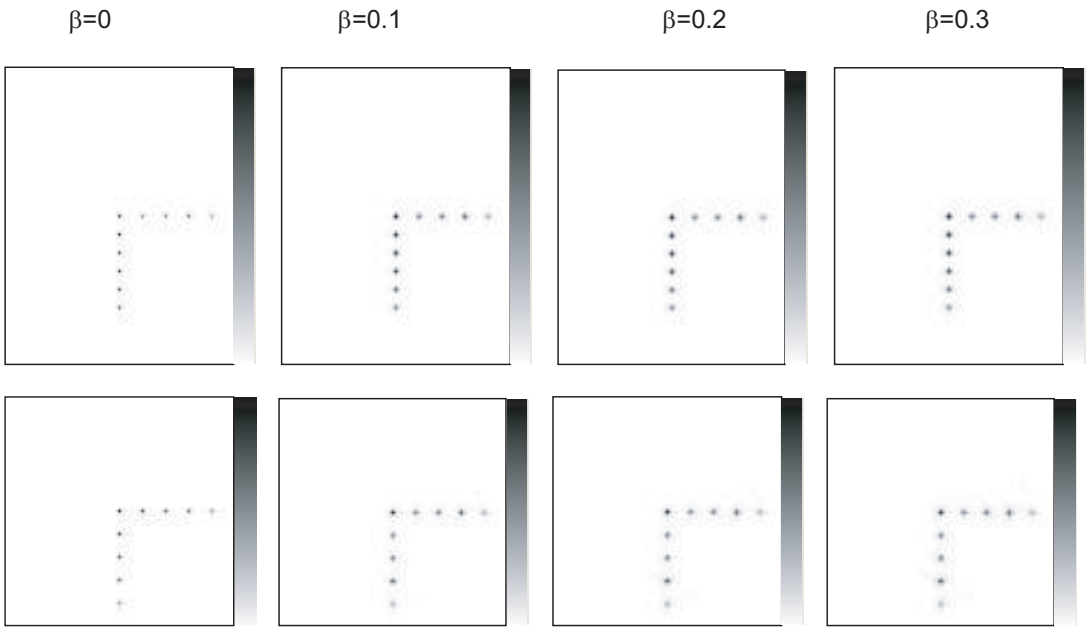

Figure 9.1: Central sagittal slices (above) and central axial slices (below) of the reconstructed images of the Chain Phantom with prior weights $\beta = 0$ (OS-EM), $\beta = 0.1$, $\beta = 0.2$ and $\beta = 0.3$.

Table 9.1: FWHM (mm^3) for the Chain Phantom images reconstructed with different prior weights (β).

β	Point Source 0	Point Source 3	Point Source 7	Point Source 11
0	1.3x1.3x1.4	1.2x1.5x1.8	1.5x1.3x1.7	1.3x1.3x1.4
0.1	1.8x1.8x2.7	1.9x2.2x2.8	2.3x1.9x2.9	1.8x1.8x2.5
0.2	2.0x1.9x2.8	2.1x2.5x3.1	2.5x2.1x3.0	2.0x2.0x2.7
0.3	2.1x2.1x2.9	2.2x2.7x3.2	2.6x2.2x3.1	2.1x2.1x2.8

9.3.2 NCAT Breast Phantom

Figures from Figure 9.2 to Figure 9.5 present the central coronal slice of the reconstructed images of the NCAT Breast Phantom with the simulated lesions reconstructed with the considered weights of the prior and the OS-MAP-OSL algorithm. Below each image is presented the profile taken along a line that passes through the center of both centered and off-centered lesions. Images in Figure 9.2 correspond to the lesion-to-background ratio L1=13:1, in Figure 9.3 to the lesion-to-background ratio L2=10:1, in Figure 9.4 to the lesion-to-background ratio L3=5:1 and in Figure 9.5 to the lesion-to-background ratio L4=4:1.

The images and plots show that the increase in the prior weight results in an increased smoothness of the image but also in a decrease in the peak-to-valley ratio of the lesion

profiles. It is also observed in the images that a slight distortion that can be observed in the lesion closer to the chest wall in the images reconstructed with OS-EM (β=0, images in the first column, last row in figures from Figure 9.2 to Figure 9.5) can not be observed in the images reconstructed with the Bayesian algorithm.

The plots presented in Figure 9.6 to Figure 9.9 show the trends in the contrast between the lesion and the background tissues against noise, for the 5 mm, 7 mm and 10 mm centered and off-centered lesions in the NCAT Breast Phantom, for all the prior weights considered. Figure 9.6 presents the plots for the case of lesion-to-background ratio L1=13:1, Figure 9.7 for the case of L2=10:1, Figure 9.8 for the case of L3=5:1 and Figure 9.9 for the case of L4:4:1. The line representing the simulated contrast is also shown in those plots.

These plots show that, independently of the contrast levels simulated or of the lesion size considered, image reconstruction with OS-EM develops significantly higher noise levels than image reconstruction with the Bayesian method. In fact, the coefficient of variation for the images reconstructed with the Bayesian algorithm is never above 0.3, while the coefficient of variation for the images reconstructed with OS-EM can easily reach values above 1.0, especially in the region closer to the chest wall. However, the values of contrast measured in the images reconstructed with the Bayesian algorithm are always lower than the contrast values measured in the images reconstructed with OS-EM.

Figures from Figure 9.10 to Figure 9.11 present the plots of the signal-to-noise ratio against contrast for the centered and off-centered simulated lesions with 5 mm, 7 mm and 10 mm diameter, for all the prior weights considered. Figure 9.10 presents the plots for the lesion-to-background ratio L1=13:1, Figure 9.11 presents the plots for L2=10:1, Figure 9.12 presents the plots for L3=5:1 and Figure 9.13 presents the plots for L4=4:1.

Usually, during the first iterations, the SNR increases as the contrast increases, but such evolution is much more pronounced for the Bayesian reconstructed images than for the images reconstructed with OS-EM. In fact, for the OS-EM reconstructed lesions, it is common that, during the first iterations, the contrast increases but the SNR remains about constant. For higher iteration numbers, and for OS-EM, the SNR tends to decrease sharply, while the contrast remains about constant. Regarding the Bayesian reconstructed images, this behavior is also observable, but not always. For instance, for the 5 mm diameter lesion, and for the lesion-to-background ratios L2, L3 and L4 (top rows of Figures 9.11, 9.12 and 9.13) by the time the iterative process is stopped, the SNR values of the images reconstructed with the Bayesian algorithm is still increasing, whatever the prior weight considered. The same happens for the contrast, although not in such a pronounced way. In other cases this behavior is observable only for the higher prior weights used. This happens, for instance, for the 7 mm and

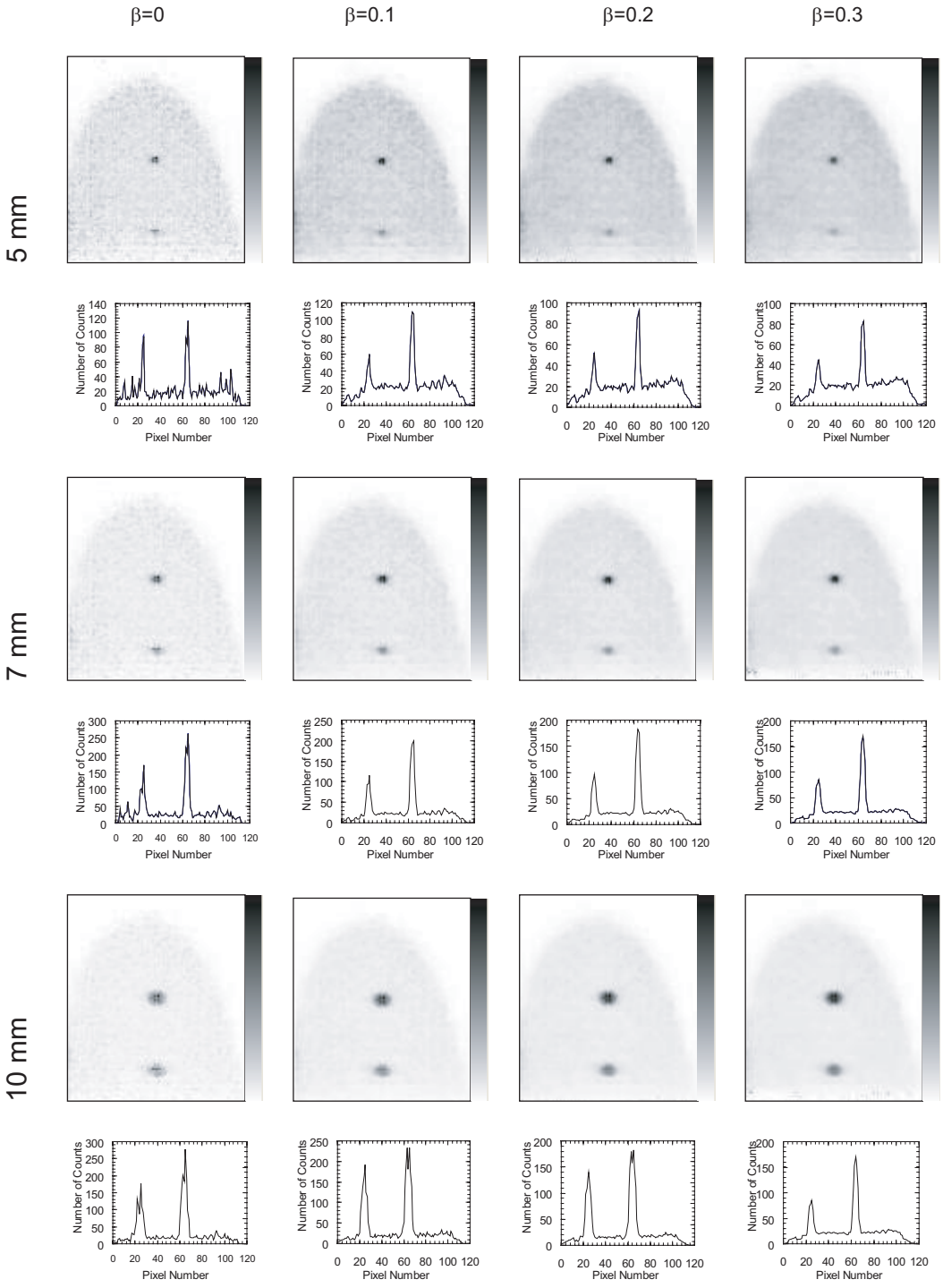

Figure 9.2: Central coronal slices of the reconstructed images of the NCAT Breast phantom with the 5 mm, 7 mm and 10 mm diameter simulated lesions and lesion-to-background ratio L1=13:1. Below each image is presented the profile taken over a line that crosses the two lesions.

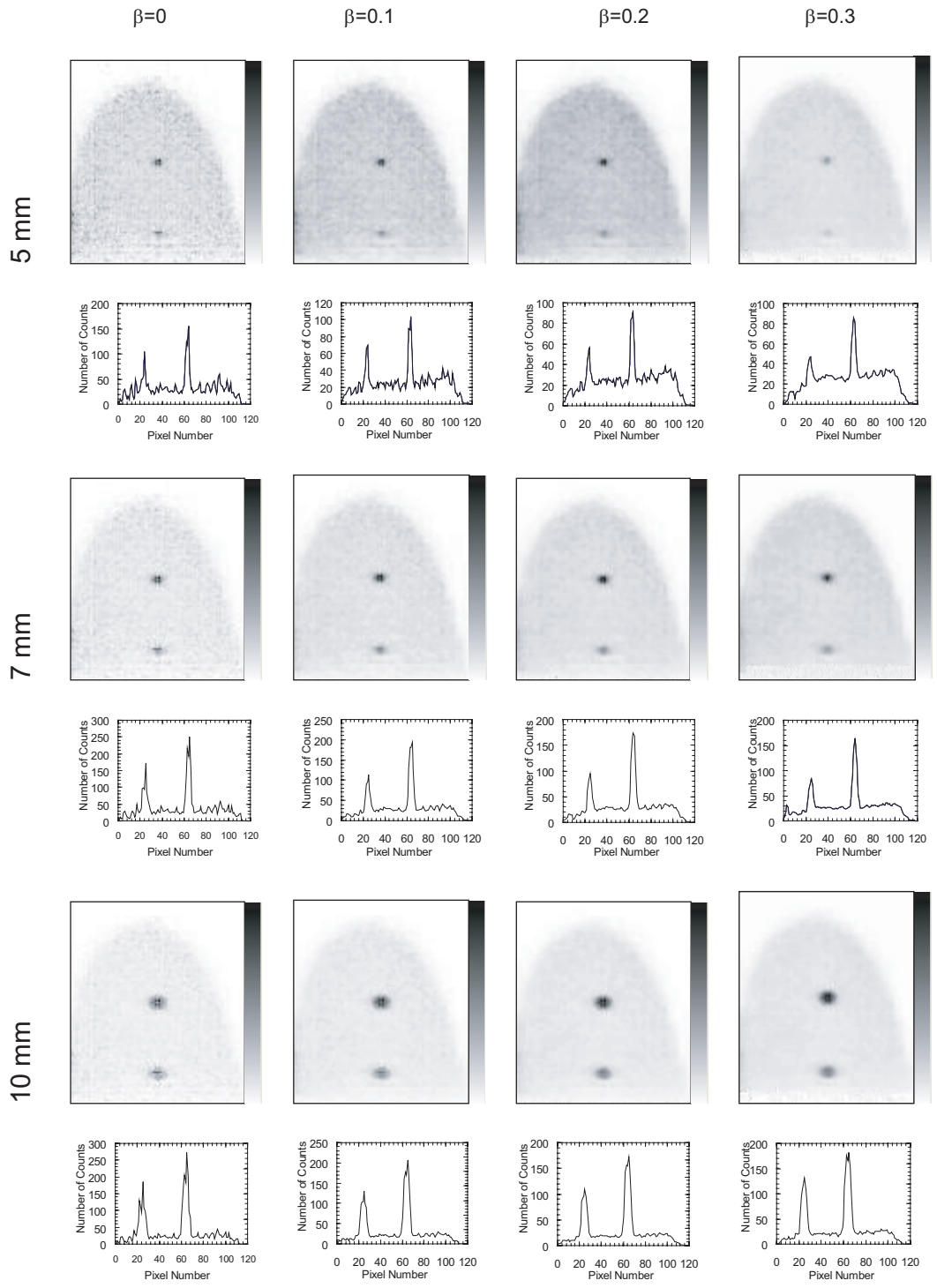

Figure 9.3: Central coronal slices of the reconstructed images of the NCAT Breast phantom with the 5 mm, 7 mm and 10 mm diameter simulated lesions and lesion-to-background ratio L2=10:1. Below each image is presented the profile taken over a line that crosses the two lesions.

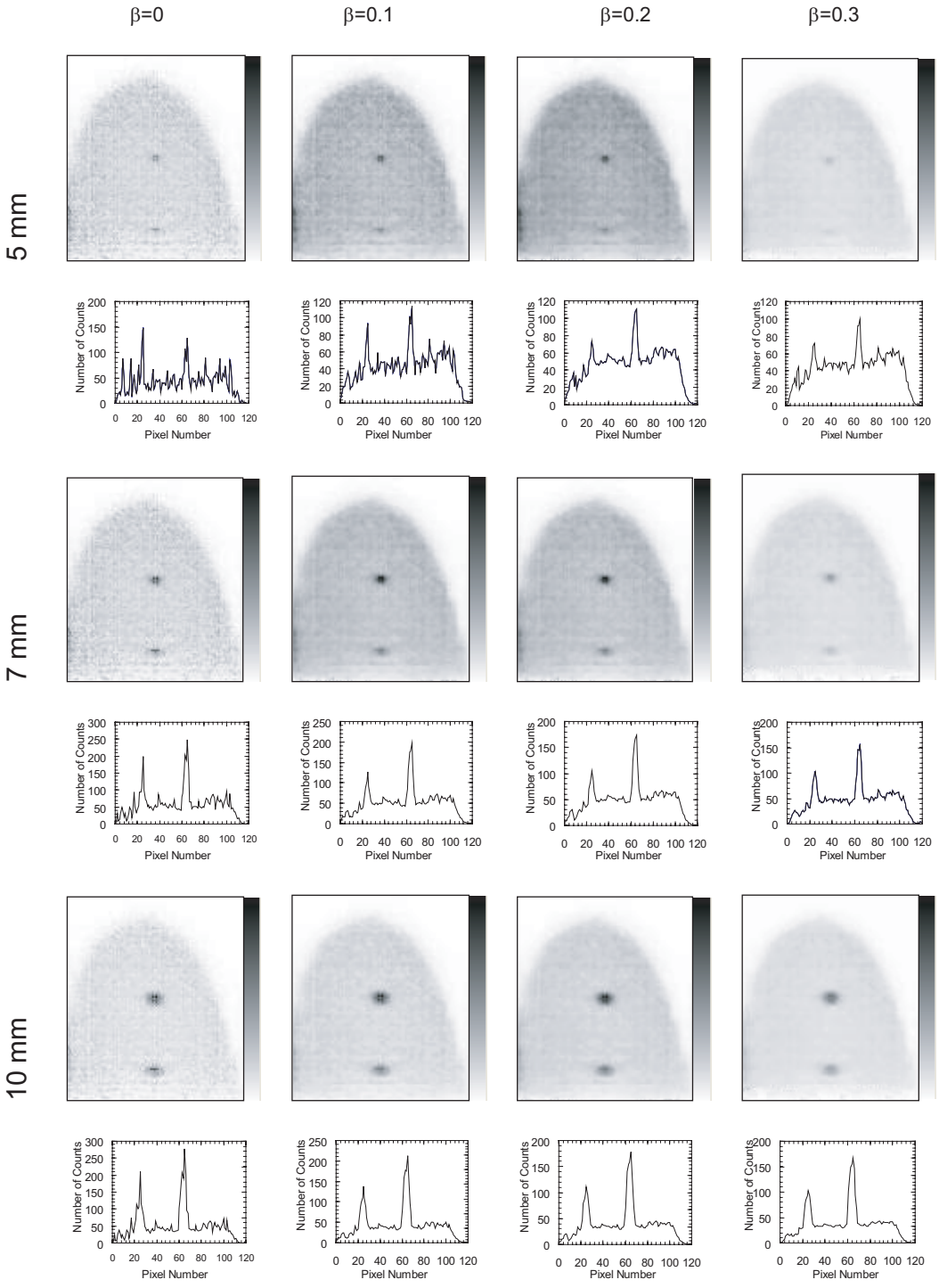

Figure 9.4: Central coronal slices of the reconstructed images of the NCAT Breast phantom with the 5 mm, 7 mm and 10 mm diameter simulated lesions and lesion-to-background ratio L3=5:1. Below each image is presented the profile taken over a line that crosses the two lesions.

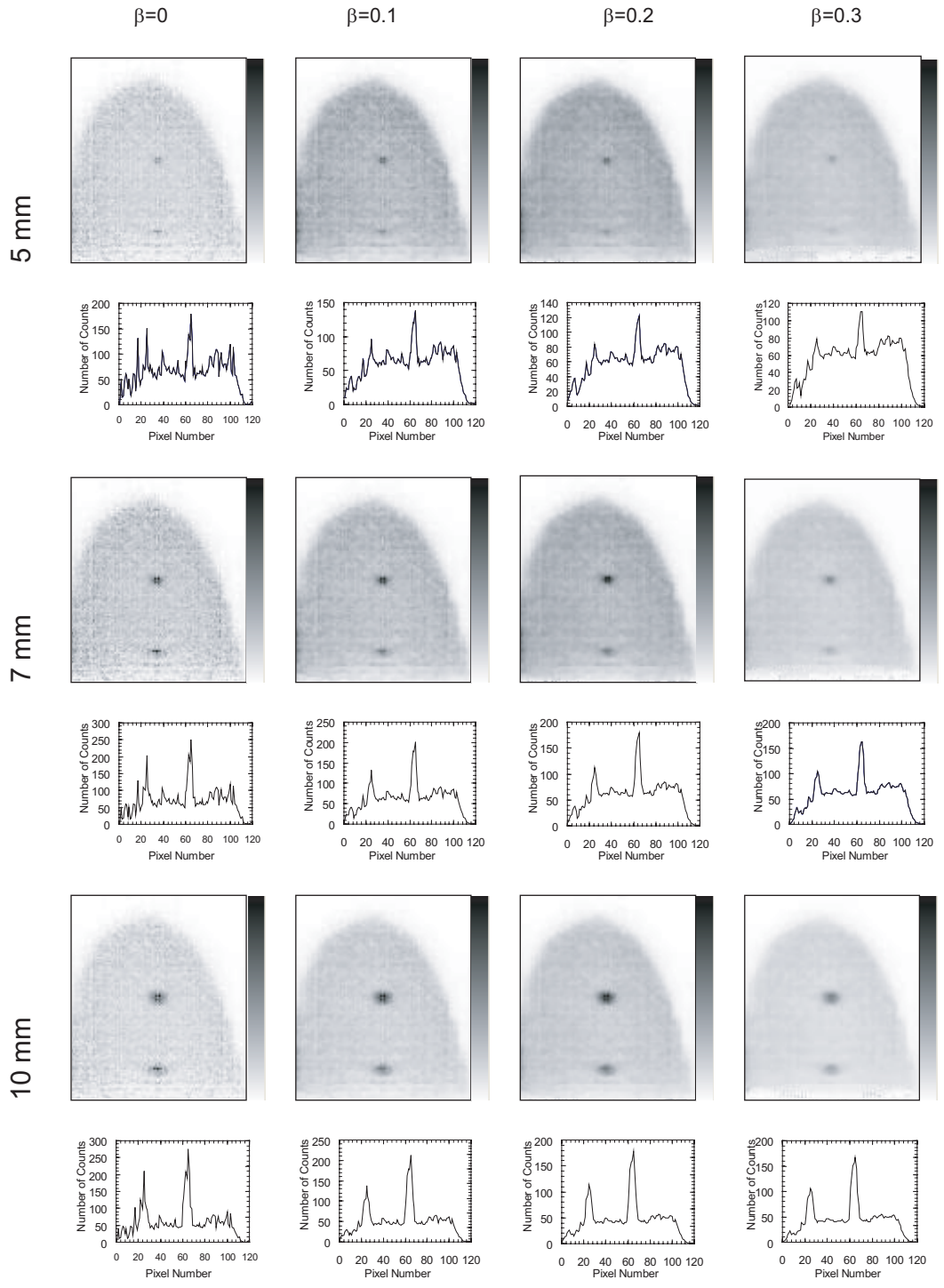

Figure 9.5: Central coronal slices of the reconstructed images of the NCAT Breast phantom with the 5 mm, 7 mm and 10 mm diameter simulated lesions and lesion-to-background ratio L4=4:1. Below each image is presented the profile taken over a line that crosses the two lesions.

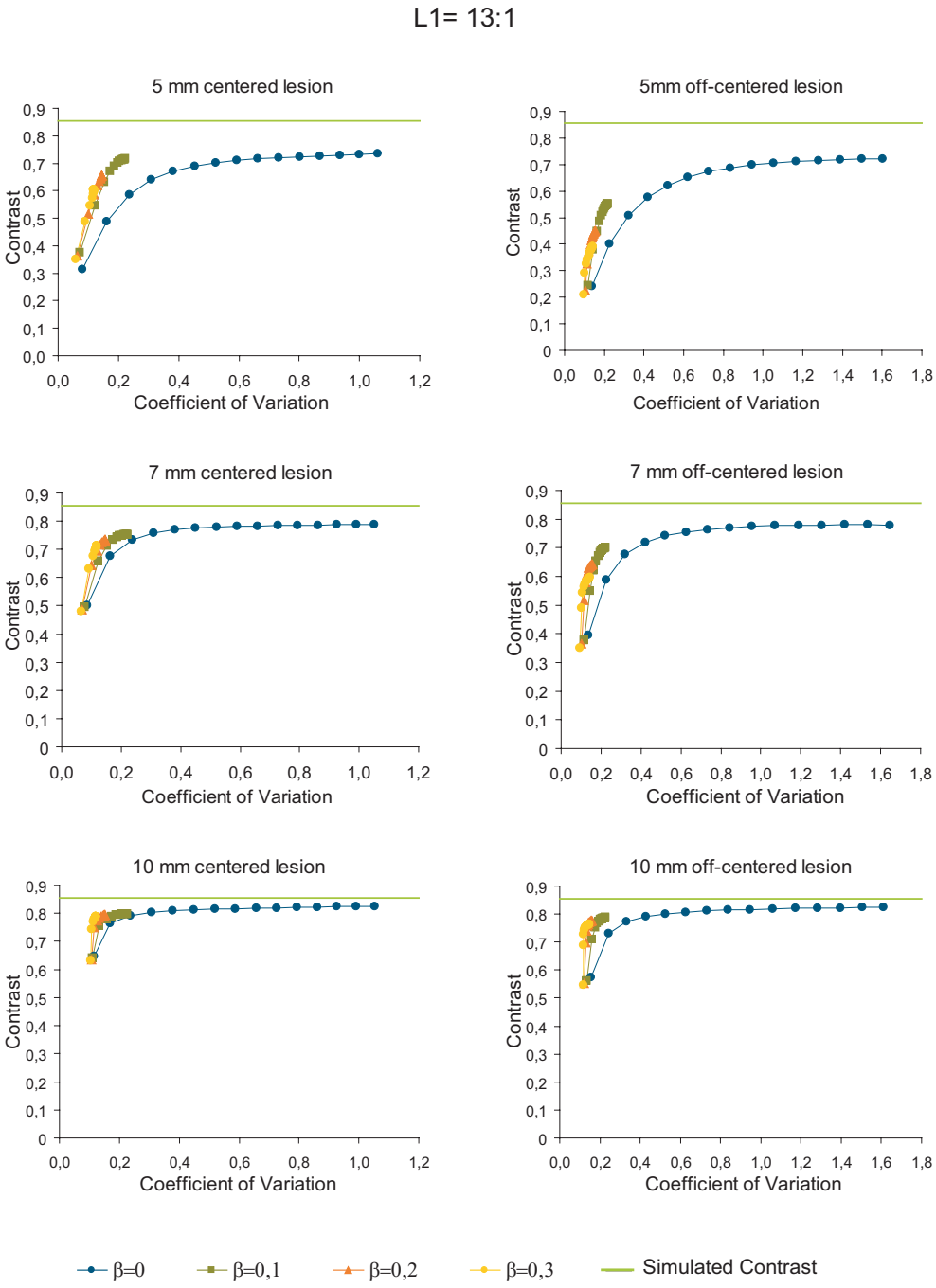

Figure 9.6: Contrast between the lesions and the background tissues against noise, presented as the coefficient of variation, measured for the NCAT Breast phantom and the simulated centered and off-centered 5 mm, 7 mm and 10 mm lesions for the lesion-to-background ratio L1=13:1. The simulated contrast appears as an horizontal green line in the plots.

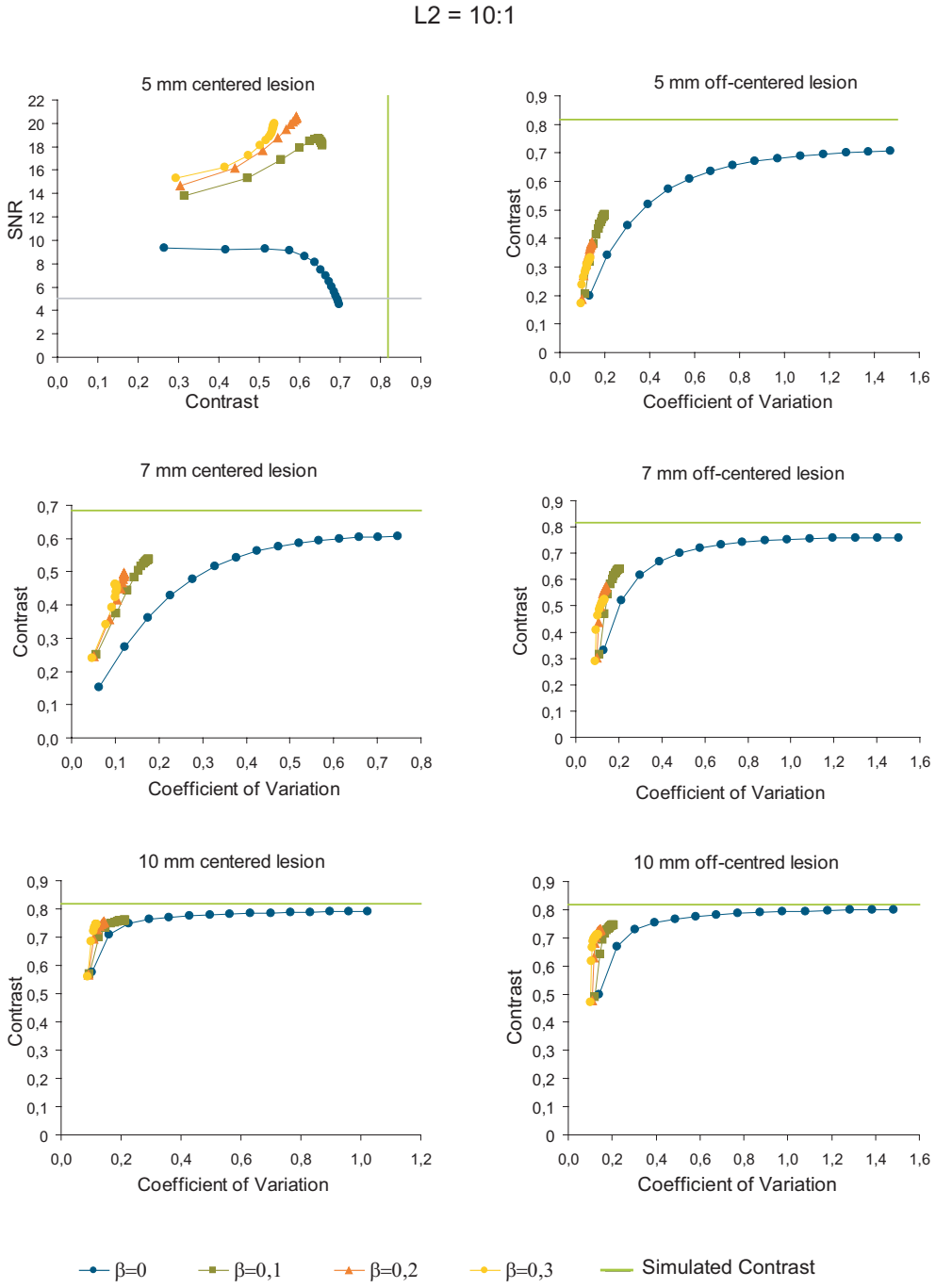

Figure 9.7: Contrast between the lesions and the background tissues against noise, presented as the coefficient of variation, measured for the NCAT Breast phantom and the simulated centered and off-centered 5 mm, 7 mm and 10 mm lesions for the lesion-to-background ratio L2=10:1. The simulated contrast appears as an horizontal green line in the plots.

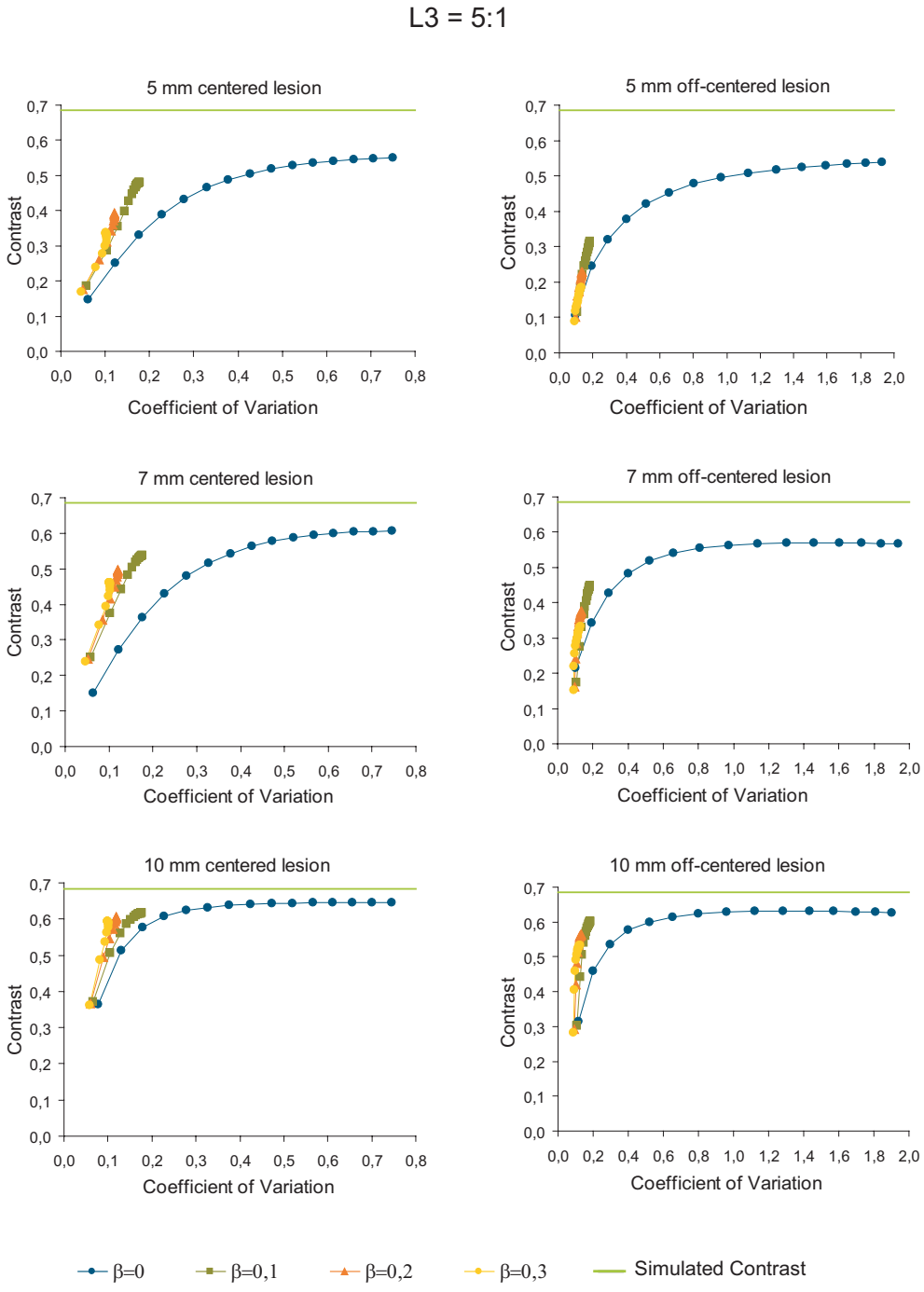

Figure 9.8: Contrast between the lesions and the background tissues against noise, presented as the coefficient of variation, measured for the NCAT Breast phantom and the simulated centered and off-centered 5 mm, 7 mm and 10 mm lesions for the lesion-to-background ratio L3=5:1. The simulated contrast appears as an horizontal green line in the plots.

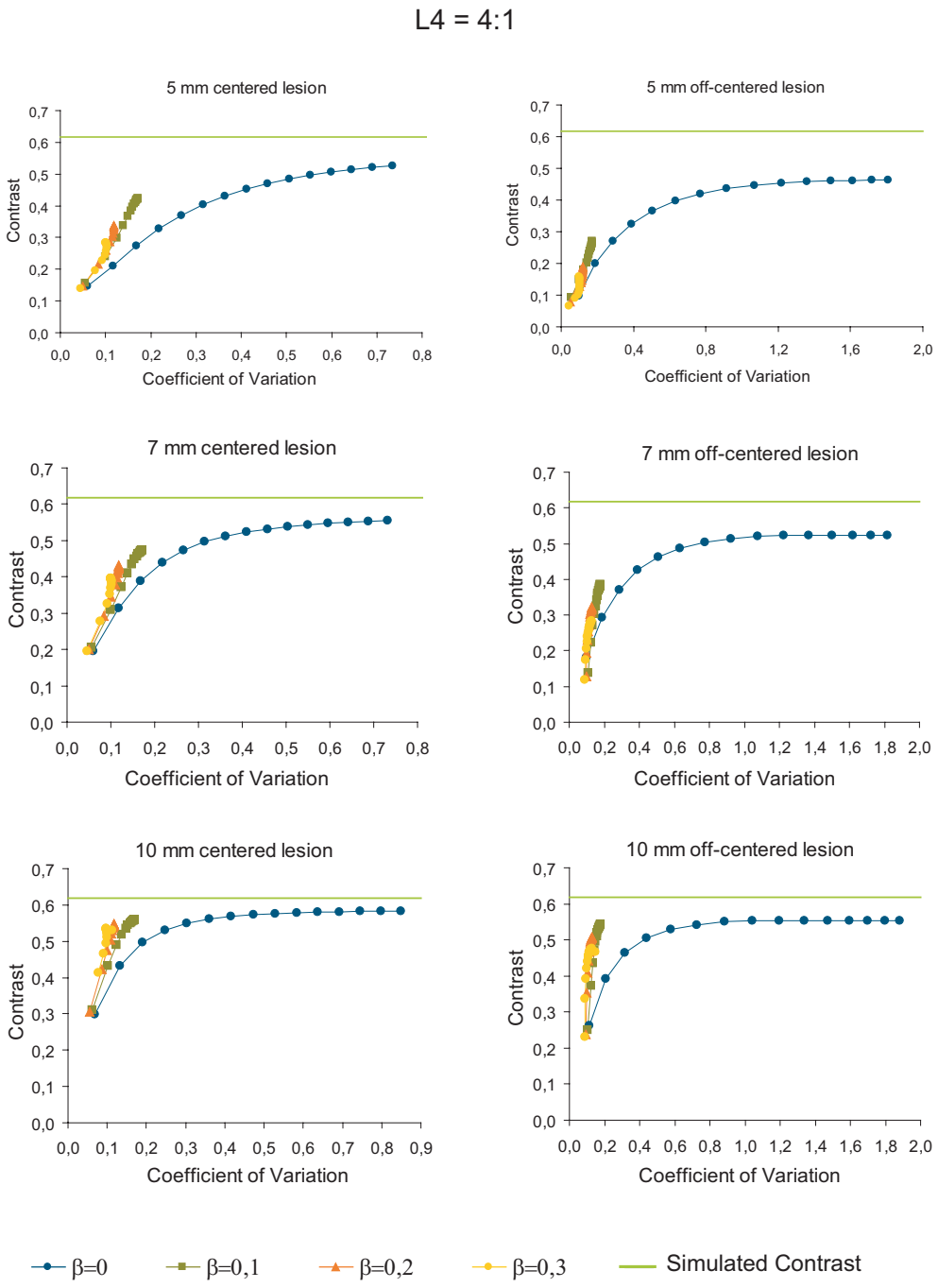

Figure 9.9: Contrast between the lesions and the background tissues against noise, presented as the coefficient of variation, measured for the NCAT Breast phantom and the simulated centered and off-centered 5 mm, 7 mm and 10 mm lesions for the lesion-to-background ratio L4=4:1. The simulated contrast appears as an horizontal green line in the plots.

10 mm diameter lesions in the lesion-to-background ratio L3 (Figures 9.12 (a) and (b)).

In any of the cases studied, and regardless of the lesion-to-background ratio, lesion diameter, lesion axial position or priori weight considered, the final SNR values attained with the OS-EM algorithm are always much lower than those attained by the Bayesian algorithm. However, it is also frequent, as it was previously seen, that the contrast values attained by the Bayesian algorithm are significantly lower than those attained by OS-EM. This is especially true for the most critical cases, that is, for the off-centered, smaller diameter lesion in highest lesion-to-background ratio.

Figure 9.14 and Figure 9.15 present the values of the contrast as a function of the diameter of the simulated lesions after convergence, for the prior weights considered, for the lesion-to-background ratios considered, and for the centered and off-centered lesions. As previously, the convergence criterion used considered convergence was achieved in the iterative image reconstruction process when a percentage variation in the contrast values of less than 1% in the subsequent iterations was found. The line of the simulated contrast in each case is also represented in the plots.

A common characteristic in these plots is that, regardless of the lesion-to-background ratio considered, lesion diameter or location studied, the contrast values obtained with the OS-EM algorithm are always higher than or equal to the ones obtained with the Bayesian algorithm. Among the contrast values measured with the Bayesian algorithm, the higher the prior weight used, the lower the contrast value after convergence. For the two lowest lesion-to-background ratios considered (L1, L2), and for the centered lesions, the values of contrast measured with the Bayesian algorithm with prior weight β=0.1 are equal or very close to the measured values with OS-EM, for any of the lesion diameters considered (plots in Figure 9.14 (a) and (b)). For the off-centered lesions, the same is true only for the 10 mm diameter lesion. For the remainder cases, the values of contrast obtained with the Bayesian algorithm, even with the lowest prior weight studied, are always significantly lower than the values obtained with OS-EM. Such a difference is even more significant when one looks at the plots corresponding to the off-centered lesion (Figure 9.15).

Figure 9.16 and Figure 9.17 present the values of the signal-to-noise ratio as a function of the diameter of the simulated lesions after the considered convergence point, for the prior weights considered, for the lesion-to-background ratios considered, and for the centered and off-centered lesions. The line of the conventional detectability limit (SNR=5) is also drawn in the plots.

A common feature shown in these plots is the fact that, regardless of the lesion-to-background ratio, lesion diameter or lesion location studied, the SNR values measured with the OS-EM algorithm after convergence are always significantly lower than the ones obtained with the Bayesian algorithm. In fact, taking the traditional detectability

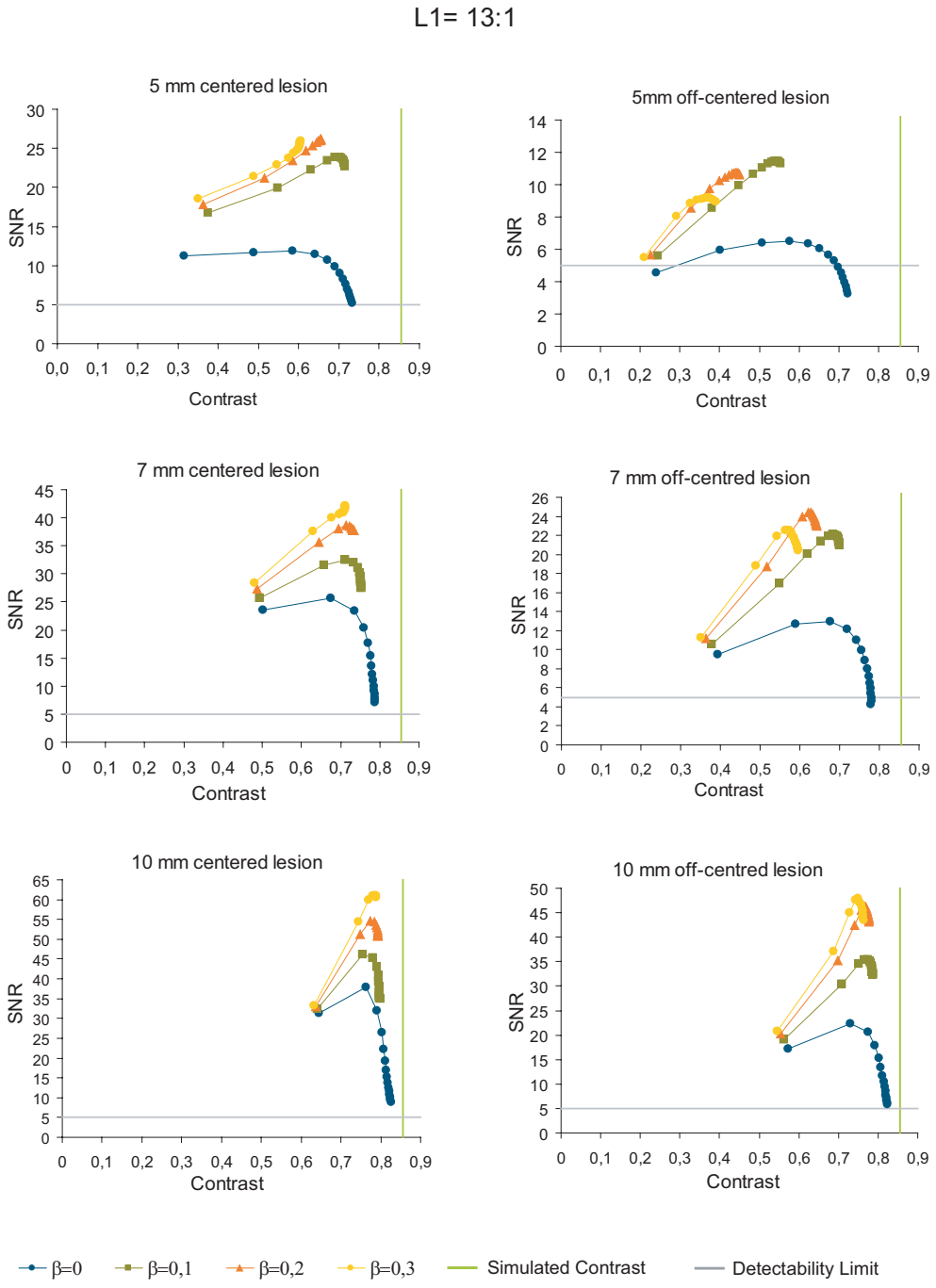

Figure 9.10: Plots of the signal-to-noise ratio against Contrast between the lesions and the background tissues for the 5 mm, 7 mm and 10 mm centered and off-centered simulated lesions, for all the prior weights considered, and for the lesion-to-background ratio L1=13:1. The simulated contrast appears in the plots as a vertical green line and the detectability limit appears as an horizontal gray line.

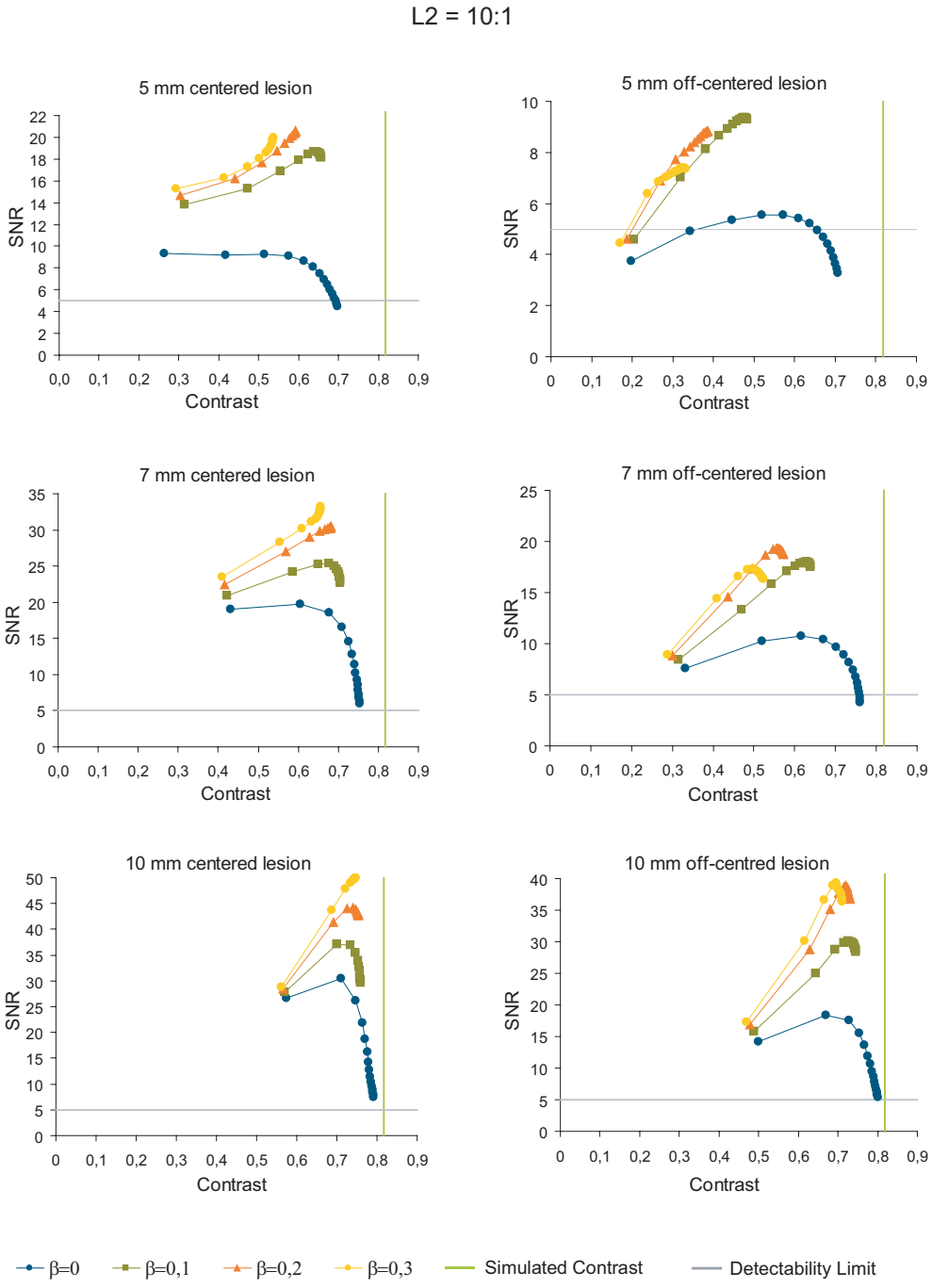

Figure 9.11: Plots of the signal-to-noise ratio against Contrast between the lesions and the background tissues for the 5 mm, 6 mm and 10 mm centered and off-centered simulated lesions, for all the prior weights considered, and for the lesion-to-background ratio L2=10:1. The simulated contrast appears in the plots as a vertical green line and the detectability limit appears as an horizontal gray line.

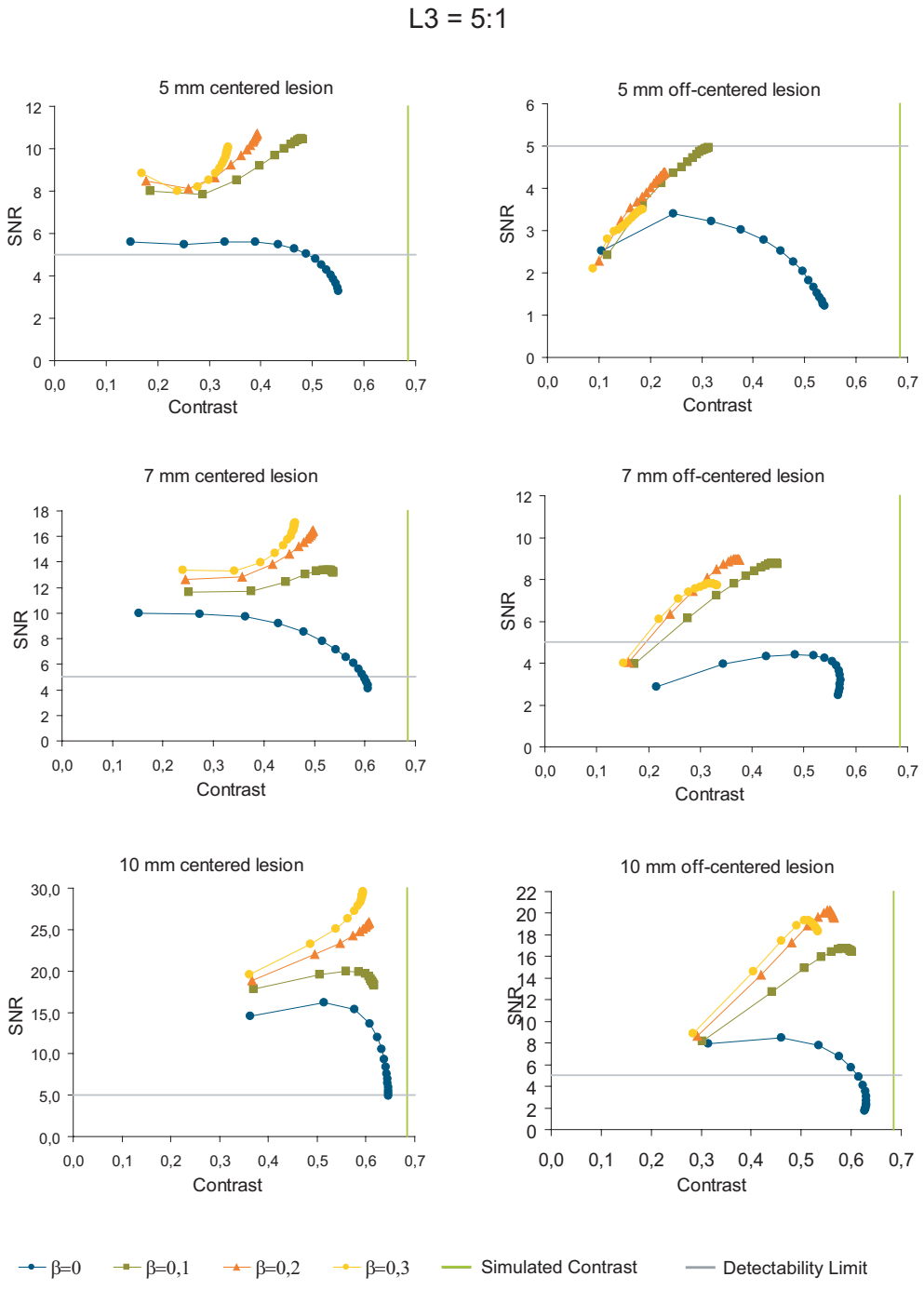

Figure 9.12: Plots of the signal-to-noise ratio against Contrast between the lesions and the background tissues for the 5 mm, 7 mm and 10 mm centered and off-centered simulated lesions, for all the prior weights considered, and for the lesion-to-background ratio L3=5:1. The simulated contrast appears in the plots as a vertical green line and the detectability limit appears as an horizontal gray line.

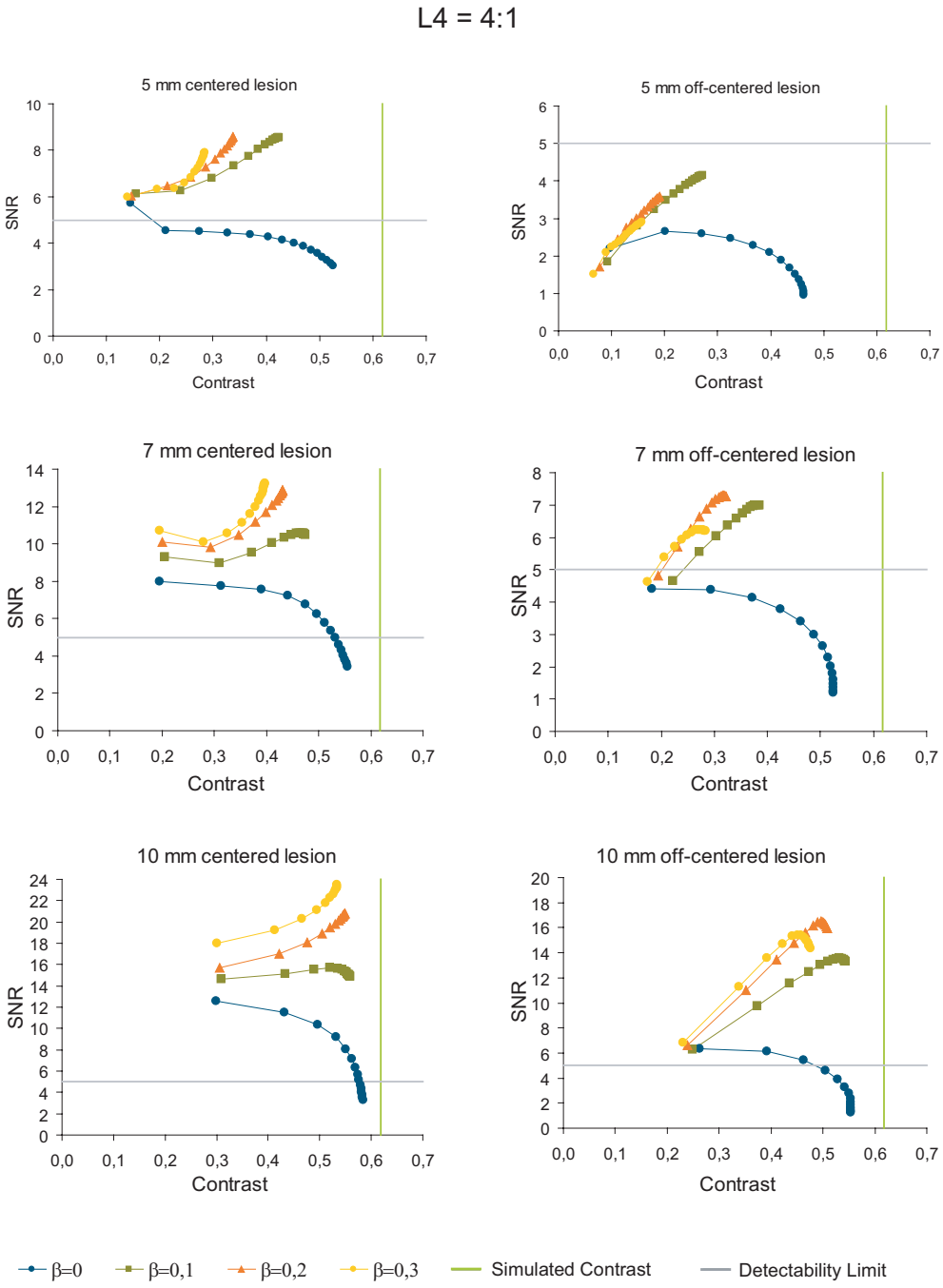

Figure 9.13: Plots of the signal-to-noise ratio against contrast for the 5 mm, 7 mm and 10 mm centered and off-centered simulated lesion, for all the prior weights considered, and for the lesion-to-background ratio L4=4:1. The simulated contrast appears in the plots as a green vertical line, and the conventional detectability limit appears as a gray horizontal line.

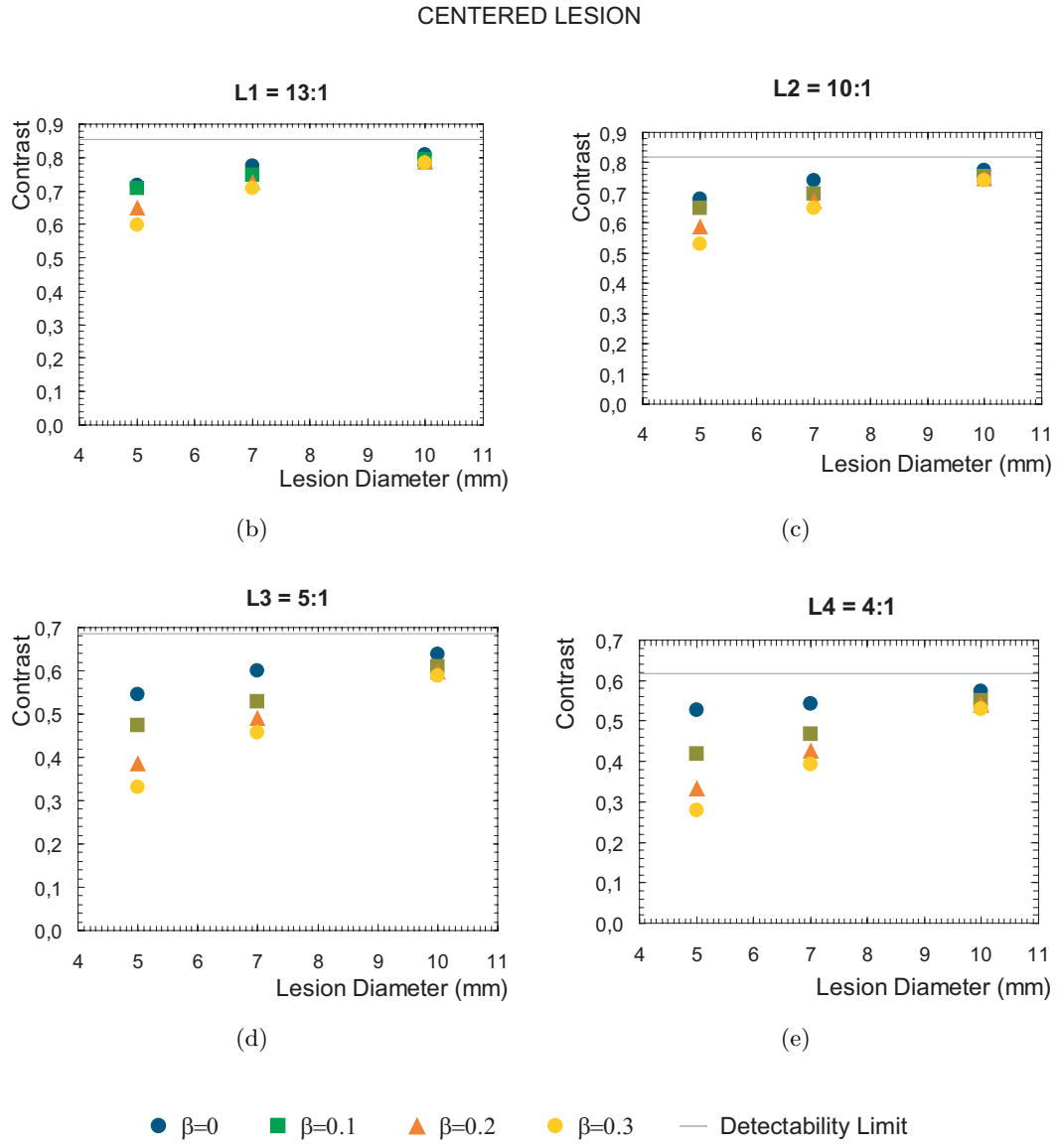

Figure 9.14: Variation of the measured contrast between lesions and background tissues with the simulated centered lesion diameter, for all the prior weights considered and for all the lesion-to-background values considered. The simulated contrast appears as an horizontal gray line in the plots.

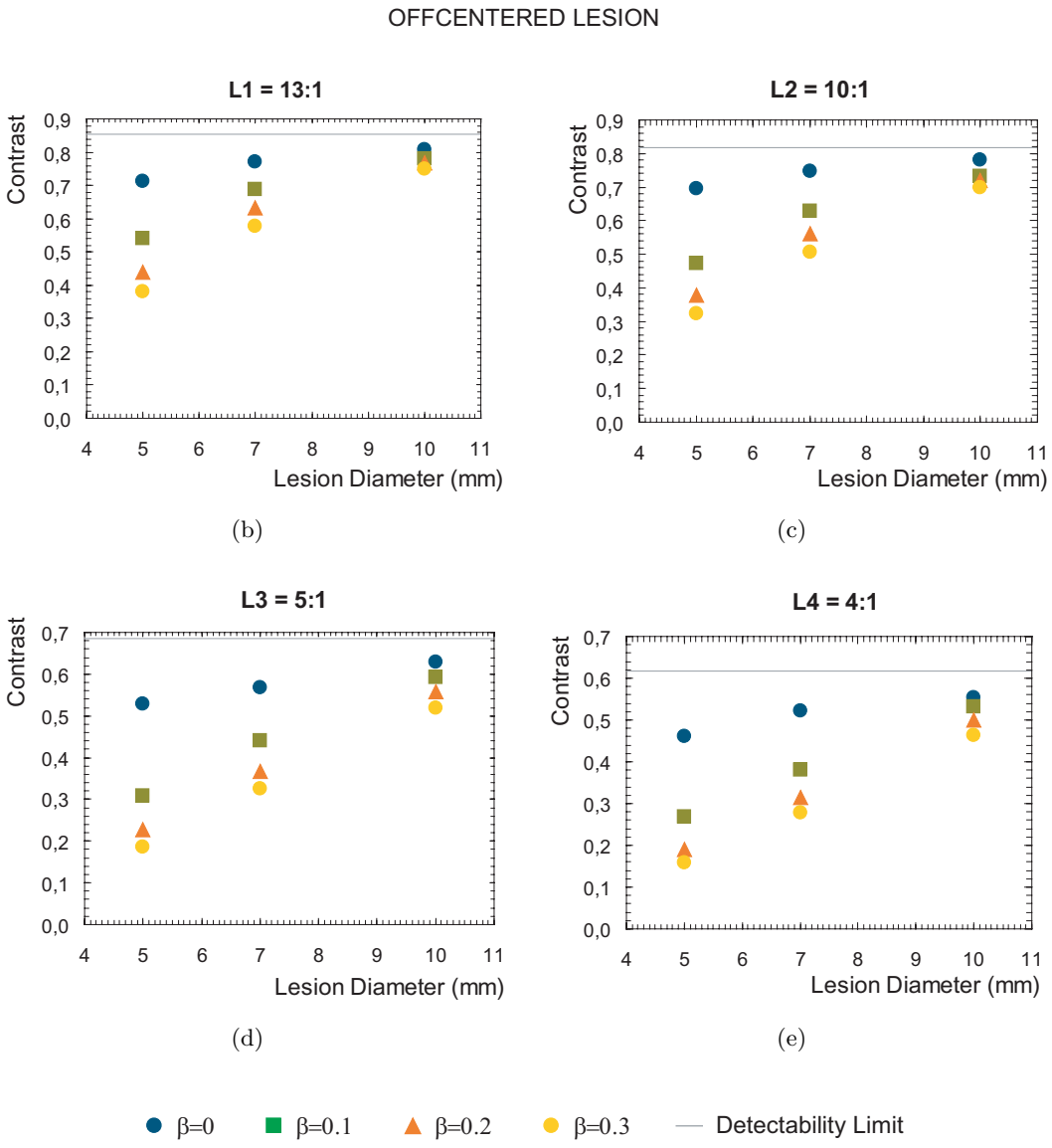

Figure 9.15: Variation of the measured contrast between lesions and background tissues with the simulated off-centered lesion diameter, for all the prior weights considered and for all the lesion-to-background values considered. The simulated contrast appears as an horizontal gray line in the plots.

line as a reference, it is notorious that the SNR values obtained with the Bayesian algorithm, is almost ever above that line. The two exceptions consist on the values measured for the off-centered 5 mm lesion in the two highest lesion-to-background ratios considered, L3 and L4 (Figure 9.17 (a) and (b)). Even for those cases, the SNR values measured with the Bayesian algorithm are much closer to the detectability line than the values measured with OS-EM.
Considering the SNR values measured with the Bayesian algorithm, the presented plots show that the values are higher for higher lesion diameter, lower lesion-to-background ratio and for the centered position of the lesion. For each scenario considered, usually the highest SNR value is measured for the highest prior weight considered. However, this does not happen for the smaller lesion diameter considered, since the SNR values obtained with any of the prior weights considered are approximately equal. The same happens for the 7 mm diameter off-centered lesion.
The results summarized in plots from Figures 9.14 to Figure 9.17 indicate that using the Bayesian algorithm with the Median Root Prior results in images that have lower contrast values between the lesions and the background tissues, with respect to the contrast values obtained with OS-EM. However, such images also present much lower noise values. As a consequence, the SNR values are significantly higher for the images reconstructed with the Bayesian algorithm. In other words, there is a trade-off between contrast and SNR when using the Bayesian algorithm. Among the prior weights studied, the best relation between contrast and SNR seems to be achieved when using the lowest value studies, β=0. In fact, using higher prior weights might sometimes (not always) result in higher SNR values, but frequently results in significantly lower contrast values.

9.4 Conclusions

In this chapter we have presented the tests that were performed with Clear−PEM simulated data and the OS-MAP-OSL algorithm with the Median Root Prior. An analysis was presented considering the trade-off between image spatial resolution, contrast, noise and signal-to-noise ratio in the reconstructed images with plain OS-EM and the Bayesian algorithm with different prior weights.
The results obtained show that, as expected, a rise in the prior weight used results in a higher degradation both on the image spatial resolution and on the contrast between the lesions and the background tissues in the reconstructed images. The analysis of the trade-off between contrast and noise shows that the Bayesian method is much more stable regarding noise than the OS-EM algorithm, but also that it results in significantly lower contrast images. However, the signal-to-noise ratio values obtained with the Bayesian method are significantly higher than those obtained with plain OS-EM.

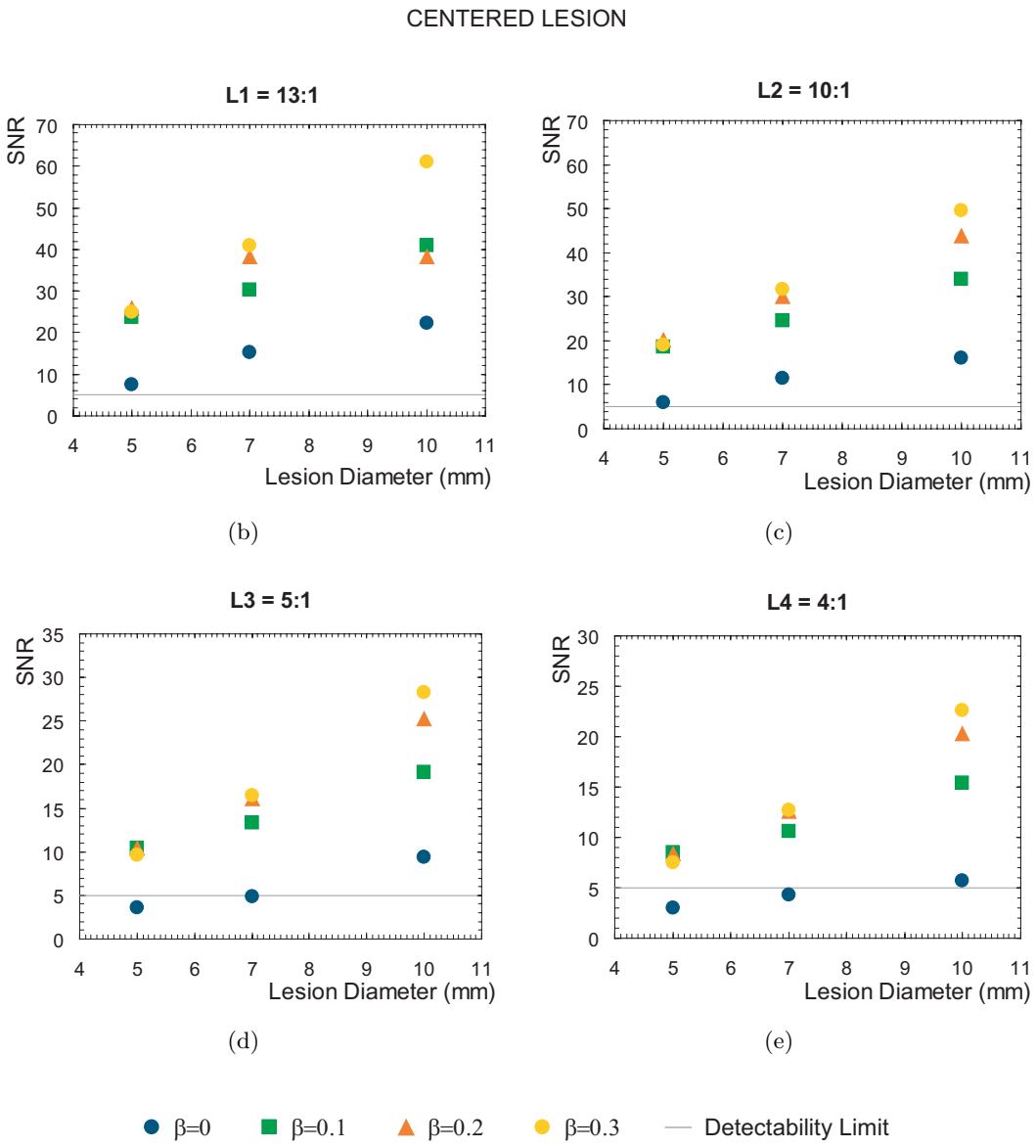

Figure 9.16: Variation of the signal-to-noise ratio with the simulated centered lesion diameter, for all the prior weights considered and for all the lesion-to-background values considered. The simulated contrast appears as an horizontal gray line in the plots.

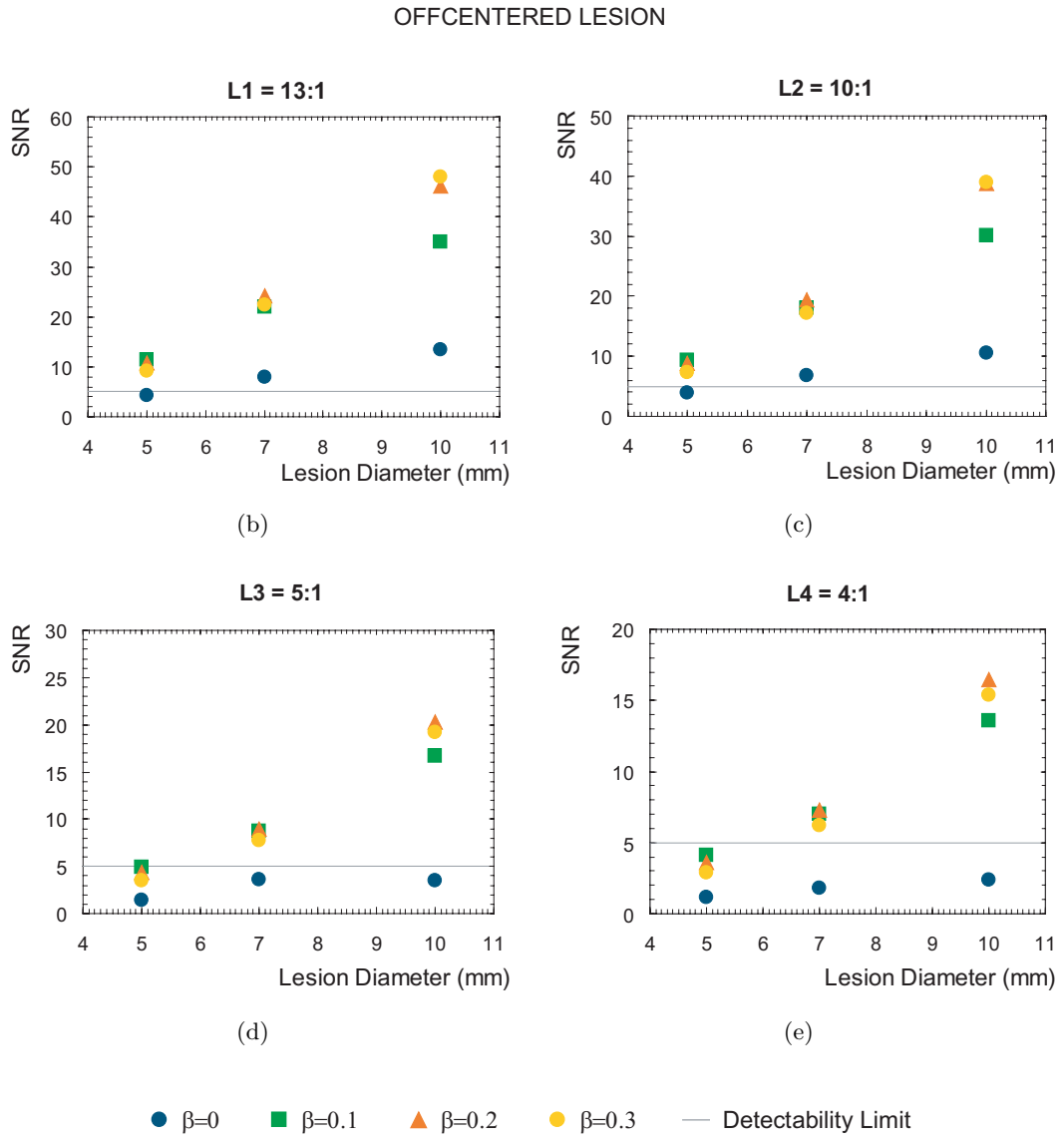

Figure 9.17: Variation of the signal-to-noise ratio with the simulated off-centered lesion diameter, for all the prior weights considered and for all the lesion-to-background values considered. The simulated contrast appears as an horizontal gray line in the plots.

Among the values studied for the prior weigh, the choice of β=0.1 seems to provide the better trade-off between image spatial resolution and contrast, on the one hand, and signal-to-noise ration, on the other hand. Higher values for the prior weight lead to low contrast, low resolution images and not necessarily higher signal-to-noise values.
In summary, the OS-MAP-OSL algorithm with the Median Root Prior has shown to be a feasible reconstruction method for the dual planar scanner data, yielding high contrast and spatial resolution images and efficiently controlling image noise.

Part V

Main Conclusions and Future Work

Chapter 10

Main Conclusions and Future Work

In this final chapter the work developed and presented in the several parts of this thesis regarding the 3D image reconstruction methods for the Clear−PEM scanner will be summarized. The several results found in the chapters contained in Part IV of the thesis will be reviewed and discussed and the suggestions and perspectives for future work will be presented.

The outline and general motivation for the work here presented were provided in an introductory chapter in Part I of this thesis.
Part II of this dissertation provided a review of the state of the art in the main knowledge fields related to the work developed. The fundamental importance of the imaging methods in the detection and management of breast cancer is presented in Chapter 2. The great potential of small dedicated cameras based on radionuclide imaging is highlighted in the context of its role in the early detection of breast cancer. In Chapter 3, the several technical aspects implied in the design and development of Positron Emission Tomography scanners are presented. A review of the state of the art of the existing or under development PEM scanners is provided, as well as the most meaningful clinical findings using those scanners. The final chapter of Part II introduces the relevant concepts and approaches used for PET image reconstruction with statistical iterative methods.
Part III of this thesis deals with the description of the Clear−PEM scanner and of the utilities that were used to develop and test the 3D image reconstruction software. The main characteristics of the Clear-PEM scanner in development are presented in Chapter 5, as well as the Monte Carlo simulation framework that was created for its design. The geometrical and anthropomorphic phantoms used in the simulations, as well as the particular settings in which they were used are described. Particular emphasis is

given on the description of the simulations that aimed at reproducing as thoroughly as possible breast exams with the Clear-PEM scanner in a clinical scenario. In Chapter 6 the image reconstruction library STIR, that was used as a basis for 3D image reconstruction for the Clear-PEM scanner, was presented. An overview was provided of the modular structure of the library, as well as of the main approaches used on the computations associated with the projection and the backprojection operators. In this chapter, the reasoning behind the implementation of the iterative statistical image reconstruction algorithm available in STIR, OS-MAP-OSL was also presented.
Part IV of this thesis contains the chapters that present the methodologies that were used to implement the 3D image reconstruction software for the Clear-PEM scanner and the results obtained with the several tests performed. The summary and the discussion of the work presented in each of the chapters, as well as the perspectives for future work, will be presented hereafter. For the sake of clarity, the discussion will be divided into sections corresponding to each of the chapters contained in Part IV of the thesis.

Enhancements in the STIR framework and initial evaluation

In Chapter 7 the reasoning that was followed to enable the STIR library to deal with data proceeding from a dual planar geometry scanner such as the Clear−PEM was presented. It was described how the data proceeding from a Clear-PEM acquisition was accommodated in the standard 3D sinogram format. It was also described how the DOI information was accounted for in the sinograms. The adopted scheme allowed avoiding an increase in the image reconstruction computation time with regard to the non-existence of DOI information, while maintaining the information provided by the DOI measure. The methods used to implement the forward and the backprojector operators were presented, as well as the geometrical symmetries that are used to speed up the computations. Next, an initial evaluation of the new features in the STIR library was performed using geometrical phantoms analytical simulated data. This involved a number of tests carried out with the aim of optimizing the parameters used in the image reconstruction algorithm and in the projector/backprojector settings. The image reconstruction operators and algorithm settings studied were the number of subsets to be used in the OS-EM algorithm, the number of rays to trace each bin in the transaxial direction in the projection operation, and the geometrical symmetries used. The ability to reconstruct data acquired with the detector plates at a single angular position was also studied. The quality of the reconstructed images was evaluated both in terms of image uniformity and image spatial resolution. Image reconstruction time was also considered. Regarding the number of subsets used with the OS-EM algorithm, it was found that 4 was the number of subsets that optimized the relation between the image quality and the time needed to achieve convergence. A higher number of subsets

resulted in a limited number of projection views in each subset, with consequent instability in the reconstruction process and degradation of the quality of the reconstructed images. Regarding the number of rays used to trace each bin in the transaxial direction in the projection and backprojection operations, as expected, a higher number of rays lead to improved image quality, since more accurate computations of the contributions of the voxels for a given bin are used. It was found that the increase in computation time needed to perform the computations with 3 rays to trace each bin in the transaxial direction was largely compensated by the improvement in the quality of the reconstructed images, both in terms of image uniformity and image spatial resolution. Regarding the use of geometrical symmetries, it was found that the use of the s, θ and z symmetry in the computations did not introduce any error in the reconstructed images. The simultaneous use of the symmetries lead to a reduction of about 12 times in the computation time with respect to the computation time required when none of the geometrical symmetries were used. Another aspect that was tested was the ability of the library to deal with data proceeding from a single angular position of the detector plates. It was found that, although the simulated structures were all correctly located in the reconstructed images, a blurring artifact was present which is consistent to the non existence of information along the direction normal to the direction defined by the detector plates. This topic was further explored in another chapter of the thesis and will be discussed later.

A number of issues regarding the work presented in this chapter deserves additional remarks. First, we address the question of the choice of the sinogram format for accommodating the 3D projection data of the Clear-PEM scanner. Other data formats exist that more intuitively fit the planar nature of the planar scanner acquisition data, such as planograms, or its 2D counterparts, linograms. However, the use of this quantities is constrained to two angular acquisitions at two perpendicular position of the detector plates. Although the Clear-PEM rotational capabilities around the breast of the patient are not further explored in this thesis, the use of sinogram-based image reconstruction software does not disregard the possibility of re-using it for acquisition scenarios involving several angular positions of the detector plates. Furthermore, those who defend the use of planograms or linograms argue that the projection and backprojection operations using linograms are faster than when using sinograms [171]. Although this is a theoretical valid argument, in practice many other factors affect the computation time associated with the image reconstruction process. For instance, some results obtained with the simulated acquisition of the Clear−PEM scanner and ML-based algorithms [172], not presented in this thesis, have shown that 2D image reconstruction using 2D sinograms can perform better, in terms of computation time, than 2D image reconstruction using linograms, with equivalent results concerning the quality of the reconstructed images.

Other aspects that deserve further investigation and development are the extension of the capability of the image reconstruction library to deal with more number of angular position of the detector plates, and the testing of the image reconstruction results with different distances of the detector plates. The first of these topics will be discussed below. The second issue is important because it is to be expected, in the clinical practice, a wide variety of breast volumes to be examined. The standard distance used in this work (10 cm distance between the front surface of the detector heads) was chosen because it was considered to be an adequate plates separation for a mean breast size. Shorter plates distances might cause discomfort to the patient, and longer plates distances imply a diminishing in the sensitivity of the scanner. However, it is important that the detector plates separation can be adequate for each individual breast size. A wider distance between the detector plates results in a wider number of projection views that are not sampled. Therefore, it is expected that some blurring artifacts might appear, especially in the regions located near the FOV edges. The existence of blurring artifacts in those regions will be discussed later. A shorter distance between the detector plates results in projection views that are sampled more than once, and this may lead to non-uniformities in the reconstructed images. However, this issue should be accounted for with the correct normalization factors incorporated in the sensitivity image used in the image reconstruction process.
An important issue that arises when 3D image reconstruction is being discussed is the question of the associated computation time. The choice of the STIR library as the basis for 3D image reconstruction for the Clear-PEM scanner had already in mind that this library had fast speed features, such as the fast projector and backprojector operators and data structures adequate to the use of geometrical symmetries. With the chosen axial sampling for the Clear-PEM data, the number of segments to be processed for a dataset is enormous (127 segments). Therefore, even if the processing time associated with a single segment is quite low, the processing time for the whole sinogram rests quite high. Therefore, an obvious and simple means to reduce the 3D image reconstruction computation time is to use axially compressed data, and to reconstruct the images accordingly. Another approach to improve the computation times for 3D image reconstruction is to use parallel computing. Although less simple to execute than the previous one, this approach certainly deserves to be explored, especially because the STIR library is a successor of a parallel computing platform for 3D image reconstruction, the ParaPET project.

3D OS-EM image reconstruction for the Clear-PEM scanner

Chapter 8 of this thesis presents several studies that were performed with Monte Carlo simulation data for the Clear-PEM scanner and the 3D OS-EM algorithm. In the first

section of the chapter Monte Carlo data simulated for a simplified version of the geometry of the scanner was used as input for the 3D OS-EM algorithm with the optimized settings that were defined in Chapter 7. The images obtained confirmed a good agreement with the simulated data. The evolution of the image spatial resolution and image uniformity with the iteration number were in agreement with what is expected for a ML-EM based image reconstruction algorithm.

In the second section of the chapter the effect of the rotation of the detector heads and of the DOI information in the spatial resolution of the reconstructed images was studied. We addressed the question of how an acquisition with the detector heads at a single angular position performs, in terms of the spatial resolution of the reconstructed images, with respect to an acquisition with the detector plates at two perpendicular angular positions. Regarding DOI information, four different scenarios were studied: non-existence of DOI information, a poor DOI resolution, the DOI resolution that is foreseen to be provided by the Clear-PEM scanner and an ideal case, exact DOI information. Regarding the reconstructed images corresponding to the data acquired in a single angular position of the detector plates, it was found that, when no DOI is available, a strong blurring occurs in a direction normal to the plane of the detector plates surface. This effect is, however, very much DOI dependent, since it is strongly attenuated with the increase of the DOI resolution. It was also found that the evolution of the values of the image spatial resolution measured in structures near the FOV edges did not tend to stabilize with the iterative process. The FWHM values rather tended to increase. This fact indicates that, even when exact DOI information is considered, the image spatial resolution near the FOV edges is a critical issue when a single angular position of the detector plates is considered. Regarding the dual angular positions of the detector plates, it was found that, as expected, there is a clear improvement in the image spatial resolution with a high DOI resolution is considered. However, as before, the spatial resolution values measured in regions close to the FOV edges do not tend to stabilize with the number of iterations, as it happens in other regions of the FOV. This happens even when the ideal scenario for the DOI resolution is considered. Furthermore, these studies have shown that, regardless of the DOI resolution considered, the impact of the detectors heads rotation on the spatial resolution is always more pronounced in the off-centered than in the centered regions of the FOV. Thus, the spatial resolution of the reconstructed images near the FOV edges might benefit from acquisitions in additional angular positions of the detector heads. It was also found that, regardless of the geometry of the acquisition, the most significant improvement in the image spatial resolution occurs when a poor DOI resolution improves to the DOI resolution value that will be provided by the Clear-PEM scanner. This improvement is even more significant than the improvement obtained with a dual angle acquisition

(while maintaining the poor DOI resolution). Overall, the dual angle simulation acquisition with the foreseen DOI resolution that will be provided by the Clear PEM scanner and the 3D image reconstruction algorithm yields an image spatial resolution that ranges from 1.3×1.3×1.4 mm^3 in the FOV center to 1.5×1.8×2.0 mm^3 at 4 cm from the FOV center.

The third part of the chapter presents the results obtained in the studies involving the NCAT breast phantom bearing simulated lesions. The simulations used in these studies aimed at reproducing as thoroughly as possible breast exams with the Clear-PEM scanner in a clinical scenario. This included 5 minute simulated acquisition of the anthropomorphic phantom considering different uptakes in the normal tissues and different diameters for simulated spherical lesions. This way, the ability of the Clear-PEM scanner to detect lesions of different dimensions in different types of radiological dense breasts (from essentially fatty breast tissue to dense breast tissue) could be evaluated. The results obtained with the OS-EM algorithm indicate that, in the clinical simulated settings, it seems to be possible to detect, with high contrast and signal-to-noise ratio, lesions located in the center of the FOV, with diameters ranging from 5 mm to 10 mm, in all of the considered breast types. The results also indicate that it seems to be possible to visualize 3 mm lesion, but only in the highest lesion-to-background ratios considered, that is, only in breasts constituted mainly by fat tissue and breasts constituted by fat and some fibroglandular tissues. It is worth mentioning, however, that the performed studies do not allow to conclude whether the 3 mm lesion could be better visualized if longer acquisition times are considered. Regarding the visualization of lesions closer to the chest wall, the studies indicate that the lesions present a good visibility when breasts fat tissue and fat with fibroglandular tissue breasts are considered. When dense or extremely dense breast tissue types are considered, the visibility or the lesions close to the chest wall remains somehow compromised.

A number of issues arise from the results obtained in this chapter. One of them is the interest in exploring the capabilities of rotation of the detector heads of the Clear-PEM. Hopefully, data acquisition at additional angular positions of the detector heads should improve the quality of the reconstructed images, especially in the regions near the FOV edges. However, issues such as the number and the positions of the detector heads that best suit the trade-off between image quality and acquisition time remain to be studied. It also remains to be studied whether longer acquisition times will allow a better visualization of 3 mm lesions and of the 5 mm lesions in the regions close to the chest wall. Another field that will certainly deserve attention once the Clear-PEM scanner is assembled and ready to acquire data is the sensitivity image. Desirably, this image will be computed from a sinogram containing the normalization coefficients that will be computed from data acquired from a planar uniform source. It will be interesting to evaluate the results obtained with such approach in a clinical setting and how they

compare with the approach used in this work.

Bayesian image reconstruction for the Clear-PEM scanner

In Chapter 9 the results of the Bayesian image reconstruction using the Median Root Prior (MRP) with the simulated data of the Clear-PEM scanner are presented. The impact of using different values for the weight of the prior was evaluated in the spatial resolution, contrast and signal-to-noise ratio of the reconstructed images. Regarding the impact in the spatial resolution of the images, it was found that the higher the prior weight studied, the lower was the spatial image resolution obtained for the reconstructed images. However, when using a low value for the prior weight (β=0.5) the values of the spatial resolution remained similar to the ones obtained with the plain OS-EM algorithm. The results obtained with the anthropomorphic phantom showed that, with respect to the OS-EM results, the Bayesian algorithm allowed improving the signal-to-noise ratio of the images, albeit resulting in lower contrast images. The improvement in the signal-to-noise ratio was especially significant in the regions closer to the chest wall, thus indicating that using the Bayesian algorithm with the Median Root Prior might allow a better visualization of lesions in that region in the breast.

Perspectives for Future Work

In this work we presented the approach followed for performing 3D image reconstruction for a scanner with a planar detector geometry. The use of the STIR library as a basis platform for such purpose has shown to lead to promising results obtained with Monte Carlo simulation data for the Clear-PEM scanner. This fact encourages the possibility of using this same approach with other scanners based on planar detector heads, namely scanners used to study other organs of the human body.

In this work we also approached the question of how Bayesian image reconstruction methods compare with the plain OS-EM algorithm for planar scanner data. Although we have used a specific prior, the Median Root Prior, many other prior types, each with its own strengths and pitfalls, can be explored. Currently, efforts are taking place toward the development of multi-modality imaging scanners that combine anatomical with functional imaging techniques. These efforts certainly encourage the use of Bayesian algorithms with anatomical priors, allowing the incorporation of anatomical information in the image reconstruction process of emission data. The use of such priors with planar scanner data is certainly a topic worthy of future work.

Concluding Remarks

The 3D image reconstruction software presented in this thesis has contributed to the evaluation of the expected performance of the Clear-PEM scanner, as well as its ability to detect small cancerous lesions in the breast. How the 3D image reconstruction software will perform in a real clinical scenario will hopefully be evaluated once the Clear-PEM scanner is ready.

Appendix A

Publications

Papers in international scientific periodicals with referees

M. C. Abreu, D. Aguiar, E. Albuquerqe, F. G. Almeida, P. Almeida, P. Amaral, E. Auffray, P. Bento, P Bruyndonckx, R. Bugalho, B. Carrico, H. Cordeiro, M. Ferreira, N. C. Ferreira, F. Goncalves, P. Lecoq, C. Leong, F. Lopes, P. Lousa, J. Luyten, M. V. Martins, N. Matela, P. R. Mendes, R. Moura, J. Nobre, N. Oliveira, C. Ortigao, L. Peralta, R. Pereira, J. Rego, R. Ribeiro, P. Rodrigues, A.I. Santos, M.M. Silva, J.C. Silva, P. Tavernier, I.C. Teixeira, J.P. Teixeira, A. Trindade, J. Trummer, J. Varela. Clear-PEM: A PET imaging system dedicated to breast cancer diagnostics. *Nuclear Instruments & Methods in Physics Research Section A - Accelerators Spectrometers Detectors and Associated Equipment*, 571(1-2):81-84, 2007.

M. C. Abreu, J. D Aguiar, F. G. Almeida, P. Almeida, P. Bento, B. Carrico, M. Ferreira, N. C. Ferreira, F. Goncalves, C. Leong, F. Lopes, P. Lousa, M. V. Martins, N. Matela, P. R. Mendes, R. Moura, J. Nobre, N. Oliveira, C. Ortigao, L. Peralta, R. Pereira, J. Rego, R. Ribeiro, P. Rodrigues, J. Sampaio, A.I. Santos, L. Silva, J.C. Silva, P. Sousa, I.C. Teixeira, J.P. Teixeira, A. Trindade, J. Varela. Design and evaluation of the Clear-PEM scanner for positron emission mammography. *IEEE Transactions on Nuclear Science*, 53(1):71-77, 2006.

M.C. Abreu, P. Almeida, F. Balau, P. Bento, N. C. Ferreira, S. Fetal, F. Fraga, M. V. Martins, N. Matela, R. Moura, C. Ortigao, L. Peralta, P. Rato, R. Ribeiro, P. Rodrigues, A.I. Santos, A. Trindade, J. Varela. Clear-PEM: A dedicated PET camera for improved breast cancer detection. *Radiation Protection Dosimetry*, 116(1-4):208-210, 2005.

R. Ribeiro, C. Abreu, P. Almeida, F. Balau, P. Bordalo, N.C. Ferreira, S. Fetal, F. Fraga, P. Lecoq, M. V. Martins, N. Matela, R. Moura, C. Ortigao, L. Peralta, S.

Ramos, P Rato, P. Rodrigues, A.I. Santos, A. Trindade, J. Varela. Breast imaging with a dedicated PEM. *Nuclear Instruments & Methods in Physics Research Section A - Accelerators Spectrometers Detectors and Associated Equipment*, 527(1-2):87-91, 2004.

G. Santin, D. Strul, D. Lazaro, L. Simon, M. Krieguer, M. V. Martins, V. Breton, C. Morel. GATE, a Geant-4 based simulation platform for PET and SPECT integrating time movement and time management. *IEEE Trans Nucl Sci*, 50(10):1516-1521, 2003.

Papers in Conference Proceedings

M. V. Martins, N. Matela, P. Rodrigues, A. Trindade, N. Oliveira, H. Cordeiro, N. C. ferreira, J. varela, P. Almeida. Bayesian Image Reconstruction for the Clear-PEM scanner. *IEEE Nuclear Science Symposium Conference Record* 5:2940-2943, 2006.

N. Matela, M. V. Martins, H. Cordeiro, M. Correira, P. Rodrigues, A. Trindade, N. Oliveira, N. C. Ferreira, J. Varela, P. Almeida, Evaluation of spatial resolution of planar detector PET systems: different strategies show different results. *European Journal of Nuclear Medicine and Molecular Imaging*, 33:S89-S90, 2006.

A. Trindade, P. Almeida, N. C. Ferreira, M. V. Martins, N. Matela, N. Oliveira, P. Rodrigues, J. Varela. Breast Cancer Imaging Studies by Monte Carlo Simulation with Clear-PEM. *IEEE Nuclear Science Symposium Conference Record*, 4:2103-2107, 2005.

M. V. Martins, N. Matela, P. Rodrigues, A. Trindade, N. Oliveira, M. Correia, H. Cordeiro, N. C. Ferreira, J. Varela, P. Almeida. Reconstruction of Clear-PEM Data with STIR. *IEEE Nuclear Science Symposium Conference Record*, 4:2098-2102, 2005.

M. C. Abreu, J. D Aguiar, E. Albuquerque, F. G. Almeida, P. Almeida, P. Amaral, P. Bento, R. Bugalho, B. Carrico, H. Cordeiro, M. Ferreira, N. C. Ferreira, F. Goncalves, C. Leong, F. Lopes, P. Lousa, M. V. Martins, N. Matela, P. R. Mendes, R. Moura, J. Nobre, N. Oliveira, C. Ortigao, L. Peralta, J. Rego, R. Ribeiro, P. Rodrigues, A.I. Santos, M. M. Silva, J.C. Silva, I.C. Teixeira, J.P. Teixeira, A. Trindade, J. Varela. First Experimental Results with the ClearPEM Detector. *IEEE Nuclear Science Symposium Conference Record*, 3:1662-1666, 2005.

M. V. Martins, N. Matela, P. Rodrigues, A. Trindade, N. Oliveira, H. Cordeiro, N. C. Ferreira, J. Varela, P. Almeida. Clear-PEM data reconstruction using STIR. *European Journal of Nuclear Medicine and Molecular Imaging* 32:S34, 2005.

M. Correia, H. Cordeiro, N. Matela, A. Trindade, M. V. Martins N. Oliveira, P. Rodrigues, N. C. ferreira, J. Varela, P. Almeida. Evaluation of Rebinning Methods in a 2D reconstruction Scenario with Linograms for Clear-PEM. *European Journal of Nuclear Medicine and Molecular Imaging*, 32:S256, 2005.

N. Matela, M. V. Martins, N. oliveira, A. Trindade, P. Rodrigues, N.C. Ferreira, P. Almeida, J. Varela. Comparison of Different Image Reconstruction Strategies in Clear-PEM. *CIMED 05 - Second International Conference on Computational Intelligence in Medicine and Healthcare, Conference Records. IEE*, 2005.

N. Matela, A. Trindade, M. V. Martins, N. Oliveira, P. Rodrigues, L. Peralta, J. Varela, P. Almeida. Algebraic Image Reconstruction Technique (ART) using linograms. *European Journal of Nuclear Medicine and Molecular Imaging*, 31:S271-S272, 2004.

A.I., Santos, P. Almeida, M. V. Martins, N. Matela, N. Oliveira, N. C. Ferreira, J. D. Aguiar, F. Almeida, F. Lopes, J. Sampaio, P. Bento, F. Goncalves, C. Leong, P. Lousa, L. Silva, I.C. Teixeira, J.P. Teixeira, M. C. Abreu, B. Carrico, P.R. Mendes, R. Pereira, P. Sousa, M. Ferreira, R. Moura, C. Ortigao, L. Peralta, R. Ribeiro, P. Rodrigues, J. C. Silva, A. Trindade, J. Varela. Design and evaluation of the clear-PEM detector for positron emission mammography. *IEEE Nuclear Science Symposium Conference Record* 1-7:3805-3809, 2004.

N. Matela, M. V. Martins, P. Rodrigues, A. Trindade, N. Oliveira, L. Peralta, N. C. Ferreira, J. Varela, P.D. Almeida. System matrix calculation for Clear-PEM using ART and linograms. *IEEE Nuclear Science Symposium Conference Record* 1-7:2601-2604, 2004.

A. Trindade, P. Almeida, F. Balau, N. C. Ferreira, S. Fetal, F. Fraga, M. V. Martins, N. Matela, P. Mendes, R. Moura, C. Ortigao, L. Peralta, R. Ribeiro, P. Rodrigues, J. Varela. Clear-PEM: Monte Carlo performance and image reconstruction studies. *IEEE Nuclear Science Symposium Conference Record* 1-5:1918-1922, 2004.

N. Matela, M. V. Martins, P. Rodrigues, A. Trindade, N. Oliveira, L. Peralta, N.C. Ferreira, J. Varela, P. Almeida. System matrix calculation for Clear-PEM using aART and linograms. *Proceedings of Bioeng2003 - 7th Portugues Conference on Biomedical Engineering*, 2003.

L. Peralta, P. Almeida, F. Balau, N. Ferreira, S. Fetal, F. fraga, M. V. Martins N. Matela, P. Mendes. R. Moura, C.Ortigo, R. Ribeiro, P. Rodrigues, A. Trindade, J. Varela. Clear-PEM: A dedicated PET camera for improved breast cancer detection. *Proceedings of Bioeng2003 - 7th Portugues Conference on Biomedical Engineering*, 2003.

G. Santin, D. Strul, D. Lazaro, L. Simon, M. Krieguer, M. V. Martins, V. Breton, C. Morel. GATE, a Geant-4 based simulation platform for PET and SPECT integrating time movement and time management. *IEEE Nuclear Science Symposium Conference Record*, 2003.

List of Tables

3.1 Properties of common scintillator crystals used in positron emission tomography. Adapted from [50]. 22

5.1 FDG concentration in normal breast tissue and in simulated lesions used with the NCAT breast phantom and the corresponding lesion-to-background ratios. 67

7.1 Values of mean a variance in large ROIs drawn in uniform images after the addition of Poisson noise 104

7.2 Values of the number of full iterations of the Analytical Cross Phantom reconstructed images needed to achieve convergence and the corresponding computation times. 108

7.3 Values of the mean number of counts in a ROI drawn over the reconstructed images of the Analytical Sphere Phantom after convergence is achieved, with the corresponding number of full iterations, for all the number of subsets studied. 110

7.4 Computation time per iteration for the image reconstruction of the Analytical Cross Phantom and of the Analytical Sphere Phantom images with 1, 2 and 3 rays used to trace each bin in the transaxial direction. . 116

7.5 Approximate computation time per iteration of the image reconstruction of the Analytical Cross Phantom and of the Analytical Sphere Phantom images for the studied combinations of the geometrical symmetries. . . . 121

8.1 Spatial resolution values parameterized as the FWHM of Gaussian fits to the profiles taken along the transverse, radial and axial profiles of all the point sources of the Cross Phantom at the iteration of convergence, in the simplified version of the simulated Clear−PEM scanner. 126

8.2 Spatial resolution values (FWHM) listed for the point sources of the Chain Phantom placed along an horizontal line in the central axial slice (point sources 0 to 4), for the simulated static acquisitions and the several DOI resolution scenarios considered. The FWHM values listed are in mm. 138

8.3 Spatial resolution values (FWHM) listed for the point sources of the Chain Phantom placed along a vertical line in the central axial slice (point sources 0 and 5 to 8), for the simulated static acquisitions and the several DOI resolution scenarios considered. The FWHM values listed are in mm. 139
8.4 Spatial resolution values (FWHM) listed for the point sources of the Chain Phantom placed along the axis of rotation of the scanner (point sources 0 and 9 to 13), for the simulated static acquisitions and the several DOI resolution scenarios considered. The FWHM values listed are in mm. 139
8.5 Spatial resolution values (FWHM) listed for the point sources of the Chain Phantom placed along an horizontal line in the central axial slice (point sources 0 to 4), for the simulated dual angle acquisitions and the several DOI resolution scenarios considered. The FWHM values listed are in mm. 145
8.6 Spatial resolution values (FWHM) listed for the point sources of the Chain Phantom placed along a vertical line in the central axial slice (point sources 0 and 5 to 8), for the simulated dual angle acquisitions and the several DOI resolution scenarios considered. The FWHM values listed are in mm. 145
8.7 Spatial resolution values (FWHM) listed for the point sources of the Chain Phantom placed along the axis of rotation of the scanner (point sources 0 and 9 to 13), for the simulated dual angle acquisitions and the several DOI resolution scenarios considered. The FWHM values listed are in mm. 145

9.1 FWHM (mm^3) for the Chain Phantom images reconstructed with different prior weights (β). 169

List of Figures

2.1 Breast cancer images obtained with several imaging modalities. 10
2.2 FDG PET-CT breast exam. 17

3.1 Schematic drawings of some of the effects that degrade spatial resolution in PET 23
3.2 Schematic drawing of the PEM-I detector 25
3.3 Weighted backprojection used in the PEM-I scanner. 26
3.4 Typical set of images obtained with the PEM-I scanner 27
3.5 The PEM Flex system. 28
3.6 Image of DCIS obtained with the PEM Flex scanner 28
3.7 Image of the West Virginia University - Jefferson Laboratory PEM system. 29
3.8 Image of the Duke University - Jefferson Laboratory PEM system. . . . 30
3.9 Representation of the geometry of the LBNL PEM scanner 32
3.10 Phantom images obtained with the YAP-PEM prototype 33

4.1 Representation of the coordinates of the LORs in a 3D Sinogram 36
4.2 Parallel projection of the object corresponds to a row in the sinogram . 37
4.3 A centered and an off-centered point source in sinogram representation. 38
4.4 LORs belonging to direct and oblique segments in a four ring scanner. . 38
4.5 Length of Intersection and Tube of Intersection computation of the system matrix elements 41
4.6 Schematic representation of a generic iterative reconstruction algorithm. 46
4.7 Schematic drawing of the use subsets. 51

5.1 Representation of the Clear-PEM system. 60
5.2 Representation of a Clear-PEM detector head, with an highlighted detector supermodule. 60
5.3 Representations of a Clear-PEM detector module with the double readout scheme. 61
5.4 Schematic representation of the Monte Carlo framework developed for Clear-PEM simulation studies. 62

5.5 Scheme of a ClearPEM standard acquisition. 63
5.6 Geometrical phantoms used in the simplified geometry studies 65
5.7 The Chain Phantom that was used in the realistic geometry studies . . 65
5.8 The NCAT Brest Phantom with two simulated lesions 66
5.9 Terminology for the body planes and for the breast planes. 68

6.1 Hierarchy of classes for describing images. 70
6.2 Coordinate system for the projection data and images used in STIR. . . 71
6.3 Axial section through the image volume and the detector rings 71
6.4 File Formats for Projection Data 72
6.5 Hierarchy of classes for storing segments. 72
6.6 Volume Mode and View Mode storage for 3D PET data sets. 73
6.7 Hierarchy of classes for geometric information of the projection data . . 73
6.8 Hierarchy of classes for Projection Matrix 75
6.9 Hierarchy of classes for Forward Projection operators 75
6.10 Central idea beyond Siddon's algorithm 76
6.11 Hierarchy of classes for Backprojection operators 77
6.12 Basic principle of backprojecting by bilinear interpolation 78
6.13 A beam, defined by four adjacent projection elements. 79
6.14 Hiarchy of classes for Data Symmetries 82
6.15 Hierarchy of classes for Symmetry Operations 83
6.16 Hierarchy of classes for Image Reconstruction. 83
6.17 Hierarchy of classes for describing image priors 87

7.1 The ProjDataInfoPlanar class in the ProjDataInfo hierarchy. 92
7.2 Different relations between the opposing detector heads distance (D) and the length of the detector heads (L) leads to different sinogram fillings . 93
7.3 Expected empty sinogram bins 94
7.4 Definition of the azimuthal shift 95
7.5 Schematic drawing of how the DOI information is taken into account in the image reconstruction process. 99
7.6 The *ProjMatrixByBinForPEM* class that has been added to the *ProjMatrixByBin* hierarchy. 100
7.7 Flux diagram for the method *calculate_proj_matrix_elems_for_one_bin* in the *ProjMatrixByBinForPEM* class. 101
7.8 Images of the central slices of the Analytical Sphere Phantom and of the Analytical Cross Phantom and central slices of the corresponding segment 0 sinograms. 103
7.9 Central slice of the the images with an uniform circular area after adding Poisson noise. 103

7.10 Central slice of segment 0 sinograms of the Analytical Sphere Phantom and of the Analytical Sphere Phantom after the addition of Poisson noise. 104
7.11 Central slice and profiles of the Analytical Sphere Phantom and Analytical Cross Phantom reconstructed images. 105
7.12 Profiles nomenclature. 106
7.13 FWHM against full iteration number for point sources in the Analytical Cross Phantom. 107
7.14 Mean number of counts and standard deviation against iteration number for the Analytical Sphere Phantom reconstructed images. 109
7.15 Mean over Standard Deviation against the number of full iterations for the Analytical Sphere Phantom reconstructed images. 110
7.16 Central slice images of the Analytical Sphere Phantom reconstructed images with ML-EM and OS-EM with the number of subsets studied, at the corresponding iteration of convergence. 112
7.17 Profiles of the Analytical Sphere Phantom reconstructed images with the different number of subsets. 112
7.18 FWHM against iteration number for point sources of the Analytical Cross Phantom reconstructed images with different number of rays to trace each bin in the transaxial direction. 113
7.19 Images of the subtraction of original Cross Phantom image and the images reconstructed number of rays in the transaxial direction. 114
7.20 Plots of the mean and standard deviation inside the ROI in the Analytical Sphere images against iteration number for the 1, 2 and 3 rays to trace each bin in the transaxial direction. 115
7.21 Image uniformity index against iteration number for the Analytical Sphere reconstructed images different number of rays in the transaxial direction. 115
7.22 Images of the Analytical Sphere Phantom reconstructed with different number of rays in the transaxial direction. 115
7.23 Image spatial resolution against the iteration number for point sources of the Analytical Cross Phantom reconstructed images with the several symmetries 117
7.24 Central slice of the images resulting from the subtraction of the Cross Phantom image reconstructed without symmetries and the images reconstructed with the symmetries 119
7.25 Plots of the mean counts and standard deviation inside the ROI against the iteration number for the images reconstructed with the studied uses of the geometrical symmetries. 119
7.26 Plots of the uniformity index against the iteration number for the images reconstructed with the studied uses of the geometrical symmetries. . . . 120

7.27 Central slice of the images resulting from the subtraction of the Sphere Phantom image reconstructed without the geometrical symmetries and the images reconstructed with the geometrical symmetries. 120
7.28 Central slices of segment 0 sinograms and reconstructed images of the Analytical Cross Phantom and of the Analytical Sphere Phantom for one angular plates position simulated acquisitions. 122

8.1 Segment 0 sinogram of the Cross Phantom Monte Carlo simulated data in the simplified version of the Clear−PEM scanner. Central slice and profile of the respective reconstructed image. 125
8.2 FWHM values against iteration number measured for the Cross Phantom reconstructed images in the simplified geometry of the Clear−PEM scanner 127
8.3 Segment 0 sinogram of the Sphere Phantom Monte Carlo simulated data in the simplified version of the Clear−PEM scanner. Central slice and profile of the respective reconstructed image. 128
8.4 Mean number of counts and standard deviation inside the ROI against iteration number for the reconstructed images of the Sphere Phantom Monte Carlo simulated data in the simplified geometry of the Clear−PEM scanner. 128
8.5 Uniformity index of the reconstructed images of the Sphere Phantom in the simplified version of the Clear−PEM scanner as a function of iteration number. 129
8.6 Simulated static acquisition reconstructed images of the Chain Phantom. 131
8.7 Profiles of some of the point sources of the Chain Phantom reconstructed images corresponding to simulated acquisitions in static mode 132
8.8 FWHM values against iteration number for the simulated static acquisition reconstructed images, for different DOI information values. 134
8.9 Acceptance angle for point source 3 and for point source 7 of the Chain Phantom in the simulated static mode acquisition 135
8.10 Plots of the volumetric FWHM against iteration number for the simulated static acquisitions, with no DOI information 5 mm FWHM DOI, 2 mm FWHM DOI and exact DOI. 136
8.11 Plots of volumetric FWHM against distance to FOV center, for the simulated static acquisitions 138
8.12 Reconstructed images of the Chain Phantom simulated data with dual angle acquisition. 141
8.13 Acceptance angle for point source 3 and for point source 7 of the Chain Phantom in the simulated dual angle acquisition 142

8.14 Profiles of some of the point sources of the Chain Phantom reconstructed images corresponding to dual angle simulated acquisitions 143
8.15 FWHM values against iteration number for the simulated dual angle acquisition reconstructed images with several values for the DOI information.144
8.16 A point source placed near the edge of the FOV contributes differently to the radial and to the transverse components of the spatial resolution 146
8.17 Plots of the volumetric FWHM against iteration number for simulated dual angle acquisitions, for different values of the DOI information. . . . 147
8.18 Plots of volumetric FWHM against distance to FOV center, for the simulated dual angle acquisitions 148
8.19 Comparison of the volumetric FWHM values as a distance to the FOV center, both for simulated static and dual angle acquisition 149
8.20 Uncorrected reconstructed image of the NCAT Breast phantom. 151
8.21 Planar source for the experimental determination of the normalization components. Adapted from [170]. 152
8.22 Surface maps of the sensitivity image calculated with Monte Carlo simulation techniques. 152
8.23 Regions of interest used to perform the analysis of the NCAT breast phantom reconstructed images. 153
8.24 Central coronal slice of the reconstructed images of the NCAT Breast phantom with the 3 mm diameter lesions for the several lesion-to-background studied. 154
8.25 Central coronal slice and profile of the reconstructed images of the NCAT Breast phantom and lesions for the lesion-to-background L1. 155
8.26 Central coronal slice and profile of the reconstructed images of the NCAT Breast phantom and lesions for the lesion-to-background ratios L2 . . . 155
8.27 Central coronal slice and profile of the reconstructed images of the NCAT Breast phantom and lesions for the lesion-to-background ratio L3. . . . 156
8.28 Central coronal slice and profile of the reconstructed images of the NCAT Breast phantom and lesions for the lesion-to-background ratio L4. . . . 156
8.29 Contrast against noise for the lesion-to-background ratio L1 in the NCAT Breast Phantom reconstructed images. 158
8.30 Contrast against noise for the lesion-to-background ratio L2 in the NCAT Breast Phantom reconstructed images. 158
8.31 Contrast against noise for the lesion-to-background ratio L3 in the NCAT Breast Phantom reconstructed images. 159
8.32 Contrast against noise for the lesion-to-background ratio L4 in the NCAT Breast Phantom reconstructed images. 159

8.33 Plots of the values of the signal-to-noise ratio against contrast for the reconstructed images of the NCAT Breast Phantom the lesion-to-background ratio L1. 160
8.34 Plots of the values of the signal-to-noise ratio against contrast for the reconstructed images of the NCAT Breast Phantom for the lesion-to-background ratio L2. 160
8.35 Plots of the values of the signal-to-noise ratio against contrast for the reconstructed images of the NCAT Breast Phantom for the lesion-to-background ratio L3. 161
8.36 Plots of the values of the signal-to-noise ratio against contrast for the reconstructed images of the NCAT Breast Phantom for the lesion-to-background ratio L4. 161
8.37 Contrast recovery against lesion diameter. 164
8.38 Signal-to-noise ratio against lesion diameter. 164

9.1 Central sagittal and axial slices of the Chain Phantom reconstructed images with the Bayesian algorithm. 169
9.2 Bayesian reconstructed images of the NCAT Breast phantom with the lesion-to-background ratio L1. 171
9.3 Bayesian reconstructed images of the NCAT Breast phantom with the lesion-to-background ratio L2. 172
9.4 Bayesian reconstructed images of the NCAT Breast phantom with the lesion-to-background ratio L3. 173
9.5 Bayesian reconstructed images of the NCAT Breast phantom with the lesion-to-background ratio L4. 174
9.6 Contrast against noise for the Bayesian reconstructed images of the NCAT Breast phantom with the lesion-to-background ratio L1. 175
9.7 Contrast against noise for the Bayesian reconstructed images of the NCAT Breast phantom with the lesion-to-background ratio L2. 176
9.8 Contrast against noise for the Bayesian reconstructed images of the NCAT Breast phantom with the lesion-to-background ratio L3. 177
9.9 Contrast against noise for the Bayesian reconstructed images of the NCAT Breast phantom with the lesion-to-background ratio L4. 178
9.10 Signal-to-noise ratio against contrast for all the prior weights of the Bayesian algorithm considered, and for the lesion-to-background ratio L1. 180
9.11 Signal-to-noise ratio against contrast for all the prior weights of the Bayesian algorithm considered, and for the lesion-to-background ratio L2. 181

9.12 Signal-to-noise ratio against contrast for all the prior weights of the Bayesian algorithm considered, and for the lesion-to-background ratio L3. 182
9.13 Signal-to-noise ratio against contrast for all the prior weights of the Bayesian algorithm considered, and for the lesion-to-background ratio L4. 183
9.14 Contrast against centered lesion diameter for the images reconstructed with the Bayesian algorithm. 184
9.15 Contrast against off-centered lesion diameter for the images reconstructed with the Bayesian algorithm. 185
9.16 Signal-to-noise ratio against centered lesion diameter for the images reconstructed with the Bayesian algorithm. 187
9.17 Signal-to-noise ratio against off-centered lesion diameter for the images reconstructed with the Bayesian algorithm. 188

Bibliography

[1] Cancer facts and figures 2007. Technical report, American Cancer Society, 2007.

[2] I. Mathieu, S. Mazy, B. Willemart, M. Destine, G. Mazy, and M. Lonneux. Inconclusive triple diagnosis in breast cancer imaging: Is there a place for scintimammography? *J Nucl Med*, 46(10):1574–1581, 2005.

[3] A. M. Wallace, C. Comstock, C. K. Hoh, and D. R. Vera. Breast imaging: a surgeon's prospective. *Nuclear Medicine and Biology*, 32(7):781–792, 2005.

[4] A. K Buck, H. Schirrmeister, T. Mattfeldt, and S. Reske. Biological characterisation of breast cancer by means of PET. *European Journal of Nuclear Medicine Molecular Imaging*, 31(0):S80–S87, 2004.

[5] J. A. Smith and E. Andreopoulou. An overview of the status of imaging screening technology for breast cancer. *Annals of Oncology*, 15(Suppl1):18–26, 2004.

[6] S. K. Shah and K. V. Greatrex. Current role of magnetic resonance imaging in breast imaging: A primer for the primary care physician. *Journal of the American Board of Family Practice*, 18(6):478–490, 2005.

[7] K. Flobbe, P. J. Nelemans, A. G. H. Kessels, G. L. Beets, M. F. von Meyenfeldt, and J. M. A. van Engelshoven. The role of ultrasonography as an adjunct to mammography in the detection of breast cancer: a systematic review. *European Journal of Cancer*, 38(8):1044–1050, 2002.

[8] S. P. Weinstein, E. F. Conant, and C. Sehgal. Technical advances in breast ultrasound imaging. *Seminars in Ultrasound, CT, and MRI*, 27(4):273–283, 2006.

[9] C. M. Sehgal, P. H. Arger, S. E. Rowling, E. F. Conant, C. Reynolds, and J. A. Patton. Quantitative vascularity of breast masses by Doppler imaging: regional variations and diagnostic implications. *J Ultrasound Med*, 19(7), 2000. Abstract.

[10] J. L. del Cura, E. Elizagaray, R. Zabala, A. Legorburu, and D. Grande. The use of unenhanced Doppler sonography in the evaluation of solid breast lesions. *Am J Roentgenol*, 184(6):1788–94, 2005.

[11] J. Kettenbach, T. H. Helbich, S. Huber, I. Zuna, and W. Dock. Computer-assisted quantitative assessment of power Doppler US: effects of microbubble contrast agent in the differentiation of breast tumors. *Eur J Radiol*, 53(2):238–244, 2005.

[12] S. G. Orel and M. D. Schnall. MR imaging of the breast for the detection, diagnosis, and staging of breast cancer. *Radiology*, 220(1):13–30, 2001.

[13] E. A. Morris. Screening for breast cancer with MRI. *Seminars on Ultrasound CT MR*, 24(1):45–54, 2003.

[14] C. K. Kuhl, W. Kuhn, and H. Schild. Management of women at high risk for breast cancer: New imaging beyond mammography. *Breast*, 14(6):480–486, 2005.

[15] A. Dardik. Use of magnetic resonance imaging in breast oncology. *J Am Coll Surg*, 200(5):742–742, 2005.

[16] D. Saslow, C. Boetes, W. Burke, S. Harms, M. O. Leach, C. D. Lehman, E. Morris, E. Pisano, M. Schnall, S. Sener, R. A. Smith, E. Warner, M. Yaffe, K. S. Andrews, and C. A. for the American Cancer Society Breast Cancer Advisory Group Russell. American cancer society guidelines for breast screening with MRI as an adjunct to Mammography. *CA Cancer J Clin*, 57(2):75–89, 2007.

[17] L. Esserman, D. Wolverton, and N. Hylton. Magnetic resonance imaging for primary breast cancer management: current role and new applications. *Endocr Relat Cancer*, 9(2):141–53, 2002.

[18] K. Planche and S. Vinnicombe. Breast imaging in the new era. *Cancer Imaging*, 4(2):39–50, 2003.

[19] F. Giammarile and A. Bremond. Diagnostic of breast cancer: what do clinicians expect from PEM? *Nuclear Instruments & Methods in Physics Research Section A: Accelerators Spectrometers Detectors and Associated Equipment*, 527(1-2):83–86, 2004.

[20] S.G. Orel, M.D. Schnall, R.W. Newman, C.M. Powell, M.H. Torosian, and E.F. Rosato. MR imaging-guided localization and biopsy of breast lesions: initial experience. *Radiology*, 193(1):97–102, 1994.

[21] B.L. Daniel, R.L. Birdwell, D.M. Ikeda, S.S. Jeffrey, J.W. Black, W.F. Block, A.M. Sawyer-Glover, G.H. Glover, and R.J. Herfkens. Breast lesion localization: a freehand, interactive MR imaging-guided technique. *Radiology*, 207(2):455–463, 1998.

[22] L. Liberman, E. A. Morris, D. D. Dershaw, C. M. Thornton, K. J. Van Zee, and L. K. Tan. Fast MRI-guided vacuum-assisted breast biopsy: Initial experience. *Am. J. Roentgenol.*, 181(5):1283–1293, 2003.

[23] O. Schillaci and J.R. Buscombe. Breast scintigraphy today: indications and limitations. *European Journal of Nuclear Medicine and Molecular Imaging*, 31(0):S35–S45, 2004.

[24] S. Vecchio and M. Salvatore. ^{99m}tc-mibi in the evaluation of breast cancer biology. *European Journal of Nuclear Medicine and Molecular Imaging*, 31(0):S88–S96, 2004.

[25] F. S. Sampalis, R. Denis, D. Picard, D. Fleiszer, G. Martin, E. Nassif, and J. S. Sampalis. International prospective evaluation of scintimammography with 99^m Technetium Sestamibi. *The American Journal of Surgery*, 185(6):544–549, 2003.

[26] I. Khalkhali, J. K. Baum, J. Villanueva-Meyer, S. L. Edell, L. G. Hanelin, C. E. Lugo, R. Taillefer, L. M. Freeman, C. E. Neal, A. M. Scheff, J. L. Connolly, S. J. Schnitt, M. J. Houlihan, J. S. Sampalis, and S. B. Haber. 99^mtc Sestamibi breast imaging for the examination of patients with dense and fatty breasts: Multicenter study. *Radiology*, 222(1):149–155, 2002.

[27] R. Taillefer. Clinical applications of Tc-99m-sestamibi scintimammography. *Seminars in Nuclear Medicine*, 35(2):100–115, 2005.

[28] D. Gopalan, J. B. Bomanji, D. C. Costa, and P. J. Ell. Nuclear medicine in primary breast cancer imaging. *Clinical Radiology*, 57(7):565–574, 2002.

[29] R. F. Brem, J. M. Schoonjans, D. A. Kieper, S. Majewski, S. Goodman, and C. Civelek. High-resolution scintimammography: a pilot study. *J Nucl Med*, 43(7):909–15, 2002. 0161-5505 (Print) Journal Article.

[30] L.R. Coover, G. Caravaglia, and P. Kuhn. Scintimammography with dedicated breast camera detects and localizes occult carcinoma. *J Nucl Med*, 45(4):553–558, 2004.

[31] F. Scopinaro, R. Pani, G. De Vincentis, A. Soluri, R. Pellegrini, and L. M. Porfiri. High-resolution scintimammography improves the accuracy of technetium-99m methoxyisobutylisonitrile scintimammography: use of a new dedicated gamma camera. *European Journal of Nuclear Medicine and Molecular Imaging*, 26(10):1279–1288, 1999.

[32] D. J. Rhodes, M. K. O'Connor, S. W. Phillips, R. L. Smith, and D. A. Collins. Molecular breast imaging: A new technique using Technetium 99^mtc scintimammography to detect small tumors of the breast. *Mayo Clin Proc*, 80(1):24–30, 2005.

[33] O. Schillaci. Is there a clinical role for scintimammography in breast cancer diagnosis? *J Nucl Med*, 46(10):1571–1573, 2005.

[34] Richard L. Wahl. Current status of PET in breast cancer imaging, staging, and therapy. *Seminars in Roentgenology Breast Imaging*, 36(3):250–260, 2001.

[35] L. Kostakoglu, Jr. Agress, H., and S. J. Goldsmith. Clinical role of FDG PET in evaluation of cancer patients. *Radiographics*, 23(2):315–340, 2003.

[36] L. Tafra. Positron emission tomography (PET) and mammography (PEM) for breast cancer: Importance to surgeons. *Annals of Surgical Oncology*, 2006.

[37] W. B. Eubank and D. A. Mankoff. Evolving role of positron emission tomography in breast cancer imaging. *Seminars in Nuclear Medicine*, 35(2):84–99, 2005.

[38] D. Vranjesevic, C. Schiepers, D.H. Silverman, A. Quon, J. Villalpando, M. Dahlbom, M.E. Phelps, and J. Czernin. Relationship between 18F-FDG uptake and breast density in women with normal breast tissue. *Journal of Nuclear Medicine*, 44(8):1238–1242, 2003.

[39] A. M. Byrne, A. D. K. Hill, S. J. Skehan, E. W. McDermott, and N. J. O'Higgins. Positron emission tomography in the staging and management of breast cancer. *British Journal of Surgery*, 91(11):1398–1409, 2004.

[40] P. Lind, I. Igerc, T. Beyer, P. Reinprecht, and K. Hausegger. Advantages and limitations of FDG PET in the follow-up of breast cancer. *European Journal of Nuclear Medicine Molecular Imaging*, 31(S1):S125–S134, 2004.

[41] K. Scheidhauer, C. Walter, and M.D. Seemann. FDG PET and other imaging modalities in the primary diagnosis of suspicious breast lesions. *European Journal of Nuclear Medicine and Molecular Imaging*, 31(0):S70–S79, 2004.

[42] K. Murthy, A. Bergman, C. Thompson, J. Robar, R. Lisbona, A. Loutfi, and J. Gagnon. Early clinical results from PEM-1: A high resolution system for positron emission mammography. In *1997 IEEE Nuclear Science Symposium - Conference Record, Vols 1 & 2*, pages 994–997, 1998.

[43] R. R. Raylman, S. Majewski, R. Wojcik, A. G. Weisenberger, B. Kross, V. Popov, J. S. Schreiman, and H. A. Bishop. An apparatus for positron emission mammography guided biopsy. In *1999 IEEE Nuclear Science Symposium - Conference Record, Vols 1-3*, pages 1323–1327, 1999.

[44] N. K. Doshi, Y. Shao, R. W. Silverman, and S. R. Cherry. Design and evaluation of an LSO PET detector for breast cancer imaging. *Medical Physics*, 27(7):1535–43, 2000.

[45] J. S. Huber, W. S. Choong, J. Wang, J. S. Maltz, J. Qi, E. Mandelli, and W. W. Moses. Development of the lbnl positron emission mammography camera. *IEEE Trans Nucl Sci*, 50(5):1650–1653, 2003.

[46] E. A. Levine, R. I. Freimanis, N. D. Perrier, K. Morton, N. M. Lesko, S. Bergman, K. R. Geisinger, R. C. Williams, C. Sharpe, V. Zavarzin, I. N. Weinberg, P. Y. Stepanov, D. Beylin, K. Lauckner, M. Doss, J. Lovelace, and L. P. Adler. Positron emission mammography: Initial clinical results. *Annals of Surgical Oncology*, 10(1):86–91, 2003.

[47] E.L. Rosen, T.G. Turkington, M.S. Soo, J.A. Baker, and R.E. Coleman. Detection of primary breast carcinoma with a dedicated, large-field-of-view FDG PET mammography device: Initial experience. *Radiology*, 234(2):527–534, 2005.

[48] L. Tafra, Z. Cheng, J. Uddo, M. B. Lobrano, W. Stein, W. A. Berg, E. Levine, I. N. Weinberg, D. Narayanan, E. Ross, D. Beylin, S. Yarnall, R. Keen, K. Sawyer, J. Van Geffen, R. L. Freimanis, E. Staab, L. P. Adler, J. Lovelace, P. Shen, J. Stewart, and S. Dolinsky. Pilot clinical trial of 18f-fluorodeoxyglucose positron-emission mammography in the surgical management of breast cancer. *Am J Surg*, 190(4):628–32, 2005.

[49] W. A. Berg, I. N. Weinberg, D. Narayanan, M. E. Lobrano, E. Ross, L. Amodei, L. Tafra, L. P. Adler, J. Uddo, 3rd Stein, W., and E. A. Levine. High-resolution fluorodeoxyglucose positron emission tomography with compression ("positron emission mammography") is highly accurate in depicting primary breast cancer. *Breast J*, 12(4):309–23, 2006.

[50] Craig Levin. Primer on molecular imaging technology. *European Journal of Nuclear Medicine and Molecular Imaging*, 32(14):S325–S345, 2005.

[51] D. L. Bayley, J. S. Karp, and S. Surti. *Physics and Instrumentation in PET*. Positron Emission Tomography. Springer-Verlag, 2003.

[52] M. Defrise, K. E. Kinanan, and M. Christian. *Image Reconstruction Algorithms in PET*. Positron Emission Tomography. Springer-Verlag, 2003.

[53] J. L. Humm, A. Rosenfeld, and A. Del Guerra. From PET detectors to PET scanners. *Eur J Nucl Med Mol Imaging*, 30(11):1574–97, 2003.

[54] P. Bruyndonckx, S. Leonard, J.G. Liu, S. Tavernier, P. Szupryczynski, and A. Fedorov. Study of spatial resolution and depth of interaction of APD-based PET detector modules using light sharing schemes. *IEEE Transactions on Nuclear Science*, 50(5, part2):1415–1419, 2003.

[55] C. Knoess, R. Boellaard, M. Lenox, S. Vollmar, M. Casey, G. Fluegge, A.A Lammertsma, K. Wienhard, and W.D. Heiss. Evaluation of the depth of interaction (doi) for the high resolution research tomograph (hrrt) - a comparison between scanners with and without doi. In *2002 IEEE Nuclear Science Symposium, Conference Records, Vols 1-3*, pages 1447–1451.

[56] L. R. MacDonald and M. Dahlbom. Parallax correction in PET using depth of interaction information. *IEEE Transactions on Nuclear Science*, 45(4):2232–2237, 1998.

[57] N. Zhang, C. J. Thompson, F. Cayouette, D. Jolly, and S. Kecani. A prototype modular detector design for high resolution positron emission mammography imaging. *IEEE Transactions on Nuclear Science*, 50(5):1624–1629, 2003.

[58] J. Joung, R. S. Miyaoka, and T. K. Lewellen. cMiCE: a high resolution animal PET using continuous LSO with a statistics based positioning scheme. *Nuclear Instruments & Methods in Physics Research Section A: Accelerators Spectrometers Detectors and Associated Equipment*, 489(1-3):584–598, 2002.

[59] B. J. Pichler and S. I. Ziegler. *Photodetectors*. Emission Tomography - The Fundamentals of PET and SPECT. Elsevier Academic Press, 2004.

[60] C. J. Thompson, K. Murthy, I. N. Weinberg, and F. Mako. Feasibility study for positron emission mammography. *Medical Physics*, 21(4):529–38, 1994.

[61] C. J. Thompson, K. Murthy, Y. Picard, I. N. Weinberg, and R. Mako. Positron emission mammography (PEM) - a promising technique for detecting breast-cancer. *IEEE Transaction on Nuclear Science*, 42(4):1012–1017, 1995.

[62] A. M. Bergman, C. J. Thompson, K. Murthy, J. L. Robar, and R. L. Clancy. Coregistration of positron emission mammography (pem) images and x-ray mammograms. In *1996 IEEE Nuclear Science Symposium - Conference Record, Vols 1-3*, pages 1812–1816, 1997.

[63] J. L. Robar, C. J. Thompson, K. Murthy, R. Clancy, and A. M. Bergman. Construction and calibration of detectors for high-resolution metabolic breast cancer

imaging. *Nuclear Instruments & Methods in Physics Research Section A: Accelerators Spectrometers Detectors and Associated Equipment*, 392(1-3):402–406, 1997.

[64] J. L. Robar, C. J. Thompson, K. Murthy, R. L. Clancy, and A. M. Bergman. Correction of spatial distortion, gain nonuniformity and efficiency variation in detectors for positron emission mammography. In *1996 IEEE Nuclear Science Symposium - Conference Record, Vols 1-3*, pages 1206–1210, 1997.

[65] K. Murthy, M. Aznar, C. J. Thompson, A. Loutfi, R. Lisbona, and J. H. Gagnon. Results of preliminary clinical trials of the positron emission mammography system PEM-I: a dedicated breast imaging system producing glucose metabolic images using fdg. *Journal of Nuclear Medicine*, 41(11):1851–8, 2000.

[66] K. Murthy, M. Aznar, A. M. Bergman, C. J. Thompson, J. L. Robar, R. Lisbona, A. Loutfi, and J. H. Gagnon. Positron emission mammographic instrument: initial results. *Radiology*, 215(1):280–5, 2000.

[67] K. Murthy, D. Jolly, M. Aznar, C. J. Thompson, P. Sciascia, A. Loutfi, R. Lisbona, and J. H. Gagnon. Quantification in positron emission mammography (PEM) with planar detectors: Contrast resolution measurements using a custom breast phantom and novel spherical hot-spots. *IEEE Transaction on Nuclear Science*, 46(6):2192–2196, 1999.

[68] S.D. Wollenweber, R.C. Williams, D. Beylin, S. Dolinsky, and I.N. Weinberg. Investigation of the quantitative capabilities of a positron emission mammography system. In *Nuclear Science Symposium Conference Record, 2004 IEEE*, volume 4, pages 2393–2395, 2004.

[69] I.N. Weinberg, P.Y. Stepanov, D. Beylin, V. Zavarzin, E. Anashkin, K. Lauckner, S. Yarnall, M. Doss, R. Pani, and L.P. Adler. PEM-2400 - a biopsy-ready PEM scanner with real-time x-ray correlation capability. In *Nuclear Science Symposium Conference Record, 2002 IEEE*, volume 2, pages 1128–1130 vol.2, 2002.

[70] I. Weinberg, D. Beylin, S. Yarnall, E. Anashkin, P. Stepanov, S. Dolinsky, V. Zavarzin, W. Peter, K. Lauckner, K. Morton, R. Freimanis, N. Lesko, E. Levine, N. Perrier, J. Lovelace, K. Geisinger, R. Williams, S. Wollenweber, D. Narayanan, M. Doss, J. Hummel, E. Sigurdson, K. Evers, M. Torosian, and L. Adler. Applications of a PET device with 1.5 mm fwhm intrinsic spatial resolution to breast cancer imaging. In *2004 2nd IEEE International Symposium on Biomedical Imaging: Macro to Nano, Vols 1 and 2*, pages 1396–1399, 2004.

[71] R. R. Raylman, S. Majewski, R. Wojcik, A. G. Weisenberger, B. Kross, and V. Popov. Corrections for the effects of accidental coincidences, compton scatter, and object size in positron emission mammography (PEM) imaging. *IEEE Transactions on Nuclear Science*, 48(3):913–923, 2001.

[72] R. R. Raylman, S. Majewski, R. Wojcik, A. G. Weisenberger, B. Kross, V. Popov, and H. A. Bishop. The potential role of positron emission mammography for detection of breast cancer. a phantom study. *Medical Physics*, 27(8):1943–54, 2000.

[73] M. Smith, L. Majewski, A. Weisenberger, D. Kieper, J. D. Kalen, and P. Fatouros. Aspects of 3-D imaging by classical tomography for dual detector PEM. In *Procedings of 2001 International Meeting on Fully 3D Image Reconstruction in Radiology and Nuclear Medicine*, 2001.

[74] R. R. Raylman, S. Majewski, A. G. Weisenberger, V. Popov, R. Wojcik, B. Kross, J. S. Schreiman, and H. A. Bishop. Positron emission mammography-guided breast biopsy. *Journal of Nuclear Medicine*, 42(6):960–6, 2001.

[75] M. F. Smith, S. Majewski, A. G. Weisenberger, D. A. Kieper, R. R. Raylman, and T. G. Turkington. Analysis of factors affecting positron emission mammography (PEM) image formation. In *2001 IEEE Nuclear Science Symposium, Conference Records, Vols 1-4*, pages 2253–2257, 2002.

[76] M. F. Smith, R. R. Raylman, S. Majewski, and A. G. Weisenberger. Positron emission mammography with tomographic acquisition using dual planar detectors: initial evaluations. *Physics in Medicine and Biology*, 49(11):2437–52, 2004.

[77] R. R. Raylman, S. Majewski, B. Kross, V. Popov, J. Proffitt, M. F. Smith, A. G. Weisenberger, and R. Wojcik. Development of a dedicated positron emission tomography system for the detection and biopsy of breast cancer. *Nuclear Instruments & Methods in Physics Research Section A: Accelerators Spectrometers Detectors and Associated Equipment*, 569(2):291–295, 2006.

[78] T. G. Turkington, S. Majewski, A. G. Weisenberg, V. Popov, M. F. Smith, W. H. Sampson, R. Wojcik, and D. Kieper. A large field of view positron emission mammography imager. In *Nuclear Science Symposium Conference Record, 2002 IEEE*, volume 2, page 1883, 2002.

[79] N. K. Doshi, R. W. Silverman, Y. Shao, and S. R. Cherry. maxPET: A dedicated mammary and axillary region PET imaging system for breast cancer. *IEEE Trans Nucl Sci*, 48(3):811–815, 2001.

[80] F. Lamare, S.L. Bowen, D. Visvikis, P. Cortes, Y. Wu, V.-H. Tran, J.M. Boone, S.R. Cherry, and R.D. Badawi. Design simulation of a rotating dual-headed PET/CT scanner for breast imaging. In *Nuclear Science Symposium Conference Record, 2005 IEEE*, volume 3, 2005.

[81] G.-C. Wang, J.S. Huber, W.W. Moses, J. Qi, and W.-S. Choong. Characterization of the LBNL PEM camera. *IEEE Transaction on Nuclear Science*, 53(3):1129–1135, 2006.

[82] J. Y. Qi, G. J. Klein, and R. H. Huesman. Image properties of list-mode likelihood reconstruction for a rectangular positron emission mammograph with doi measurements. *IEEE Transaction on Nuclear Science*, 48(4):1343–1349, 2001.

[83] J. Y. Qi, C. C. Kuo, R. H. Huesman, G. J. Klein, W. W. Moses, and B. W. Reutter. Comparison of rectangular and dual-planar positron emission mammography scanners. In *2001 IEEE Nuclear Science Symposium, Conference Records, Vols 1-4*, pages 1246–1250, 2002.

[84] W. W. Moses, S. E. Derenzo, C. L. Melcher, and R. A. Manente. Room-temperature LSO pin photodiode PET detector module that measures depth of interaction. *IEEE Transactions on Nuclear Science*, 42(4):1085–1089, 1995.

[85] G. C. Wang, J. S. Huber, W. W. Moses, W. S. Choong, and J. S. Maltz. Calibration of a PEM detector with depth of interaction measurement. *IEEE Transactions on Nuclear Science*, 51(3):775–781, 2004.

[86] P. R. G. Virador, W. W. Moses, and R. H. Huesman. Reconstruction in PET cameras with irregular sampling and depth of interaction capability. *IEEE Transaction on Nuclear Science*, 45(3):1225–1230, 1998.

[87] P. R. G. Virador, W. W. Moses, R. H. Huesman, and J. Qi. 3-D reconstruction in PET cameras with irregular sampling and depth of interaction. *IEEE Transaction on Nuclear Science*, 48(4):1524–1529, 2001.

[88] R. H. Huesman, G. J. Klein, W. W. Moses, J. Qi, B. W. Reutter, and P. R. Virador. List-mode maximum-likelihood reconstruction applied to positron emission mammography (PEM) with irregular sampling. *IEEE Transactions on Medical Imaging*, 19(5):532–537, 2000.

[89] J. Y. Qi and R. H. Huesman. Lesion detection and quantitation of positron emission mammography. In *2001 IEEE Nuclear Science Symposium, Conference Records, Vols 1-4*, pages 2248–2252, 2002.

[90] A. Del Guerra, N. Belcari, W. Bencivelli, Motta A, and et al. Monte Carlo study and experimental measurements of breast tumor detectability with the YAP-PEM prototype. In *2002 IEEE Nuclear Science Symposium, Conference Records, Vols 1-4*, IEEE Nuclear Science Symposium - Conference Record, 2002.

[91] N. Belcari, M. Camarda, A. Del Guerra, D. Herbert, A. Motta, A. Vaiano, G. Di Domenico, and G. Zavattini. Development of a planar head PEM system based on an array of pspmt and yap crystals. volume 3, pages 2179–2182 Vol.3, 2003.

[92] A. Motta, A. D. Guerra, N. Belcari, S. Moehrs, D. Panetta, S. Righi, and D. Valentini. Fast 3D-EM reconstruction using planograms for stationary planar positron emission mammography camera. *Computerized Medical Imaging Graphics*, 29(8):587–96, 2005.

[93] D. Brasse, P. E. Kinahan, R. Clackdoyle, M. Defrise, C. Comtat, and D. W. Townsend. Fast fully 3-D image reconstruction in PET using planograms. *IEEE Transaction on Medical Imaging*, 23(4):413–25, 2004.

[94] J. A. Fessler. Isbi tutorial: Iterative methods for image reconstruction. *www.eecs.umich.edu/ fessler/papers/talk.html.*, 2006.

[95] D. Townsend and M. Defrise. Image reconstruction methods in positron tomography. In *Lectures given in the Academic Training Programme of CERN 1992-1993*. CERN, Geneva, 1993.

[96] A. J. Rockmore and A. Macovski. Maximum likelihood approach to emission image-reconstruction from projections. *IEEE Transactions on Nuclear Science*, 23(4):1428–1432, 1976.

[97] M.E. Daubewitherspoon and Muehllehner. Treatment of axial data in 3-dimensional PET. *Journal of Nuclear Medicine*, 28(11):1717–1724, 1987.

[98] M. Defrise, P. E. Kinahan, D. W. Townsend, C. Michel, M. Sibomana, and D. F. Newport. Exact and approximate rebinning algorithms for 3-D PET data. *IEEE Transactions on Medical Imaging*, 16(2):145–158, 1997.

[99] M. Jacobson, R. Levkovitz, A. Ben-Tal, K. Thielemans, T. Spinks, D. Belluzzo, E. Pagani, V. Bettinardi, M. C. Gilardi, A. Zverovich, and G. Mitra. Enhanced 3D PET OSEM reconstruction using inter-update metz filtering. *Physics in Medicine and Biology*, 45(8):2417–2439, 2000.

[100] H. Labbé, C.and Zaidi, Morel, and K C. Thielemans. Glossary for STIR, version 0.9.

[101] H. H. Barrett, L. Parra, and White T. List-mode likelihood. *Journal of the Optical Society of America A*, 14(11), 1997.

[102] J. A. Fessler. Penalized weighted least-squares image-reconstruction for positron emission tomography. *IEEE Transactions on Medical Imaging*, 13(2):290–300, 1994.

[103] R. M. Lewitt and S. Matej. Overview of methods for image reconstruction from projections in emission computed tomography. *Proceedings of the IEEE*, 91(10):1588–1611, 2003.

[104] R. M. Leahy and J. Y. Qi. Statistical approaches in quantitative positron emission tomography. *Statistics and Computing*, 10(2):147–165, 2000.

[105] R. M. Lewitt. Alternatives to voxels for image representation in iterative reconstruction algorithms. *Physics in Medicine and Biology*, 37(3):705–716, 1992.

[106] T. Frese, C. A. Bouman, and K. Sauer. Adaptive wavelet graph model for bayesian tomographic reconstruction. *Image Processing, IEEE Transactions on*, 11(7):756–770, 2002. 1057-7149.

[107] G. T. Gullberg, Y. L. Hsieh, and G. L. Zeng. An svd reconstruction algorithm using a natural pixel representation of the attenuated radon transform. *IEEE Transactions on Nuclear Science*, 43(1):295–303, 1996.

[108] S. Matej and R. M. Lewitt. Practical considerations for 3-d image reconstruction using spherically symmetric volume elements. *IEEE Transactions on Medical Imaging*, 15(1):68–78, 1996.

[109] W. Chlewicki, F. Hermansen, and S. B. Hansen. Noise reduction and convergence of bayesian algorithms with blobs based on the huber function and median root prior. *Physics in Medicine and Biology*, 49(20):4717–4730, 2004.

[110] J. Llacer and J. D. Meng. Matrix-based image-reconstruction methods for tomography. *IEEE Transactions on Nuclear Science*, 32(1):855–864, 1985.

[111] K. J. Kearfott. A statistical-model for positron emission tomography - practical considerations - comment. *Journal of the American Statistical Association*, 80(389):26–28, 1985.

[112] J. Qi, R. M. Leahy, S. R. Cherry, A. Chatziioannou, and T. H. Farquhar. High-resolution 3D bayesian image reconstruction using the microPET small-animal scanner. *Physics in Medicine and Biology*, 43(4):1001–13, 1998.

[113] M. L. Egger. *Fast Volume Reconstruction in Positron Emission Tomography: implementation of four algorithms on a high performance scalable parallel platform.* Ph.D dissertation, Université de Lausanne, 1996.

[114] R. L. Siddon. Fast calculation of the exact radiological path for a three-dimensional ct array. *Medical Physics*, 12(2):252–5, 1985.

[115] S.R. Cherry, J.A. Sorenson, and M. E. Phelps. *Physics in Nuclear Medicine.* Saundners, 3rd edition, 2003.

[116] M. Yavuz and J. A. Fessler. New statistical models for randoms-precorrected PET scans. *Information Processing in Medical Imaging*, 1230:190–203, 1997.

[117] R. Gordon. Tutorial on art - algebraic reconstruction techniques. *IEEE Transactions on Nuclear Science*, NS21(3):78–93, 1974.

[118] D. S. Lalush and M. N. Wernick. *Iterative Image Reconstruction.* Emission Tomography - The Fundamentals of PET and SPECT. Elsevier Academic Press, 2004.

[119] Fisher. On the "probable error" of a coefficient of correlation deduced from a small sampler. *Metron*, 1(1):3–32, 1921.

[120] T. K. Moon. The expectation-maximization algorithm. *IEEE Signal Processing Magazine*, 13(6):47–60, 1996.

[121] J. Llacer and E. Veklerov. Feasible images and practical stopping rules for iterative algorithms in emission tomography. *IEEE Transactions on Medical Imaging*, 8(2):186–193, 1989.

[122] L. A. Shepp and Y. Vardi. Maximum likelihood reconstruction for emission tomography. *IEEE Transactions on Medical Imaging*, MI-1(2):113–122, 1982.

[123] K. Lange and R. Carson. Em reconstruction algorithms for emission and transmission tomography. *Journal of Computerized Assisted Tomography*, 8(2):306–316, 1984.

[124] H. M. Hudson and R. S. Larkin. Accelerated image-reconstruction using ordered subsets of projection data. *IEEE Transactions on Medical Imaging*, 13(4):601–609, 1994.

[125] C. A. Johnson, J. Seidel, R. E. Carson, W. R. Gandler, A. Sofer, M. V. Green, and M. E. DaubeWitherspoon. Evaluation of 3D reconstruction algorithms for a small animal PET camera. In *1996 IEEE Nuclear Science Symposium - Conference*

Record, Vols 1-3, IEEE Nuclear Science Symposium - Conference Record, pages 1481–1485. I E E E, New York, 1997.

[126] S. Vandenberghe, Y. D'Asseler, R. Van de Walle, T. Kauppinen, M. Koole, L. Bouwens, K. Van Laere, I. Lemahieu, and R. A. Dierckx. Iterative reconstruction algorithms in nuclear medicine. *Computerized Medical Imaging Graphics*, 25(2):105–11, 2001.

[127] D. Pestana and S. Velosa. *Introdução à probabilidade e à estatística*. Fundação Calouste Gulbenkian, 2002.

[128] Y. Vardi, L. A. Shepp, and L. Kaufman. A statistical-model for positron emission tomography. *Journal of the American Statistical Association*, 80(389):8–20, 1985.

[129] S. Geman and D. Geman. Stochastic relaxation, gibbs distributions, and the bayesian restoration of images. *IEEE Transactions on Pattern Analysis and Machine Intelligence*, 6(6):721–741, 1984.

[130] Jinyi Qi and Richard M. Leahy. Iterative reconstruction techniques in emission computed tomography. *Physics in Medicine and Biology*, 51(15):R541–R578, 2006.

[131] R. Levitan and G. T. Herman. A maximum a posteriori probability expectation maximization algorithm for image reconstruction in emission tomography. *IEEE Transactions on Medical Imaging*, 6:185–192, 1997.

[132] D. F. Yu and J. A. Fessler. Edge-preserving tomographic reconstruction with nonlocal regularization. *IEEE Transactions on Medical Imaging*, 21(2):159–173, 2002.

[133] C. Comtat, P. E. Kinahan, J. A. Fessler, T. Beyer, D. W. Townsend, M. Defrise, and C. Michel. Clinically feasible reconstruction of 3D whole-body PET/CT data using blurred anatomical labels. *Physics in Medicine and Biology*, 47(1):1–20, 2002.

[134] J. Nuyts, K. Baete, D. Beque, and P. Dupont. Comparison between MAP and postprocessed ML for image reconstruction in emission tomography when anatomical knowledge is available. *Medical Imaging, IEEE Transactions on*, 24(5):667–675, 2005.

[135] S. Alenius and U. Ruotsalainen. Bayesian image reconstruction for emission tomography based on median root prior. *European Journal of Nuclear Medicine*, 24(3):258–65, 1997.

[136] T. Hebert and R. Leahy. A generalized EM algorithm for 3-D bayesian reconstruction from Poisson data using Gibbs priors. *IEEE Transactions on Medical Imaging*, 8(2):194–202, 1989.

[137] P. J. Green. Bayesian reconstruction from emission tomography data using a modified EM algortihm. *IEEE Transactions on Medical Imaging*, 9(1):84–93, 1990.

[138] K. Lange. Convergence of EM image reconstruction algorithms with Gibbs smoothing. *IEEE Transactions on Medical Imaging*, 9(4):439–446, 1990.

[139] S. Alenius, U. Ruotsalainen, and J. Astola. Using local median as the location of the prior distribution in iterative emission tomography image reconstruction. *IEEE Transactions on Nuclear Science*, 45(6):3097–3104, 1998.

[140] S. Alenius. *On Noise Reduction in Iterative Image Reconstruction Algorithms for Emission Tomography: Median Root Prior*. Ph.D dissertation, Tampere University of Technology, 1999.

[141] V. Bettinardi, E. Pagani, M. C. Gilardi, S. Alenius, K. Thielemans, M. Teras, and F. Fazio. Implementation and evaluation of a 3d one-step late reconstruction algorithm for 3d positron emission tomography brain studies using median root prior. *European Journal of Nuclear Medicine and Molecular Imaging*, 29(1):7–18, 2002.

[142] P. Lecoq and J. Varela. Clear-PEM, a dedicated PET camera for mammography. *Nuclear Instruments & Methods in Physics Research Section A: Accelerators, Spectrometers, Detectors and Associated Equipment*, 486(1-2):1–6, 2002.

[143] P. Bento, F. Gonçalves, C. Leong, P. Lousa, J. Nobre, J. Rego, P. Relvas, P. Rodrigues, J. C. Silva, L. Silva, I. C. Teixeira, J. P. Teixeira, A. Trindade, and J. Varela. Performance simulation studies of the Clear-PEM DAQ/trigger system. *IEEE Transactions on Nuclear Science*, 53(4):2102–2111, 2006.

[144] P. Amaral, P. Bruyndonckx, B. Carriço, M. Ferreira, J. Luyten, R. Moura, C. Ortigão, P. Rodrigues, J. C. da Silva, A. Trindade, and J. Varela. Long-term stability of the Clear-PEM detector modules. *Nuclear Instruments & Methods in Physics Research Section A: Accelerators Spectrometers Detectors and Associated Equipment*, 571(1-2):488–492, 2007.

[145] M.C. Abreu, J.D. Aguiar, F.G. Almeida, P. Almeida, P. Bento, B. Carriço, M. Ferreira, N.C. Ferreira, F. Goncalves, C. Leong, F. Lopes, P. Lousa, M.V. Martins, N. Matela, P.R. Mendes, R. Moura, J. Nobre, N. Oliveira, C. Ortigão,

L. Peralta, R. Pereira, J. Rego, R. Ribeiro, P. Rodrigues, J. Sampaio, A.I. Santos, L. Silva, J.C. Silva, P. Sousa, I.C. Teixeira, J.P. Teixeira, A. Trindade, and J. Varela. Design and evaluation of the Clear-PEM scanner for positron emission mammography. *IEEE Transactions on Nuclear Science*, 53(1):71–77, 2006.

[146] M. Ljungberg. Introduction to the Monte Carlo method. In M. Ljungberg and S-E. Strand, editors, *Monte Carlo Calculations in Nuclear Medicine: Applications in Diagnostic Imaging*. Institute of Physics Publishing, 1998.

[147] S. Agostinelli, J. Allison, K. Amako, H. Araujo, P. Arce, M. Asai, D. Axen, S. Banerjee, G. Barrand, F. Behner, J. Boudreau, L. Broglia, A. Brunengo, S. Chauvie, J. Chuma, R. Chytracek, G. Cooperman, G. Cosmo, P. Degtyarenko, A. Dell'Acqua, G. Depaola, D. Dietrich, A. Feliciello, C. Ferguson, G. Folger, F. Foppiano, A. Forti, S. Garelli, S. Giani, D. Gibin, J. J. G. Cadenas, I. Gonzalez, K. Hashimoto, H. Hasui, A. Heikkinen, A. Howard, V. Ivanchenko, A. Johnson, F. W. Jones, J. Kallenbach, N. Kanaya, M. Kawabata, Y. Kawabata, M. Kawaguti, S. Kelner, P. Kent, A. Kimura, M. Nagamatu, R. Nartallo, P. Nieminen, K. Ohtsubo, M. Okamura, S. O'Neale, Y. Oohata, K. Paech, J. Perl, A. Pfeiffer, M. G. Pia, F. Ranjard, A. Rybin, S. Sadilov, E. Di Salvo, G. Santin, et al. Geant4-a simulation toolkit. *Nuclear Instruments & Methods in Physics Research Section A: Accelerators Spectrometers Detectors and Associated Equipment*, 506(3):250–303, 2003.

[148] P. Rodrigues, R. Moura, C. Ortigão, L. Peralta, M. G. Pia, A. Trindade, and J. Varela. Geant4 applications and developments for medical physics experiments. *IEEE Transactions on Nuclear Science*, 51(4):1412–1419, 2004.

[149] A. Trindade. *Design and Evaluation of a Positron Emission Tomograph for Breast Cancer Imaging.* Ph.D dissertation, Technical University of Lisbon, 2007.

[150] R. Brun and F. Rademakers. ROOT - an object oriented data analysis framework. *Nuclear Instruments & Methods in Physics Research Section A: Accelerators, Spectrometers, Detectors and Associated Equipment*, 389:81–86, 1987.

[151] W. Segars. *Development of a new dynamic NURBS-based cardiac-torso (NCAT) phantom.* Ph.D dissertation, University of North Carolina, 2000.

[152] A. Trindade. Personal communication (Clear-PEM lesion detectability studies with OSEM-3D), 2005.

[153] L. Liberman and J.H. Menell. Breast imaging reporting and data system (BI-RADS). *Radiologic Clinics of North America*, 40(3):409–430, 2002.

[154] Y. Sugawara, M.A. Helvie, K.R. Zasadny, A.W. Neuhoff, S.M. Carlson, P.A. Saran, and R.L. Wahl. Normal breast FDG uptake on PET versus patient body weight, age and mammography density (abstract). *J Nucl Med*, 40:248P, 1999.

[155] N. Avril, S. Bense, S. I. Ziegler, J. Dose, W. Weber, C. Laubenbacher, W. Romer, F. Janicke, and M. Schwaiger. Breast imaging with fluorine-18-fdg pet: Quantitative image analysis. *Journal of Nuclear Medicine*, 38(8):1186–1191, 1997.

[156] SEER's Web-based Training Modules . *http* : *//training.seer.cancer.gov/module*$_a$*natomy/unit*1_3_*terminology*2_*planes.html*, Access date: September 2007.

[157] C. Labbé, K. Thielemans, H. Zaidi, and C. Morel. An object-oriented library incorporating efficient projection/backprojection operators for volume reconstruction in 3D PET. In *Procedings of 1999 International Meeting on Fully 3D Image Reconstruction in Radiology and Nuclear Medicine*, pages 138–141, 1999.

[158] Sauge, C. Labbé, C. Morel, M. Jacobson, A. Zverovich, and K Thielemans. STIR user's guide, version 1.0.

[159] K Thielemans. STIR - Overview for developers, version 1.0.

[160] M. L. Egger, C. Joseph, and C. Morel. Incremental beamwise backprojection using geometrical symmetries for 3D PET reconstruction in a cylindrical scanner geometry. *Physics in Medicine and Biology*, 43(10):3009–3024, 1998.

[161] M. L. Egger and C. Morel. Execution times of five reconstruction algorithms in 3D positron emission tomography. *Phys Med Biol*, 43(3):703–12, 1998.

[162] K. Thielemans, M.W. Jacobson, and D. Belluzzo. On various approximations for the projectors in iterative reconstruction algorithms for 3D-PET. In *Proceedings of 1999 International Meeting on Fully 3D Image Reconstruction in Radiology and Nuclear Medicine*, 1999.

[163] T. J. Hebert and R. Leahy. Fast methods for including attenuation in the EM algorithm. *IEEE Transactions on Nuclear Science*, 37(2):754–758, 1990.

[164] S. Mustafovic and K. Thielemans. Additive and multiplicative versions of the maximum a posteriori algorithm with median root prior. In *2001 IEEE Nuclear Science Symposium - Conference Record, Vols 1-4*, pages 1783–1785, 2002.

[165] P. R. Edholm and G. T. Herman. Linograms in image-reconstruction from projections. *IEEE Transactions on Medical Imaging*, 6(4):301–307, 1987.

[166] N. Matela, M. V. Martins, P. Rodrigues, A. Trindade, N. Oliveira, L. Peralta, N. C. Ferreira, J. Varela, and P. D. Almeida. System matrix calculation for Clear-PEM using ART and linograms. In *2004 IEEE Nuclear Science Symposium Conference Record, Vols 1-7*, pages 2601–2604. 2004.

[167] R. D. Badawi and P. K. Marsden. Developments in component-based normalization for 3D PET. *Phys Med Biol*, 44(2):571–94, 1999.

[168] N. C. Ferreira. *Contribuição para a quantificação em Tomografia por Emissão de Positrões no modo 3D*. Ph.D dissertation, Faculdade de Medicina da Universidade de Coimbra, 2001.

[169] C. Guerreiro, R. Bugalho, P. Rodrigues, N. Oliveira, M. V. Martins, N. Matela, H. Cordeiro, A. Trindade, N. C. Ferreira, P. Almeida, and J. Varela. Desenvolvimento de metodologias para correcção de normalização num tomógrafo PET aplicado à mamografia. Presented at V Congresso de Investigação em Medicina: Pedagogia e Ciência, Coimbra, 23-24 Novembro 2006.

[170] A. Trindade. Personal communication, 2006.

[171] P. Kinahan, R. R. Raylman, and D. Brasse. Planogram-based reconstruction using OSEM for a PEM-PET scanner. In *Procedings of 2005 International Meeting on Fully 3D Image Reconstruction in Radiology and Nuclear Medicine*, 2005.

[172] M.V. Martins, N. Matela, P. Rodrigues, A. Trindade, N. Oliveira, M. Correia, H. Cordeiro, N.C. Ferreira, J. Varela, and P. Almeida. Reconstruction of Clear-PEM data with STIR. In *Nuclear Science Symposium Conference Record, 2005 IEEE*, volume 4, pages 2098–2102, 2005.